frontiers | Research Topics

Cardiovascular neuromodulation: Mechanisms and therapies

Edited by
Khaled Qanud, Marco Mongillo, Tania Zaglia, Marianna Meo and Deborah Hunt

Published in
Frontiers in Cardiovascular Medicine

ISSN 1664-8714
ISBN 978-2-8325-3588-2
DOI 10.3389/978-2-8325-3588-2

About Frontiers

Frontiers is more than just an open access publisher of scholarly articles: it is a pioneering approach to the world of academia, radically improving the way scholarly research is managed. The grand vision of Frontiers is a world where all people have an equal opportunity to seek, share and generate knowledge. Frontiers provides immediate and permanent online open access to all its publications, but this alone is not enough to realize our grand goals.

Frontiers journal series

The Frontiers journal series is a multi-tier and interdisciplinary set of open-access, online journals, promising a paradigm shift from the current review, selection and dissemination processes in academic publishing. All Frontiers journals are driven by researchers for researchers; therefore, they constitute a service to the scholarly community. At the same time, the *Frontiers journal series* operates on a revolutionary invention, the tiered publishing system, initially addressing specific communities of scholars, and gradually climbing up to broader public understanding, thus serving the interests of the lay society, too.

Dedication to quality

Each Frontiers article is a landmark of the highest quality, thanks to genuinely collaborative interactions between authors and review editors, who include some of the world's best academicians. Research must be certified by peers before entering a stream of knowledge that may eventually reach the public - and shape society; therefore, Frontiers only applies the most rigorous and unbiased reviews. Frontiers revolutionizes research publishing by freely delivering the most outstanding research, evaluated with no bias from both the academic and social point of view. By applying the most advanced information technologies, Frontiers is catapulting scholarly publishing into a new generation.

What are Frontiers Research Topics?

Frontiers Research Topics are very popular trademarks of the *Frontiers journals series*: they are collections of at least ten articles, all centered on a particular subject. With their unique mix of varied contributions from Original Research to Review Articles, Frontiers Research Topics unify the most influential researchers, the latest key findings and historical advances in a hot research area.

Find out more on how to host your own Frontiers Research Topic or contribute to one as an author by contacting the Frontiers editorial office: frontiersin.org/about/contact

Cardiovascular neuromodulation: Mechanisms and therapies

Topic editors

Khaled Qanud — Feinstein Institute for Medical Research, United States
Marco Mongillo — University of Padua, Italy
Tania Zaglia — University of Padova, Italy
Marianna Meo — Boston Scientific, Netherlands
Deborah Hunt — Adelphi University, United States

Citation

Qanud, K., Mongillo, M., Zaglia, T., Meo, M., Hunt, D., eds. (2023). *Cardiovascular neuromodulation: Mechanisms and therapies*. Lausanne: Frontiers Media SA.
doi: 10.3389/978-2-8325-3588-2

Table of contents

frontiers | Frontiers in Cardiovascular Medicine

TYPE Editorial
PUBLISHED 23 May 2023
DOI 10.3389/fcvm.2023.1214496

OPEN ACCESS

EDITED AND REVIEWED BY
Guido Iaccarino,
University of Naples Federico II, Italy

*CORRESPONDENCE
Khaled Qanud
✉ kqanud@northwell.edu

†These authors have contributed equally to this work

RECEIVED 29 April 2023
ACCEPTED 08 May 2023
PUBLISHED 23 May 2023

CITATION
Hunt D, Mongillo M, Meo M, Zaglia T and Qanud K (2023) Editorial: Cardiovascular neuromodulation: mechanisms and therapies. Front. Cardiovasc. Med. 10:1214496. doi: 10.3389/fcvm.2023.1214496

Editorial: Cardiovascular neuromodulation: mechanisms and therapies

Deborah Hunt[1†], Marco Mongillo[2†], Marianna Meo[3†], Tania Zaglia[2†] and Khaled Qanud[4*]

[1]College of Nursing and Public Health, Adelphi University, Garden City, NY, United States, [2]Biomedical Sciences, University of Padova, Padova, Italy, [3]Boston Scientific, Boston Scientific, Kerkrade, Netherlands, [4]Bioelectronic Medicine, Feinstein Institutes for Medical Research, Manhasset, NY, United States

KEYWORDS

heart, neuromodulation, autonomic nervous system, heart failiure, hypertension, vagus nerve stimulation

Editorial on the Research Topic
Cardiovascular neuromodulation: mechanisms and therapies

High cardiovascular disease (CVDs) prevalence is projected to impact a large population across the world (1). Future therapeutic development efforts should take these estimates into account and provide new treatment modalities.

Modern neuromodulation therapies are an emerging non-pharmacological approach for the treatment of several disease conditions in basic research and clinical studies. The principial basis is to reduce or enhance, selectively, the altered neural activity that determined by the pathophysiological mechanisms, using neuro-medical devices (2). The main attractive subject is the autonomic nervous system (ANS) which maintains the body homeostasis, and the disruption of its integrity cornubites to the development and progression of many diseases including those affecting cardiovascular system and the immune components (3, 4).

The cardiac autonomic nervous system provides a closed-loop control of the heart and vascular system through a rich highly organized neural network composed of the brainstem, extracardiac sympathetic ganglia, vagus nerve and the intrinsic cardiac nerves system. Dysregulation at any level could lead ANS imbalance and, also, could trigger the chronic inflammatory process (5–7). Initially, dysregulation of the ANS may serve as a compensatory mechanism to maintain blood pressure and cardiac output in response to a cardiovascular insult, such as myocardial infarction and heart failure that associated with exaggerated sympathetic overflow and reduction of parasympathetic tone. However, if this dysregulation is not relieved by therapy, it becomes maladaptation and can lead to the development of a wide range of cardiovascular and non-cardiovascular conditions over time (8, 9). The beneficial effects of cardiac-brain-axis modulation were highlighted in multiple pre-clinical and clinical studies. For example, these studies included: renal denervation (RDN) to treat resistant hypertension, restore the baroreflex tone to treat orthostatic hypotension (OT), cardiac sympathectomy to suppress arrhythmias and vagus nerve stimulation (VNS) to reduce the progression of HF (**Figure 1**) (10–15).

In this issue the review by Ottaviani et al. has explored in detail the histological structure and the physiological role of vagus nerve, as the main tool to provide cardiovascular neuromodulation, and presented preclinical studies aimed at overcoming VNS limitations

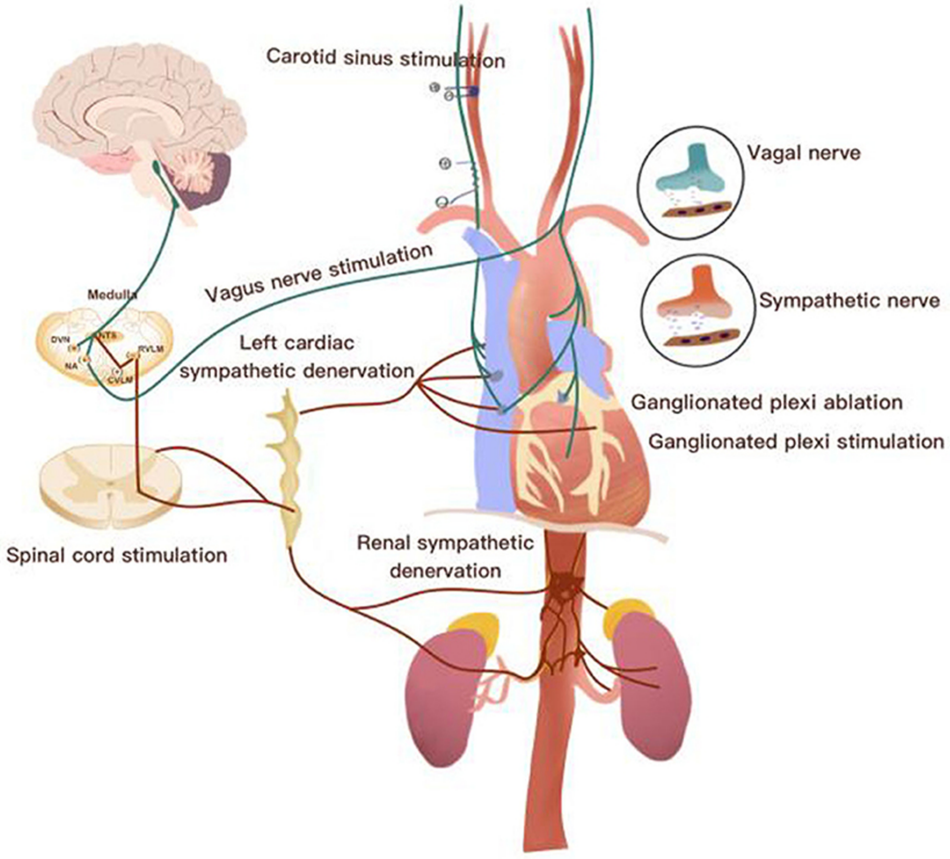

FIGURE 1
Overview of the neurocardiac axis and invasive neuromodulation approaches [Adapted from Chen et al., (10)].

through optimization of anatomical targets, development of novel neural interface technologies, and design of efficient VNS closed-loop protocols. The interesting findings that were documented in the manuscript by Rodrigues et al. who measured blindly the effects of acute and short-term transcranial direct current stimulation (tDCS) sessions on blood pressure and autonomic modulation in RHT subjects and showed a reduction in the central blood pressure. The heart rate variability (HRV) as a measure of ANS balance was reduced in association with post MI arrhythmic events which increased the mortality in the study that was conducted by Pizzo et al. There was also a U-shaped association between HRVI and mortality in hemodialysis AF patients as found in the data from Braunisch et al. The sophisticated study by Neely et al. examined whether macrophages could drive the sympathetic phenotype in Spontaneously Hypertensive Rats (SHR), before animals develop high pressure; their findings showed that macrophages can be potent enhancers of sympathetic neuronal calcium responsiveness and plays a role in peripheral sympathetic hyperactivity observed in the initial stages of hypertension.

Cardiovascular neuromodulation is an emerging field with ongoing research and clinical trials to investigate its safety and efficacy in various cardiovascular conditions. It has the potential to offer new treatment options for patients with cardiovascular conditions that fail to respond to the traditional therapies. However, further research is needed to fully understand its mechanisms of action and long-term outcomes.

Author contributions

The first four authors are equally contributed. All authors listed have made a substantial, direct, and intellectual contribution to the work and approved it for publication.

Acknowledgments

We thank all authors for their contribution to our Research Topic.

Conflict of interest

The authors declare that the research was conducted in the absence of any commercial or financial relationships that could be construed as a potential conflict of interest.

Publisher's note

References

1. Mohebi R, et al. Cardiovascular disease projections in the United States based on the 2020 census estimates. *J Am Coll Cardiol*. (2022) 80(6):565–78. doi: 10.1016/j.jacc.2022.05.033

2. Pathak YJ, et al. Digital health integration with neuromodulation therapies: the future of patient-centric innovation in neuromodulation. *Front Digit Health*. (2021) 3:618959. doi: 10.3389/fdgth.2021.618959

3. McCorry LK. Physiology of the autonomic nervous system. *Am J Pharm Educ*. (2007) 71(4):78. doi: 10.5688/aj710478

4. Kenney MJ, Ganta CK. Autonomic nervous system and immune system interactions. *Compr Physiol*. (2014) 4(3):1177–200. doi: 10.1002/cphy.c130051

5. Ross R. Atherosclerosis—an inflammatory disease. *N Engl J Med*. (1999) 340 (2):115–26. doi: 10.1056/NEJM199901143400207

6. Eskandari F, Webster JI, Sternberg EM. Neural immune pathways and their connection to inflammatory diseases. *Arthritis Res Ther*. (2003) 5(6):1–15. doi: 10.1186/ar1002

7. Malpas SC. Sympathetic nervous system overactivity and its role in the development of cardiovascular disease. *Physiol Rev*. (2010) 90(2):513–57. doi: 10.1152/physrev.00007.2009

8. Zhang DY, Anderson AS. The sympathetic nervous system and heart failure. *Cardiol Clin*. (2014) 32(1):33–45. doi: 10.1016/j.ccl.2013.09.010

9. Iaccarino G, et al. Role of the sympathetic nervous system in cardiac remodeling in hypertension. *Clin Exp Hypertens*. (2001) 23(1–2):35–43. doi: 10.1081/CEH-100001195

10. Chen M, Wang S, Li X, Yu L, Yang H, Liu Q, et al. Non-invasive autonomic neuromodulation is opening new landscapes for cardiovascular diseases. *Frontiers in physiology*. (2020) 11:550578.

11. Yoshida K, et al. Electrical vagal nerve stimulation ameliorates pulmonary vascular remodeling and improves survival in rats with severe pulmonary arterial hypertension. *JACC Basic Transl Sci*. (2018) 3(5):657–71. doi: 10.1016/j.jacbts.2018.07.007

12. Sabbah HN, et al. Vagus nerve stimulation in experimental heart failure. *Heart Fail Rev*. (2011) 16:171–8. doi: 10.1007/s10741-010-9209-z

13. Bertog SC, Sobotka PA, Sievert H. Renal denervation for hypertension. *JACC Cardiovasc Interv*. (2012) 5(3):249–58. doi: 10.1016/j.jcin.2011.12.011

14. O'Callaghan EL, et al. Deep brain stimulation for the treatment of resistant hypertension. *Curr Hypertens Rep*. (2014) 16:1–10. doi: 10.1007/s11906-014-0493-1

15. Zafeiropoulos S, et al. Autonomic neuromodulation for atrial fibrillation following cardiac surgery: JACC review topic of the week. *J Am Coll Cardiol*. (2022) 79(7):682–94. doi: 10.1016/j.jacc.2021.12.010

frontiers in Cardiovascular Medicine

ORIGINAL RESEARCH
published: 29 November 2021
doi: 10.3389/fcvm.2021.751052

U-Shaped Association of the Heart Rate Variability Triangular Index and Mortality in Hemodialysis Patients With Atrial Fibrillation

Matthias C. Braunisch[1], Christopher C. Mayer[2], Stanislas Werfel[1], Axel Bauer[3,4], Bernhard Haller[1,5], Georg Lorenz[1], Roman Günthner[1], Julia Matschkal[1], Quirin Bachmann[1], Stephan Thunich[1,6], Michaela Schlegl[1], Maximilian Ludwig[1], Christopher Holzmann-Littig[1], Tarek Assali[1], Martin Pachmann[7], Claudius Küchle[1], Lutz Renders[1], Siegfried Wassertheurer[2], Alexander Müller[1,8], Georg Schmidt[1,8], Uwe Heemann[1], Marek Malik[9,10] and Christoph Schmaderer[1]**

[1] Department of Nephrology, School of Medicine, Klinikum Rechts der Isar, Technical University of Munich, Munich, Germany, [2] Center for Health and Bioresources, Biomedical Systems, AIT Austrian Institute of Technology GmbH, Vienna, Austria, [3] University Hospital for Internal Medicine III, Medical University Innsbruck, Innsbruck, Austria, [4] Department of Cardiology, Munich University Clinic, DZHK (German Centre for Cardiovascular Research), Ludwig-Maximilians University, Munich, Germany, [5] School of Medicine, Klinikum Rechts der Isar, Institute of Medical Informatics, Statistics and Epidemiology (IMedIS), Technical University of Munich, Munich, Germany, [6] School of Medicine, Deutsches Herzzentrum München, Technical University of Munich, Munich, Germany, [7] Nephrocare DIZ-München, Rindermarkt, Munich, Germany, [8] School of Medicine, Klinik für Innere Medizin I, Klinikum Rechts der Isar, Technical University of Munich, Munich, Germany, [9] National Heart and Lung Institute, Imperial College London, London, United Kingdom, [10] Department of Internal Medicine and Cardiology, Faculty of Medicine, Masaryk University, Brno, Czechia

OPEN ACCESS

Edited by:
Khaled Qanud, Feinstein Institute for Medical Research, United States

Reviewed by:
Ankit Gilani, Weill Cornell Medicine, United States
Massimo Walter Rivolta, University of Milan, Italy

***Correspondence:**
Matthias C. Braunisch
Matthias.Braunisch@mri.tum.de
Christoph Schmaderer
Christoph.Schmaderer@mri.tum.de

Specialty section:
This article was submitted to Hypertension, a section of the journal Frontiers in Cardiovascular Medicine

Received: *31 July 2021*
Accepted: *31 October 2021*
Published: *29 November 2021*

Citation:
Braunisch MC, Mayer CC, Werfel S, Bauer A, Haller B, Lorenz G, Günthner R, Matschkal J, Bachmann Q, Thunich S, Schlegl M, Ludwig M, Holzmann-Littig C, Assali T, Pachmann M, Küchle C, Renders L, Wassertheurer S, Müller A, Schmidt G, Heemann U, Malik M and Schmaderer C (2021) U-Shaped Association of the Heart Rate Variability Triangular Index and Mortality in Hemodialysis Patients With Atrial Fibrillation. Front. Cardiovasc. Med. 8:751052. doi: 10.3389/fcvm.2021.751052

Background: Atrial fibrillation (AF) is common in hemodialysis patients and contributes to increased mortality. We aimed to examine heart rate variability triangular index (HRVI) in hemodialysis patients with AF as it has recently been reported to predict mortality in AF patients without kidney disease.

Methods: A total of 88 patients on hemodialysis with a medical history of AF or newly diagnosed AF underwent 24-h electrocardiography recordings. The primary endpoint of cardiovascular mortality was recorded during a median follow up of 3.0 years. Risk prediction was assessed by Cox regression, both unadjusted and adjusted for the Charlson Comorbidity Index and the Cardiovascular Mortality Risk Score.

Results: Median age was 76 years, median dialysis vintage was 27 months. Altogether, 22 and 44 patients died due to cardiovascular and non-cardiovascular causes. In 55% of patients AF was present during the recording. Kaplan-Meier plots of HRVI quartiles suggested a non-linear association between HRVI, cardiovascular, and all-cause mortality which was confirmed in non-linear Cox regression analysis. Adjusted linear Cox regression revealed a hazard ratio of 6.2 (95% CI: 2.1–17.7, $p = 0.001$) and 2.2 (95% CI: 1.3–3.8, $p = 0.002$) for the outer quartiles (combined first and fourth quartile) for cardiovascular and all-cause mortality, respectively. Patients in the first quartile were

more likely to have sinus rhythm whereas patients in the fourth quartile were more likely to have AF.

Conclusions: We found a U-shaped association between HRVI and mortality in hemodialysis AF patients. The results might contribute to risk stratification independent of known risk scores in hemodialysis AF patients.

Keywords: atrial fibrillation, heart rate variability triangular index, HRVi, cardiovascular mortality, hemodialysis, risk prediction

INTRODUCTION

End-stage kidney disease patients on hemodialysis have a markedly increased risk of cardiovascular morbidity and mortality (1). In long term 6-month recordings with implantable loop recorders, atrial fibrillation (AF) was detected in up to 41% of hemodialysis patients (2). Dialysis-specific factors such as a higher ultrafiltration is associated with a higher incidence of AF (3). The incidence and prevalence of AF are higher in hemodialysis patients than in the general population (4, 5). This is contributed by multiple factors including age, dialysis vintage, left atrial dilatation, and high overall disease burden of hemodialysis patients (4, 6). Among hemodialysis patients, those suffering from AF have higher morbidity and mortality (7). AF is therefore a common problem in hemodialysis patients and contributes to the increased cardiovascular risk (7).

Rapid shifts of electrolytes, plasma volume and acidosis changes impair electrophysiology and expose hemodialysis patients to an increased risk of arrhythmogenic conditions (8). Peri-dialytic fluid and electrolyte flux stimulates a sympathetic reaction responsible for the increased prevalence of AF during and immediately following hemodialysis (2).

Analysis of the cardiac autonomic nervous system by non-invasive assessment of the heart rate variability (HRV) has been restricted to patients without AF, thus, limiting risk prediction in AF patients. In patients without kidney disease, cardiac autonomic dysfunction was associated with a higher AF incidence during 19 years of follow-up (9). The atria have a close autonomic innervation and the AV node is susceptible to input form the autonomic nervous system (10–13). Therefore, the autonomic nervous system is likely also involved in AF. Overall, data on risk prediction in hemodialysis patients with AF is scarce and primarily focused on anticoagulation agents (14–16).

Recent data from the Swiss-AF study reported that in AF patients without kidney disease, heart rate variability triangular index (HRVI) predicted cardiovascular mortality (17) and identified clinically silent strokes (18). HRVI is an estimate of total variability of RR intervals and approximates sympathovagal imbalance.

We thus hypothesized that an association of HRVI with mortality might also be present in hemodialyzed AF patients.

MATERIALS AND METHODS

Study Design

The study investigated the "rISk strAtification in end-stage Renal disease" (ISAR)-cohort, obtained in a multicenter, prospective longitudinal observational cohort study (ClinicalTrials.gov; identifier number: NCT01152892) (19). The study protocol, conforming to the ethical guidelines of the Helsinki Declaration, was approved by the Medical Ethics Committee of the Klinikum Rechts der Isar of the Technical University Munich and of the Bavarian State Board of Physicians and is compliant with the STROBE guidelines. Patients were recruited from 17 hemodialysis centers in the greater Munich area between April 2010 and January 2014. All participants gave informed written consent. Inclusion criteria were age $\geq$18 years and dialysis vintage $\geq$90 days (19). Patients were excluded if pregnant or if suffering from ongoing infection or malignancy with a life expectancy $\leq$24 months (19). Out of the 519 patients meeting inclusion criteria, 390 consented to undergo 24-h Holter electrocardiogram (ECG) recording. Out of these patients, 25 were excluded due to paced rhythm while 6 other patients had technically unsuitable ECG data. In 271 patients, AF was absent both in the medical reports and in the 24-h ECGs. The subsequent HRV analysis utilized the remaining 88 patients (corresponding flow-chart shown in **Figure 1**).

Clinical Characteristics

Baseline demographic and clinical data were obtained from dialysis protocols and medical records. Medical records were screened for the diagnosis of AF and, where specified, coded into persistent/permanent or paroxysmal. Blood chemistry parameters were obtained prior to a midweek dialysis session. Comorbidities were assessed using an adapted version of the *Charlson Comorbidity Index* that has previously been validated for mortality prediction in hemodialysis patients (20). The index assigns numerical weights to comorbid conditions that range between 0 and 21 (20). Further, to assess cardiovascular mortality risk, the *Cardiovascular Mortality Risk Score* was calculated which has previously been developed and validated for the prediction of 2-year cardiovascular mortality in hemodialysis patients (21). The cardiovascular mortality risk score ranges between −11 and 39 points (21). The stroke risk factors are summarized in the CHA_2DS_2-VASc [Congestive heart failure, Hypertension, Age $\geq$75 years, Diabetes mellitus, Stroke, Vascular disease, Age 65–74 years, Sex category (female)] score (22).

Endpoints

Mortality was assessed using medical records, databases of individual dialysis centers, or by contacting the attending physician and/or the next of kin. Using this information, the ISAR Endpoint Committee classified the underlying causes of death (19). For the purposes of the present study, cardiovascular

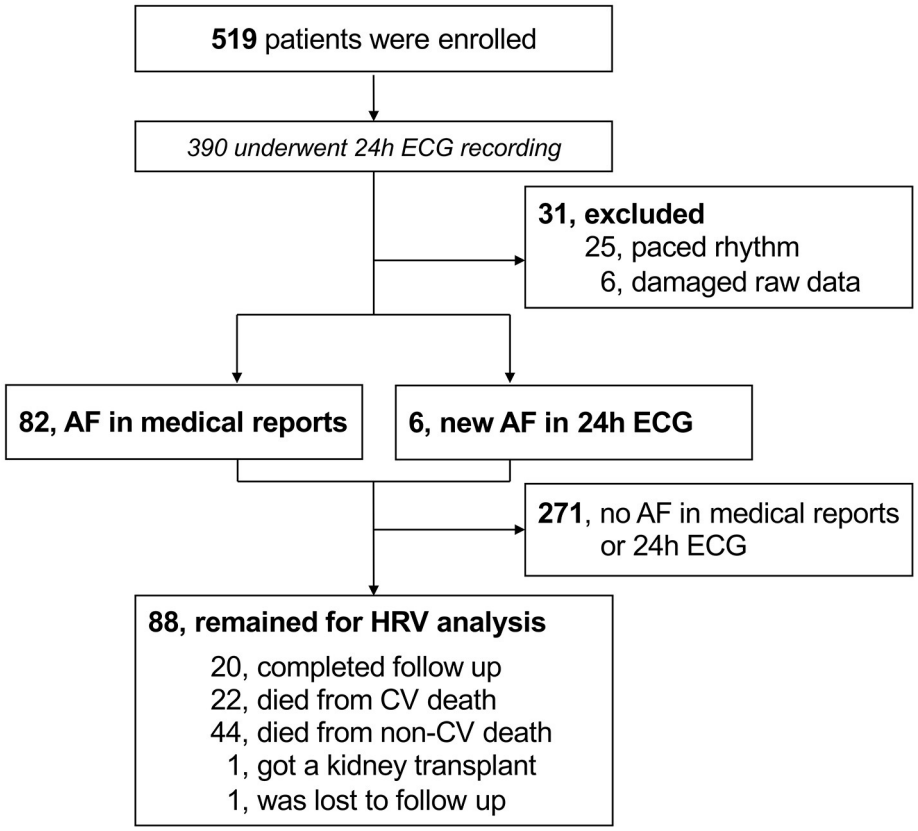

FIGURE 1 | Flow-chart of participants. AF, atrial fibrillation; CV, cardiovascular; ECG, electrocardiogram; HRV, heart rate variability.

and all-cause mortality was considered as the primary and secondary endpoint, respectively.

Electrocardiography

In each patient, a 24-h 12-lead ECG recording was obtained using the Lifecard CF digital Holter recorder (Delmar Reynolds/Spacelabs Healthcare, Nuremberg, Germany). All recordings started before a mid-week dialysis session. Reference ECG annotations, RR-interval measurements, and artifact elimination were performed using the software tools of the equipment (Pathfinder, Delmar Reynolds/Spacelabs Healthcare, Nuremberg, Germany; V9.027) (23). Afterwards, all RR-intervals of normal heart beats were exported to Matlab R2020a (the MathWorks, Inc., Natick, MA) and HRV parameters were computed using the 24-h RR interval series according to established standards (24). HRVI was calculated by dividing the total number of normal-to-normal (NN) intervals (HRVI numerator) by the number of NN-intervals in the modal 1/128-s bin (HRVI denominator) according to guidelines (24). Additional HRV parameters included expressions of overall long-term variability by the standard deviation of all NN intervals (SDNN), the standard deviation of the averages of NN intervals in all 5 min segments (SDANN), and the ultra-low frequency power range of $\leq$ 0.003 Hz (ULF); and expressions of short-term variability by the square root of the mean square of differences between adjacent NN intervals (RMSSD). Initially, AF episodes were detected and quantified in the 24-h recordings by the AF algorithm integrated in the Pathfinder software. Additionally, all 24-h ECGs were reviewed for the presence of AF manually. Electrocardiographic diagnosis of AF was made in agreement with the definition of the European Society of Cardiology, i.e., irregularly irregular RR-intervals, absence of distinct repeating P waves, and irregular atrial activations (22). If AF was confirmed in the manual review the relative duration of AF during the recording indicated by the pathfinder software was recorded. Paroxysmal AF was defined as an AF burden $\leq$20% in the 24-h recording.

Statistical Analysis

Categorical data are presented as frequencies and percentages. Continuous variables are expressed as mean $\pm$ standard deviation (SD) for normally distributed variables and as median and interquartile range (IQR) for variables with skewed distribution. To test for group differences, χ^2 test was used for categorical variables and independent samples *t*-test or Mann-Whitney-*U* test for continuous variables, as appropriate.

In survival analysis, we first used Kaplan-Meier curves comparing quartiles to reveal possible violations of proportional hazard assumptions, thus identifying non-linear (non-proportional) associations. Subsequently, we fitted univariate

TABLE 1 | Baseline characteristics.

	HRVI quartiles			
	Total ($n = 88$)	**Inner ($n = 44$)**	**Outer ($n = 44$)**	***P***
Age (years)	75.7 (±8.5)	75.1 (±9.4)	76.4 (±7.5)	0.48
Sex (female)	25 (28.4%)	10 (22.7%)	15 (31.8%)	0.34
Body mass index (kg/m^2)	25.6 (23.0–28.4)	25.4 (23.3–28.9)	25.8 (23.0–27.9)	0.91
Dialysis vintage (months)	27.0 (13.8–60.2)	27.0 (12.5–58.2)	27.5 (14.8–62.8)	0.61
Ultrafiltration rate (mL/h)	518.7 (±273.3)	511.1 (±275.4)	526.4 (±274.2)	0.79
Net ultrafiltration (L)	1.7 (±1.3)	1.8 (±1.2)	1.6 (±1.3)	0.56
Heart rate (bpm)	73.0 (±13.5)	76.9 (±13.0)	69.0 (±12.8)	0.005
Systolic blood pressure (mmHg)	130.5 (±25.5)	125.9 (±27.9)	135.1 (±22.4)	0.092
Diastolic blood pressure (mmHg)	67.9 (±15.3)	67.6 (±14.8)	68.2 (±15.9)	0.86
Kt/V	1.34 (±0.32)	1.36 (±0.28)	1.33 (±0.36)	0.62
Blood urea nitrogen (mg/dL)	58.5 (±17.4)	58.1 (±18.4)	59.0 (±16.5)	0.83
Phosphate (mmol/L)	1.68 (1.39–2.01)	1.69 (1.40–2.10)	1.60 (1.35–1.99)	0.43
Total calcium (mmol/L)	2.31 (±0.17)	2.29 (±0.17)	2.33 (±0.17)	0.26
Calcium *x* phosphate (mmol^2/L^2)	4.06 (±1.67)	4.24 (±2.03)	3.88 (±1.20)	0.31
Creatinine (mg/dL)	7.1 (±2.3)	7.3 (±2.3)	6.9 (±2.3)	0.43
High-sensitivity CRP (mg/dL)	0.58 (0.22–1.20)	0.57 (0.22–1.30)	0.59 (0.26–0.98)	0.92
Albumin (g/dL)	3.90 (3.70–4.20)	3.90 (3.70–4.11)	3.90 (3.67–4.20)	0.99
Parathyroid hormone (pg/mL)	226.5 (128.5–359.6)	246.0 (131.9–359.0)	197.0 (126.0–334.3)	0.61
Leukocytes (G/L)	7.01 (±2.04)	6.70 (±1.87)	7.32 (±2.18)	0.16
Total cholesterol (mg/dL)	173.6 (±47.6)	172.3 (±36.2)	174.9 (±57.0)	0.80
Charlson comorbidity index (0–21)	6.0 (4.0–8.0)	6.0 (4.0–8.0)	6.0 (4.0–8.0)	0.68
Cardiovascular mortality risk score (−11 to 39)	14.0 (10.0–17.0)	14.0 (9.0–18.0)	14.0 (11.0–16.0)	0.75
Diabetes mellitus	38 (43.2%)	19 (43.2%)	19 (43.2%)	1.00
History of myocardial infarction	25 (28.4%)	7 (15.9%)	18 (40.9%)	0.017
Left ventricular hypertrophy	30 (34.1%)	13 (29.5%)	17 (38.6%)	0.50
Left ventricular ejection fraction (%), $n = 22$	47 (±16)	45 (±17)	50 (±15)	0.48
Heart failure	25 (28.4%)	11 (25.0%)	14 (31.8%)	0.64
Peripheral artery disease	26 (29.5%)	15 (34.0%)	11 (25.0%)	0.48
Hypertension	84 (95.5%)	43 (97.8%)	41 (93.2%)	0.62
Coronary heart disease	39 (44.3%)	16 (36.4%)	23 (59.0%)	0.20
Cerebrovascular disease	17 (19.3%)	9 (20.5%)	8 (18.2%)	0.78
Smoking (ever)	14 (15.9%)	10 (22.7%)	4 (9.0%)	0.14
CHA_2DS_2-VASc score	3.5 (3.0–4.0)	3.0 (3.0–5.0)	4.0 (3.0–5.0)	0.28
Anticoagulation for hemodialysis				0.71
Heparin	73 (83.0%)	37 (84.0%)	36 (81.8%)	
Low-molecular-weight heparin	12 (13.6%)	5 (11.4%)	7 (15.9%)	
Argatroban	3 (3.4%)	2 (4.5%)	1 (2.3%)	
ß-blocker	64 (72.7%)	31 (70.5%)	33 (75.0%)	0.81
Additional anticoagulation				0.49
None	54 (61.4%)	29 (65.9%)	25 (56.8%)	
Vitamin K antagonists	30 (34.1%)	14 (31.8%)	16 (36.4%)	
Low-molecular-weight heparin	4 (4.5%)	1 (2.3%)	3 (6.8%)	
Antiplatelet therapy				0.74
None	37 (42.0%)	21 (47.7%)	16 (36.4%)	
ASS	42 (47.7%)	19 (43.2%)	23 (52.3%)	
ADP receptor blocker	4 (4.5%)	2 (4.5%)	2 (4.5%)	
Dual antiplatelet therapy	5 (5.7%)	2 (4.5%)	3 (6.8%)	
Amiodarone	4 (4.5%)	1 (2.3%)	3 (6.8%)	0.62
Antihypertensive medication	83 (94.3%)	41 (93.2%)	42 (95.5%)	1.0

Results are presented as mean (±SD) and median (interquartile range) for normally and non-normally distributed data, respectively; categorical data as total number (percentage). P-values present the results of group-wise comparisons of patients within the inner and outer quartiles of heart rate variability triangular index (HRVI). CHA_2DS_2-VASc, Congestive heart failure, Hypertension, Age ≥75 years, Diabetes mellitus, Stroke, Vascular disease, Age 65–74 years, Sex category (female).

and adjusted Cox regression models using penalized spline transformation with two degrees of freedom on HRVI (survival and splines packages). Adjusted models accounted for the *Charlson Comorbidity Index* and the *Cardiovascular Mortality Risk Score*. To overcome interpretation limitations of non-linear associations, values were dichotomized when in the first and forth quartile (outer quartiles) or in the second and third quartile (inner quartiles). Subsequently the dichotomized parameters were analyzed with regular univariate, and adjusted Cox regression models to estimate hazard ratios (HRs) for respective groups. Median follow-up was assessed by reverse Kaplan-Meier (25).

The predictive performance of the 24-h measurement vs. 5 min segments for HRVI and SDNN were compared using Harrell's C-index. For this purpose, 1000 adjusted Cox regressions for cardiovascular mortality with randomly selected 5 min intervals from the 24-h recordings were calculated. The mean ± SD C-indices were then compared with the C-index of the Cox regression model based on the 24-h measurement. Descriptive comparison of significant *p*-values for linear Cox regressions with 1000 randomly selected 5 min intervals were stratified for sinus rhythm and AF.

Kruskal-Wallis test was used to compare AF percentages amongst HRVI quartiles. *Post-hoc* analysis was performed with the Wilcoxon test and adjusted for multiple testing using the Bonferroni method.

Multivariable binary logistic regression with AF as dependent variable and the HRVI numerator and denominator as independent variables was used to obtain odds ratios with corresponding 95% confidence interval.

All tests were conducted two-sided and $p < 0.05$ were considered significant. Statistical analysis was performed using R version 4.0.2 (R Foundation for statistical Computing, Vienna, Austria).

RESULTS

Patient Characteristics

The final study population included 88 patients (25 women) with a median follow-up of 3.0 years (IQR 1.5–5.8) (**Figure 1**). The median age was 76.4 years (70.6–80.6). The median dialysis vintage was 27.0 months (13.8–60.2). ß-blockers were taken by 64 patients (72.7%). Amiodarone was prescribed to 4 patients (4.5%) (**Table 1**). Sex differences are listed in **Supplementary Table 1**. Female patients had a significant higher dialysis vintage, systolic blood pressure, had significantly less frequently a history of myocardial infarction and coronary heart disease and were significantly less likely to smoke (**Supplementary Table 1**). **Table 2** shows HRV measurements. Median HRVI was 26.3, quartiles of HRVI ranged from ≤18.245 ($n = 22$), 18.246–26.279 ($n = 22$), 26.280–34.307 ($n = 22$), and ≥34.08 ($n = 22$). Patients in the external quartiles were not significantly different from patients in the inner quartiles, except for heart rate which was significantly higher in patients in the inner quartiles and a history of myocardial infarction which was significantly more often present in patients in the outer quartiles (**Table 1**).

TABLE 2 | Measures of heart rate variability.

Parameter	Unit	Value
HRVI		28.3 ±12.7
SDNN	ms	102.0 (77.5–136.9)
SDANN	ms	83.1 ± 28.0
RMSSD	ms	33.5 (16.2–60.9)
ULF	ms^2	3970.1 (2460.4–6020.8)

Mean ± standard deviation or median and interquartile range, as appropriate. HRVI, HRV triangular index: number of NN intervals over the number of NN-intervals in the modal bin; SDNN, standard deviation of all NN intervals; SDANN, standard deviation of the averages of NN intervals in all 5-min segments of 24 h recording; RMSSD, square root of the mean square of differences between adjacent NN intervals; ULF, ultra-low frequency.

In 6 patients (2.2%) AF was newly diagnosed using the 24-h ECG (**Figure 1**). At baseline, 42 (47.7%), 6 (6.8%), and 40 (45.5%) patients presented with permanent AF, paroxysmal AF, and sinus rhythm, respectively. The median percentage of AF burden in the 24-h recordings was 99.7% (87.3–99.9), 3.0% (1.1–3.8), and 0% (0–0) in patients with permanent AF, paroxysmal AF, and sinus rhythm, respectively. Of the 40 patients in sinus rhythm, paroxysmal and permanent AF had been previously documented in medical reports of 25 and 13 patients, respectively. In two patients, the type of the previously documented AF was not specified.

In comparison to the overall ISAR cohort, the patient population of the current study was significantly older, sicker and had higher cardiovascular mortality risk scores and shorter dialysis vintage (**Supplementary Table 2**).

Anticoagulation

Overall, the median CHA_2DS_2-VASc score was 3.5 (3.0–4.0). A CHA_2DS_2-VASc score of ≥2 was present in 87 patients (98.9%). Anticoagulation for dialysis was prescribed in 73 (83.0%) with heparin, in 12 (13.6%) with low-molecular-weight heparin, and in 3 (3.4%) with argatroban. Additional anticoagulation was prescribed in 34 patients (38.6%), with 30 (34.1%) patients taking vitamin K antagonists and 4 (4.5%) taking low-molecular-weight heparin. No novel oral anticoagulants were prescribed. Antiplatelet therapy was present in 42 patients (47.7%) on acetylsalicylic acid, 4 (4.5%) on adenosine diphosphate (ADP) receptor inhibitors, and 5 (5.7%) on dual antiplatelet therapy.

Association of HRVI and Mortality

Altogether, 22 and 44 patients died due to cardiovascular and non-cardiovascular causes, respectively. Details of cardiovascular and non-cardiovascular mortality are presented in **Supplementary Table 3**. One patient was censored due to kidney transplantation and one patient was lost to follow-up.

Kaplan-Meier plots of HRVI quartiles suggested a non-linear association between HRVI, cardiovascular, and all-cause mortality (**Figures 2A,B**). **Figures 2C,D** depict the hazard ratios relative to the median HRVI resulting from univariate non-linear Cox regression analysis for cardiovascular and all-cause mortality, respectively. Non-linear Cox regression analysis revealed a non-linear behavior of HRVI in univariate and

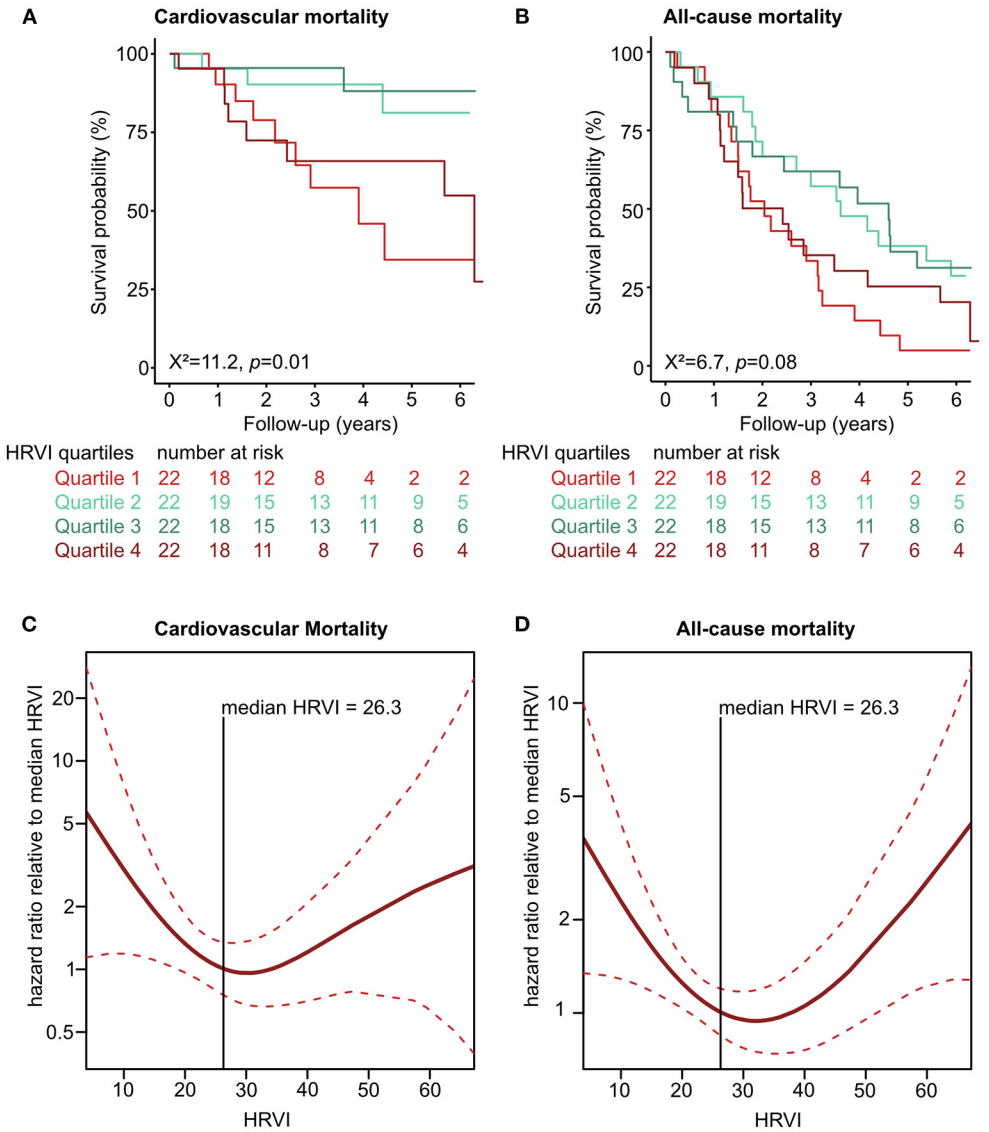

FIGURE 2 | Non-linear association of HRVI with mortality. Univariate association of HRVI with cardiovascular **(A)** and all-cause mortality **(B)** in Kaplan-Meier analyses. Non-linear univariate Cox regression analysis using penalized smoothing splines for cardiovascular **(C)** and all-cause mortality **(D)**. HRVI, heart rate variability triangular index.

adjusted analysis for cardiovascular mortality (**Table 3**) and all-cause mortality (**Table 4**). When categorizing HRVI into the inner and outer quartiles a value within the outer quartiles was associated with a 6.1- and 2.2-times increased risk for cardiovascular mortality and all-cause mortality in adjusted analysis, respectively. The 3-year cardiovascular mortality rate was 6.8 and 29.5% for the inner and outer HRVI quartile group, respectively, whilst the corresponding 6-year cardiovascular mortality rates were 11.4 and 36.4%, respectively (**Figure 3A**). For all-cause mortality the 3-year mortality rate was 38.6 and 61.4%, and the 6-year mortality rate was 65.9 and 81.8% for the inner and outer HRVI quartile group, respectively (**Figure 3B**). **Figure 4** shows similar results when the cohort is stratified at the border of the first HRVI quartile. Exploratory analysis of HRVI numerator and denominator revealed heterogenous results (**Supplementary Figure 1** and **Supplementary Table 4**).

C-index comparison of adjusted non-linear Cox regressions showed that the concordance of the Cox regression with the 24-h HRVI measurement was 7 and 5% higher than the mean concordances of 1000 Cox regressions with randomly selected 5 min HRVI segments for cardiovascular and all-cause mortality, respectively (cardiovascular mortality: 0.73 vs. 0.68 ± 0.02; all-cause mortality: 0.68 vs. 0.65 ± 0.01). Similarly, C-index comparison for 24-h SDNN measurements vs. 5 min segments differed by 12% for cardiovascular mortality (0.73 vs. 0.65 ± 0.01). Furthermore, when stratifying patients into sinus rhythm

TABLE 3 | Linear and non-linear associations of risk variables with cardiovascular mortality in unadjusted and adjusted Cox regression analysis.

		Linear term				Non-linear term			
		Unadjusted		Adjusted		Unadjusted		Adjusted	
Variable	**Unit**	**HR (95% CI)**	***P***	**HR (95% CI)**	***P***	**HR (95% CI)**	***P***	**HR (95% CI)**	***P***
HRVI	1	–	–	–	–	NA	0.031	NA	0.032
HRVI (quartiles)	2 + 3 vs. 1 + 4	4.6 (1.7–12.6)	0.003	6.1 (2.1–17.7)	0.001	–	–	–	–
Cardiovascular mortality risk score	1 point	1.1 (0.9–1.2)	0.09	1.2 (1.0–1.3)	0.032	–	–	1.1 (0.9–1.2)	0.094
Charlson Comorbidity Index	1 point	1.1 (0.9–1.2)	0.29	1.1 (0.9–1.2)	0.54	–	–	1.0 (0.9–1.2)	0.64

TABLE 4 | Linear and non-linear associations of risk variables with all-cause mortality in unadjusted and adjusted Cox regression analysis.

		Linear term				Non-linear term			
		Unadjusted		Adjusted		Unadjusted		Adjusted	
Variable	**Unit**	**HR (95% CI)**	***P***	**HR (95% CI)**	***P***	**HR (95% CI)**	***P***	**HR (95% CI)**	***P***
HRVI	1	–	–	–	–	NA	0.004	NA	0.003
HRVI (quartiles)	2 + 3 vs. 1 + 4	1.8 (1.1–3.0)	0.018	2.2 (1.3–3.8)	0.002	–	–	–	–
Cardiovascular mortality risk score	1 point	1.1 (1.0–1.2)	0.0004	1.1 (1.1–1.2)	0.0006	–	–	1.1 (1.0–1.2)	0.0008
Charlson Comorbidity Index	1 point	1.1 (1.0–1.2)	0.02	1.1 (0.9–1.2)	0.11	–	–	1.1 (0.09–1.2)	0.21

Adjusted model for Charlson Comorbidity Index and Cardiovascular Mortality Risk Score. CI, confidence interval; NA, not applicable due to non-linear fitting of the models on two degrees of freedom on HRVI.

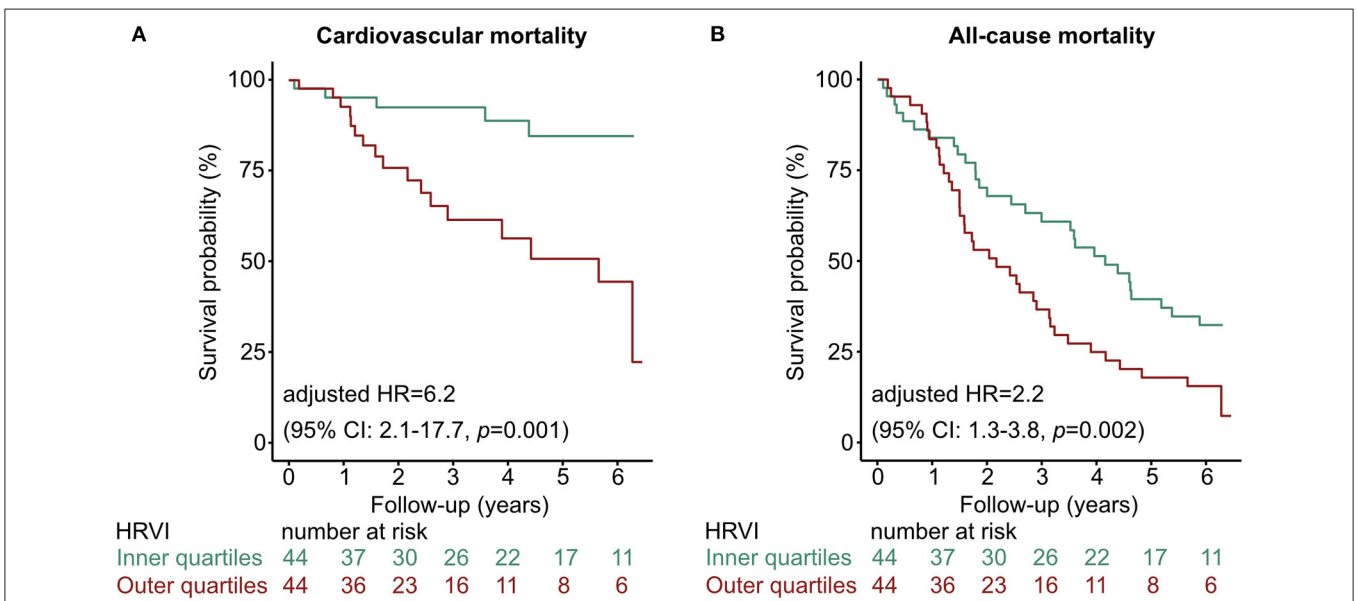

FIGURE 3 | Kaplan-Meier curves of the inner vs. outer quartiles of HRVI for **(A)** cardiovascular mortality and **(B)** all-cause mortality. Hazard ratio after adjustment for the *Charlson Comorbidity Index* and the *Cardiovascular Mortality Risk Score*. CI, confidence interval; HR, hazard ratio; HRVI, heart rate variability triangular index.

and AF, patients in sinus rhythm were descriptively more likely to have a significant *p*-value in the linear Cox regression model than AF patients (**Supplementary Figure 2**).

The median percentage of AF burden during 24-h recordings in the 48 patients with AF was 22.7% (6.6–45.5), 99.9% (85.8–99.9), 98.8% (88.0–99.9), and 99.8% (88.0–99.9) in the quartiles of HRVI ($p = 0.008$). *Post-hoc* analysis revealed significant difference of percentages between the first and the second (adjusted $p = 0.03$) and the first and the fourth quartile (adjusted $p = 0.003$). **Figure 5** displays stratifications of patients in AF or sinus rhythm. Median follow up was 2.0 and 3.9 years for patients with AF or sinus rhythm, respectively. The mean heart rate was significantly higher in AF patients compared to patients in sinus rhythm (76.6 ± 14.2 vs. 68.7 ± 11.2 bpm, $p = 0.006$). However,

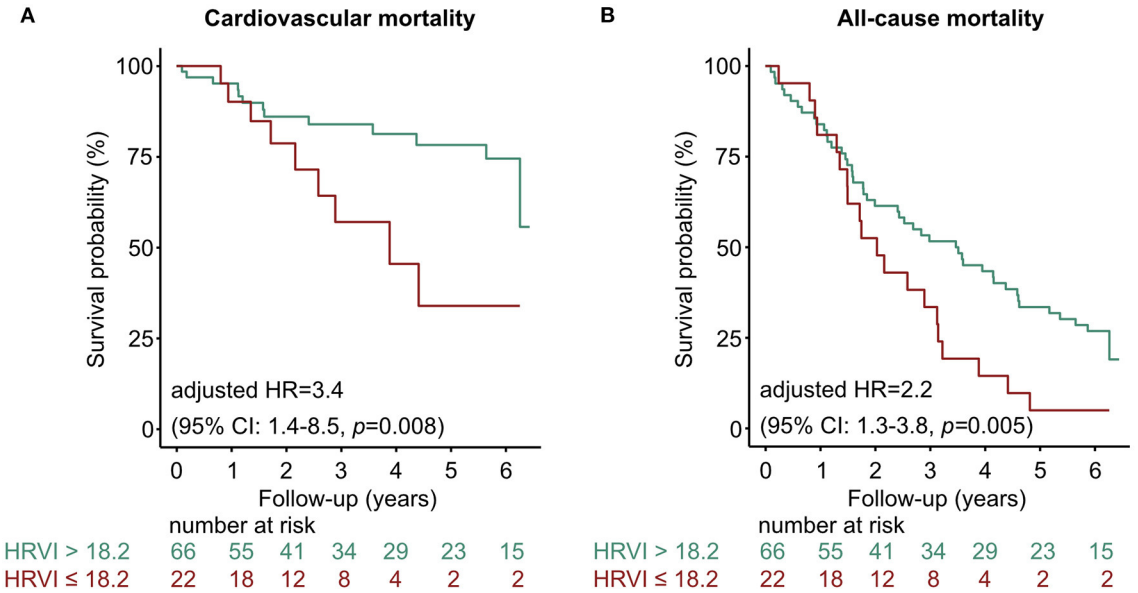

FIGURE 4 | Kaplan-Meier curves stratified at the border of the first HRVI quartile for **(A)** cardiovascular and **(B)** all-cause mortality. The 3-year cardiovascular mortality rate was 31.8 and 13.6% if HRVI was ≤18.246 and >18.246, respectively. The 6-year cardiovascular mortality rate was 40.9 and 18.2% if HRVI was ≤18.246 and >18.246, respectively. For all-cause mortality the 3-year mortality rate was 63.4 and 45.5%, and the 6-year mortality rate was 90.9 and 68.2% if HRVI was ≤18.246 and >18.246, respectively. Hazard ratios are adjusted for the *Charlson Comorbidity Index* and the *Cardiovascular Mortality Risk Score* and show a 3.4- and 2.2-times increased risk of cardiovascular and all-cause mortality if HRVI was ≤ 18.246, respectively. CI, confidence interval; HR, hazard ratio; HRVI, heart rate variability triangular index.

patients with AF had significantly lower ratios of normal to all beats (39.8% [31.3–52.0] vs. 93.4% [85.3–96.5], $p < 0.001$). The median ratio of normal beats was 84.5% (71.3–95.6), 90.1% (52.7–96.4), 54.3% (45.1–92.4), and 32.7% (25.8–40.0) in the quartiles of HRVI ($p < 0.001$). *Post-hoc* analysis revealed significant differences of the fourth to the first, second or third quartile (each adjusted $p < 0.001$). Addition of the presence of AF or sinus rhythm or the normal beat ratio to the adjusted Cox regression models did not change the results (**Tables 5**, **6**). Furthermore, only the HRVI numerator was associated with the presence of AF (odds ratio per 1,000 normal-to-normal intervals: 0.92, 95% confidence interval: 0.88–0.96, $p < 0.001$). **Figure 6** displays the HRVI numerator and denominator with stratification for AF or sinus rhythm, cardiovascular and all-cause mortality.

Exploratory analysis of other HRV parameters that express overall long-term (SDNN, SDANN, ULF) and short-term (RMSSD) variability towards mortality revealed inconsistent results (**Table 7**).

DISCUSSION

In this study, we found a U-shaped association of HRVI and mortality in hemodialysis AF patients. Stratification into inner and outer quartiles of HRVI was significantly associated with cardiovascular and all-cause mortality with a hazard ratio of 6.1 and 2.2 in adjusted models.

The left part of the U-shaped curve corresponds to depressed variability with impaired function of the autonomic nervous system which was primarily present in patients in sinus rhythm who had an AF history. According to the HRV Task Force, HRVI<15 is severely depressed (24). In the Swiss-AF study, dichotomizing the cohort at HRVI median of 14.3 led to association with mortality. In the present study, the cut-off of the first quartile was 18.2. When used to stratify patients below or above 18.2, patients below this cut-off were similarly exposed to increased mortality as when stratified by inner and outer HRVI quartiles. Furthermore, in our dataset it seems that HRVI values below the cohort median of 26.3, which comprises primarily patients in sinus rhythm, have an almost linear relationship to mortality. When randomly selecting 5 min segments, patients in sinus rhythm were more likely to have a significant *p*-value in the linear Cox regression model. HRVI has not yet been examined in hemodialyzed AF patients. In 120 hemodialysis patients without AF, HRVI was associated to cardiac death with a cohort median of 23.5 (26). Therefore, HRVI values might be higher in hemodialysis patients compared to patients without kidney disease.

The right part of the U-shaped curve could be explained by a higher prevalence of AF and a lower ratio of normal beats in the fourth HRVI quartile which is in line with a higher odds ratio for AF in case of lower HRVI numerator. Higher HRVI values correspond to a more diffuse pattern of RR intervals. Importantly, adding the presence of AF or the ratio of normal beats to the adjusted models did not change the non-linear association between HRVI and mortality. Linear relationships had been observed for patients without kidney disease with and without AF (17, 27). Limited evidence for a U-shaped behavior of HRV could be found and might

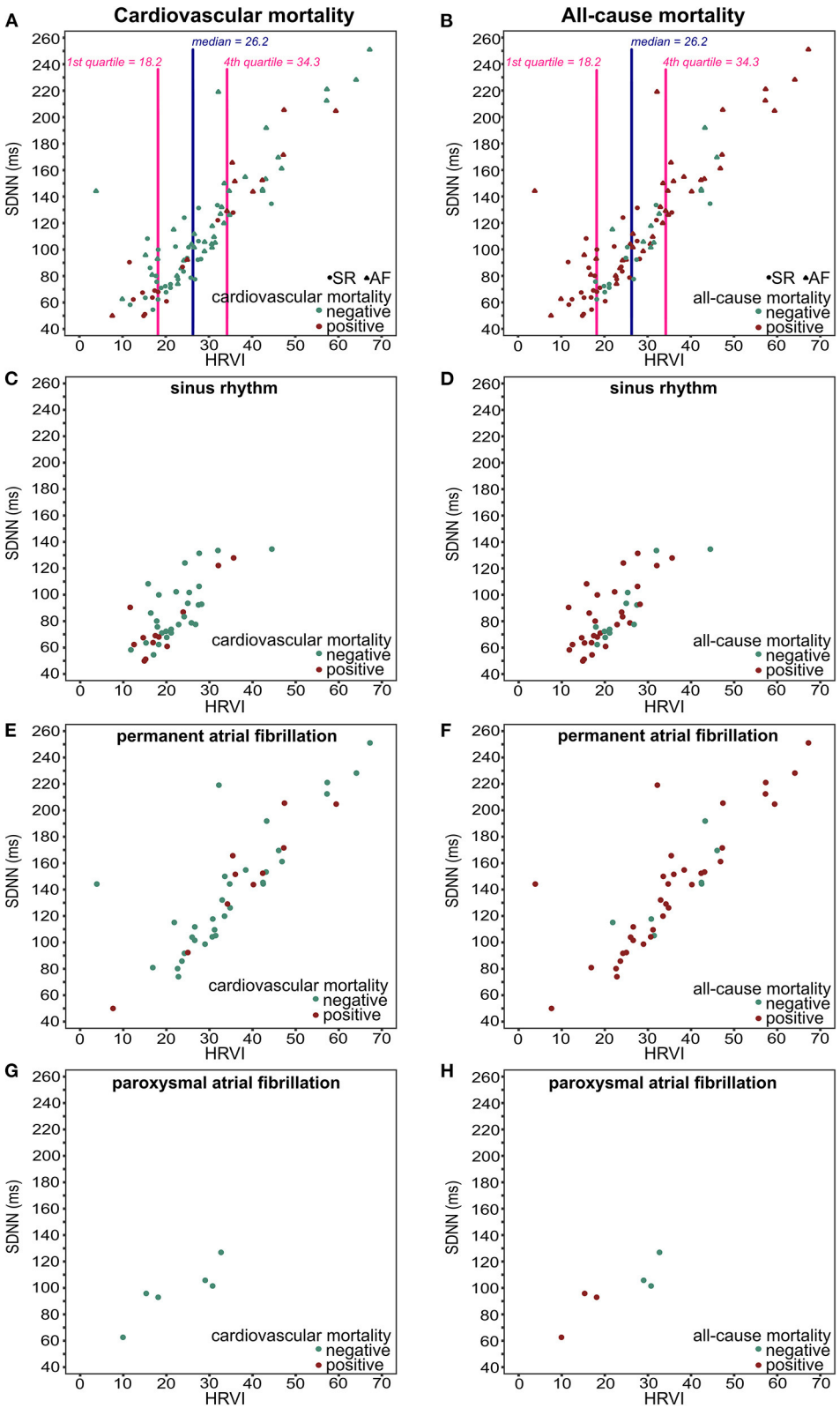

FIGURE 5 | Scatter plots of HRVI and SDNN for all patients **(A,B)**, patients in sinus rhythm **(C,D)**, patients in permanent atrial fibrillation **(E,F)**, and patients in paroxysmal atrial fibrillation **(G,H)** displayed for cardiovascular mortality (left column), and for all-cause mortality (right column). HRVI, heart rate variability triangular index; SDNN, standard deviation of all NN intervals.

TABLE 5 | Sensitivity analysis of adjusted linear and non-linear Cox regression models additionally including the presence of atrial fibrillation (AF) or sinus rhythm (SR) for **(A)** cardiovascular and **(B)** all-cause mortality.

Variable	Unit	Adjusted model			
		linear		Non-linear	
		HR (95% CI)	*P*	HR (95% CI)	*P*
(A) Cardiovascular mortality					
HRVI	1	–	–	NA	0.027
HRVI (quartiles)	2 + 3 vs. 1 + 4	6.7 (2.2–19.9)	0.0007	–	–
Cardiovascular mortality risk score	1 point	1.2 (1.0–1.3)	0.020	1.1 (0.9–1.2)	0.08
Charlson Comorbidity Index	1 point	1.0 (0.9–1.2)	0.61	1.0 (0.9–1.2)	0.70
AF or SR	AF present	0.6 (0.3–1.5)	0.31	0.9 (0.3–2.3)	0.75
(B) All-cause mortality					
HRVI	1	–	–	NA	0.0034
HRVI (quartiles)	2 + 3 vs. 1+4	2.1 (1.3–3.6)	0.005	–	–
Cardiovascular mortality risk score	1 point	1.1 (1.0–1.2)	0.002	1.1 (1.0–1.2)	0.007
Charlson Comorbidity Index	1 point	1.1 (1.0–1.2)	0.09	1.1 (1.0–1.2)	0.09
AF or SR	AF present	1.3 (0.8–2.1)	0.36	1.8 (1.0–3.2)	0.06

Adjusted model includes HRVI, the Charlson Comorbidity Index and Cardiovascular Mortality Risk Score, and atrial fibrillation vs. sinus rhythm. CI, confidence interval; HR, hazard ratio; HRVI, heart rate variability triangular index; NA, not applicable due to non-linear fitting of the models on two degrees of freedom on HRVI.

TABLE 6 | Sensitivity analysis of adjusted linear and non-linear Cox regression models additionally including the ratio of normal beats for **(A)** cardiovascular and **(B)** all-cause mortality.

Variable	Unit	Adjusted model			
		linear		Non-linear	
		HR (95% CI)	*P*	HR (95% CI)	*P*
(A) Cardiovascular mortality					
HRVI	1	–	–	NA	0.037
HRVI (quartiles)	2 + 3 vs. 1 + 4	6.4 (2.1–19.3)	0.001	–	–
Cardiovascular mortality risk score	1 point	1.2 (1.0–1.3)	0.030	1.1 (1.0–1.2)	0.15
Charlson Comorbidity Index	1 point	1.1 (0.9–1.2)	0.52	1.0 (0.9–1.2)	0.65
Ratio of normal beats	1%	1.4 (0.3–6.3)	0.70	0.4 (0.1–2.5)	0.35
(B) All-cause mortality					
HRVI	1	–	–	NA	0.003
HRVI (quartiles)	2 + 3 vs. 1 + 4	2.1 (1.2–3.7)	0.007	–	–
Cardiovascular mortality risk score	1 point	1.1 (1.0–1.2)	0.002	1.1 (1.0–1.2)	0.006
Charlson Comorbidity Index	1 point	1.1 (1.0–1.2)	0.12	1.1 (1.0–1.2)	0.21
Ratio of normal beats	1%	0.8 (0.3–2.0)	0.64	0.4 (0.1–1.0)	0.06

Adjusted model includes HRVI, the Charlson Comorbidity Index and Cardiovascular Mortality Risk Score, and ratio of normal to overall beats. CI, confidence interval; HR, hazard ratio; HRVI, heart rate variability triangular index; NA, not applicable due to non-linear fitting of the models on two degrees of freedom on HRVI.

be physiologically plausible (28). Dividing the HRVI in its numerator and denominator was not able to further explain the U-shaped profile. However, we assume that the U-shape displays rather irregular heart periods than an actual autonomic influence. Still, it is unclear if autonomic nervous system modulations influence the RR-interval irregularity in AF. Further studies have to confirm the non-linear risk relationships in AF patients on hemodialysis and to investigate whether disease-specific cut-offs exist. Furthermore, it might be of interest to examine HRVI in larger cohorts of only permanent AF patients. In general, however, examination of non-linear relationships should be considered when examining HRVI.

Patients in the Swiss-AF study were younger (73 vs. 76 years) and kidney disease was not present (17). Also, the Swiss-AF study recorded short-term ECGs of ≥5 min whereas we recorded 24-h ECGs. We found shorter recording periods to be less accurate for risk prediction than 24-h recordings. Most probably due to longer recording times in the present study, sinus rhythm in the ECG was present in 46% of our patients whereas in 58% of patients in the Swiss-AF study which might furthermore

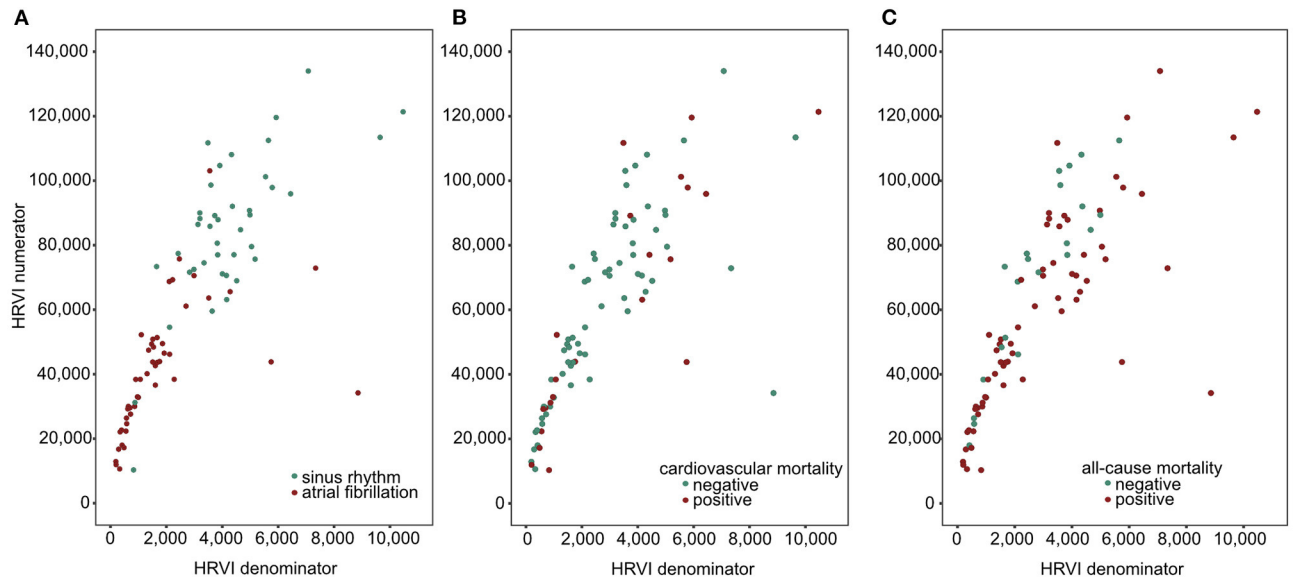

FIGURE 6 | Scatter plots of HRVI numerator and denominator coded for atrial fibrillation or sinus rhythm **(A)**, cardiovascular **(B)**, and all-cause mortality **(C)**. HRVI, heart rate variability triangular index.

TABLE 7 | Linear and non-linear associations of risk variables with **(A)** cardiovascular mortality and **(B)** all-cause mortality in unadjusted and adjusted Cox regression analysis.

		Linear term				Non-linear term			
		Unadjusted		Adjusted		Unadjusted		Adjusted	
Variable	**Unit**	**HR (95% CI)**	***P***	**HR (95% CI)**	***P***	**HR (95% CI)**	***P***	**HR (95% CI)**	***P***
(A) Cardiovascular mortality									
SDNN	ms	0.9 (0.9–1.0)	0.92	0.9 (0.9–1.0)	0.62	NA	0.033	NA	0.032
SDANN	ms	0.9 (0.9–1.0)	0.36	1.0 (0.9–1.0)	0.25	NA	0.16	NA	0.21
RMSSD	ms	1.0 (0.9–1.0)	0.59	1.0 (0.9–1.0)	0.76	NA	0.26	NA	0.19
ULF	ms^2	0.9 (0.9–1.0)	0.18	1.0 (1.0–1.0)	0.19	NA	0.072	NA	0.12
(B) All-cause mortality									
SDNN	ms	1.0 (0.9–1.0)	0.32	1.0 (1.0–1.0)	0.93	NA	0.17	NA	0.18
SDANN	ms	1.0 (1.0–1.0)	0.73	1.0 (1.0–1.0)	0.35	NA	0.031	NA	0.07
RMSSD	ms	1.1 (1.0–1.0)	0.049	1.0 (1.0–1.0)	0.14	NA	0.43	NA	0.35
ULF	ms^2	1.0 (1.0–1.0)	0.18	1.0 (1.0–1.0)	0.15	NA	0.007	NA	0.037

Adjusted model includes the predictor, the Charlson Comorbidity Index, and Cardiovascular Mortality Risk Score. CI, confidence interval; HR, hazard ratio; NA, not applicable; SDNN, standard deviation of all NN intervals; SDANN, standard deviation of the averages of NN intervals in all 5-min segments of 24 h recording; RMSSD, square root of the mean square of differences between adjacent NN intervals; ULF, ultra-low frequency.

explain why we found a U-shaped association instead of a linear association between HRVI and mortality.

Compared to other HRV parameters that express overall variability only HRVI was able to predict both cardiovascular and all-cause mortality. Interestingly, other parameters such as SDNN and ULF also displayed a non-linear relationship to mortality. HRVI might be more robust and reproducible as it is, by design, less affected by artifacts and noise (29–31) and as it does not require artifact-clear ECG recognition (32).

One third of the dialysis cohort had either a medical history of AF or AF on the recorded ECG. This prevalence of AF in our cohort is comparable to similar hemodialysis populations (6). In 2% of patients, we made a new AF diagnosis. Although this might seem to represent a low proportion, higher morbidity and mortality in AF (6, 7) suggest that regular long-term ECG recordings should be considered since AF might be undetected in non-permanent recordings, e.g., by implantable loop recorders (2).

Hemodialysis patients with AF are characterized by a high morbidity and frailty (6, 7). Also, patients from our cohort were much sicker and older compared to hemodialysis patients without AF participating in the ISAR study. When

dividing the cohort into inner and outer quartiles of HRVI, patients did not differ in comorbidities, age, and other factors. Interestingly, the *Charlson Comorbidity Index*, considered to have a strong predictive power of mortality in hemodialysis patients, was not associated with mortality in our data. In clinical practice, a detailed assessment of comorbidities generally allows approximate clinical estimates of individual risk. Nevertheless, this is unlikely sufficient in hemodialysis AF patients. Thus, HRVI has added benefit in hemodialysis AF patients with predicted risk independent of the *Cardiovascular Mortality Risk Score* (21).

Analysis of HRVI might also be possible in patients with a considerable AF burden in the recorded ECG. Furthermore, it seems particularly useful in AF patients. Consistent with other reports (33), we have not found an association of HRVI and cardiovascular mortality in hemodialysis patients without AF (34), even when considering non-linear associations (data not shown).

Finally, given the high risk of mortality in AF hemodialysis patients, establishing a clinical tool for identification of high-risk among this group is important. Results from this and previous trials might allow a general inclusion of AF patients into analyses of the autonomic nervous system when focusing on HRV parameters linked to the total variability (17, 18). Future studies should also investigate morbidities and instances of non-fatal hemorrhagic and thromboembolic strokes or bleeding events. Possibly, HRVI might also help in stratifying patients for oral anticoagulation which, in hemodialysis patients, is subject to an ongoing debate.

LIMITATIONS

Limitations of the present study have to be considered. This is a rather small cohort, though one of the largest prospective dialysis cohorts where 24-h ECGs are available. The method of HRV calculation which was originally only developed for analyses in sinus rhythm ECGs was also used in AF patients. Therefore, it has to be taken into account that lower percentages of normal beats in AF and arrhythmic patterns that can make it difficult to discriminate normal heart beats might limit the interpretation of HRVI in AF patients. Sex differences are well-known in AF (35). In our cohort, sex distribution was not balanced between the groups and some sex differences were present. However, the sex distribution of our cohort is typical for a hemodialysis cohort. Furthermore, adding sex to the Cox regression models did not change the results (data not shown). The high frailty in our cohort limited the number of available ECGs. Due to a low number of cardiovascular events, adjusted Cox regression analysis was limited.

CONCLUSION

In conclusion, the study found a non-linear association of HRVI to cardiovascular and all-cause mortality independent of known strong risk factors in hemodialysis AF patients. Stratification into inner and outer quartiles of HRVI identified high-risk hemodialysis AF patients, who are known to be at increased mortality risk compared to hemodialysis patients without AF.

DATA AVAILABILITY STATEMENT

The datasets for this manuscript are not publicly available because written informed consent did not include wording on data sharing (German data protection laws). Reasonable requests to access the datasets should be directed to Matthias C. Braunisch, Matthias.Braunisch@mri.tum.de.

ETHICS STATEMENT

The studies involving human participants were reviewed and approved by Medical Ethics Committee of the Klinikum Rechts der Isar of the Technical University Munich and Bavarian State Board of Physicians. The patients/participants provided their written informed consent to participate in this study.

AUTHOR CONTRIBUTIONS

This article was conceptualized by MB and CS. MB wrote the first draft of the manuscript. MB, SWe, and BH performed the statistical analysis. MB, GL, RG, JM, QB, ST, MS, ML, CH-L, TA, and MP contributed to the data acquisition. Raw ECG data processing was performed by CM, SWa, and AM. CS, AB, CK, LR, GS, UH, and MM contributed to the supervision. All co-authors were involved with data interpretation, revising the work, and provided important intellectual content. All authors have seen and approved the final manuscript.

FUNDING

This work was supported by the Klinikum Rechts der Isar of the Technical University of Munich.

ACKNOWLEDGMENTS

We would like to thank all patients for their participation in the study.

SUPPLEMENTARY MATERIAL

The Supplementary Material for this article can be found online at: https://www.frontiersin.org/articles/10.3389/fcvm.2021.751052/full#supplementary-material

REFERENCES

1. Foley RN, Parfrey PS, Sarnak MJ. Clinical epidemiology of cardiovascular disease in chronic renal disease. Am J Kidney Dis. (1998) 32:S112–9. doi: 10.1053/ajkd.1998.v32.pm9820470
2. Roy-Chaudhury P, Tumlin JA, Koplan BA, Costea AI, Kher V, Williamson D, et al. Primary outcomes of the Monitoring in Dialysis Study indicate that clinically significant arrhythmias are common in hemodialysis patients and related to dialytic cycle. Kidney Int. (2018) 93:941–51. doi: 10.1016/j.kint.2017.11.019
3. Flythe, J. E., Liu, S., Montez-Rath, M. E., Winkelmayer, W. C., and Chang, T. I. (2021). Ultrafiltration rate and incident atrial fibrillation among older individuals initiating hemodialysis. Nephrol Dial Transplant. doi: 10.1093/ndt/gfaa332
4. Winkelmayer WC, Patrick AR, Liu J, Brookhart MA, Setoguchi S. The increasing prevalence of atrial fibrillation among hemodialysis patients. J Am Soc Nephrol. (2011) 22:349–57. doi: 10.1681/ASN.2010050459
5. Zimmerman D, Sood MM, Rigatto C, Holden RM, Hiremath S, Clase CM. Systematic review and meta-analysis of incidence, prevalence and outcomes of atrial fibrillation in patients on dialysis. Nephrol Dial Transplant. (2012) 27:3816–22. doi: 10.1093/ndt/gfs416
6. Genovesi S, Pogliani D, Faini A, Valsecchi MG, Riva A, Stefani F, et al. Prevalence of atrial fibrillation and associated factors in a population of long-term hemodialysis patients. Am J Kidney Dis. (2005) 46:897–902. doi: 10.1053/j.ajkd.2005.07.044
7. Genovesi S, Vincenti A, Rossi E, Pogliani D, Acquistapace I, Stella A, et al. Atrial fibrillation and morbidity and mortality in a cohort of long-term hemodialysis patients. Am J Kidney Dis. (2008) 51:255–62. doi: 10.1053/j.ajkd.2007.10.034
8. Buiten MS, De Bie MK, Rotmans JI, Gabreëls BA, Van Dorp W, Wolterbeek R, et al. The dialysis procedure as a trigger for atrial fibrillation: new insights in the development of atrial fibrillation in dialysis patients. Heart. (2014) 100:685–90. doi: 10.1136/heartjnl-2013-305417
9. Agarwal SK, Norby FL, Whitsel EA, Soliman EZ, Chen LY, Loehr LR, et al. Cardiac Autonomic Dysfunction and Incidence of Atrial Fibrillation: Results From 20 Years Follow-Up. J Am Coll Cardiol. (2017) 69:291–9. doi: 10.1016/j.jacc.2016.10.059
10. Chiou CW, Eble JN, Zipes DP. Efferent vagal innervation of the canine atria and sinus and atrioventricular nodes. The third fat pad Circulation. (1997) 95:2573–84. doi: 10.1161/01.CIR.95.11.2573
11. Pauza DH, Skripka V, Pauziene N, Stropus R. Morphology, distribution, and variability of the epicardiac neural ganglionated subplexuses in the human heart. Anat Rec. (2000) 259:353–82. doi: 10.1002/1097-0185(20000801)259:4<353::AID-AR10>3.0.CO;2-R
12. Bauer A, Deisenhofer I, Schneider R, Zrenner B, Barthel P, Karch M, et al. Effects of circumferential or segmental pulmonary vein ablation for paroxysmal atrial fibrillation on cardiac autonomic function. Heart Rhythm. (2006) 3:1428–35. doi: 10.1016/j.hrthm.2006.08.025
13. Shen MJ, Choi EK, Tan AY, Lin SF, Fishbein MC, Chen LS, et al. Neural mechanisms of atrial arrhythmias. Nat Rev Cardiol. (2011) 9:30–9. doi: 10.1038/nrcardio.2011.139
14. Siontis KC, Zhang X, Eckard A, Bhave N, Schaubel DE, He K, et al. Outcomes Associated With Apixaban Use in Patients With End-Stage Kidney Disease and Atrial Fibrillation in the United States. Circulation. (2018) 138:1519–29. doi: 10.1161/CIRCULATIONAHA.118.035418
15. Mavrakanas TA, Garlo K, Charytan DM. Apixaban versus No Anticoagulation in Patients Undergoing Long-Term Dialysis with Incident Atrial Fibrillation. Clin J Am Soc Nephrol. (2020) 15:1146–54. doi: 10.2215/CJN.11650919
16. Rebora P, Moia M, Carpenedo M, Valsecchi MG, Genovesi S. Best quality indicator of vitamin K antagonist therapy to predict mortality and bleeding in haemodialysis patients with atrial fibrillation. Blood Transfus. (2020).
17. Hämmerle, P., Eick, C., Blum, S., Schlageter, V., Bauer, A., Rizas, K. D., et al. (2020). Heart Rate Variability Triangular Index as a Predictor of Cardiovascular Mortality in Patients With Atrial Fibrillation. Journal of the American Heart Association. doi: 10.1161/JAHA.120.016075
18. Hämmerle P, Eick C, Bauer A, Rizas KD, Coslovsky M, Krisai P, et al. Impaired heart rate variability triangular index to identify clinically silent strokes in patients with atrial fibrillation. Eur Heart J. (2020) 41. doi: 10.1093/ehjci/ehaa946.2438
19. Schmaderer C, Tholen S, Hasenau AL, Hauser C, Suttmann Y, Wassertheurer S, et al. Rationale and study design of the prospective, longitudinal, observational cohort study "rISk strAtification in end-stage renal disease" (ISAR) study. BMC Nephrol. (2016) 17:161. doi: 10.1186/s12882-016-0374-8
20. Liu J, Huang Z, Gilbertson DT, Foley RN, Collins AJ. An improved comorbidity index for outcome analyses among dialysis patients. Kidney Int. (2010) 77:141–51. doi: 10.1038/ki.2009.413
21. Anker SD, Gillespie IA, Eckardt KU, Kronenberg F, Richards S, Drueke TB, et al. Development and validation of cardiovascular risk scores for haemodialysis patients. Int J Cardiol. (2016) 216:68–77. doi: 10.1016/j.ijcard.2016.04.151
22. Hindricks, G., Potpara, T., Dagres, N., Arbelo, E., Bax, J. J., Blomström-Lundqvist, C., et al. (2020). 2020 ESC Guidelines for the diagnosis and management of atrial fibrillation developed in collaboration with the European Association of Cardio-Thoracic Surgery (EACTS). Eur Heart J. doi: 10.1093/eurheartj/ehaa612
23. Molgaard H. Evaluation of the Reynolds Pathfinder II system for 24 h heart rate variability analysis. Eur Heart J. (1991) 12:1153–62. doi: 10.1093/eurheartj/12.11.1153
24. Camm AJ, Malik M, Bigger JT, Breithardt G, Cerutti S, Cohen RJ, et al. Heart rate variability: standards of measurement, physiological interpretation and clinical use. Task Force of the European Society of Cardiology and the North American Society of Pacing and Electrophysiology Circulation. (1996) 93:1043–65. doi: 10.1161/01.CIR.93.5.1043
25. Schemper M, Smith TL. A note on quantifying follow-up in studies of failure time. Control Clin Trials. (1996) 17:343–6. doi: 10.1016/0197-2456(96)00075-X
26. Fukuta H, Hayano J, Ishihara S, Sakata S, Mukai S, Ohte N, et al. Prognostic value of heart rate variability in patients with end-stage renal disease on chronic haemodialysis. Nephrol Dial Transplant. (2003) 18:318–25. doi: 10.1093/ndt/18.2.318
27. Wijbenga JA, Balk AH, Meij SH, Simoons ML, Malik M. Heart rate variability index in congestive heart failure: relation to clinical variables and prognosis. Eur Heart J. (1998) 19:1719–24. doi: 10.1053/euhj.1998.1148
28. Almeida-Santos MA, Barreto-Filho JA, Oliveira JL, Reis FP, Da Cunha Oliveira CC, Sousa AC. Aging, heart rate variability and patterns of autonomic regulation of the heart. Arch Gerontol Geriatr. (2016) 63:1–8. doi: 10.1016/j.archger.2015.11.011
29. Malik M, Cripps T, Farrell T, Camm AJ. Prognostic value of heart rate variability after myocardial infarction. A comparison of different data-processing methods Medical and Biological Engineering and Computing. (1989) 27:603. doi: 10.1007/BF02441642
30. Malik M, Farrell T, Cripps T, Camm AJ. Heart rate variability in relation to prognosis after myocardial infarction: selection of optimal processing techniques. Eur Heart J. (1989) 10:1060–74. doi: 10.1093/oxfordjournals.eurheartj.a059428
31. Ziegler D, Piolot R, Strassburger K, Lambeck H, Dannehl K. Normal ranges and reproducibility of statistical, geometric, frequency domain, and non-linear measures of 24-hour heart rate variability. Horm Metab Res. (1999) 31:672–9. doi: 10.1055/s-2007-978819
32. Malik M, Farrell T, Camm AJ. Circadian rhythm of heart rate variability after acute myocardial infarction and its influence on the prognostic value of heart rate variability. Am J Cardiol. (1990) 66:1049–54. doi: 10.1016/0002-9149(90)90503-S
33. Suzuki M, Hiroshi T, Aoyama T, Tanaka M, Ishii H, Kisohara M, et al. Nonlinear measures of heart rate variability and mortality risk in hemodialysis patients. Clin J Am Soc Nephrol. (2012) 7:1454–60. doi: 10.2215/CJN.09430911
34. Braunisch MC, Mayer CC, Bauer A, Lorenz G, Haller B, Rizas KD, et al. Cardiovascular Mortality Can Be Predicted by Heart Rate Turbulence in Hemodialysis Patients. Front Physiol. (2020) 11:77. doi: 10.3389/fphys.2020.00077

35. Magnussen C, Niiranen TJ, Ojeda FM, Gianfagna F, Blankenberg S, Njølstad I, et al. Sex Differences and Similarities in Atrial Fibrillation Epidemiology, Risk Factors, and Mortality in Community Cohorts: Results From the BiomarCaRE Consortium (Biomarker for Cardiovascular Risk Assessment in Europe). Circulation. (2017) 136:1588–97. doi: 10.1161/CIRCULATIONAHA.117.028981

Conflict of Interest: MB reports received personal fees from Vifor Pharma unrelated to the project. MP is employed by Nephrocare. CM and SWa are employed by the Austrian Institute of Technology GmbH, a non-profit research organization.

The remaining authors declare that the research was conducted in the absence of any commercial or financial relationships that could be construed as a potential conflict of interest.

Publisher's Note: All claims expressed in this article are solely those of the authors and do not necessarily represent those of their affiliated organizations, or those of the publisher, the editors and the reviewers. Any product that may be evaluated in this article, or claim that may be made by its manufacturer, is not guaranteed or endorsed by the publisher.

frontiers in Cardiovascular Medicine

ORIGINAL RESEARCH
published: 27 January 2022
doi: 10.3389/fcvm.2021.807904

Macrophages Can Drive Sympathetic Excitability in the Early Stages of Hypertension

Oliver C. Neely, Ana I. Domingos and David J. Paterson**

Department of Physiology, Anatomy and Genetics, University of Oxford, Oxford, United Kingdom

Hypertension is a major health burden worldwide with many cases resistant to current treatments. Hyperactivity of the sympathetic nervous contributes to the etiology and progression of the disease, where emerging evidence suggests that inflammation may underpin the development of sympathetic dysautonomia. This study examined whether macrophages could drive the sympathetic phenotype in Spontaneously Hypertensive Rats (SHR) before animals develop high pressure. Stellate neurons from wild-type control Wistar rats and SHRs were co-cultured with blood leukocytes from their own strain, and also crossed cultured between strains. The calcium transient response to nicotinic stimulation was recorded using Fura-2 calcium imaging, where SHR neurons had a greater calcium transient compared with Wistar neurons. However, when co-cultured with leukocytes, Wistar neurons began to phenocopy the SHR sympathetic hyperactivity, while the SHR neurons themselves were unaltered. Resident leukocyte populations of the SHR and Wistar stellate ganglia were then compared using flow cytometry, where there was a shift in monocyte-macrophage subset proportions. While classical monocyte-macrophages were predominant in the Wistar, there were relatively more of the non-classical subset in the SHR, which have been implicated in pro-inflammatory roles in a number of diseases. When bone marrow-derived macrophages (BMDMs) were co-cultured with stellate neurons, they made Wistar neurons recapitulate the SHR nicotinic stimulated calcium transient. Wistar BMDMs however, had no effect on SHR neurons, even though SHR BMDMs increased SHR neuron responsiveness further above their hyper-responsive state. Taken together, these findings show that macrophages can be potent enhancers of sympathetic neuronal calcium responsiveness, and thus could conceivably play a role in peripheral sympathetic hyperactivity observed in the early stages of hypertension.

Keywords: hypertension, dysautonomia, macrophages, SHR, calcium imaging, flow cytometry, stellate neurons

OPEN ACCESS

Edited by:
Marco Mongillo,
University of Padua, Italy

Reviewed by:
Cheng-Chao Ruan,
Fudan University, China
Attila Kiss,
Medical University of Vienna, Austria
Marcello Rattazzi,
University of Padua, Italy

****Correspondence:***
Oliver C. Neely
oliver.neely@gtc.ox.ac.uk
David J. Paterson
david.paterson@dpag.ox.ac.uk

Specialty section:
This article was submitted to Hypertension, a section of the journal Frontiers in Cardiovascular Medicine

Received: *02 November 2021*
Accepted: *21 December 2021*
Published: *27 January 2022*

Citation:
Neely OC, Domingos AI and Paterson DJ (2022) Macrophages Can Drive Sympathetic Excitability in the Early Stages of Hypertension. Front. Cardiovasc. Med. 8:807904. doi: 10.3389/fcvm.2021.807904

INTRODUCTION

A key pathophysiological feature of essential hypertension involves sympathetic hyperactivity (1–5) and impaired vagal parasympathetic tone (2). The sympathetic component of this is by far the best studied and is observed in all stages of essential hypertension (6–9), moreover it can precede hypertension itself (10–12). Persistent

heightened sympathetic tone leads to a range of other hypertensive co-morbidities, including cardiac hypertrophy (13, 14), arrhythmia (15), vascular dysfunction (16), insulin resistance (17) and inflammation (18).

Inflammation has emerged as a key pathological feature of essential hypertension (19). Crucially, a simple bone marrow transplant from SHR to Wistar rats increases blood pressure, while the converse decreases it (20), implying the SHR's immune system as a causative factor of the blood pressure phenotype. Clinically, higher levels of C-reactive protein (a common marker of systemic inflammation) (21–24) or IL-6 (an inflammatory cytokine released along with CRP) (23, 24) strongly predict future development of hypertension. This suggests that both inflammation and sympathetic hyperexcitability are co-features of a "pre-hypertensive" state, before any overt cardiovascular disease is evident. Although it has not been established whether inflammation itself is a key driver of the sympathetic phenotype.

There is evidence that the hypertensive inflammatory phenotype may interact with the sympathetic nervous system, in a similar way to that in which immune cells interact with sympathetic neurons in adipose tissue in obesity (25), this being a co-feature of hypertension in the metabolic syndrome. In the central nervous system inflammation can raise sympathetic outflow, which can experimentally induce hypertension in the rat (26). Inhibition of microglial activation with minocycline can stop this (26), and is associated with reduced sympathetic tone, inflammation and blood pressure in the SHR (20). It is also well established that sympathetic hyperactivity occurs at the level of the peripheral ganglia themselves in the SHR, which exhibit greater stimulation-evoked noradrenaline release (27, 28), and show increased firing responsiveness to a given electrical stimulus (29). In neuropathic pain (30) and post-MI (31–33), inflammatory reactions induce states of local peripheral neuronal activity, mediated by cytokines and other neuronal growth factors. Interestingly, following sensory nerve injury, macrophage-released IL-6 contributes to the sprouting of sympathetic nerve fibers into the dorsal root ganglia (34), suggesting this classic inflammatory mediator, which is positively associated with blood pressure in humans (35), could produce sympathetic hyperactivity.

We therefore tested the hypothesis that a pathological immune system reaction within the sympathetic ganglia of pre-hypertensive animals drives local neuronal hyperactivity. Here we show that macrophages can enhance the intracellular calcium responsiveness of sympathetic neurons *in vitro*, which may underpin aspects of the increases in sympathetic hyperactivity seen in the early stages of hypertension.

METHODS AND MATERIALS

Animals

Male Wistar and Spontaneously Hypertensive rats were purchased from Envigo, UK and housed in the local Biomedical Services Building prior to experimental use. Rats were used mainly at the age of 3–4 weeks, as this is an age at which the SHR exhibits dysautonomia, but this is not yet confounded by any increase in arterial blood pressure (36, 37). These SHRs are therefore termed "pre-hypertensive SHRs".

To excise stellate ganglia for cell culture, rats were culled using an approved UK Home Office Schedule 1 method involving overdose of pentobarbitone (under isoflurane anesthesia), followed by exsanguination. In cases where a pure blood sample was required for co-culture with stellate neurons, a needle was inserted into the heart of terminally anesthetized rats, and ∼1 ml of blood was withdrawn into a syringe containing ∼100 μL EDTA solution (100 mM). Finally, to prepare tissues for flow cytometry, as tissue-resident leukocytes were to be examined, it was necessary to flush out blood leukocytes from the circulation. To achieve this, a small incision was made in the right atria of terminally anesthetized animals, and then 50–100 ml cold PBS containing 10 U/ml heparin was injected into the ventricles. Blood samples for flow cytometry were obtained by collecting some of the blood flushed out by this method.

Cell Culture

Cleaned ganglia were cut into ∼6 pieces each before enzymatic digestion in collagenase IV (1 mg/ml in L-15) for 25 min, followed by trypsin (2 mg/ml in Ca^{2+}- and Mg^{2+}-free Hank's Balanced Salt Solution; Merck or Thermofisher, both US) for 30 min; both at 37°C. Digested ganglia were then washed in blocking medium (Neurobasal Plus medium with 10% heat-inactivated fetal bovine serum and 1% penicillin/streptomycin; all Thermofisher, US; penicillin/streptomycin also Merck, US) at room temperature, twice for 5 min each. Next, the ganglia were mechanically triturated in complete neuronal medium (Neurobasal Plus medium with 2% B-27 supplement, 1.5 mM Glutamax, 5 ng/ml 2.5S NGF and 0.5% penicillin/streptomycin; all Thermofisher, US except NGF, Merck US) using two glass Pasteur pipettes in series, the second, fire-polished to narrow the opening. The resultant single-cell suspension was plated onto poly-D-lysine (0.1 mg/ml; Merck, US) and laminin- (0.048 mg/ml; Thermofisher, US) coated 6 mm glass coverslips in 4-well culture plates. These were incubated at 37°C under 5% CO_2 for ∼48 h prior to experimentation.

For some experiments ganglia were co-cultured with blood-derived leukocytes. These were prepared from blood samples taken from 3 to 4 week old Wistar rats and SHRs by transthoracic cardiac puncture, as detailed previously. Using this method 1–2 ml of fresh blood could be obtained per 3–4 week old animal. 1 ml of each sample was added to 10 ml of eBioscience red blood cell lysis buffer (Thermofisher, US) as per the manufacturer's instructions, and incubated at room temperature for 10 min on a shaker. To arrest the reaction, 10 ml of DMEM containing 10% FBS was added to each sample and the suspensions were centrifuged at 400 rcf for 4 min to obtain a pellet. Blood cell suspensions were then either depleted of monocytes using clodronate liposomes (Encapsula Nanosciences, US), according to a protocol developed by Claassen et al. (38), or incubated with PBS-containing liposomes as a control. The pellets were resuspended in the ganglionic culture medium containing either 100 μl clodrosomes, or the same concentration of the control liposomes, and incubated at 37°C for 1–2 h. After this the cells were pelleted and resuspended in fresh ganglionic culture

medium and this suspension was used to culture the ganglionic explants. The products of each original 1 ml blood sample were resuspended in 2 ml of such medium; this being split across two ganglia so that each ganglion received approximately the number of leukocytes derived from 0.5 ml of rat blood. SHR blood may contain a higher concentration of leukocytes than that of Wistar rats (39–41), so this difference would therefore be incorporated in the culture conditions of ganglia treated with blood from each respective strain.

The following protocol was adapted from Muschter et al. (42). Tibiae and femurae were extracted from 3 to 4 week old Wistar rats, cleaned of soft tissue and stored in PBS at 4°C for up to 24 h. These were then sprayed with 70% ethanol and one at a time the ends of each bone were cut off with a scalpel. A syringe and 25 G needle were used to flush out the bone marrow into a petri dish, using ∼6 ml cold PBS. The combined effluent from all bones was then passed through a 70 μm filter and collected in a 50 ml falcon tube, before being centrifuged at 300 rpm for 5 min. The cell pellet was resuspended in complete BMDM media (Dulbecco's Modified Eagle's Medium with 10% heat-inactivated fetal bovine serum, 1% penicillin/streptomycin and 20 ng/ml recombinant rat M-SCF), 4 ml/bone. The cells were plated in 10 cm petri dishes, 8 ml per dish, and incubated at 37°C/5% CO_2. Four days later half the media was removed and replaced with fresh BMDM. Two days after this, all media was removed and the plates washed with PBS, before ∼4 ml TrypLE (Thermofisher, US), or EDTA (2 mM in PBS; where cells were being processed for flow cytometry) was added to each. After 3–4 min once the cells had detached the suspension was removed and combined with an equal volume of α-MEM + 10% FBS media, and this was then centrifuged at 300 rpm for 5 min. Cells were then plated onto the required format, for example, 6 mm glass coverslips, re-suspended and prepared for flow cytometry.

Co-cultures of stellate neurons and blood leukocytes or BMDMs were prepared on 6 mm poly-D-lysine/laminin-coated coverslips. For leukocyte co-culture, stellate neurons were prepared in the same way as for their solitary culture, but in half the normal volume of medium. Blood leukocytes, prepared in the same way as described above for culture with whole ganglia, with either clodronate or PBS-filled liposomes, were then added to the neurons in an equal volume of neuronal culture medium. To separate these cells from the liposomes, after the incubation 10 ml of Neurobasal plus containing 21.5% Optiprep (Merck, US) was added to each ml of cell suspension, and the mixture centrifuged at 400 g for 15 min with no brake. The liposomes floated to the top while the cells formed a pellet at the bottom. These were resuspended in neuronal culture medium. Each ml of blood provided leukocytes for three wells of four 6 mm coverslips.

In the case of BMDM co-culture, the neurons were once again plated in half the normal volume of culture medium, and day 6 harvested BMDMs were added to this in the same volume of media, but containing 40 ng/ml M-CSF, to produce a final concentration of 20 ng/ml. These BMDMs had been previously cultured in 10 cm dishes at a density of 2 bones per dish, and were plated at an approximately equivalent density, adjusting for well surface area.

All co-culture preparations were incubated at 37°C, 5% CO_2 for 48 h before imaging.

Calcium Imaging

Stellate neurons were plated onto 6 mm laminin and poly-D-Lysine coated glass coverslips. Prior to imaging, these were incubated in culture medium containing 2 μM Fura-2 AM, at 37°C for 30 min, before being washed with Tyrode's solution (containing, in mM: NaCl 135, KCl 4.5, HEPES 20, Glucose 11, $CaCl_2$ 2, $MgCl_2$ 1) three times for 5 min each. The coverslips were then imaged in a 100 μL, gravity-fed perfusion chamber, in 37°C Tyrode's solution at a flow rate of ∼3–4 ml/min. An inverted Nikon microscope, with a 40× oil-immersion objective, was used to obtain the images, which were captured by QICLICK digital CCD camera, using Optofluor QICLICK software.

Neurons were identified by their large size and thick borders, as compared to other cells present on the coverslips, and only those which appeared healthy, showing no obvious signs of damage or blebbing, were selected for imaging. Images were captured every 2 s, during which the coverslips were excited sequentially at wavelengths of 355 and 380 nm, and the emission intensities at 510 nm recorded. Background 510 nm emissions were subtracted from that of the cells for both excitation wavelengths in each image, and the resultant values used to calculate the 355/380 ratio. This was then normalized to a baseline ratio for each cell, which was taken as the average of the final 5 images prior to addition of the first treatment.

Flow Cytometry

All rat tissue samples were first prepared for subsequent staining and flow cytometric analysis or sorting. In the case of sympathetic ganglia, the cut ganglion pieces underwent simultaneous enzymatic digestion in HBSS with hyaluronidase (1,000 U/ml), collagenase II (1 mg/ml) and DNase I (5 U/ml) for 30 min at 37°C. Subsequently these were centrifuged at 400 rcf for 4 min, the supernatant was discarded, and then the tissue was mechanically triturated in 1 ml PBS using two glass Pasteur pipettes in series, the second fire-polished to narrow the opening.

Heparinised blood samples, obtained during cardiac perfusion, were passed through a 70 μm filter and centrifuged at 400 rcf for 4 min. Next these were resuspended in ∼10 ml red blood cell lysis buffer and left at room temperature for 10–15 min, before the reaction was stopped by addition of an equal volume of FACS buffer, and the whole suspension was centrifuged again at the same settings as before. The pellet was then resuspended in PBS, spun down at 400 rcf for 4 min once more, before a final resuspension in fresh PBS. For experiments in which monocyte-macrophages were to be isolated by FACS, blood samples were instead obtained from rats by cardiac puncture under terminal anesthesia, with EDTA used as the anti-coagulant.

Renal tissue was prepared for flow cytometry using a protocol adapted from Rubio-Navarro et al. (43). Pairs of kidneys were stripped of their capsules by hand, the hila were removed. The remaining renal tissue was finely cut up using scissors and then pushed through a 40 μm filter using the plunger from a 10 ml syringe, the resultant pulp being washed through with

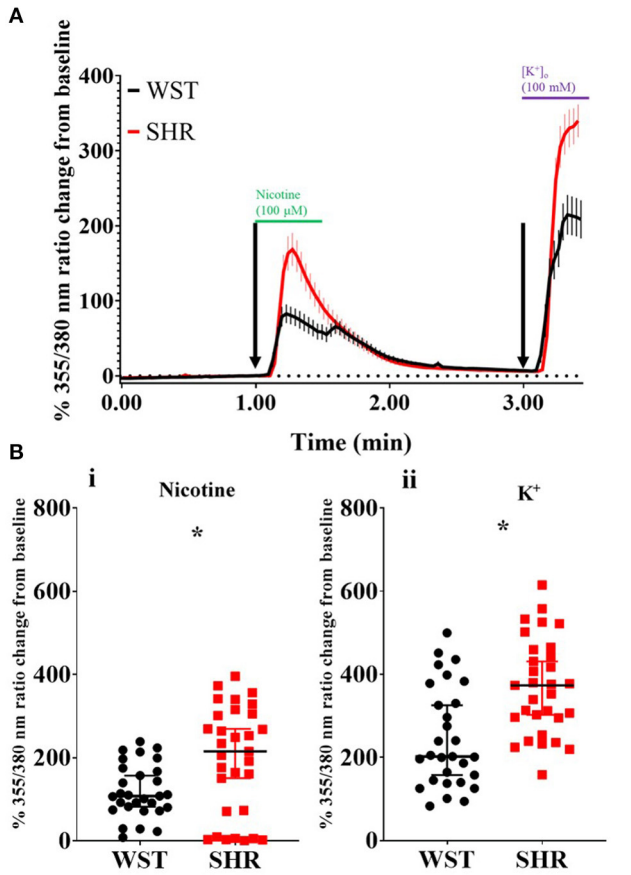

FIGURE 1 | Wistar ($n = 29$ neurons, 5 cultures, 2–4 rats per culture) and SHR ($n = 31$ neurons, 6 cultures, 2–4 rats per culture) stellate neuron Ca^{2+} transients in response to pharmacological stimulation. **(A)** Mean trace (with SEM) of stellate neuron $[Ca^{2+}]_i$ during the experimental protocol involving exposure to 100 μM nicotine, followed by 100 mM K^+. **(B)** Peak stellate neuron $[Ca^{2+}]_i$ transient in response to nicotine (i) and K^+ (ii). Peak response data are presented as median with IQR; * signifies $p < 0.05$ for Wistar vs. SHR, Mann-Whitney test.

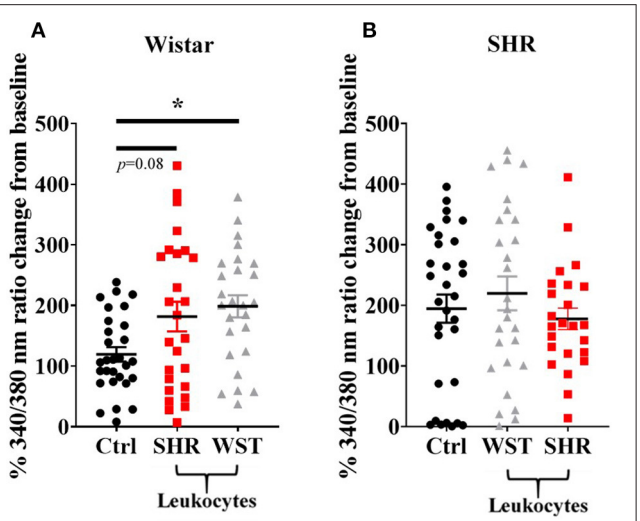

FIGURE 2 | Peak $[Ca^{2+}]_i$ transient responses of stellate neurons co-cultured with blood leukocytes in response to 100 μM nicotine: **(A)** Wistar neurons (with SHR leukocytes: $n = 26$ neurons, 3 cultures, 2–3 rats per culture; with Wistar leukocytes: $n = 26$ neurons, 3 cultures, 2–3 rats per culture) and **(B)** SHR neurons (with Wistar leukocytes: $n = 27$ neurons, 3 cultures, 2–3 rats per culture; with SHR leukocytes: $n = 24$ neurons, 3 cultures, 2-3 rats per culture). Data are presented as mean ± SEM; * signifies $p < 0.05$ between the indicated groups; normal data were analyzed using Brown-Forsythe and Welch's ANOVAs with Dunnett's T3 multiple comparisons test, while non-normal data were analyses with a Kruskall-Wallis test followed by Dunn's multiple comparisons test.

15 ml of FACS buffer. The filtered suspension was centrifuged at 400 rcf for 4 min and resuspended in ∼15 ml red blood cell lysis buffer, which was left at room temperature for 90 s, before lysis was terminated by dilution with 15 ml of FACS buffer. The solution was centrifuged under the same settings as before, resuspended in 10 ml PBS, and 1 ml of this was taken forward for analysis.

The resultant single-cell suspensions were stained with 0.5 μL eBioscience™ Fixable *Via*bility Dye eFluor™ 780 (Thermofisher, US) for 30 min at 4°C, and then 1 ml of FACS buffer was added, and the suspension centrifuged at 400 rcf for 4 min to wash off the dye. The cells were next incubated for 10 min in anti-rat CD32 (1:100 in FACS buffer) at 4°C to prevent FcR-mediated antibody binding, prior to incubation for 30 min in appropriate panel of fluorescently-tagged flow cytometry antibodies.

For flow cytometry, a BD LSRFortessa™ X-20 was used, equipped with 5 lasers, and a total of 18 filter sets, each corresponding to an emission wavelength on a specific laser. Single color controls were prepared using compensation beads according to the manufacturer's instructions, and FMO controls were also used for each antibody panel to aid gating. Data were later processed using FlowJo 10 software.

Immunohisto-/Cyto-Chemistry

Clean stellates were immersed in cold 4% PFA (Alfa Aesar, US) and stored at room temperature on a rotator for ∼1–2 h; spleens were incubated in the same solution overnight. For cryoprotection, the tissues were transferred to 15% sucrose (Merck, US) in PBS solution for ∼6–12 h, or until the tissue had sunk, and subsequently put into 30% sucrose for the effect. The tissue was then embedded in OCT and stored at −20°C as required. 20 μm sections were cut on a cryostat, transferred to microscope slides, and returned to −20°C for further storage. In the case of cell culture staining, neuron and macrophage co-cultures were plated directly onto 35 mm glass-bottomed dishes, before fixation for 15 min in 2% PFA.

For staining, microscope slides were thawed in room temperature PBS and then the tissue circled with a PAP pen. The sections or cell-containing dishes were then incubated in a PBS-based blocking and permeabilisation solution (PBS with 3% bovine serum albumin, 2% goat serum, 1% Triton X-100 and 0.1% NaN_3), for 1 hr, before incubation in primary antibody solution overnight at 4°C in a humid box. The following day the stained slides/dishes were washed three times each for 5 min in PBS and then incubated in secondary antibody and DAPI

for 1 h at room temperature. Finally, the samples were washed three times for 5 min in PBS once again, prior to mounting using ProLong™ Gold Antifade Mountant (Thermofisher, US). Imaging was carried out on a confocal microscope within a day of mounting, and the recorded images processed using ImageJ software.

Statistical Analysis

All statistical analyses were performed using Graphpad Prism 8 software. All data analyzed in this publication were treated as continuous. Data normality was examined using Anderson-Darling, D'Agostino and Pearson, Shapiro-Wilk and Kolmogorov-Smirnov tests, and parametric or non-parametric tests selected based on the outcome of these. For comparison of two groups Welch's *t*-tests (parametric) or Mann-Whitney tests (non-parametric) were employed, with the two-step set up method of Benjamini, Krieger and Yekutieli used to produce *q*-values to account for multiple comparisons. Where three of more groups were to be compared, Brown-Forsythe and Welch's ANOVAs (parametric) or Kruskall-Wallis tests (non-parametric), with appropriate *post-hoc* tests for multiple comparisons were used. Results were considered statistically significant where $p < 0.05$.

RESULTS

Pre-hypertensive SHR Neurons Exhibit Larger Ca^{2+} Transients in Response to Nicotinic Stimulation or High K^+ Induced-Depolarization

It has been previously reported that pre-hypertensive SHR stellate neurons show enhanced calcium transients ($[Ca^{2+}]_i$) compared to Wistar neurons, when depolarized using high $[K^+]_o$ Tyrode's solution (36). We first confirmed this while also examining the relative responses of these neurons to a more physiological stimulation with 100 μM nicotine. In both cases, the SHR neuron responsiveness was greater than that of Wistar neurons (expressed as % ratio change from baseline): nicotine: 194.5 ± 23.4 vs. 119.5 ± 11.87, $p = 0.022$; K^+: 369.7 ± 20.74 vs. 246.1 ± 22.51, $p = 0.00020$ (**Figure 1**). Since the nicotinic response mimicked physiological post-ganglionic neuron synaptic activation, and also showed a difference between Wistar and SHR, the $[Ca^{2+}]_i$ response was taken forward as a surrogate measure of stellate neuronal activity.

Whole Blood Leukocytes Increase Wistar, but Not SHR Responsiveness to Nicotinic Stimulation

Co-culturing Wistar stellate neurons with their own blood leukocytes significantly increased their responsiveness to nicotine. With SHR leukocytes there was a clear trend to this effect (**Figure 2**), although not significant ($p = 0.080$). However, the nicotinic response with SHR leukocytes did not differ significantly from that with the Wistar leukocytes, where these responses were much closer in magnitude than the baseline and SHR leukocyte co-culture. By contrast, SHR neurons showed no differences when co-cultured with these leukocytes (**Figure 2**).

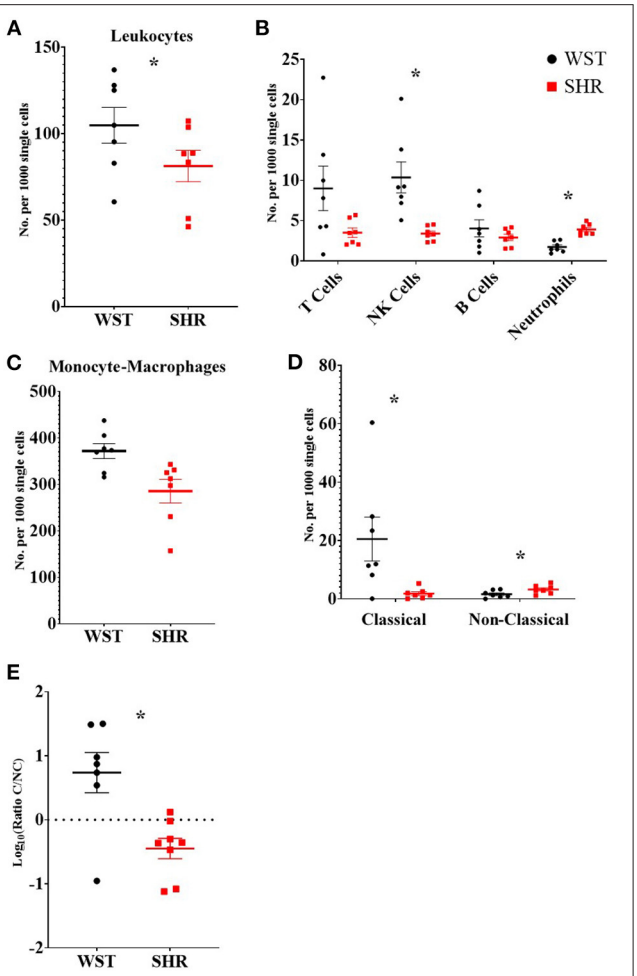

FIGURE 3 | Numbers of different leukocyte populations found within the stellate ganglia of 3-week old Wistar rats ($n = 7$ samples, 2–3 rats per sample) and pre-SHRs ($n = 7$ samples, 2–3 rats per sample). **(A)** Numbers of leukocytes. **(B)** Stratification of $CD45^+$ cells into major leukocyte populations; monocyte-macrophages shown in **(C)**. **(D)** Classical and non-classical monocytes-macrophages. **(E)** Ratio of classical/non-classical monocyte-macrophages. In **(A–D)** the values are expressed as numbers per 1,000 single cells to allow comparison between samples which contained a different total number of cells. In **(E)** the ratio is presented as $\log_{10}$ to allow visualization of the size of the ratio in either direction. Data are expressed as mean ± SEM. * signifies $p < 0.05$ WST vs. SHR; normal data were analyzed using Welch's t-tests and multiple comparisons accounted for using *q* values determined by the two-stage set-up method of Benjamini, Krieger and Yekutieli.

The SHR Exhibits a Shift in the Proportions of the Classical and Non-classical Monocyte-Macrophage Subsets

Given that leukocytes can potentiate stellate neuron responsiveness to nicotinic stimulation, we next examined the immune cell environment of the stellate ganglia in both strains of rat. Ganglia were separated into single cell

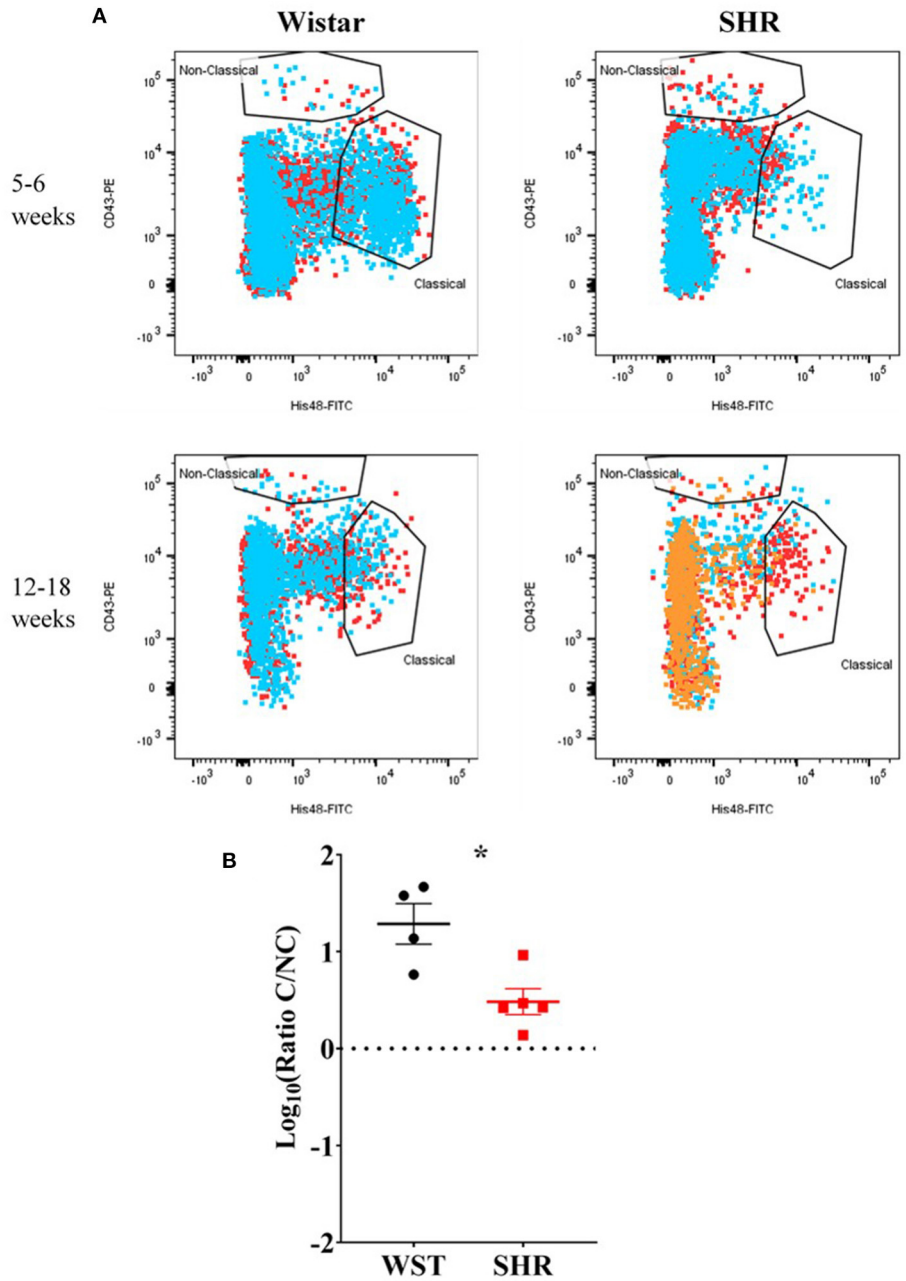

FIGURE 4 | Monocyte-macrophages from the stellate ganglia of SHR $n = 5$ samples, 3 rats per sample, and age-matched Wistars ($n = 4$ samples, 3 rats per sample) at 5–6 weeks (developing hypertension) and 12–18 weeks (established hypertension). **(A)** Flow cytometry plots of all samples; each color represents a separate sample of ganglia from 2–3 rats. **(B)** Classical/non-classical monocyte-macrophage ratio from all 5-18 week old animals; Data are expressed as mean ± SEM. *signifies $p < 0.05$ WST vs. SHR, Welch's t-test.

suspensions, stained for markers of the main leukocyte populations, and analyzed using flow cytometry. As the ganglia were of different sizes, and those of the SHR tended to be smaller in size than Wistar ganglia, cell counts were normalized to the total number of single cells recorded for each sample, and expressed as the number per 1,000 single cells.

There were significantly more leukocytes (defined at $CD45^+$) in the Wistar compared to SHR stellates (372 ± 16.1 vs. 285 ± 25.5 per 1,000 single cells; $p = 0.014$; $q = 0.025$; **Figure 3A**).

Part of this increase in leukocytes was accounted for by increased numbers of NK cells (10.3 ± 1.91 vs. 3.39 ± 0.329 per 1,000 single cells; $p = 0.0037$; $q = 0.0097$; **Figure 3B**) in the Wistar strain, while the SHR had higher numbers of neutrophils (3.90 ± 0.259 vs. 1.73 ± 0.253; $p < 0.0001$; $q = 0.00033$; **Figure 3B**).

Despite no differences in the overall numbers of monocyte-macrophages between the two strains (**Figure 3C**), there was a striking difference in the proportions of the subtypes between these two strains: the ratio of classical ($His48^{high}/CD43^{low}$) to non-classical ($CD43^{high}/His48^{low-int}$) monocyte-macrophages was significantly higher in the Wistar (13.8 ± 4.77 vs. 0.551 ± 0.148; $p = 0.0082$; **Figure 3E**). This appeared to made up of both more classical (20.52 ± 7.54 vs. 1.81 ± 0.662; $p = 0.029$; $q = 0.039$; **Figure 3D**), and fewer non-classical (1.60 ± 0.476 vs. 3.24 ± 0.556; $p = 0.047$; $q = 0.0497$; **Figure 3D**), monocyte-macrophages in the Wistar compared to SHR. This finding was also replicated in the stellate ganglia of older (5–6 week and 12–18 week old) animals (**Figure 4**).

The same flow cytometry panel was then employed on two other SHR sympathetic ganglia to examine whether this was an SNS-wide phenomenon: the coeliac ganglion (which innervates the kidney, so is likely important to hypertensive pathophysiology) and the superior cervical ganglion (innervating the head, so likely has minimal impact on hypertension, except possibly *via* bone-marrow effects (44).

In the SCG, the Wistar ganglia had a significantly higher classical/non-classic monocyte-macrophage ratio (8.99 ± 2.46 vs. 0.359 ± 0.148; $p = 0.0023$; $q = 0.0012$), while in the coeliac ganglion there was a clear trend in the same direction (0.391 ± 0.145 vs. 0.112 ± 0.021), although not significant ($p = 0.12$; $q = 0.032$; **Figure 5**). A similar monocyte-macrophage subset ratio result was apparent in the whole blood compared between strains (Wistar: 0.123 ± 0.0422 vs. SHR: 0.0337 ± 0.00600; $p = 0.0323$, $q = 0.011$; **Figure 5**), suggesting this phenomenon is not specific to the SNS, but occurs systemically. Finally, this was also the case in the kidneys (Wistar: 0.0742 ± 0.107 vs. SHR: 0.0151 ± 0.0853; $p = 0.0014$; $p = 0.0012$; **Figure 5**), typically referred to as the "final common node of hypertensive pathophysiology" (Crowley and Coffman, 2014). However, no differences in any of the other leukocyte populations were detected in either the blood or kidneys. Bone marrow-derived macrophages potentiate stellate neuron responsiveness to nicotinic stimulation.

Immunohistochemistry was used to examine the spatial localization of the stellate ganglion monocyte-macrophages relative to the neurons. This revealed large numbers of spindle-shaped $CD68^+$ cells, scattered amongst the TH^+ sympathetic neurons, of both the Wistar (**Figure 6A**) and SHR (**Figure 6B**) stellates. Additionally, the appearance of large nucleus-free cavities within the tissue suggested that the ganglionic vasculature had been substantially flushed of circulating cells. A no primary antibody negative control (**Figure 6C**), and a splenic sample serving as a positive control for $CD68^+$ macrophages (**Figure 6D**) are also shown.

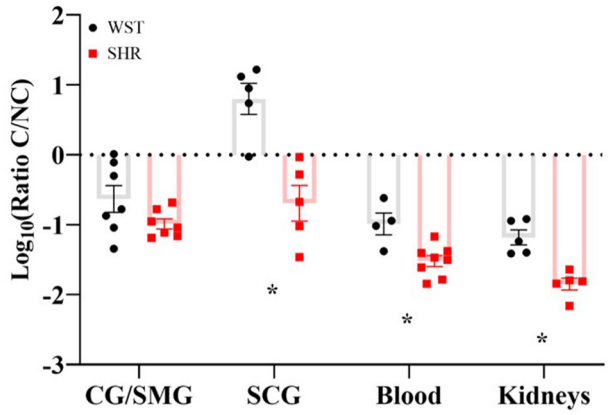

FIGURE 5 | Classical/non-classical monocyte-macrophage ratios in the coeliac/superior mesenteric ganglia (CG/SMG; Wistar: $n = 7$ samples, 2 rats per sample; SHR: $n = 7$ samples, 2-4 rats per sample), superior cervical ganglia (SCG; in both strains: $n = 5$ samples, 2 rats per sample), blood (Wistar $n = 4$ samples, SHR $n = 8$ samples, 1 rat per sample) and kidneys (both strains $n = 5$ samples, 1 rat per sample) of 3-week old Wistar rats and pre-SHRs. Data are expressed as mean ± SEM. * signifies $p < 0.05$ WST vs. SHR, Welch's t-tests with q values determined by the two-stage set-up method of Benjamini, Krieger and Yekutieli.

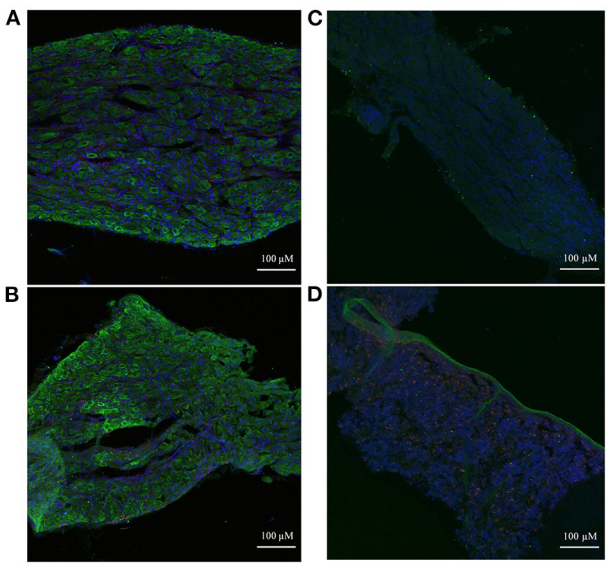

FIGURE 6 | Immunohistochemical images of sympathetic neurons (TH) and macrophages (CD68) in 3-week old Wistar and pre-SHR rat tissue. **(A)** Wistar stellate ganglion, **(B)** SHR stellate ganglion. These ganglia comprise a large number of sympathetic neurons (green) with some small macrophages (red) amongst them. The acellular spaces within the tissue likely reflect empty blood vessels following cardiac perfusion. **(C)** Wistar stellate ganglion stained with only DAPI and the secondary antibodies, serving as a negative control. There appears to be some 488 nm auto-fluorescence, but the tissue clearly lacks the cellular pattern of **(A)**. **(D)** Wistar spleen stained as a positive control for $CD68^+$ macrophages; many punctate cells appear similarly to those of **(A,B)**. A large TH^+ ribbon which penetrates the rest of the tissue is interestingly also present, likely representing a sympathetic nerve fiber.

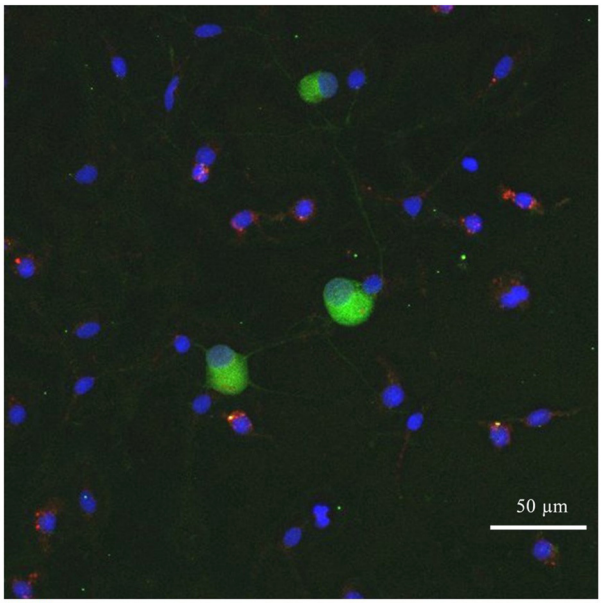

FIGURE 7 | Immunocytochemical image of Wistar stellate neurons (TH^+, green), with BMDMs ($CD68^+$, red).

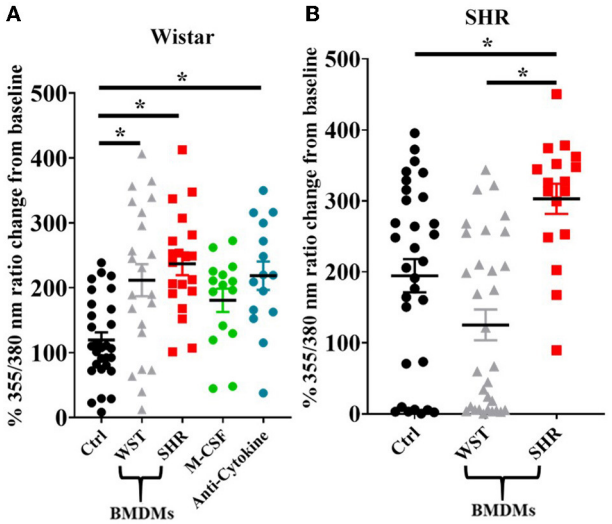

FIGURE 8 | Peak $[Ca^{2+}]_i$ transient responses of stellate neurons co-cultured with BMDMs in response to 100 μM nicotine: **(A)** Wistar neurons (with Wistar BMDMs: $n = 20$ neurons, 2 cultures, 2 rats; with SHR BMDMs: $n = 22$ neurons, 1 culture, 2 rats; M-CSF control: $n = 15$ neurons, 2 cultures, 2–4 rats per culture, anti-cytokine: $n = 15$, 2 cultures, 2 rats per culture) and **(B)** SHR neurons (with Wistar BMDMs: $n = 31$ neurons, 3 cultures; with SHR BMDMs: $n = 17$ neurons, 2 cultures). Data are presented as mean ± SEM; * signifies $p < 0.05$ between the indicated groups; normal data were analyzed using Brown-Forsythe and Welch's ANOVAs with Dunnett's T3 multiple comparisons test, while non-normal data were analyses with a Kruskall-Wallis test followed by Dunn's multiple comparisons test.

Co-culture With Bone Marrow-Derived Macrophages Enhances Wistar Stellate Neuron Nicotinic Responsiveness, but SHR Neurons Are Only Further Enhanced by Co-culture With Their Own Strain of Macrophages

As the most striking difference between the pre-hypertensive SHR and Wistar rats was the altered monocyte-macrophage subset ratio, we examined the effect of co-culturing stellate neurons from these strains with macrophages (bone-marrow derived) from either strain. We had previously attempted to FAC-sort macrophages from SHR and WST stellate ganglia, but unfortunately as there are such low numbers of these cells it is impossible to extract enough for culture. For this reason, we used bone marrow-derived macrophages (BMDMs), which arise from the same bone marrow monocyte precursor thought to give rise to the stellate monocyte-macrophages (45).

First, we confirmed successful co-culture of sympathetic stellate neurons (TH^+) with BMDMs ($CD68^+$), using immunocytochemistry, which revealed the presence of both cell types in close proximity (**Figure 7**).

Upon BMDM co-culture, as with the blood leukocytes, the Wistar stellate neurons showed increased nicotine responsiveness in the presence of BMDMs from either strain, while the SHR neurons only showed an increased response when cultured with their own BMDMs, not those of Wistar rats (**Figures 8A,B**). As the BMDM co-culture required addition of M-CSF to keep the BMDMs alive, control experiments were performed in which Wistar neurons alone were cultured with the same concentration of this factor. These neurons did not display a nicotinic response differing significantly from baseline, and there was no significant difference between this response and those from the BMDM co-cultures (**Figure 8A**).

As the presence of BMDMs increased Wistar stellate neuron responsiveness to nicotine, an attempt was made to identify potential mediating factors. Macrophages contribute to neuronal hyperactivity through release of pro-inflammatory cytokines, therefore we tested the effect of combined blockade of the classical triad of inflammatory cytokines: TNF-α, IL-1β and IL-6. However, the nicotinic responsiveness of Wistar stellate neurons co-cultured with Wistar BMDMs was still enhanced in the presence of antibodies targeted against TNF-α (100 ng/ml), IL-1β (140 ng/ml) and IL-6 (833 ng/ml) (**Figure 8A**).

The results of all such co-culture experiments are summarized in **Table 1**.

DISCUSSION

This study reports three novel findings: (1) The SHR sympathetic ganglia, blood and kidneys display a reduced classical/non-classical monocyte ratio, when compared to sympathetic ganglia from age matched Wistar rats. (2) Co-culturing

Wistar blood leukocytes with Wistar stellate neurons increases their $[Ca^{2+}]_i$ transient to nicotinic stimulation, making them phenocopy those of the SHR, although SHR leukocytes did not significantly affect pre-hypertensive SHR neurons. (3) Co-culturing either Wistar or SHR bone marrow-derived macrophages (BMDMs) with Wistar stellate neurons increases their $[Ca^{2+}]_i$ transient to nicotinic stimulation, but only SHR (and not Wistar) BMDMs further enhances the responsiveness of SHR neurons.

Monocyte-Macrophage Subset Shift: A Feature of Hypertension?

The pre-SHR displays a lack of classical monocyte-macrophages in its sympathetic ganglia, and a relative enrichment of non-classical monocyte-macrophages. This lower classical/non-classical monocyte ratio is observed in the blood and kidneys of the pre-SHR. This was the most striking and consistently observed difference between the SHR and Wistar strains.

What is the significance of this finding? Many other inflammatory-related diseases feature a relative enrichment of non-classical blood monocytes, including: systemic lupus erythomatosis (46, 47), sepsis (46), obesity and metabolic syndrome (48), and rheumatoid arthritis (49). Furthermore, these cells seem to exhibit a pro-inflammatory phenotype (46, 50–52), which has been implicated in these disease states, suggesting the altered monocyte-macrophage ratio might also be an immunological feature of essential hypertension.

Role of Macrophages in Sympathetic Neuron Hyperactivity?

Non-classical monocytes are major producers of inflammatory cytokines (46, 50, 52) and possess a strong ability to activate naïve T cells (51). In each of these cases the non-classical monocytes were observed to be the most potent monocyte subset. Zhu et al. (47) also showed $CD16^+$ monocytes were strong activators of B cells, although they grouped non-classical and intermediate monocytes together, so a specific non-classical effect cannot be determined. Furthermore, looking at more specific disease contexts, $CD16^+$ from SLE patients display enhanced inflammatory attributes, and in the murine serum-transfer rheumatoid arthritis model, clodronate-depletion of monocytes and replacement with non-classical monocytes enhances disease, while replacement with classical ones delays it (53). By contrast, pro-phagocytic, homeostatic roles for classical monocytes have been observed (46, 54).

If the SHR stellate has lost a homeostatic cell type, and gained a pathological one, this may interfere with local neuronal functioning. Local inflammation promotes states of local neuronal hyper-excitability in a number of contexts, many involving the sympathetic nervous system (20, 26, 30–33). Moreover, anti-TNFα treatment infliximab causes an increase in circulating non-classical monocytes in Crohn's disease patients (55), along with an increase in all $CD16^+$ monocytes in rheumatoid arthritis patients (56). The latter study showed a concomitant reduction in circulating CCL2 causing them to hypothesize that this increase in blood non-classical monocytes was due to reduced recruitment to inflamed tissues. However, CCL2 is mainly a chemoattractant for *classical* monocytes (57). The mechanism would thus have to involve reduced classical monocyte recruitment to the tissues and therefore reduced subsequent differentiation into non-classical monocytes. Since blood classical monocyte numbers increased in our study though, this seems unlikely.

In the pre-hypertensive SHR stellate ganglia of this study, there were higher relative numbers of neutrophils, an important inflammatory cell type, which are known to drive monocyte recruitment and polarization toward an inflammatory phenotype (58). Moreover, SHR neutrophils tend to produce higher levels of ROS (40, 59, 60), which tend to enhance inflammation. This certainly suggests some form of immunological reaction occurring in this tissue.

Very interestingly though, whole blood leukocytes in co-culture increase Wistar stellate neuron $[Ca^{2+}]_i$ transients, but not those from the SHR. Moreover, BMDMs of either strain increase Wistar neuron responsiveness to stimulation, while only SHR BMDMs increase that of SHR neurons. It seems unlikely (though not impossible) that these macrophages or other leukocytes interact physically with the neurons, at least to any substantial

TABLE 1 | Summary of stellate neuronal $[Ca^{2+}]_i$ transient responsiveness to nicotinic stimulation in co-culture experiments.

		Control	Leukocytes		BMDMs		
			WST	SHR	WST	SHR	WST with TNF-α, IL-1β and IL-6 blockade
Stellate neuron strain	WST	Baseline	+	Baseline[a]	+	+	+
	SHR	+	+	+	+	++	Not tested

Wistar neurons in monoculture are taken as the baseline and all other permutations described relative to this.

[a] *The nicotinic responsiveness of Wistar stellate neurons co-cultured with SHR leukocytes did not quite statistically significantly differ from baseline ($p = 0.080$). For reasons discussed in Chapter V, it seems possible that this result was a type II error and that SHR leukocytes should increase Wistar neuron $[Ca^{2+}]_i$ transient responsiveness to stimulation. This is due to the observations that: (1) the nicotinic response of Wistar stellate neurons co-cultured with SHR leukocytes did not differ significantly from that of those cultured with Wistar leukocytes, which were themselves significantly different from baseline; (2) the responses of these two populations were much closer together in magnitude than that of the neurons cultured with SHR leukocytes compared to baseline; and (3) SHR leukocytes significantly increased the responsiveness of Wistar neurons to high $[K^+]_o$ depolarization.*

extent. We think it more probable that these immune cells release a factor (or group of factors), which sensitizes the sympathetic neurons. However, our multi-cytokine blockade experiment does not support a role for TNF-α, IL-1β or IL-6. The observation that SHR neurons are unaffected by whole blood leukocytes, may imply they have already been exposed to a sensitizing stimulus. Nevertheless, SHR BMDMs can still increase the activity of SHR stellate neurons (while those from Wistar rats cannot), suggesting a property specific to these SHR macrophages can promote the excitability of already hyperactive neurons, where their general leukocytes cannot. Taken together with the altered monocyte-macrophage composition of the SHR stellate ganglion, it is likely that macrophages play a role in SHR peripheral sympathetic hyperactivity.

DATA AVAILABILITY STATEMENT

The raw data supporting the conclusions of this article will be made available by the authors, without undue reservation.

ETHICS STATEMENT

Ethical review and approval was not required for the animal study because the keeping and use of these animals was covered by the UK Home Office Project License (PPL) of D. J. Paterson: 30/3031 and P707EB251. The use of animals in the experiments of this publication complied with the University of Oxford Local Ethical Guidelines and the Animals (Scientific Procedures) Act 1986 of the United Kingdom.

AUTHOR CONTRIBUTIONS

OCN designed and performed the experiments, analyzed the data, and drafted the manuscript. DJP and AID helped design the experiments and edited the manuscript. All authors contributed to the article and approved the submitted version.

FUNDING

This study was funded by the British Heart Foundation Centre of Research Excellence and a BHF programme grant, UK (*RG*/17/14/33085) awarded to DJP. OCN was funded by a BHF Ph.D. studentship. AID is supported by the European Research Council (ERC-2017-COG-771431), and by Wellcome (208576/Z/17/Z).

ACKNOWLEDGMENTS

The authors would like to thank Dr. Harvey Davis and Dr. Chelsea Larabee for their scientific and technical advice, and Dr. Michal Maj and Robert Hedley for their efficient running and maintenance of the flow cytometry facility at the Sir William Dunn School of Pathology, University of Oxford.

REFERENCES

1. Grassi G. Assessment of sympathetic cardiovascular drive in human hypertension achievements and perspectives. *Hypertension.* (2009) 54:690–7. doi: 10.1161/HYPERTENSIONAHA.108.119883
2. Mancia G, Grassi G. The autonomic nervous system and hypertension. *Circ Res.* (2014) 114:1804–14. doi: 10.1161/CIRCRESAHA.114.302524
3. Grassi G, Mark A, Esler M. The sympathetic nervous system alterations in human hypertension. *Circ Res.* (2015) 116:976–90. doi: 10.1161/CIRCRESAHA.116.303604
4. Grassi G, Seravalle G, Quarti-Trevano F. The 'neuroadrenergic hypothesis' in hypertension: current evidence. *Exp Physiol.* (2010) 95:581–6. doi: 10.1113/expphysiol.2009.047381
5. Herring N, Kalla M, Paterson DJ. The autonomic nervous system and cardiac arrhythmias: current concepts and emerging therapies. *Nat Rev Cardiol.* (2019) 16:707–26. doi: 10.1038/s41569-019-0221-2
6. Grassi G, Cattaneo BM, Seravalle G, Lanfranchi A. Baroreflex control of sympathetic nerve activity in essential and secondary hypertension. *Hypertension.* (1998) 31:68–72. doi: 10.1161/01.HYP.31.1.68
7. Grassi G, Seravalle G, Bertinieri G, Turri C, Dell'oro R, Stella ML. Sympathetic and reflex alterations in systo-diastolic and systolic hypertension of the elderly. *J Hypertens.* (2000) 18:587–93. doi: 10.1097/00004872-200018050-00012
8. Smith PA, Graham LN, Mackintosh AF, Stoker JB. Relationship between central sympathetic activity and stages of human hypertension. *Am J Hypertens.* (2004) 17:217–22. doi: 10.1016/j.amjhyper.2003.10.010
9. Floras JS, Hara, K. Sympathoneural and hemodynamic characteristics of young subjects with mild essential-hypertension. *J Hypertens.* (1993) 11:647–55. doi: 10.1097/00004872-199306000-00009
10. Yamada Y, Miyajima E, Tochikubo O, Matsukawa T, Shionoiri H, Ishii M. Impaired baroreflex changes in muscle sympathetic-nerve activity in adolescents who have a family history of essential-hypertension. *J Hypertens.* (1988) 6:S525–8. doi: 10.1097/00004872-198812040-00165
11. Masuo K, Mikami H, Ogihara T. Sympathetic nerve hyperactivity precedes hyperinsulinemia and blood pressure elevation in a young, nonobese Japanese population. *Am J Hypertens.* (1997) 10:77–83. doi: 10.1016/S0895-7061(96)00303-2
12. Ferrier C, Cox H, Esler M. Elevated total-body noradrenaline spillover in normotensive members of hypertensive families. *Clin Sci.* (1993) 84:225–30. doi: 10.1042/cs0840225
13. Burns J, Sivananthan MU, Ball SG, Mackintosh AF, Mary DASG. Relationship between central sympathetic drive and magnetic resonance imaging-determined left ventricular mass in essential hypertension. *Circulation.* (2007) 115:1999–2005. doi: 10.1161/CIRCULATIONAHA.106.668863
14. Levick SP, Murray DB, Janicki JS. Sympathetic nervous system modulation of inflammation and remodeling in the hypertensive heart. *Hypertension.* (2010) 55:270–U129. doi: 10.1161/HYPERTENSIONAHA.109.142042
15. Lown B, Verrier RL. Neural activity and ventricular-fibrillation. *N Engl J Med.* (1976) 294:1165–70. doi: 10.1056/NEJM197605202942107
16. Fisher JP, Young CN, Fadel PJ. Central sympathetic overactivity: Maladies and mechanisms. *Auton Neurosci Basic Clin.* (2009) 148:5–15. doi: 10.1016/j.autneu.2009.02.003
17. Julius S, Valentini M. Consequences of the increased autonomic nervous drive in hypertension, heart failure and diabetes. *Blood Press Suppl.* (1998) 3:5–13. doi: 10.1080/080370598438410-1
18. Singh MV, Chapleau MW, Harwani SC. The immune system and hypertension. *Immunol Res.* (2014) 59:243–53. doi: 10.1007/s12026-014-8548-6
19. Rodriguez-Iturbe B, Pons H, Johnson RJ. Role of the immune system in hypertension. *Physiol Rev.* (2017) 97:1127–64. doi: 10.1152/physrev.00031.2016

20. Santisteban MM, Ahmari N, Carvajal JM, Zingler MB, Qi YF, Kim S, et al. Involvement of bone marrow cells and neuroinflammation in hypertension. *Circ Res*. (2015) 117:178–91. doi: 10.1161/CIRCRESAHA.117.305853
21. Sesso HD, Buring JE, Rifai N, Blake GJ, Gaziano JM. C-reactive protein and the risk of developing hypertension. *JAMA*. (2003) 290:2945–51. doi: 10.1001/jama.290.22.2945
22. King DE, Egan BM, Mainous AG. Elevation of C-reactive protein in people with prehypertension. *J Clin Hypertens.* (2004) 6:562–8. doi: 10.1111/j.1524-6175.2004.03577.x
23. Lakoski SG, Cushman M, Siscovick DS, Blumenthal RS, Palmas W, Burke G. The relationship between inflammation, obesity and risk for hypertension in the Multi-Ethnic Study of Atherosclerosis (MESA). *J Hum Hypertens.* (2011) 25:73–9. doi: 10.1038/jhh.2010.91
24. Jayedi A, Rahimi K, Bautista LE, Nazarzadeh M, Zargar MS. Inflammation markers and risk of developing hypertension: a meta-analysis of cohort studies. *Heart.* (2019) 105:686–92. doi: 10.1136/heartjnl-2018-314216
25. Larabee CM, Neely OC, Domingos AI. Obesity: a neuroimmunometabolic perspective. *Nat Rev Endocrinol.* (2020) 16:30–43. doi: 10.1038/s41574-019-0283-6
26. Wu KLH, Chan SHH, Chan JYH. Neuroinflammation and oxidative stress in rostral ventrolateral medulla contribute to neurogenic hypertension induced by systemic inflammation. *J Neuroinflammation.* (2012) 9. doi: 10.1186/1742-2094-9-212
27. Shanks J, Manou-Stathopoulou S, Lu CJ, Li D, Paterson DJ. Cardiac sympathetic dysfunction in the prehypertensive spontaneously hypertensive rat. *Am J Physiol Heart Circ Physiol.* (2013) 305:H980–6. doi: 10.1152/ajpheart.00255.2013
28. Bardsley EN, Davis H, Buckler KJ. Neurotransmitter switching coupled to beta-adrenergic signaling in sympathetic neurons in prehypertensive states. *Hypertension.* (2018) 71:1226–38. doi: 10.1161/HYPERTENSIONAHA.118.10844
29. Davis H, Herring N, Paterson DJ. Downregulation of M current is coupled to membrane excitability in sympathetic neurons before the onset of hypertension. *Hypertension.* (2020) 76:1915–23. doi: 10.1161/HYPERTENSIONAHA.120.15922
30. Scholz J, Woolf CJ. The neuropathic pain triad: neurons, immune cells and glia. *Nat Neurosci.* (2007) 10:1361–8. doi: 10.1038/nn1992
31. Zhou SM, Chen LS, Miyauchi Y, Miyauchi M, Kar S, Kangavari S, et al. Mechanisms of cardiac nerve sprouting after myocardial infarction in dogs. *Circ Res.* (2004) 95:76–83. doi: 10.1161/01.RES.0000133678.22968.e3
32. Hasan W, Jama A, Donohue T, Wernli G, Onyszchuk G, Al-Hafez B, et al. Sympathetic hyperinnervation and inflammatory cell NGF synthesis following myocardial infarction in rats. *Brain Res.* (2006) 1124:142–54. doi: 10.1016/j.brainres.2006.09.054
33. Wernli G, Hasan W, Bhattacherjee A, Van Rooijen N. Macrophage depletion suppresses sympathetic hyperinnervation following myocardial infarction. *Basic Res Cardiol.* (2009) 104:681–93. doi: 10.1007/s00395-009-0033-3
34. Ramer MS, Murphy PG, Richardson PM. Spinal nerve lesion-induced mechanoallodynia and adrenergic sprouting in sensory ganglia are attenuated in interleukin-6 knockout mice. *Pain.* (1998) 78:115–21. doi: 10.1016/S0304-3959(98)00121-3
35. Fernandez-Real JM, Vayreda M, Richart C, Gutierrez C, Broch M, Vendrell J. Circulating interleukin 6 levels, blood pressure, and insulin sensitivity in apparently healthy men and women. *J Clin Endocrinol Metab.* (2001) 86:1154–9. doi: 10.1210/jcem.86.3.7305
36. Li D, Lee CW, Buckler K, Parekh A, Herring N. Abnormal intracellular calcium homeostasis in sympathetic neurons from young prehypertensive rats. *Hypertension.* (2012) 59:642–U282. doi: 10.1161/HYPERTENSIONAHA.111.186460
37. Dickhout JG, Lee R. Blood pressure and heart rate development in young spontaneously hypertensive rats. *Am J Physiol Heart Circ Physiol.* (1998) 274:H794–800. doi: 10.1152/ajpheart.1998.274.3.H794
38. Claassen I, Vanrooijen N, Claassen E. A new method for removal of mononuclear phagocytes from heterogeneous cell-populations invitro, using the liposome-mediated macrophage suicide techniquE. *J Immunol Methods.* (1990) 134:153–61. doi: 10.1016/0022-1759(90)90376-7
39. Burba-Anczewska I. Leukocyte system in spontaneously hypertensive rats. *Acta Physiol Pol.* (1978) 29:353–8.
40. Schmidschonbein GW, Seiffge D, Delano FA, Shen K. Leukocyte counts and activation in spontaneously hypertensive and normotensive rats. *Hypertension.* (1991) 17:323–30. doi: 10.1161/01.HYP.17.3.323
41. Reed JP, Hendley ED. Blood-cell changes in spontaneously hypertensive rats are not all associated with the hypertensive phenotype. *J Hypertens.* (1994) 12:391–9. doi: 10.1097/00004872-199404000-00009
42. Muschter D, Gottl C, Vogel M, Grifka J, Straub RH. Reactivity of rat bone marrow-derived macrophages to neurotransmitter stimulation in the context of collagen II-induced arthritis. *Arthritis Res Ther.* (2015) 17:169. doi: 10.1186/s13075-015-0684-4
43. Rubio-Navarro A, Guerrero-Hue M, Martn-Fernandez B, Cortegano I, Olivares-Alvaro E, Heras NDL, et al. Phenotypic characterization of macrophages from rat kidney by flow cytometry. *J Vis Exp.* (2016) 116:54599. doi: 10.3791/54599
44. Scheiermann C, Kunisaki Y, Lucas D, Chow A, Jang, JE, Zhang D, et al. Adrenergic nerves govern circadian leukocyte recruitment to tissues. *Immunity.* (2012) 37:290–301.
45. Pirzgalska RM, Seixas E, Seidman JS, Link VM, Sanchez, NM, Mahu I, et al. Sympathetic neuron-associated macrophages contribute to obesity by importing and metabolizing norepinephrine. *Nat Med.* (2017) 23:1309–18.
46. Mukherjee R, Barman PK, Thatoi PK, Tripathy R, Das BK. Non-Classical monocytes display inflammatory features: validation in Sepsis and Systemic Lupus Erythematous. *Sci Rep.* (2015) 5:13886. doi: 10.1038/srep13886
47. Zhu HQ, Hu FL, Sun XL, Zhang XY, Zhu L, Liu X, et al. CD 16(+) monocyte subset was enriched and functionally exacerbated in driving T-cell activation and B-cell response in systemic lupus erythematosus. *Front Immunol.* (2016) 7:512. doi: 10.3389/fimmu.2016.00512
48. Poitou C, Dalmas E, Renovato M, Benhamo V, Hajduch F, Abdennour M. CD14. (dim)CD16(+) and CD14(+)CD16(+) monocytes in obesity and during weight loss relationships with fat mass and subclinical atherosclerosis. *Arterioscler Thromb Vasc Biol.* (2011) 31:2322-U372. doi: 10.1161/ATVBAHA.111.230979
49. Lacerte P, Brunet A, Egarnes B, Duchene B, Brown JP. Overexpression of TLR2 and TLR9 on monocyte subsets of active rheumatoid arthritis patients contributes to enhance responsiveness to TLR agonists. *Arthritis Res Ther.* (2016) 18:10. doi: 10.1186/s13075-015-0901-1
50. Wong KL, Tai JJY, Wong WC, Han H, Sem X, Yeap WH, et al. Gene expression profiling reveals the defining features of the classical, intermediate, and nonclassical human monocyte subsets. *Blood.* (2011) 118:E15–30. doi: 10.1182/blood-2010-12-326355
51. Liu BY, Dhanda A, Hirani S, Williams EL, Sen HN, Estrada FM. CD14. (++)CD16(+) monocytes are enriched by glucocorticoid treatment and are functionally attenuated in driving effector T cell responses. *J Immunol.* (2015) 194:5150–60. doi: 10.4049/jimmunol.1402409
52. Ong S-M, Hadadi E, Dang T-M, Yeap W-H, Tan CT-Y, Ng T-P, et al. The pro-inflammatory phenotype of the human non-classical monocyte subset is attributed to senescence. *Cell Death Dis.* (2018) 9:266. doi: 10.1038/s41419-018-0327-1
53. Misharin AV, Cuda CM, Saber R, Turner JD, Gierut AK, Haines GK. Nonclassical Ly6C(-) monocytes drive the development of inflammatory arthritis in mice. *Cell Rep.* (2014) 9:591–604. doi: 10.1016/j.celrep.2014.09.032
54. Cros J, Cagnard N, Woollard K, Patey N, Zhang SY, Senechal B. Human CD14(dim) monocytes patrol and sense nucleic acids and viruses *via* TLR7 and TLR8 receptors. *Immunity.* (2010) 33:375–86. doi: 10.1016/j.immuni.2010.08.012
55. Nazareth N, Magro F, Silva J, Duro M, Gracio D, Coelho R, et al. Infliximab therapy increases the frequency of circulating CD16(+) monocytes and modifies macrophage cytokine response to bacterial infection. *Clin Exp Immunol.* (2014) 177:703–11. doi: 10.1111/cei.12375
56. Aeberli D, Kamgang R, Balani D, Hofstetter W, Villiger PM. Regulation of peripheral classical and non-classical monocytes on infliximab treatment in patients with rheumatoid arthritis and ankylosing spondylitis. *Rmd Open.* (2016) 2:e000079. doi: 10.1136/rmdopen-2015-000079
57. Geissmann F, Jung S, Littman DR. Blood monocytes consist of two principal subsets with distinct migratory properties. *Immunity.* (2003) 19:71–82. doi: 10.1016/S1074-7613(03)00174-2
58. Soehnlein O, Steffens S, Hidalgo A, Weber C. Neutrophils as protagonists and targets in chronic inflammation. *Nat Rev Immunol.* (2017) 17:248–61. doi: 10.1038/nri.2017.10

59. Ohmori M, Kitoh Y, Harada K, Sugimoto K. Polymorphonuclear leukocytes (PMNs) functions in SHR, L-NAME- and DOCA/salt-induced hypertensive rats. *J Hypertens.* (2000) 18:703–7. doi: 10.1097/00004872-200018060-00007
60. Chatterjee M, Saluja R, Tewari S, Barthwal MK, Goel SK. Augmented nitric oxide generation in neutrophils: Oxidative and pro-inflammatory implications in hypertension. *Free Radic Res.* (2009) 43:1195–204. doi: 10.3109/10715760903247256

Conflict of Interest: The authors declare that the research was conducted in the absence of any commercial or financial relationships that could be construed as a potential conflict of interest.

Publisher's Note: All claims expressed in this article are solely those of the authors and do not necessarily represent those of their affiliated organizations, or those of the publisher, the editors and the reviewers. Any product that may be evaluated in this article, or claim that may be made by its manufacturer, is not guaranteed or endorsed by the publisher.

frontiers in Cardiovascular Medicine

PERSPECTIVE
published: 10 February 2022
doi: 10.3389/fcvm.2022.842656

Untangling Peripheral Sympathetic Neurocircuits

*Courtney Clyburn[1], Michael C. Andresen[1], Susan L. Ingram[2] and Beth A. Habecker[1]**

[1] Department of Chemical Physiology and Biochemistry, Oregon Health and Science University, Portland, OR, United States, [2] Department of Neurological Surgery, Oregon Health and Science University, Portland, OR, United States

The sympathetic nervous system plays a critical role in regulating many autonomic functions, including cardiac rhythm. The postganglionic neurons in the sympathetic chain ganglia are essential components that relay sympathetic signals to target tissues and disruption of their activity leads to poor health outcomes. Despite this importance, the neurocircuitry within sympathetic ganglia is poorly understood. Canonically, postganglionic sympathetic neurons are thought to simply be activated by monosynaptic inputs from preganglionic cholinergic neurons of the intermediolateral cell columns of the spinal cord. Early electrophysiological studies of sympathetic ganglia where the peripheral nerve trunks were electrically stimulated identified excitatory cholinergic synaptic events in addition to retrograde action potentials, leading some to speculate that excitatory collateral projections are present. However, this seemed unlikely since sympathetic postganglionic neurons were known to synthesize and release norepinephrine and expression of dual neurochemical phenotypes had not been well recognized. *In vitro* studies clearly established the capacity of cultured sympathetic neurons to express and release acetylcholine *and* norepinephrine throughout development and even in pathophysiological conditions. Given this insight, we believe that the canonical view of ganglionic transmission needs to be reevaluated and may provide a mechanistic understanding of autonomic imbalance in disease. Further studies likely will require genetic models manipulating neurochemical phenotypes within sympathetic ganglia to resolve the function of cholinergic collateral projections between postganglionic neurons. In this perspective article, we will discuss the evidence for collateral projections in sympathetic ganglia, determine if current laboratory techniques could address these questions, and discuss potential obstacles and caveats.

Keywords: sympathetic ganglia, neurocircuits, synaptic inputs, co-transmission, collaterals

OPEN ACCESS

Edited by:
Tania Zaglia,
University of Padova, Italy

Reviewed by:
Nazareno Paolocci,
Johns Hopkins University,
United States
Matthew W. Kay,
George Washington University,
United States
Michael Rubart,
Indiana University Bloomington,
United States

****Correspondence:***
Beth A. Habecker
habecker@ohsu.edu

Specialty section:
This article was submitted to Hypertension, a section of the journal Frontiers in Cardiovascular Medicine

Received: *24 December 2021*
Accepted: *19 January 2022*
Published: *10 February 2022*

Citation:
Clyburn C, Andresen MC, Ingram SL and Habecker BA (2022) Untangling Peripheral Sympathetic Neurocircuits. Front. Cardiovasc. Med. 9:842656. doi: 10.3389/fcvm.2022.842656

INTRODUCTION

Technical advances have long driven new insights into the mechanistic basis of neurophysiology. From the identification of the action potential in the nineteenth century (1) to the work of Joseph Erlanger and Herbert Gasser who revolutionized neurophysiological research by developing sensitive oscilloscopes that allowed for the visualization and analysis of nerve impulses previously below the threshold of detection (2, 3). With these technological advancements, researchers set out to decode the complex autonomic signals that regulate visceral functions, including cardiac

activity (4–6). Several important hypotheses arose from this work, but were untested due to experimental limitations that existed at the time. These questions include whether or not collateral projections are present between postganglionic neurons in sympathetic ganglia and what neurotransmitters may be involved in sympathetic signaling pathways. Since these first studies, significant advancements in neurophysiological equipment and scientific methods have allowed for substantial progress in understanding the neurophysiology of peripheral sympathetic activity (7–11), but the neurocircuitry within sympathetic ganglia remains poorly understood. The purpose of this article is to review the primary data that support these untested hypotheses, determine if current technology and experimental methods can be used to answer these important questions, and discuss any potential obstacles that may arise.

Canonical Neurocircuitry of Cervical Sympathetic Ganglia

Several well-written review articles are available that thoroughly summarize our current understanding of the sympathetic neurocircuitry that regulates visceral functions and cardiac activity (12–16). To briefly summarize, sympathetic signals originate in the hypothalamus and brainstem and travel to the preganglionic neurons in the intermediolateral cell column of the spinal cord. These preganglionic neurons send cholinergic projections to postganglionic neurons in the cervical sympathetic chain ganglia. These neurons in the sympathetic ganglia then send noradrenergic projections through the postganglionic nerve trunk to innervate the target tissue. This general organization is conserved across species. However, there is significant biological variability in the anatomy and physiology of the cervical sympathetic ganglia which clouds our understanding of peripheral sympathetic neurocircuits. The cervical sympathetic chain includes the superior, middle, and inferior cervical ganglia and exhibits significant anatomical variability between species, between individuals, and even between the left and right ganglia. In approximately 80% of humans, for example, the inferior cervical ganglion is fused with the first thoracic ganglion to form the cervicothoracic (commonly known as stellate) ganglion. Additionally, the middle cervical ganglion is completely absent in ∼20% of the population (17–20). In considering the variability in the sympathetic nervous system in humans and animal models as well as the murkiness that surrounds the functional organization of the cervical sympathetic ganglia, we will consider data from all cervical sympathetic ganglia interchangeably as we discuss peripheral sympathetic neurocircuitry.

Evidence for Collateral Projections in Sympathetic Ganglia

In addition to the ambiguity surrounding the anatomy of the sympathetic ganglia, the functional organization of the sympathetic neurocircuitry within these ganglia remains poorly defined. Current literature usually describes and illustrates the neurocircuitry within cervical sympathetic ganglia as simple monosynaptic connections from cholinergic preganglionic neurons to the noradrenergic postganglionic neurons that innervate visceral targets and the heart (21, 22). However, Erulkar and Woodward (23) made intracellular recordings of postganglionic sympathetic neurons from rabbit superior cervical ganglia (SCG) *in situ* which suggest this neurocircuitry may be more complicated. In these early experiments, they found that stimulation of the external carotid nerve produced single, short latency spikes followed by long-lasting hyperpolarizations (presumably action potentials) in some neurons. In these experiments, electrical stimulation of the postganglionic nerve trunk evoked antidromic, or retrograde, action potentials that traveled up the axon to the cell body in the SCG. Surprisingly, the majority of neurons exhibited an early spike followed by a long-lasting depolarization. This depolarization suggested that stimulation of the postganglionic nerve trunk elicited excitatory synaptic activity within the SCG. Erulkar and Woodward proposed several hypotheses that would account for this phenomenon, but state that the simplest explanation would be that recurrent excitatory collateral fibers from postganglionic axons project to neighboring cells within the SCG (**Figure 1**). Upon stimulation of the preganglionic nerve trunk, Erulkar and Woodward also observed that a significant proportion of SCG neurons exhibited multi-spike responses which were uncovered at increasing stimulation intensities. While they acknowledge these results may be caused by different populations of preganglionic fibers with different thresholds and conduction velocities that converge onto the same cell, this explanation seems highly unlikely. Instead, they note that the multi-spike responses are consistent with the collateral hypothesis and that the late-arriving impulses may have traveled through another indirect pathway.

Excitatory synaptic events in postganglionic sympathetic neurons following electrical stimulation of the postganglionic nerve trunk have also been observed in the cat, rat and guinea pig (24–26). In 1970, Perri et al. extended the observations by Erulkar and Woodward by investigating the neurotransmitter that may be involved in these synaptic events. Curare, a nicotinic acetylcholine (ACh) receptor antagonist, applied to the ganglionic preparation abolished these synaptic events, indicating they were likely cholinergic in nature (25). If these excitatory events originated from postganglionic collateral projections, this would mean that these sympathetic neurons express ACh *and* norepinephrine (NE). Although we now know that postganglionic sympathetic neurons and other neurons can express a dual neurochemical phenotype (27–31), at the time this was thought to be unlikely. Thus, researchers sought alternative explanations. These included the possibility that errant preganglionic fibers may be running up the postganglionic nerve trunk and forming excitatory synaptic connections with postganglionic neurons (**Figure 1**) (25). A second possibility raised was that sensory afferent neurons were the source of synaptic excitation. Sympathetic ganglia have long been linked to sensory afferents of the cardiac region of the thoracic viscera (6) but on the bases of such anatomical findings broadly dismissed as only passing through the ganglia on their way to the spinal cord. Thus, sketches commonly depict that a portion of these afferent paths include sympathetic ganglia

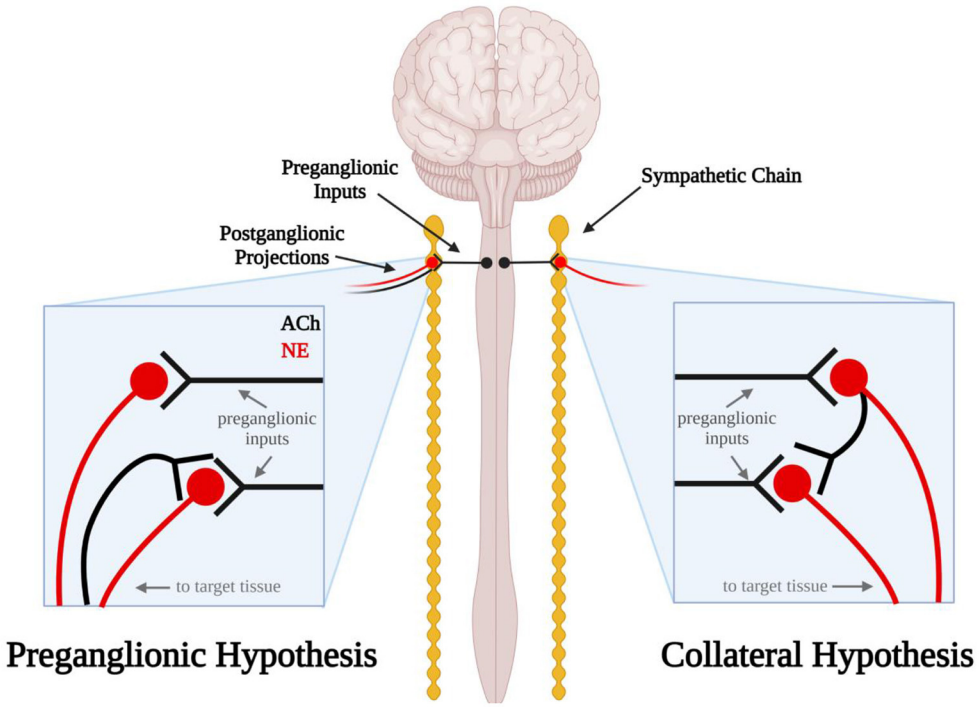

FIGURE 1 | Schematic diagram illustrating the errant preganglionic fiber and collateral hypotheses. In the preganglionic hypothesis (left), mis-routed cholinergic (black) preganglionic fibers travel back up the efferent nerves through which sympathetic axons travel to the target tissue. In the collateral hypothesis (right) postganglionic sympathetic neurons send noradrenergic projections (red) to the target tissue and cholinergic projections (black) to other sympathetic neurons in the sympathetic chain ganglia.

(e.g., cervical and stellate) (32). However, functional studies related to cardiovascular regulation, for example, indicate that activation of cardiac sensory afferents traveling via the stellate ganglia act to increase blood pressure by augmenting sympathetic motor neuron activity directed to the systemic vasculature and such responses are abolished by severing ganglion connections to the spinal cord (33). Dye tracing and electrical activity recordings indicate that such afferent neurons arise from the dorsal root ganglia and traverse peripheral sympathetic ganglia to their visceral targets (34). Although it seemed unlikely at the time, our current understanding of dual neurochemical phenotypes in sympathetic neurons has persuaded us that further studies are needed to investigate the potential presence of cholinergic collateral projections between postganglionic neurons in sympathetic ganglia.

Evidence for Dual Neurochemical Phenotypes in Sympathetic Neurons

In 1935, Henry Dale put forth the "one neuron, one neurotransmitter" hypothesis which was later termed as "Dale's Principle" (35, 36) and stated that one neuron was only capable of releasing one neurotransmitter at any one time [reviewed by: (37)]. By the mid-1970s, evidence disputing Dale's Principle began to emerge when Jan and colleagues made intracellular recordings of sympathetic frog neurons and observed slow synaptic potentials which were mediated by the peptide, luteinizing hormone-releasing hormone, in addition to the canonical cholinergic transmission (38, 39). Since these initial studies, co-transmission of several neuromodulators, including ATP and neuropeptide Y (NPY) (40–44), as well as the co-transmission of fast primary neurotransmitters have been well established throughout the central and peripheral nervous system (45–47).

Some of the earliest evidence supporting co-expression of primary neurotransmitters comes from cardiac myocyte—sympathetic neuron co-cultures (48). In 1976, Furshpan et al. used electrophysiological recordings of sympathetic SCG principal neurons cultured with cardiac myocytes from newborn rats and described a population of neurons that secreted ACh *and* NE (48–51). This work sparked a series of studies to determine if sympathetic neurons produced ACh *in vivo* and to identify the differentiation factors that determine the fates of sympathetic neurons (52). Several "cholinergic differentiation factors" are now known to induce ACh expression in noradrenergic sympathetic neurons including leukemia inhibitor factor (LIF), ciliary neurotrophic factor (CNTF), cardiotrophin-1 (CT-1), neurotrophin-3 (NT-3) and glial cell line-derived neurotrophic factor (GDNF) (53–61). While the cholinergic transdifferentiation of postganglionic sympathetic neurons *in vivo* was first thought to be confined to developmental periods, more recent studies have shown that inflammatory cytokines can induce cholinergic transdifferentiation in cardiac

disease (30, 62). Early studies have revealed key aspects of the neurochemical phenotype of sympathetic neurons: dual and malleable neurochemical capacity. These studies of cultured neurons indicated that these postganglionic neurons could form synapses between neurons and could display adrenergic/cholinergic dual function (50). In culture, the neurotrophin brain-derived neurotrophic factor (BDNF) rapidly shifted sympathetic neuron release of norepinephrine to ACh indicating the dual neurochemical phenotype of these postganglionic neurons (31). Subsequent work also in cultured neurons supported both segregation as well as plasticity of functional release sites of NE and ACh (63). In light of this evidence, it appears that the cholinergic hypothesis originally proposed by Erulkar and Woodward in 1968 was dismissed prematurely before fully testing the idea. Gaining a clear insight into the neurocircuitry within sympathetic ganglia can provide better understanding of the mechanisms underlying autonomic imbalance in disease and may highlight novel therapeutic targets for cardiac patients.

Challenges and Potential Caveats

The dual expression of ACh and NE in sympathetic neurons provides support for the collateral hypothesis, but there are still many questions that remain. When dual neurochemical phenotypes were first described, these neurons were generally classified into two mechanistic subtypes, co-release and co-transmission (37, 64). Co-release describes the packaging of multiple neurotransmitters into the same synaptic vesicle so they there are released together and co-transmission originally described different neurotransmitters packaged into different vesicles within the same presynaptic terminal (37, 64). Dale's Principle was updated in 1986 to state that neurons release the same group of neurotransmitters/peptides from all presynaptic terminals (64, 65). However, the collateral hypothesis challenges this view because the primary data indicates that ACh is released from the collateral terminals. The excitatory synaptic events that are observed following stimulation of the postganglionic nerve trunk are completely blocked by the application of nicotinic acetylcholine antagonists (24, 25). In the collateral model, this could suggest the biased expression of ACh and NE at different synapses within the same neuron. Based on the updated version of Dale's hypothesis, we would expect that both ACh and NE would be released from collateral synapses. As adrenergic receptors are G-protein coupled receptors, synaptic release of NE cannot be detected with the electrophysiological techniques used in these previous studies (25). Future experiments could utilize new biosensor technology to determine if NE is also released from collateral projections (66–68). If NE is not released from collateral projections, there are several mechanisms that have been described in the CNS that could explain biased release of different vesicular pools. These include differing release probabilities and altered coupling to presynaptic Ca^{2+} channels (69, 70), "kiss-and-run" release mechanisms, and even neurotransmitter segregation to separate axons (64, 71–74). Studies in cultured sympathetic neurons have observed segregation of the vesicular NE and ACh transporters (VMAT2 and VAChT, respectively) in distinct varicosities, suggesting release of each transmitter is independent and spatially segregated (63). Considering how target-derived factors and cytokines can induce cholinergic transdifferentiation in postganglionic sympathetic neurons, it is conceivable that factors in the microenvironment are involved in determining different neurochemical identities of synaptic terminals in the ganglia and target tissues.

Putative afferent fibers could have an important physiological role in allowing sensory feedback to regulate the activity of postganglionic sympathetic neurons in the event that inputs from the central nervous system are disrupted. This sensory feedback loop would also allow for the fast adaptation of sympathetic neuron activity to rapidly changing stimuli (24). However, the synaptic events that are observed following stimulation of the postganglionic nerve trunk are mediated by acetylcholine and, therefore, unlikely to be mediated by sensory fibers, which utilize glutamatergic signaling. The physiological consequence of putative cholinergic collateral projections is less obvious. Collateral projections between postganglionic sympathetic neurons may also have a significant physiological role in maintaining autonomic control of the heart and other tissues. Excitatory collateral projections between postganglionic sympathetic neurons would increase the probability that these neurons fire synchronously and may amplify preganglionic signals from the spinal cord. Given the importance of neural timing for cardiopulmonary integration, the synchronization of sympathetic inputs could potentially play a critical role in maintaining appropriate cardiac activity. Furthermore, disruption of this synchronization following injury or disease could exacerbate autonomic imbalance. Early studies hypothesized that single spikes in recordings of cardiac sympathetic nerve activity represent synchronized activity of multiple postganglionic neurons (75), but the potential role of collateral synapses in this synchronization is purely speculative.

It was not possible in the past to distinguish preganglionic cholinergic transmission from putative post-ganglionic collateral projections, but transgenic mouse models and genetic tools provide the means to address this issue now. Targeted deletion of ACh production (*chat* gene) or release (*slc18A3* gene) from neurons expressing tyrosine hydroxylase (*th* gene), dopamine beta hydroxylase (*dbh* gene), or norepinephrine transporter (*slc6a2* gene) would remove cholinergic transmission selectively from post-ganglionic neurons within the ganglion. Likewise, targeting expression of channelrhodopsin-2 or other stimulatory optogenetic tools to noradrenergic neurons would allow selective stimulation of those cells, coupled with recordings of resulting synaptic activity. Combining these approaches with the use of genetically encoded calcium sensors would allow testing the functional impact of putative cholinergic collateral transmission *in situ*. Mouse lines to facilitate these studies, which directly address the issue of potential cholinergic collaterals, are available from public repositories. If cholinergic collaterals are an important aspect of transmission by post-ganglionic sympathetic neurons then we would expect them to be present and detectable throughout

the sympathetic chain, and lead to changes in transmission to target tissues.

DISCUSSION

While some of the first studies investigating sympathetic nerve impulses proposed that collateral projections may be present in the sympathetic ganglia, this model was dismissed because of our incomplete understanding of dual neurochemical phenotypes. In hindsight, given our understanding of co-transmission of ACh and NE in postganglionic sympathetic neurons, it is clear that studies should be carried out to clarify the neurocircuitry within the sympathetic ganglia. The postganglionic neurons within sympathetic ganglia are critical components of the neurocircuitry responsible for relaying autonomic signals from the central nervous system to several visceral targets, including the heart. The activity of postganglionic sympathetic neurons is disrupted in many pathologies and sympathetic hyperactivity elevates risk for cardiac arrhythmias and sudden cardiac death and contributes to the development of heart failure. A detailed understanding sympathetic neurocircuitry is needed to understand how peripheral sympathetic activity is disrupted in pathophysiological conditions and to develop novel therapeutic strategies.

DATA AVAILABILITY STATEMENT

The original contributions presented in the study are included in the article, further inquiries can be directed to the corresponding author.

AUTHOR CONTRIBUTIONS

CC, MA, SI, and BH contributed to drafting the work and revising it critically for important intellectual content. All authors approved the final version of the manuscript and agree to be accountable for all aspects of the work. All persons designated as authors qualify for authorship, and all those who qualify for authorship are listed.

FUNDING

This work was supported by the National Institutes of Health Grant HL146833.

ACKNOWLEDGMENTS

The figure in this article was created with BioRender.com.

REFERENCES

1. Schuetze SM. The discovery of the action potential. *Trends Neurosci.* (1983) 6:164–8. doi: 10.1016/0166-2236(83)90078-4
2. Erlanger J, Bishop G, Gasser H. Experimental analysis of the simple action potential wave in nerve by the cathode ray oscillograph. *Am J Physiol Legacy Content.* (1926) 78:537–73. doi: 10.1152/ajplegacy.1926.78.3.537
3. Erlanger J, Gasser H. The action potential in fibers of slow conduction in spinal roots and somatic nerves. *Am J Physiol.* (1930) 92:43–82. doi: 10.1152/ajplegacy.1930.92.1.43
4. Adrian ED, Bronk DW, Phillips G. Discharges in mammalian sympathetic nerves. *J Physiol.* (1932) 74:115–33. doi: 10.1113/jphysiol.1932.sp002832
5. Langley JN. On axon-reflexes in the pre-ganglionic fibres of the sympathetic system. *J Physiol.* (1900) 25:364–98. doi: 10.1113/jphysiol.1900.sp000803
6. Ranson S, Billingsley P. The superior cervical ganglion and the cervical portion of the sympathetic trunk. *J Comp Neurol.* (1918) 29:313–358. doi: 10.1002/cne.900290403
7. Briant LJ, Paton JF, Pickering AE, Champneys AR. Modelling the vascular response to sympathetic postganglionic nerve activity. *J Theor Biol.* (2015) 371:102–16. doi: 10.1016/j.jtbi.2015.01.037
8. Carter JR. Microneurography and sympathetic nerve activity: a decade-by-decade journey across 50 years. *J Neurophysiol.* (2019) 121:1183–94. doi: 10.1152/jn.00570.2018
9. Greaney JL, Kenney WL. Measuring and quantifying skin sympathetic nervous system activity in humans. *J Neurophysiol.* (2017) 118:2181–93. doi: 10.1152/jn.00283.2017
10. Hart EC, Head GA, Carter JR, Wallin BG, May CN, Hamza SM, et al. Recording sympathetic nerve activity in conscious humans and other mammals: guidelines and the road to standardization. *Am J Physiol Heart Circ Physiol.* (2017) 312:H1031–51. doi: 10.1152/ajpheart.00703.2016
11. Macefield VG. Sympathetic microneurography. *Handb Clin Neurol.* (2013) 117:353–64. doi: 10.1016/B978-0-444-53491-0.00028-6
12. Dampney RA. Central neural control of the cardiovascular system: current perspectives. *Adv Physiol Educ.* (2016) 40:283–96. doi: 10.1152/advan.00027.2016
13. Fukuda K, Kanazawa H, Aizawa Y, Ardell JL, Shivkumar K. Cardiac innervation and sudden cardiac death. *Circ Res.* (2015) 116:2005–19. doi: 10.1161/CIRCRESAHA.116.304679
14. Habecker BA, Anderson ME, Birren SJ, Fukuda K, Herring N, Hoover DB, et al. Molecular and cellular neurocardiology: development, and cellular and molecular adaptations to heart disease. *J Physiol.* (2016) 594:3853–75. doi: 10.1113/JP271840
15. Rajendran PS, Challis RC, Fowlkes CC, Hanna P, Tompkins JD, Jordan MC, et al. Identification of peripheral neural circuits that regulate heart rate using optogenetic and viral vector strategies. *Nat Commun.* (2019) 10:1944. doi: 10.1038/s41467-019-09770-1
16. Scalco A, Moro N, Mongillo M, Zaglia T. Neurohumoral cardiac regulation: optogenetics gets into the groove. *Front Physiol.* (2021) 12:726895. doi: 10.3389/fphys.2021.726895
17. Fazliogullari Z, Kilic C, Karabulut AK, Yazar F. A morphometric analysis of the superior cervical ganglion and its surrounding structures. *Surg Radiol Anat.* (2016) 38:299–302. doi: 10.1007/s00276-015-1551-3
18. Narouze S. Ultrasound-guided stellate ganglion block: safety and efficacy. *Curr Pain Headache Rep.* (2014) 18:424. doi: 10.1007/s11916-014-0424-5
19. Pather N, Partab P, Singh B, Satyapal KS. The sympathetic contributions to the cardiac plexus. *Surg Radiol Anat.* (2003) 25:210–5. doi: 10.1007/s00276-003-0113-2
20. Yin Z, Yin J, Cai J, Sui T, Cao X. Neuroanatomy and clinical analysis of the cervical sympathetic trunk and longus colli. *J Biomed Res.* (2015) 29:501–7. doi: 10.7555/JBR.29.20150047
21. Jänig W. Organization of the sympathetic nervous system: peripheral and central aspects. *Neuroimmune Biol.* (2008) 7:55–85. doi: 10.1016/S1567-7443(07)00204-9
22. Vegh AMD, Duim SN, Smits AM, Poelmann RE, Ten Harkel ADJ, DeRuiter MC, et al. Part and parcel of the cardiac autonomic nerve system: unravelling its cellular building blocks during development. *J Cardiovasc Dev Dis.* (2016) 3:28. doi: 10.3390/jcdd3030028
23. Erulkar SD, Woodward JK. Intracellular recording from mammalian superior cervical ganglion in situ. *J Physiol.* (1968) 199:189–203. doi: 10.1113/jphysiol.1968.sp008648

24. Bosnjak ZJ, Kampine JP. Cardiac sympathetic afferent cell bodies are located in the peripheral nervous system of the cat. *Circ Res.* (1989) 64:554–62. doi: 10.1161/01.RES.64.3.554
25. Perri V, Sacchi O, Casella C. Synaptically mediated potentials elicited by the stimulation of post-ganglionic trunks in the guinea-pig superior cervical ganglion. *Pflugers Arch*. (1970) 314:55–67. doi: 10.1007/BF00587046
26. Wallis D, Watson AH, Mo N. Cardiac neurones of autonomic ganglia. *Microsc Res Tech.* (1996) 35:69–79. doi: 10.1002/(SICI)1097-0029(19960901)35:1andlt;69::AID-JEMT6andgt;3.0.CO;2-N
27. Bosnjak ZJ, Kampine JP. Intracellular recordings from the stellate ganglion of the cat. *J Physiol.* (1982) 324:273–83. doi: 10.1113/jphysiol.1982.sp014112
28. Bosnjak ZJ, Kampine JP. Electrophysiological and morphological characterization of neurons in stellate ganglion of cats. *Am J Physiol.* (1985) 248:R288–292. doi: 10.1152/ajpregu.1985.248.3.R288
29. Hoard JL, Hoover DB, Mabe AM, Blakely RD, Feng N, Paolocci N. Cholinergic neurons of mouse intrinsic cardiac ganglia contain noradrenergic enzymes, norepinephrine transporters, and the neurotrophin receptors tropomyosin-related kinase A and p75. *Neuroscience.* (2008) 156:129–42. doi: 10.1016/j.neuroscience.2008.06.063
30. Kanazawa H, Ieda M, Kimura K, Arai T, Kawaguchi-Manabe H, Matsuhashi T, et al. Heart failure causes cholinergic transdifferentiation of cardiac sympathetic nerves via gp130-signaling cytokines in rodents. *J Clin Invest.* (2010) 120:408–21. doi: 10.1172/JCI39778
31. Yang B, Slonimsky JD, Birren SJ. A rapid switch in sympathetic neurotransmitter release properties mediated by the p75 receptor. *Nat Neurosci.* (2002) 5:539–45. doi: 10.1038/nn0602-853
32. Coleridge JC, Kidd C, Sharp JA. The distribution, connexions and histology of baroreceptors in the pulmonary artery, with some observations on the sensory innervation of the ductus arteriosus. *J Physiol.* (1961) 156:591–602. doi: 10.1113/jphysiol.1961.sp006695
33. Peterson DF, Brown AM. Pressor reflexes produced by stimulation of afferent fibers in the cardiac sympathetic nerves of the cat. *Circ Res.* (1971) 28:605–10. doi: 10.1161/01.RES.28.6.605
34. Oldfield BJ, McLachlan EM. Localization of sensory neurons traversing the stellate ganglion of the cat. *J Comp Neurol.* (1978) 182:915–22. doi: 10.1002/cne.901820509
35. Dale H. Pharmacology and nerve-endings (walter ernest dixon memorial lecture): (section of therapeutics and pharmacology). *Proc R Soc Med.* (1935) 28:319–32. doi: 10.1177/003591573502800330
36. Eccles JC, Fatt P, Koketsu K. Cholinergic and inhibitory synapses in a pathway from motor-axon collaterals to motoneurones. *J Physiol.* (1954) 126:524–62. doi: 10.1113/jphysiol.1954.sp005226
37. Vaaga CE, Borisovska M, Westbrook GL. Dual-transmitter neurons: functional implications of co-release and co-transmission. *Curr Opin Neurobiol.* (2014) 29:25–32. doi: 10.1016/j.conb.2014.04.010
38. Jan LY, Jan YN. Peptidergic transmission in sympathetic ganglia of the frog. *J Physiol.* (1982) 327:219–46. doi: 10.1113/jphysiol.1982.sp014228
39. Jan YN, Jan LY, Kuffler SW. A peptide as a possible transmitter in sympathetic ganglia of the frog. *Proc Natl Acad Sci USA.* (1979) 76:1501–5. doi: 10.1073/pnas.76.3.1501
40. Alston EN, Parrish DC, Hasan W, Tharp K, Pahlmeyer L, Habecker BA. Cardiac ischemia-reperfusion regulates sympathetic neuropeptide expression through gp130-dependent and independent mechanisms. *Neuropeptides.* (2011) 45:33–42. doi: 10.1016/j.npep.2010.10.002
41. Browning KN, Lees GM. Inhibitory effects of NPY on ganglionic transmission in myenteric neurones of the guinea-pig descending colon. *Neurogastroenterol Motil.* (2000) 12:33–41. doi: 10.1046/j.1365-2982.2000.00178.x
42. Burnstock G. Physiology and pathophysiology of purinergic neurotransmission. *Physiol Rev.* (2007) 87:659–797. doi: 10.1152/physrev.00043.2006
43. Pernow J, Schwieler J, Kahan T, Hjemdahl P, Oberle J, Wallin BG, et al. Influence of sympathetic discharge pattern on norepinephrine and neuropeptide Y release. *Am J Physiol.* (1989) 257:H866–872. doi: 10.1152/ajpheart.1989.257.3.H866
44. Verhaeghe RH, Vanhoutte PM, Shepherd JT. Inhibition of sympathetic neurotransmission in canine blood vessels by adenosine and adenine nucleotides. *Circ Res.* (1977) 40:208–15. doi: 10.1161/01.RES.40.2.208
45. Johnson MD. Synaptic glutamate release by postnatal rat serotonergic neurons in microculture. *Neuron.* (1994) 12:433–42. doi: 10.1016/0896-6273(94)90283-6
46. Jonas P, Bischofberger J, Sandkuhler J. Corelease of two fast neurotransmitters at a central synapse. *Science.* (1998) 281:419–24. doi: 10.1126/science.281.5375.419
47. Walker MC, Ruiz A, Kullmann DM. Monosynaptic GABAergic signaling from dentate to CA3 with a pharmacological and physiological profile typical of mossy fiber synapses. *Neuron.* (2001) 29:703–15. doi: 10.1016/S0896-6273(01)00245-8
48. Furshpan EJ, MacLeish PR, O'Lague PH, Potter DD. Chemical transmission between rat sympathetic neurons and cardiac myocytes developing in microcultures: evidence for cholinergic, adrenergic, and dual-function neurons. *Proc Natl Acad Sci USA.* (1976) 73:4225–9. doi: 10.1073/pnas.73.11.4225
49. Furshpan EJ, Landis SC, Matsumoto SG, Potter DD. Synaptic functions in rat sympathetic neurons in microcultures. I Secretion of norepinephrine and acetylcholine. *J Neurosci.* (1986) 6:1061–79. doi: 10.1523/JNEUROSCI.06-04-01061.1986
50. Potter DD, Landis SC, Matsumoto SG, Furshpan EJ. Synaptic functions in rat sympathetic neurons in microcultures. II Adrenergic/cholinergic dual status and plasticity. *J Neurosci.* (1986) 6:1080–98. doi: 10.1523/JNEUROSCI.06-04-01080.1986
51. Reichardt LF, Patterson PH. Neurotransmitter synthesis and uptake by isolated sympathetic neurones in microcultures. *Nature.* (1977) 270:147–51. doi: 10.1038/270147a0
52. Schotzinger RJ, Landis SC. Cholinergic phenotype developed by noradrenergic sympathetic neurons after innervation of a novel cholinergic target in vivo. *Nature.* (1988) 335:637–9. doi: 10.1038/335637a0
53. Apostolova G, Dorn R, Ka S, Hallbook F, Lundeberg J, Liser K, et al. Neurotransmitter phenotype-specific expression changes in developing sympathetic neurons. *Mol Cell Neurosci.* (2007) 35:397–408. doi: 10.1016/j.mcn.2007.03.014
54. Brodski C, Schaubmar A, Dechant G. Opposing functions of GDNF and NGF in the development of cholinergic and noradrenergic sympathetic neurons. *Mol Cell Neurosci.* (2002) 19:528–38. doi: 10.1006/mcne.2001.1093
55. Brodski C, Schnurch H, Dechant G. Neurotrophin-3 promotes the cholinergic differentiation of sympathetic neurons. *Proc Natl Acad Sci USA.* (2000) 97:9683–8. doi: 10.1073/pnas.160080697
56. Habecker BA, Pennica D, Landis SC. Cardiotrophin-1 is not the sweat gland-derived differentiation factor. *Neuroreport.* (1995) 7:41–4. doi: 10.1097/00001756-199512000-00009
57. Hiltunen PH, Airaksinen MS. Sympathetic cholinergic target innervation requires GDNF family receptor GFR alpha 2. *Mol Cell Neurosci.* (2004) 26:450–7. doi: 10.1016/j.mcn.2004.04.003
58. Rao MS, Patterson PH, Landis SC. Multiple cholinergic differentiation factors are present in footpad extracts: comparison with known cholinergic factors. *Development.* (1992) 116:731–44. doi: 10.1242/dev.116.3.731
59. Rao MS, Sun Y, Escary JL, Perreau J, Tresser S, Patterson PH, et al. Leukemia inhibitory factor mediates an injury response but not a target-directed developmental transmitter switch in sympathetic neurons. *Neuron.* (1993) 11:1175–85. doi: 10.1016/0896-6273(93)90229-K
60. Stanke M, Duong CV, Pape M, Geissen M, Burbach G, Deller T, et al. Target-dependent specification of the neurotransmitter phenotype: cholinergic differentiation of sympathetic neurons is mediated in vivo by gp 130 signaling. *Development.* (2006) 133:141–50. doi: 10.1242/dev.02189
61. Yamamori T, Fukada K, Aebersold R, Korsching S, Fann MJ, Patterson PH. The cholinergic neuronal differentiation factor from heart cells is identical to leukemia inhibitory factor. *Science.* (1989) 246:1412–6. doi: 10.1126/science.2512641
62. Olivas A, Gardner RT, Wang L, Ripplinger CM, Woodward WR, Habecker BA. Myocardial infarction causes transient cholinergic transdifferentiation of cardiac sympathetic nerves via gp130. *J Neurosci.* (2016) 36:479–88. doi: 10.1523/JNEUROSCI.3556-15.2016
63. Vega A, Luther JA, Birren SJ, Morales MA. Segregation of the classical transmitters norepinephrine and acetylcholine and the neuropeptide Y in sympathetic neurons: modulation by ciliary neurotrophic factor or prolonged growth in culture. *Dev Neurobiol.* (2010) 70:913–28. doi: 10.1002/dneu.20834

64. Cifuentes F, Morales MA. Functional implications of neurotransmitter segregation. *Front Neural Circuits.* (2021) 15:738516. doi: 10.3389/fncir.2021.738516
65. Eccles JC. Chemical transmission and Dale's principle. *Prog Brain Res.* (1986) 68:3–13. doi: 10.1016/S0079-6123(08)60227-7
66. Condon AF, Robinson BG, Asad N, Dore TM, Tian L, Williams JT. The residence of synaptically released dopamine on D2 autoreceptors. *Cell Rep.* (2021) 36:109465. doi: 10.1016/j.celrep.2021.109465
67. Tedjo W, Nejad JE, Feeny R, Yang L, Henry CS, Tobet S, et al. Electrochemical biosensor system using a CMOS microelectrode array provides high spatially and temporally resolved images. *Biosens Bioelectron.* (2018) 114:78–88. doi: 10.1016/j.bios.2018.04.009
68. Tjahjono N, Jin Y, Hsu A, Roukes M, Tian L. Letting the little light of mind shine: Advances and future directions in neurochemical detection. *Neurosci Res Nov.* (2021) 2021:30. doi: 10.1016/j.neures.2021.11.012
69. Silm K, Yang J, Marcott PF, Asensio CS, Eriksen J, Guthrie DA. Synaptic vesicle recycling pathway determines neurotransmitter content and release properties. *Neuron.* (2019). 102:786–800 e785. doi: 10.1016/j.neuron.2019.03.031
70. Takacs VT, Cserep C, Schlingloff D, Posfai B, Szonyi A, Sos KE, et al. Co-transmission of acetylcholine and GABA regulates hippocampal states. *Nat Commun.* (2018) 9:2848. doi: 10.1038/s41467-018-05136-1
71. Fortin GM, Ducrot C, Giguere N, Kouwenhoven WM, Bourque MJ, Pacelli C, et al. Segregation of dopamine and glutamate release sites in dopamine neuron axons: regulation by striatal target cells. *FASEB J.* (2019) 33:400–17. doi: 10.1096/fj.201800713RR
72. Granger AJ, Wang W, Robertson K, El-Rifai M, Zanello AF, Bistrong K, et al. Cortical ChAT(+) neurons co-transmit acetylcholine and GABA in a target- and brain-region-specific manner. *Elife.* (2020) 9:57749. doi: 10.7554/eLife.57749.sa2
73. Liang K, Wei L, Chen L. Exocytosis, endocytosis, and their coupling in excitable cells. *Front Mol Neurosci.* (2017) 10:109. doi: 10.3389/fnmol.2017.00109
74. von Twickel A, Kowatschew D, Salturk M, Schauer M, Robertson B, Korsching S, et al. Individual dopaminergic neurons of lamprey SNc/VTA project to both the striatum and optic tectum but restrict co-release of glutamate to striatum only. *Curr Biol.* (2019) 29:677–685 e676. doi: 10.1016/j.cub.2019.01.004
75. Ninomiya I, Malpas SC, Matsukawa K, Shindo T, Akiyama T. The amplitude of synchronized cardiac sympathetic nerve activity reflects the number of activated pre- and postganglionic fibers in anesthetized cats. *J Auton Nerv Syst.* (1993) 45:139–47. doi: 10.1016/0165-1838(93)90125-E

Conflict of Interest: The authors declare that the research was conducted in the absence of any commercial or financial relationships that could be construed as a potential conflict of interest.

Publisher's Note: All claims expressed in this article are solely those of the authors and do not necessarily represent those of their affiliated organizations, or those of the publisher, the editors and the reviewers. Any product that may be evaluated in this article, or claim that may be made by its manufacturer, is not guaranteed or endorsed by the publisher.

frontiers in Cardiovascular Medicine

ORIGINAL RESEARCH
published: 11 March 2022
doi: 10.3389/fcvm.2022.853427

Acute and Short-Term Autonomic and Hemodynamic Responses to Transcranial Direct Current Stimulation in Patients With Resistant Hypertension

Bruno Rodrigues[1,2†], Catarina A. Barboza[1†], Eliezer G. Moura[1], Gabriela Ministro[1], Silvia E. Ferreira-Melo[2], Javier B. Castaño[1], Wilton M. S. Nunes[1], Cristiano Mostarda[3], Antonio Coca[4], Lauro C. Vianna[5] and Heitor Moreno-Junior[2]*

[1] Laboratory of Cardiovascular Investigation & Exercise, School of Physical Education, University of Campinas (UNICAMP), Campinas, Brazil, [2] Laboratory of Cardiovascular Pharmacology & Hypertension, School of Medical Sciences, University of Campinas (UNICAMP), Campinas, Brazil, [3] Physical Education Department, Federal University of Maranhão (UFMA), São Luís, Brazil, [4] Hypertension and Vascular Risk Unit, Hospital Clínic, University of Barcelona, Barcelona, Spain, [5] NeuroV̇ASQ̇ - Integrative Physiology Laboratory, Faculty of Physical Education, University of Brasília, Brasília, Brazil

OPEN ACCESS

Edited by:
Tania Zaglia,
University of Padova, Italy

Reviewed by:
Marco Mongillo,
University of Padua, Italy
RaffaEle Coppini,
University of Florence, Italy

***Correspondence:**
Bruno Rodrigues
prof.brodrigues@gmail.com

[†] These authors have contributed equally to this work

Specialty section:
This article was submitted to Hypertension, a section of the journal Frontiers in Cardiovascular Medicine

Received: 12 January 2022
Accepted: 18 February 2022
Published: 11 March 2022

Citation:
Rodrigues B, Barboza CA, Moura EG, Ministro G, Ferreira-Melo SE, Castaño JB, Nunes WMS, Mostarda C, Coca A, Vianna LC and Moreno-Junior H (2022) Acute and Short-Term Autonomic and Hemodynamic Responses to Transcranial Direct Current Stimulation in Patients With Resistant Hypertension. Front. Cardiovasc. Med. 9:853427. doi: 10.3389/fcvm.2022.853427

Previously, we demonstrated that acute transcranial direct current stimulation (tDCS) reduced blood pressure (BP) and improved autonomic modulation in hypertensives. We hypothesized that acute and short-term tDCS intervention can promote similar benefits in resistant hypertensive patients (RHT). We assessed the impact of one (acute intervention) and ten (short-term intervention) tDCS or SHAM (20 min, each) sessions on BP, pulse interval (PI) and systolic blood pressure variabilities, humoral mechanisms associated with BP regulation, and cytokines levels. True RHT subjects ($n = 13$) were randomly submitted to one and ten SHAM and tDCS crossing sessions (1 week of "washout"). Hemodynamic (Finometer®, Beatscope), office BP, and autonomic variables (accessed through spectral analysis of the pulse-to-pulse BP signal, in the time and frequency domain – Fast Fourrier Transform) were measured at baseline and after the short-term intervention. 24 h-ambulatory BP monitoring was measured after acute and short-term protocols. Acute intervention: tDCS reduced BP, cardiac output, and increase high-frequency band of PI (vagal modulation to the heart). Short-term protocol: tDCS did not change BP and cardiac output parameters. In contrast, central systolic BP (−12%), augmentation index (−31%), and pulse wave velocity (34%) were decreased by the short-term tDCS when compared to SHAM. These positive results were accompanied by a reduction in the low-frequency band (−37%) and an increase of the high-frequency band of PI (+62%) compared to SHAM. These findings collectively indicate that short-term tDCS concomitantly improves resting cardiac autonomic control and pulse wave behavior and reduces central BP in RHT patients, https://ensaiosclinicos.gov.br/rg/RBR-8n7c9p.

Keywords: transcranial direct current stimulation (tDCS), resistant hypertension, blood pressure, autonomic nervous system, biochemical analyses

INTRODUCTION

Resistant hypertension (RHT) is a clinical condition defined as above-goal elevated blood pressure in a patient, despite optimal use of ≥3 antihypertensive classes of drugs (which includes a diuretic agent), administered at maximally tolerated doses (1). Patients with RHT are at higher risk for target organ damage, morbidity, and mortality despite ongoing antihypertensive drug therapy (2). Elevated sympathetic activation and impaired renin-angiotensin-aldosterone components have been established in the early stages of hypertension, suggesting that neurohormonal dysregulation may play a pivotal role in its etiology (3), the progression of hypertension, and subsequent end-organ damage, such as raised arterial stiffness (4). However, despite standard drug therapy, sympathetic nerve activity remains high in RHT patients making the autonomic nervous system a primary target in the treatment of RHT (5, 6). As such, newer interventional strategies are needed to enhance the autonomic neural control of the cardiovascular system and potentially improve the clinical prognosis for RHT patients (7). Given the significant financial costs associated with developing novel pharmaceutical drugs, there is increasing interest in non-pharmacological alternatives.

Technological devices were developed to treat RHT by inhibiting sympathetic activity, including activation of the carotid baroreceptors using electrical stimuli (8) and selective renal sympathetic denervation (9), providing relevant results of blood pressure lowering (7–11). However, these device-based approaches require an invasive surgical procedure, and as such, this may limit its viability for RHT therapy. Given these considerations, noninvasive brain electrical stimulation has been tested, with beneficial cardiovascular outcomes for healthy subjects and hypertension patients (12–14). Briefly, transcranial direct current stimulation (tDCS) (13) is a non-pharmacological and noninvasive intervention for treating or preventing depressive episodes, epilepsy crisis, stroke motor sequela, migraine, fibromyalgia, chronic pain control (12), and other neuropsychiatric disorders (15, 16). Low-intensity tDCS in humans appears to be safe. Of note, no serious adverse events have been reported in more than 18,000 sessions administered to healthy subjects or neurological and psychiatric patients (16). Two other favorable characteristics are the relatively low cost and the straightforward operation of the equipment. Although the current literature indicates a potential role of tDCS on blood pressure control via an increase of vagal modulation (17–20), to our knowledge, no studies have specifically examined the effects of tDCS on autonomic and cardiovascular responses as the primary outcome in patients with RHT.

Since those studies using functional magnetic resonance imaging to assess the connection of the M1 area and autonomic nervous system were not found, it is already known that cortical motor areas, including M1, project directly to the reticular formation regions and the spinal cord (21–23), and motor network on the adrenal medulla is mediated by corticospinal and corticobulbo-spinal pathways. Classical physiologic studies demonstrated that stimulation of M1, primary somatic sensory cortex (S1), and dorsal premotor areas evoked changes in blood pressure (24, 25).

We have previously demonstrated that an acute session of tDCS in M1 area tDCS promoted positive adjustments on cardiac autonomic control and reduced 24-hs blood pressure values of non-RHT patients (14). Here, we hypothesized that an acute session of tDCS could also reduce sympathetic modulation, increase vagal modulation, and decrease blood pressure in RHT patients. Furthermore, we believed that ten consecutive sessions of tDCS could exert a positive summation effect on this regulatory mechanism and blood pressure values.

Given this background, the purpose of the present clinical trial was to rigorously assess the effects of one (i.e., acute) and ten (i.e., short-term) tDCS sessions on the blood pressure levels and neurohumoral mechanisms in RHT subjects. Considering that vagal activation seems to suppress pro-inflammatory cytokines production (26–28), we also measured inflammatory cytokines (interleukin-10 and TNF-α) and circulating hormones (cortisol and noradrenaline).

MATERIALS AND METHODS

Patients

Thirteen resistant hypertensive volunteers from the Outpatient Hypertension Clinic of the University of Campinas (UNICAMP, Campinas, Brazil) were screened for this study. This protocol was approved by the Ethical in Research Committee of the School of Medical Sciences, University of Campinas (Campinas, Brazil) and performed following the Declaration of Helsinki. All participants signed a written consent form before being included in the study (approval no.2.681.083/CAAE: 86618317.0.0000.5404). This study was registered at the Brazilian Registry of Clinical Trials (ReBEC) under Register Number: RBR-8n7c9p.stem.

Patients were included after at least a 6-month screening protocol for diagnosing RHT and check the adherence to pharmacological and non-pharmacological therapy. Two ambulatory blood pressure monitoring (ABPM) were performed to exclude white-coat hypertension, and pill counts assessed lack of adherence. Patients with an adherence rate below 80% of the prescribed medication were excluded from our sample. We tested patients for: renal artery stenosis, pheochromocytoma, primary hyperaldosteronism (aldosterone renin ratio – ARR > 20 ng/dL per ng/mL per hour), Cushing syndrome (by assessing cortisol and adrenocorticotropic hormone levels), and obstructive sleep apnea (classified as "high risk" according to Berlin questionnaire), to exclude secondary causes of hypertension. Thus, after patients were screened for possible causes of pseudo-RH, they were defined as those using ≥3 antihypertensive agents of different classes, including a diuretic (5).

Other exclusion criteria were: clinically evident coronary artery or cerebrovascular diseases, significant impaired renal or liver function, myocardial infarction or peripheral vascular disease, use of pacemakers or other implanted electronic devices, and depression (≥17 points on Hamilton's scale) (29).

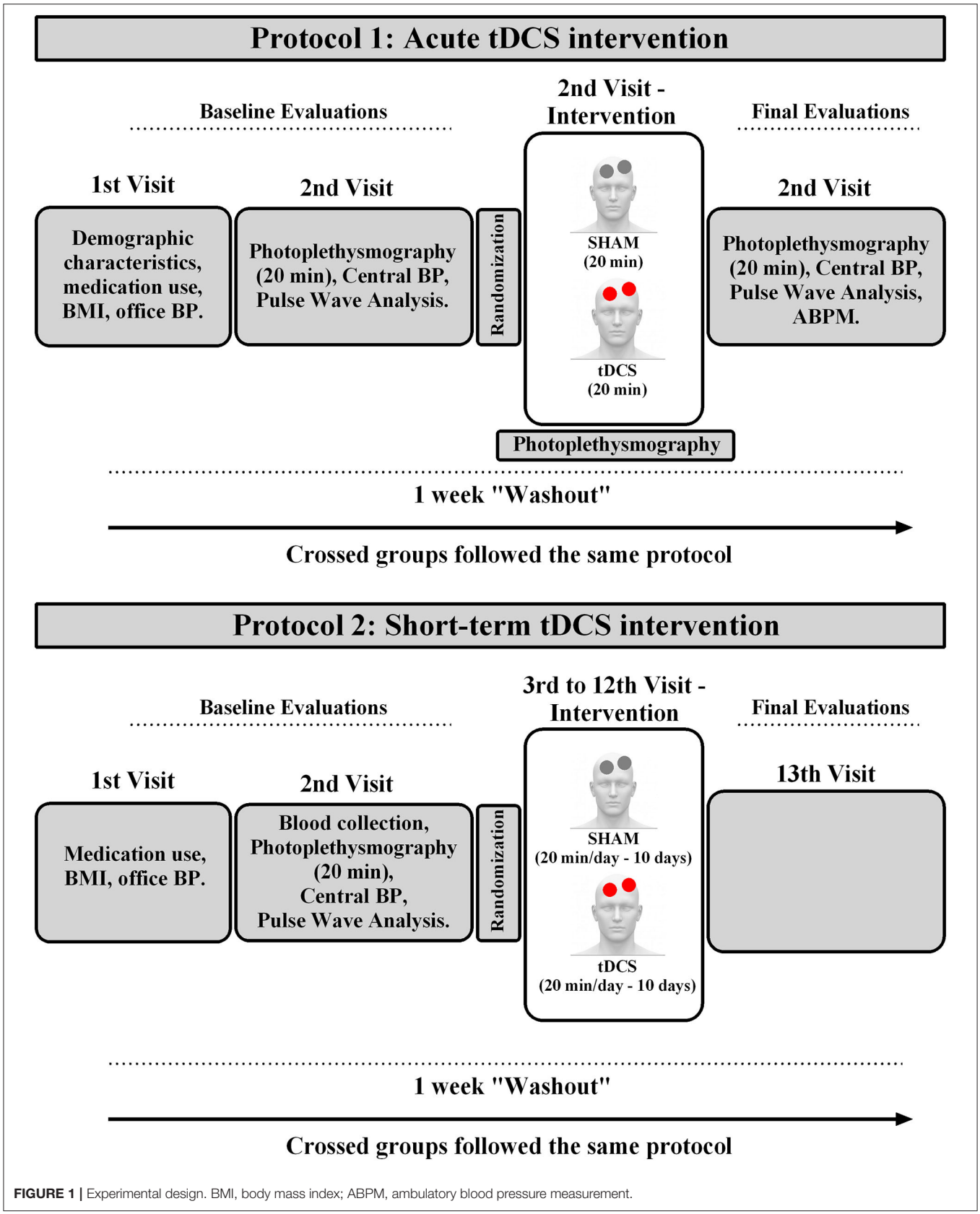

FIGURE 1 | Experimental design. BMI, body mass index; ABPM, ambulatory blood pressure measurement.

TABLE 1 | Characteristics of patients enrolled in acute and short-term protocols.

Resistant Hypertensive Subjects ($n = 13$)	
Clinical data	
Age (yrs)	68 ± 7
Women, *n* (%)	7 (63)
Diabetes mellitus, *n* (%)	4 (36)
BMI (Kg/m^2)	29.3 ± 9.4
Free fat mass (kg)	56 (45–73)
Fat mass (kg)	27 ± 9
Office SBP (mmHg)	148 ± 14
Office DBP (mmHg)	87 ± 13
Heart rate (bpm)	77 ± 12
Antihypertensive drugs	
N. of Classes	4 ± 1
Diuretics, *n* (%)	13 (100)
Espironolactone, *n* (%)	3 (27)
Beta-blockers, *n* (%)	6 (54)
ACEi and ARBs, *n* (%)	12 (92)
CCBs, *n* (%)	8 (72)

BMI, body mass index; SBP, systolic blood pressure; DBP, diastolic blood pressure; ACEi, angiotensin-converting enzyme inhibitors; ARBs, angiotensin receptor blockers; CCBs, calcium channel blockers.

Study Design

This study had a double-blind, randomized crossover with a placebo (SHAM) design. Participants were involved in the study for two protocols, as showed in **Figure 1**.

Protocol-1: Acute Intervention

The participants were interviewed for their demographic characteristics and medication use on the first visit, assessed for body weight, height, and office blood pressure. On the second visit, applanation tonometry was performed to assess noninvasive central hemodynamic variables (SphygmoCor CPV system, AtCor Medical, USA). After this procedure, subjects were assessed to 20 min of photoplethysmography with beat-to-beat signal (Finometer®, Finapres Medical System BV, Netherlands) to evaluate hemodynamic and autonomic variables. Then, subjects participated in the first randomized stage of the protocol. An investigator not involved in the assessment, intervention, or statistical analysis conducted the randomization (1:1) of subjects and programmed the device for the tDCS or SHAM sessions. After device programming by this investigator, another researcher started the session, blinded to the type of intervention that the device was programmed. tDCS (Model DC-Stimulator Plus; NeuroConn GmbH, Germany) was performed with anodal excitation, 0.06 mA/cm^2, in the primary motor cortex, M1 region, for 20 min. Placebo (SHAM) sessions were constituted by the electrode positions and stimulation parameters identical to that used for anodal stimulus. The excitation stopped after a ramp-up and ramp-down period of the 30s each to provide an equivalent scalp sensation. Hemodynamic and autonomic measurements were conducted during the 20 min of SHAM and tDCS stimulation. (photoplethysmography). After the acute intervention, for 20 min, beat-to-beat photoplethysmography continued being assessed. Then, central hemodynamic variables were evaluated, and 24 h-ambulatory blood pressure measurements (ABPM) were started. After 1 week of "washout," subjects were submitted to the same procedures, crossing the type of intervention (SHAM or tDCS).

Protocol-2: Short-Term Intervention

After 1 week of Protocol 1, the same subjects were enrolled in thirteenth visits over 3 weeks. The participants were interviewed for their medication use on the first visit, assessed for body weight, height, and office blood pressure. After 12 h of fasting, on the second visit, blood samples were collected (8:00–9:00 h a.m.) to analyze biochemical markers. After a standardized breakfast, subjects were assessed for 20 min of photoplethysmography with a beat-to-beat signal to evaluate hemodynamic and autonomic variables. Then, applanation tonometry was performed to assess noninvasive central hemodynamic variables and pulse wave analysis.

On the third visit, subjects participated in the first randomized stage of the protocol. An investigator not involved in the assessment, treatment, or statistical analysis conducted the randomization (1:1) of subjects and programmed the device for the tDCS or SHAM sessions. After device programming by this investigator, another researcher started the session, blinded to the type of intervention that the device was programmed. tDCS and SHAM sessions were similar to the acute protocol and occurred between 8:00–12:00 h a.m. after patients took their usual antihypertensive medication. Such protocols were applied for 10 days.

Thereby, patients received tDCS or Sham interventions on consecutive days from the third to the twelfth visit. On the thirteenth visit (24 h after the last tDCS session), patients were reassessed by biochemical markers, office blood pressure, hemodynamic and autonomic variables, as well as central blood pressure and pulse wave analyses. Immediately after the recording, 24 h-ABPM was carried out. After 1 week of "washout," participants initiated the same experimental sequence performed with the crossing of subjects, i.e., those selected for Sham stimulation in the previous stage, tDCS was performed, and vice-versa.

Procedures

Office BP Measurements

Office BP was measured using a certified digital sphygmomanometer (HEM-907 XL OMRON Healthcare Inc., Bannockburn, IL, USA) by a trained health professional, according to the European Society Hypertension (ESH) 2018 guidelines (30).

Biochemical Analyses

Blood samples were collected by venipuncture in heparinized vacutainers after 12 hs fasting and immediately centrifuged at 4,000 rpm for 5 min to separate plasma. The TNF-α, IL-10, noradrenaline, and cortisol concentrations were determined in peripheral blood by the enzyme-linked immunosorbent assay

TABLE 2 | Acute intervention: hemodynamic assessments of resistant hypertensive patients at baseline, during, and after tDCS or SHAM conditions.

		Baseline	During	After	*P* Intragroup	*P* vs. Sham - After
Hemodynamic variables						
SBP (mmHg)	SHAM	130 ± 17	128 ± 13	132 ± 18	0.5471	0.0152
	TDCS	138 ± 14	121 ± 12	116 ± 10†*	0.0023	
DBP (mmHg)	SHAM	84 ± 8	87 ± 9	87 ± 6	0.6012	0.0012
	TDCS	87 ± 13	77 ± 14*	67 ± 11†*	0.0010	
MBP (mmHg)	SHAM	99 ± 8	101 ± 8	101 ± 8	0.6471	<0.0001
	TDCS	104 ± 10	91 ± 10†	83 ± 8†#*	0.0002	
HR (bpm)	SHAM	65 ± 10	65 ± 11	65 ± 11	0.7023	0.7587
	TDCS	66 ± 12	66 ± 10	67 ± 11	0.6987	
CO (L/min)	SHAM	6 ± 2	6 ± 2	6 ± 1	0.8795	0.0002
	TDCS	7 ± 2	5 ± 1†*	5 ± 1†*	0.0001	
PVR (dyn.s/cm^5)	SHAM	4,536 ± 2,128	5,220 ± 2,204	5,187 ± 2,692	0.5907	0.0005
	TDCS	5,362 ± 1,854	3,320 ± 1,749	2,006 ± 1,226†*	0.0002	
Autonomic variables						
PI Variance (ms^2)	SHAM	576 ± 124	627 ± 49	623 ± 48	0.7457	0.0042
	TDCS	625 ± 64	961 ± 65	1600 ± 62†*	0.0025	
RMSSD (ms)	SHAM	32 ± 16	29 ± 13	31 ± 14	0.6981	0.0033
	TDCS	29 ± 7	37 ± 10†	48 ± 9†*	0.0022	
LF-PI (n.u.)	SHAM	71 ± 10	71 ± 10	73 ± 9	0.5782	0.0001
	TDCS	67 ± 13	62 ± 17	26 ± 10†*	0.0001	
HF-PI (n.u.)	SHAM	29 ± 10	28 ± 10	27 ± 9	0.6201	0.0045
	TDCS	32 ± 10	47 ± 16	73 ± 9*†	0.0052	
LF/HF	SHAM	2.87 ± 1.47	2.96 ± 1.46	3.19 ± 1.68	0.5211	0.0002
	TDCS	2.60 ± 1.71	1.45 ± 1.04†*	0.45 ± 0.21#†*	0.0004	
SBP Variance (mmHg^2)	SHAM	72.3 ± 12	72.6 ± 11	73.9 ± 9	0.6830	<0.0001
	TDCS	69.1 ± 9	55.2 ± 7*	46.1 ± 6†*	0.0001	
LF-SBP (mmHg^2)	SHAM	15 ± 4.8	13 ± 3.9	13. ± 4.4	0.4877	0.0004
	TDCS	14 ± 4.7	9 ± 4.4†*	6.5 ± 3.6†*	0.0002	

*Data are expressed as mean ± standard deviation. Repeated measures ANOVA with Bonferroni post-hoc. SBP, systolic blood pressure; DBP, diastolic blood pressure; MBP, mean arterial pressure; HR, heart rate; CO, cardiac output; SDNN, average of the standard deviations of the normal pulse intervals every 5 min; VAR-PI, pulse interval variance; RMSSD, the root of the mean of the square of the differences between adjacent normal pulse intervals; LF-PI, low-frequency band of the pulse interval; HF-PI, the high-frequency band of the pulse interval. *$P < 0.05$ vs. SHAM at after moment; †$P < 0.05$ vs. Baseline in the same condition; #$P < 0.05$ vs. During in the same condition.*

(ELISA) technique using high detection sensitivity kits (R&D System, a biotech brand, Quantikine ELISA, Inc., Minneapolis, USA) with ranges between 15.6–1,000 pg/mL for TNF-α, and 7.8–500 pg/ml for IL-10. Intra- and inter-assay variations (%) were 4.2–5.2 and 4.6–7.4 for TNF-α, and 1.7–5.0 and 5.9–7.5 for IL-10. Noradrenaline ranges between 0.313 and 20 ng/mL, and cortisol ranged from 8.5 to 23.8 μg/dL. Intra- and inter-assay variations (%) were 5.5–8.4 for noradrenaline and 7.2–10.9 for cortisol.

Hemodynamic and Autonomic Indexes

With patients in a sitting position, after 15 min of rest, continuous beat-to-beat blood pressure waves were obtained by a digital photoplethysmography device (Finometer®, Finapress Medical System BV, Netherlands) for 20 min. A software program (BeatScope) used BP curves and patient data (age, sex, body mass, and stature) to calculate systolic and diastolic BP (SBP and DBP), heart rate (HR), cardiac output (CO), and peripheral vascular resistance (PVR). The waveforms were simultaneously recorded on another computer equipped to acquire and convert the biological signals AT/MCA-CODAS (DATAC Instruments Inc., Akron, Ohio, USA). The sampling frequency of signals was 1,000 Hz.

The stored data from photoplethysmography underwent a routine analysis (spectral analysis) to provide pulse interval (PI) and systolic blood pressure (SBP) variability. Although the PI variability assessment may be considered may be less accurate than measuring heart rate variability by electrocardiogram, some studies have demonstrated the agreement between heart rate variability and PI variability (31, 32).

Beat-to-beat BP was analyzed using a specialized algorithm for spectral data analysis (CardioSeries Software, version 2.4, Ribeirão Preto, SP, Brazil), which automatically detects SBP and DBP waves. Pulse interval (PI) was calculated as the difference between the cycle's start and endpoints (t1-t0). The spectral power density of the SBP and the PI range were computed using the Fast Fourier Transform and the Welch method. To set the window length was established in 5 min.

TABLE 3 | Acute intervention: 24-hs-ambulatory blood pressure measurements (ABPM) in resistant hypertensive patients after SHAM or tDCS conditions.

	SHAM	TDCS	*P*
24 h			
SBP (mmHg)	137 ± 9	122 ± 10*	0.0039
DBP (mmHg)	90 ± 6	64 ± 8*	0.0041
MBP (mmHg)	96 ± 7	82 ± 9*	0.0002
PP (mmHg)	57 ± 7	54 ± 6*	0.0215
Daytime			
SBP (mmHg)	138 ± 7	127 ± 7	0.8182
DBP (mmHg)	91 ± 7	69 ± 6	0.1661
MBP (mmHg)	97 ± 8	89 ± 7	0.3955
PP (mmHg)	57 ± 7	53 ± 5*	0.0146
Nighttime			
SBP (mmHg)	135 ± 15	118 ± 13*	0.0046
DBP (mmHg)	77 ± 8	62 ± 8*	0.0017
MBP (mmHg)	92 ± 10	80 ± 9*	0.0023
PP (mmHg)	58 ± 10	54 ± 9*	0.0036

*Data are expressed as mean ± standard deviation. 2-tailed paired t-test. SBP, systolic blood pressure; DBP, diastolic blood pressure; MBP, mean blood pressure; PP, pulse pressure. *P < 0.05 vs. SHAM.*

In the time domain, we analyzed: SDNN [standard deviation of normal-to-normal (NN) PI] and PI Variance (total variance of PI); RMSSD (the square root of the mean of the sum of the squares of differences between adjacent NN intervals, which represents cardiac vagal modulation of PI) and SBP Variance (variance of systolic blood pressure in short-time). The spectral bands evaluated for humans were defined as very-low-frequency (VLF: 0.007–0.04 Hz), low-frequency (LF: 0.04–0.15 Hz), high-frequency (HF: 0.15–0.4 Hz), and total power. The normalized values (nu) for the LF and HF bands were then calculated using the predefined formulae: LF (n.u.) = LF/(total power spectral density – VLF) × 100 or HF (n.u.) = HF/(total power spectral density – VLF) × 100. The ratio for the absolute values for the LF band of PI and HF band of PI (LF/HF) was also calculated as a representative of autonomic balance.

The HF component of PI variability has been related to the efferent vagal modulation. However, the interpretation of the LF component of PI is more controversial since that includes the influences of sympathetic and parasympathetic modulation (33). Also, there is evidence that the LF component of SBP variability is influenced by sympathetic modulation of vascular tone and myogenic vascular function (34). Furthermore, the assessment of blood pressure variability in very short-term (beat-to-beat) reflects the influences of central and reflex autonomic modulation, elastic properties of arteries, humoral and emotional factors (35).

Central Blood Pressure and Pulse Wave Assessment

Applanation tonometry was performed to assess noninvasive central hemodynamic variables and pulse wave velocity (PWV) using the SphygmoCor system (AtCor Medical, Sydney, Australia). Consecutive measurements of the carotid and femoral artery pulse waves were electrocardiogram gated. The distance between the two sites was measured on the body surface to determine aortic PWV in meters/second (m/s). The total distance between the carotid and femoral arteries was used for measurement. The average measurements throughout 8 s (9–10 cardiac cycles) were calculated after excluding extreme values (values above or below four standard deviations).

After 20 sequential waveforms were acquired and averaged, a validated generalized mathematical transfer function was used to synthesize the corresponding central aortic pressure wave (36).

The Augmentation Index (AIx), defined by the ratio between the pressure exerted by the reflected wave and the ejection wave, was evaluated (37). This index is expressed as a percentage of the Central Pulse Pressure [AIx = BP/central pulse pressure (cPP) × 100%]. Since AIx is influenced by heart rate, an index normalized for 75 bpm was used too. The patients were required to abstain from smoking and consuming alcohol or coffee 24-h before the procedure.

Transcranial Direct Current Stimulation (tDCS)

The primary motor cortex region (M1) was chosen as the target for tDCS and was stimulated by a constant current stimulator (Model DC-Stimulator Plus; NeuroConn GmbH, Germany). With a 5.0 × 7.0 cm electrode (35 cm^2 area) housed in saline-soaked sponges, an anodal stimulation in the M1 region was positioned in the C3 area (using the International 10–20 EEG system) the cathode was placed in the supraorbital region. A current density of 0.06 mA/cm^2 and an intensity of 2.0 mA were applied on the scalp during 20 min per active session. For placebo SHAM, the electrode positions and stimulation parameters were the same as those used for anodal stimulation. The stimulation stopped after a ramp-up and ramp-down period of the 30 s each to provide an equivalent scalp sensation. Thus, for SHAM stimulation, the device switched off automatically after the 30 s of stimulation. The device display remained, indicating the stimulation time, regardless of whether the active or SHAM current was provided. Previous work demonstrated that this type of blinding is effective at low stimulation intensities (38). In the first session (SHAM and tDCS), we encouraged patients to describe stimulation sensation. Afterward, we asked if the perceived sensation was similar to the previous session (14).

Ambulatory Blood Pressure Measurement (ABPM)

ABPM was carried out with an automatic oscillometer device (Spacelabs 90207, Spacelabs Inc), and only records with more than 85% of total measures were analyzed. Those patients who had more than 25% of incomplete measurements should retake the exam. However, no patient had to be re-examined. The device was then set to obtain four blood pressure readings per hour (one every 15 min). The parameters measured were average 24-h, daytime and nighttime of systolic BP, diastolic BP, mean BP, and pulse pressure.

Statistical Analyses

Analyses were performed using the GraphPad Prism 6.0 software. The normality of data and homogeneity of variance were assessed using the Shapiro-Wilk and Levene tests, respectively. Mauchly's

TABLE 4 | Short-term intervention (10 sessions): hemodynamic variables at baseline and final of the tDCS or SHAM conditions.

		SHAM	TDCS	*P* Intragroup	*P* vs. Sham - Final
SBP (mmHg)	Baseline	133.4 ± 7.8	139.6 ± 15.5	0.3211	0.4357
	Final	134.8 ± 12.3	137.2 ± 8.2	0.2341	
DBP (mmHg)	Baseline	68.6 ± 13.3	73.1 ± 11.5	0.6540	0.4532
	Final	79.2 ± 13.6	78.2 ± 8.5	0.7421	
MBP (mmHg)	Baseline	92.4 ± 15.0	95.7 ± 16.1	0.4410	0.2653
	Final	102.8 ± 12.1	101.2 ± 9.2	0.5023	
PP (mmHg)	Baseline	58.4 ± 4.2	66.6 ± 9.9	0.1240	0.5648
	Final	55.6 ± 8.32	58.2 ± 13.2	0.2988	
HR (bpm)	Baseline	64.4 ± 6.9	58.1 ± 8.2	0.0878	0.3455
	Final	71.2 ± 13.1	69.1 ± 4.9	0.6674	
CO (L/min)	Baseline	6.3 ± 3.1	6.6 ± 2.8	0.7455	0.4892
	Final	6.4 ± 2.6	5.5 ± 3.7	0.5212	
PVR (dyn.s/cm^5)	Baseline	11,989.2 ± 5,763.6	11,698.2 ± 4,835.7	0.7742	0.5982
	Final	12,397.3 ± 6,874.2	10,458.4 ± 5,231.8	0.0755	

Data are expressed as mean ± standard deviation. Repeated measures ANOVA with Bonferroni post-test. SBP, systolic blood pressure; DBP, diastolic blood pressure; MBP, mean blood pressure; PP, pulse pressure; HR, heart rate; CO, cardiac output; PVR, peripheral vascular resistance.

test was used to evaluate the sphericity assumption and, whenever sphericity was violated, Greenhouse-Geiser epsilon correction was used. We estimated sample size was using G*Power software to ANOVA (version 3.1.9.2.), based on the magnitude of the mean differences in systolic blood pressure levels among tDCS or SHAM sessions (13). The sample size was estimated to be 10 participants per group, considering an ES set at 0.45 (13), a power of 80%, and a level of significance at 5%. G*Power calculations are based on a nondirectional χ2-test situation. ABPM was analyzed with a 2-tailed paired *t*-test. Hemodynamic, autonomic, and biochemical parameters were analyzed by repeated-measures two-way ANOVA, followed by Bonferroni post-test. The significance level was set at $p \leq 0.05$. Data are expressed as mean ± standard deviation. Pearson's correlation was used to analyze the associations between variables at final moment (short-term protocol) of SHAM and tDCS conditions. Considering that the LF band of PI represents, at least partly, the influence of sympathetic modulation, this parameter was chosen as an independent variable for associations with cortisol levels and central blood pressure. As vagal activation has been related to a reduction in the inflammatory profile (26–28), we chose the HF band of PI as the independent variable and tested its association with IL-10 levels. Finally, knowing that inflammatory profile can directly influence vascular morphology and modify pulse wave behavior, IL-10 levels were chosen as an independent variable in the association with AIx. The variance inflation factor (VIF) was used to check the co-linearity. The reported relationships remained while controlling for other predictor variables.

RESULTS

The sample consisted of 13 RHT subjects (68 ± 7 years old; 7 women). **Table 1** shows the characteristics of the subjects enrolled in the present study. All subjects tolerated tDCS well, and most patients reported scalp tingling sensations that decreased in intensity over time in all SHAM and tDCS sessions. None of them reported any side effects upon request.

Protocol 1. tDCS Acutely Reduces Blood Pressure, Possibly Meditated by Positive Changes in Autonomic Modulation

Since the hemodynamic effects of tDCS in resistant hypertensive patients are not known, we tested its acute effects on blood pressure and associated variables. To begin to uncover it, we assessed the pulse moment-by-moment (plethysmography) at Baseline, During, and After tDCS or SHAM session, as observed in **Table 2**. tDCS lead to a reduction in the systolic, diastolic and mean blood pressure, as well as in cardiac output, and peripheral vascular resistance after stimulation as compared with Baseline, and SHAM at after moment.

Next, we focused on autonomic modulation and investigated whether this regulatory mechanism can explain the observed effects of tDCS on blood pressure (**Table 2**). As expected, the SHAM protocol did not cause changes in cardiac and peripheral autonomic variables. It was possible to observe that tDCS increased the variance of pulse interval (PI Variance); the root of the mean of the square of the differences between adjacent normal RR intervals (RMSSD); the high-frequency band of pulse interval (HF-PI) if compared with the baseline evaluations and SHAM at after moment. Low-frequency band of pulse interval (LF-PI); LF/HF ratio; the variance of systolic blood pressure (SBP Variance), and low-frequency band of systolic blood pressure (LF-SBP) were reduced after tDCS stimulation compared with the baseline evaluation and SHAM at after moment.

To determine whether tDCS can extend its effects beyond 20 min post-stimulation, we evaluated 24-h blood pressure through ambulatory blood pressure monitoring (ABPM). At 24-h measurement, SBP, DBP, mean BP (MBP), and pulse pressure (PP) were reduced by tDCS. During the daytime, tDCS did not change these variables, except for PP values,

TABLE 5 | Short-term intervention (10 sessions): 24-hs-ambulatory blood pressure measurements (ABPM) in resistant hypertensive patients at baseline and after 10 sessions of SHAM or tDCS.

		SHAM	TDCS	*P* Intragroup	*P* vs. Sham - Final
24 h					
SBP (mmHg)	Baseline	145 ± 10	141 ± 10	0.3441	0.1095
	Final	147 ± 11	148 ± 10	0.4214	
DBP (mmHg)	Baseline	90 ± 10	87 ± 9	0.2987	0.3139
	Final	92 ± 9	89 ± 8	0.1240	
MBP (mmHg)	Baseline	97 ± 9	96 ± 10	0.5474	0.3439
	Final	94 ± 8	95 ± 9	0.6102	
PP (mmHg)	Baseline	57 ± 5	53 ± 6	0.0781	0.0712
	Final	55 ± 7	51 ± 5	0.0702	
Daytime					
SBP (mmHg)	Baseline	138 ± 10	139 ± 10	0.7441	0.4889
	Final	139 ± 10	138 ± 11	0.7101	
DBP (mmHg)	Baseline	91 ± 10	90 ± 12	0.8704	0.3141
	Final	92 ± 13	89 ± 8	0.3223	
MBP (mmHg)	Baseline	97 ± 10	98 ± 11	0.3321	0.1911
	Final	96 ± 12	96 ± 10	0.8955	
PP (mmHg)	Baseline	58 ± 5.06	56 ± 7	0.2214	0.0389
	Final	55 ± 9	49 ± 6$^{\dagger *}$	0.0425	
Nighttime					
SBP (mmHg)	Baseline	132 ± 12	129.50 ± 10.41	0.3322	0.3544
	Final	130 ± 15	127 ± 10	0.2141	
DBP (mmHg)	Baseline	75 ± 10	74 ± 10	0.5574	0.6570
	Final	77 ± 11	74 ± 13	0.1232	
MBP (mmHg)	Baseline	92 ± 9	91 ± 14	0.5512	0.4985
	Final	93 ± 12	93 ± 11	0.7422	
PP (mmHg)	Baseline	55 ± 7	52 ± 5	0.1244	0.2559
	Final	54 ± 6	53 ± 4	0.1011	

Data are expressed as mean ± standard deviation. Repeated measures ANOVA with Bonferroni post-test. SBP, systolic blood pressure; DBP, diastolic blood pressure; MBP, mean blood pressure; PP, pulse pressure. $^{\dagger}P < 0.05$ *vs. Baseline in the same condition;* $^{*}P < 0.05$ *vs. SHAM at Final moment.*

which were reduced after tDCS. In the nighttime, tDCS reduced SBP, DBP, MBP, and PP (**Table 3**). These results indicate that acute tDCS presents positive effects on office blood pressure, possibly mediated by improved autonomic modulation, reducing cardiac and peripheral sympathetic modulation, and increasing parasympathetic regulation to the heart. The hemodynamic effects of tDCS were extended during 24-h, as evaluated by ABPM.

Protocol 2. Short-Term (10 Sessions) tDCS Intervention Does Not Change Peripheral Blood Pressure, Despite Improving Central Blood Pressure and Autonomic Modulation

Knowing that acutely tDCS promotes blood pressure reduction and improved autonomic modulation, we tested whether short-term stimulation can promote similar benefits in these patients. To test this hypothesis, we submitted the resistant hypertensive patients to ten sessions of tDCS and SHAM stimulation (randomized, double-blinded crossover design, with the crossing occurring after 1 week of each intervention).

Despite the results observed in the acute protocol, ten sessions of tDCS did not change systolic, diastolic, mean blood pressures, pulse pressure, heart rate, cardiac output, and peripheral vascular resistance as compared with SHAM at the end of intervention (**Table 4**).

Regarding 24 h-ambulatory blood pressure measurements, after short-term tDCS intervention, we did not observe changes in 24 h, daytime, and nighttime of systolic, diastolic, and mean blood pressure. Pulse pressure values were reduced at daytime after tDCS when compared with baseline and SHAM at final moment (**Table 5**).

To determine whether 10 sessions of tDCS affects central blood pressure and pulse wave behavior, we used the applanation tonometry method. tDCS reduced central systolic blood pressure [$P = 0.0225$] (**Figure 2A**), did not change central diastolic blood pressure (**Figure 2B**), and reduced mean blood pressure [$P = 0.0320$] (**Figure 2C**) at the final moment in relation to SHAM. Pulse wave amplification indexes (AIx%, **Figure 2D**) [$P = 0.0421$]), AIx@HR75% [$P < 0.0001$] (**Figure 2E**), and the pulse wave velocity (PWV, **Figure 2F**) [$P = 0.0093$] showed a reduction in their values at the final moment

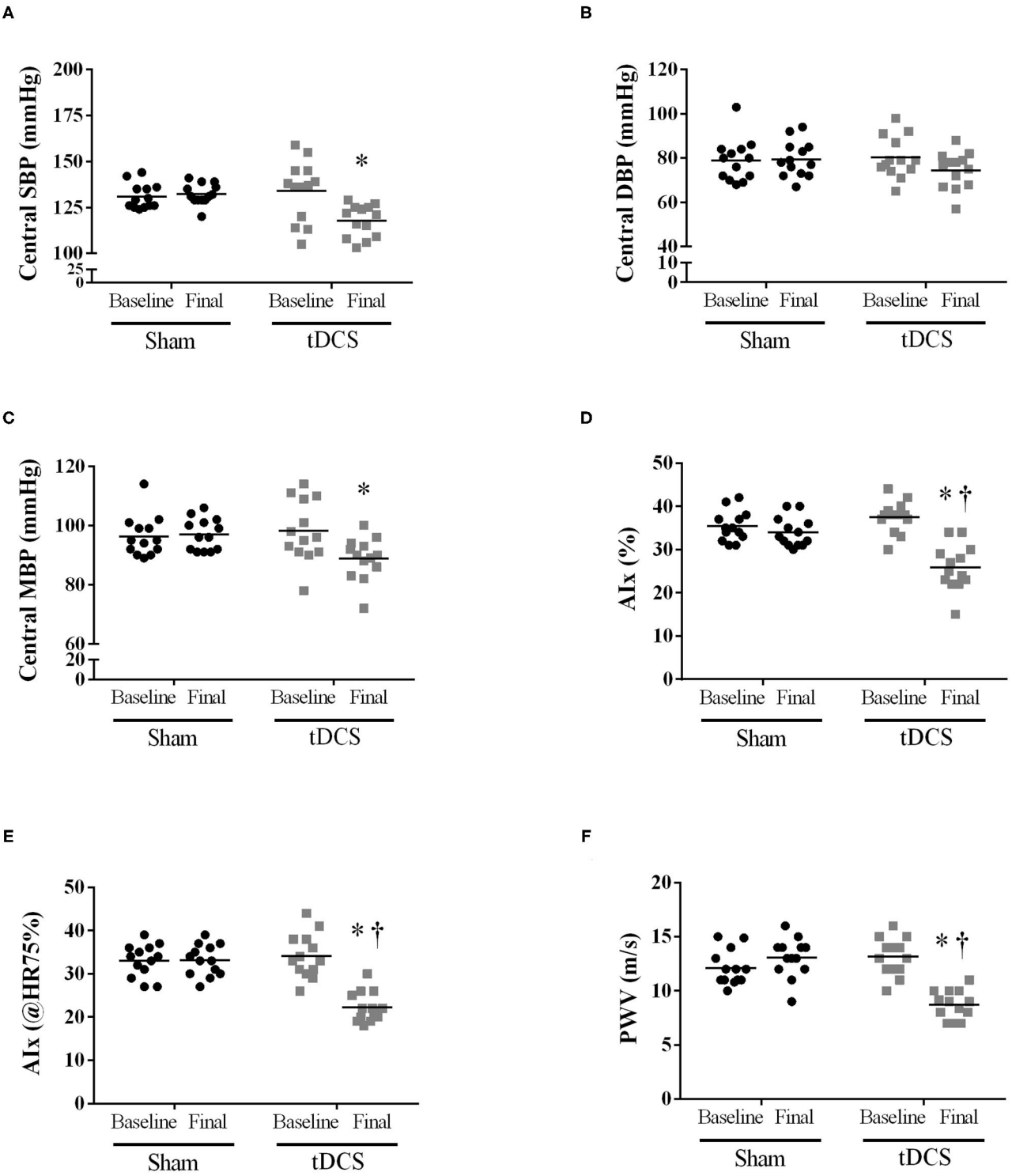

FIGURE 2 | Short-term intervention (10 sessions): Applanation tonometry method to determine whether short-term tDCS (10 sessions) could affect the central blood pressure and pulse waves behavior. **(A)** Central SBP [$P = 0.0225$ vs. SHAM; Interaction – $P = 0.0016$]; **(B)** Central diastolic blood pressure [$p = 0.2655$ vs. SHAM; Interaction – $P = 0.0106$]; **(C)** Central mean blood pressure [$P = 0.0320$ vs. SHAM; Interaction – $P = 0.0002$]; **(D)** Augmentation Index (AIx) expressed in % [$P = 0.0421$ vs. SHAM; Interaction – $P = 0.0002$]; **(E)** AIx normalized for a heart rate of 75 bpm [$P = 0.0010$ vs. SHAM; Interaction – $P < 0.0001$]; **(F)** PWV – pulse wave velocity [$P = 0.0093$ vs. SHAM; Interaction – $P < 0.0001$]. Repeated-measures two-way ANOVA, followed by Bonferroni post-test. *Difference vs. SHAM at final moment; $^{\dagger}P < 0.05$ vs. tDCS baseline in the same condition.

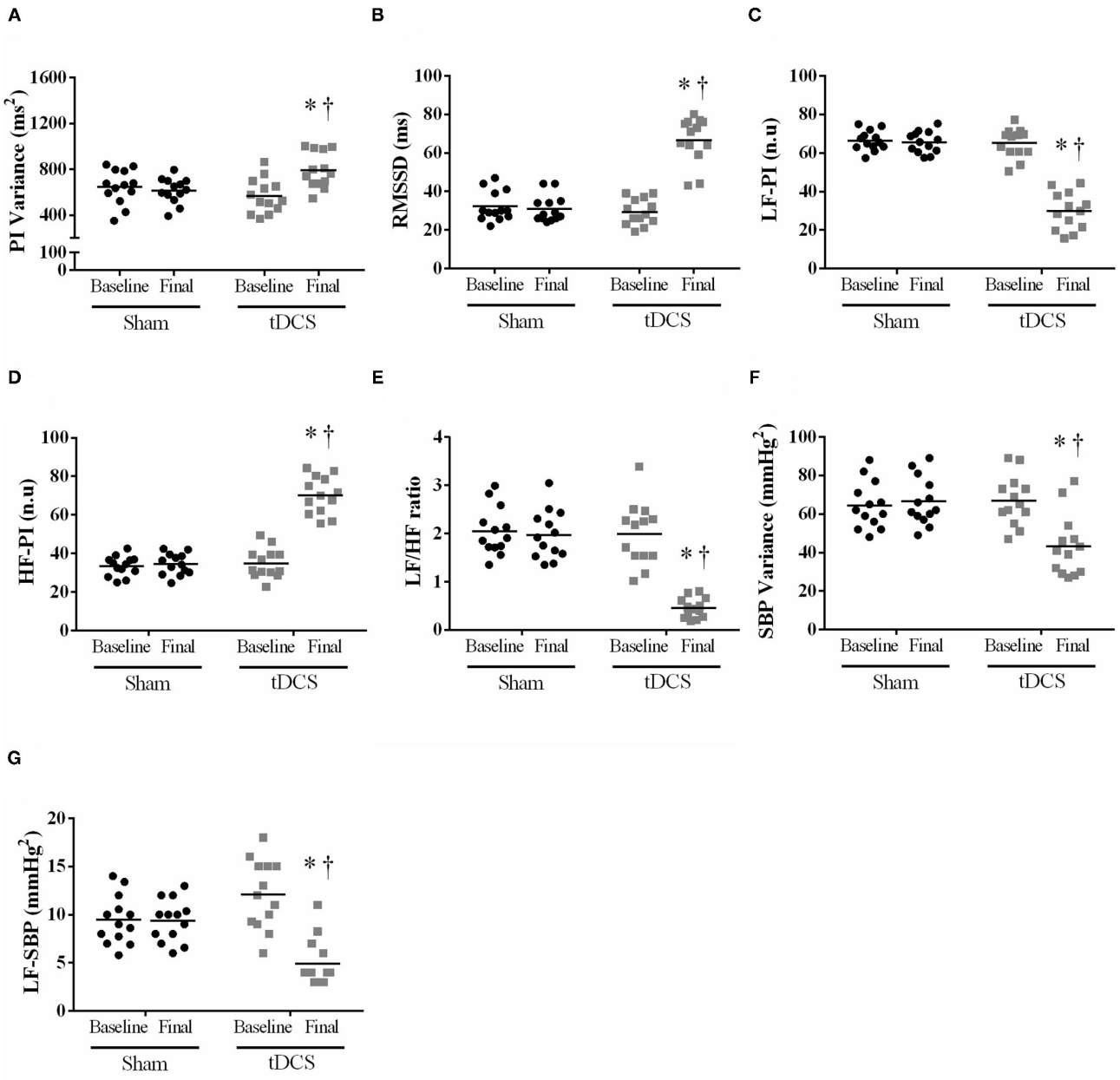

FIGURE 3 | Short-term intervention (10 sessions): tDCS or SHAM effects on pulse interval and systolic blood pressure variability. Repeated measures ANOVA with Bonferroni post-test. **(A)** PI Variance - pulse interval variance [$P = 0.0006$ vs. SHAM; Interaction – $P = 0.0002$]; **(B)** RMSSD - square root of the mean of the square of the differences between adjacent standard RR intervals [$P = 0.0421$ vs. SHAM; Interaction – $P = 0.0033$]; **(C)** LF-PI - low-frequency band of the pulse interval expressed in n.u. [$P = 0.0002$ vs. SHAM; Interaction – $P = 0.0003$]; **(D)** HF-PI - a high-frequency band of the pulse interval expressed in n.u. [$P < 0.0001$ vs. SHAM; Interaction – $P < 0.0001$]; **(E)** LF/HF ratio - autonomic balance [$P < 0.0001$ vs. SHAM; Interaction – $P < 0.0001$]; **(F)** SBP Variance - variance of systolic blood pressure [$P = 0.0018$ vs. SHAM; Interaction – $P < 0.0001$]; **(G)** LF-SBP - low-frequency band of systolic blood pressure [$P = 0.0012$ vs. SHAM; Interaction – $P < 0.0001$]. *Difference vs. SHAM at the final moment; $^{\dagger}P < 0.05$ vs. tDCS baseline.

in tDCS condition vs. SHAM. Also, tDCS improved these parameters as related to baseline evaluations, as seen to AIx% [$P = 0.0421$], AIx@HR75% [$P = 0.0010$], and PWV [$P = 0.0093$].

Given the blood pressure is regulated by the autonomic nervous system, we also investigated whether ten sessions of tDCS can improve cardiac and peripheral autonomic modulation. As can be seen in **Figure 3**, tDCS increased PI Variance [**Figure 3A**; $P = 0.0006$], RMSSD [**Figure 3B**; $P = 0.0421$], reduced LF-PI (n.u.) [**Figure 3C**; $P = 0.0002$], increased HF-PI (n.u.) [**Figure 3D**; $P < 0.0001$], as well as decreased LF-HF-ratio [**Figure 3E**; $P < 0.0001$], SBP Variance [**Figure 3F**; $P =$

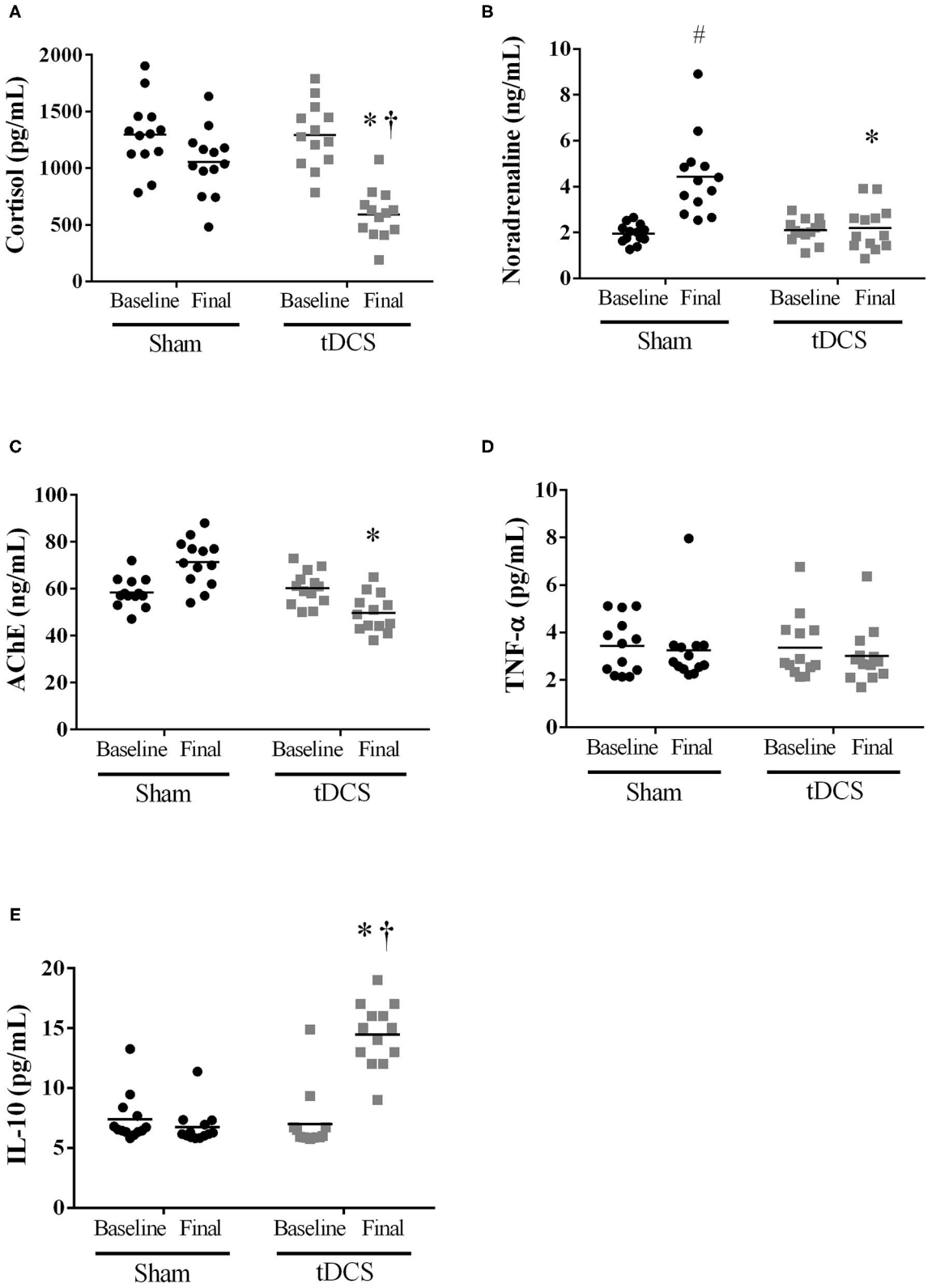

FIGURE 4 | Short-term intervention (10 sessions): Humoral mechanisms associated with BP regulation {**(A)** cortisol [$P = 0.0056$ vs. SHAM; Interaction – $P = 0.0072$]; **(B)** noradrenaline [$P = 0.0004$ vs. SHAM; Interaction – $P < 0.0001$]; **(C)** acetylcholinesterase [$P < 0.0001$ vs. SHAM; Interaction – $P < 0.0001$]} and inflammatory cytokines {**(D)** TNF-α [P=0.5774 vs. SHAM; Interaction – P=0.8195], and **(E)** IL-10 [$P = 0.0053$ vs. SHAM; Interaction – $P = 0.0062$]}. #Difference vs. SHAM baseline; †$P < 0.05$ vs. tDCS baseline; *Difference vs. SHAM at final moment.

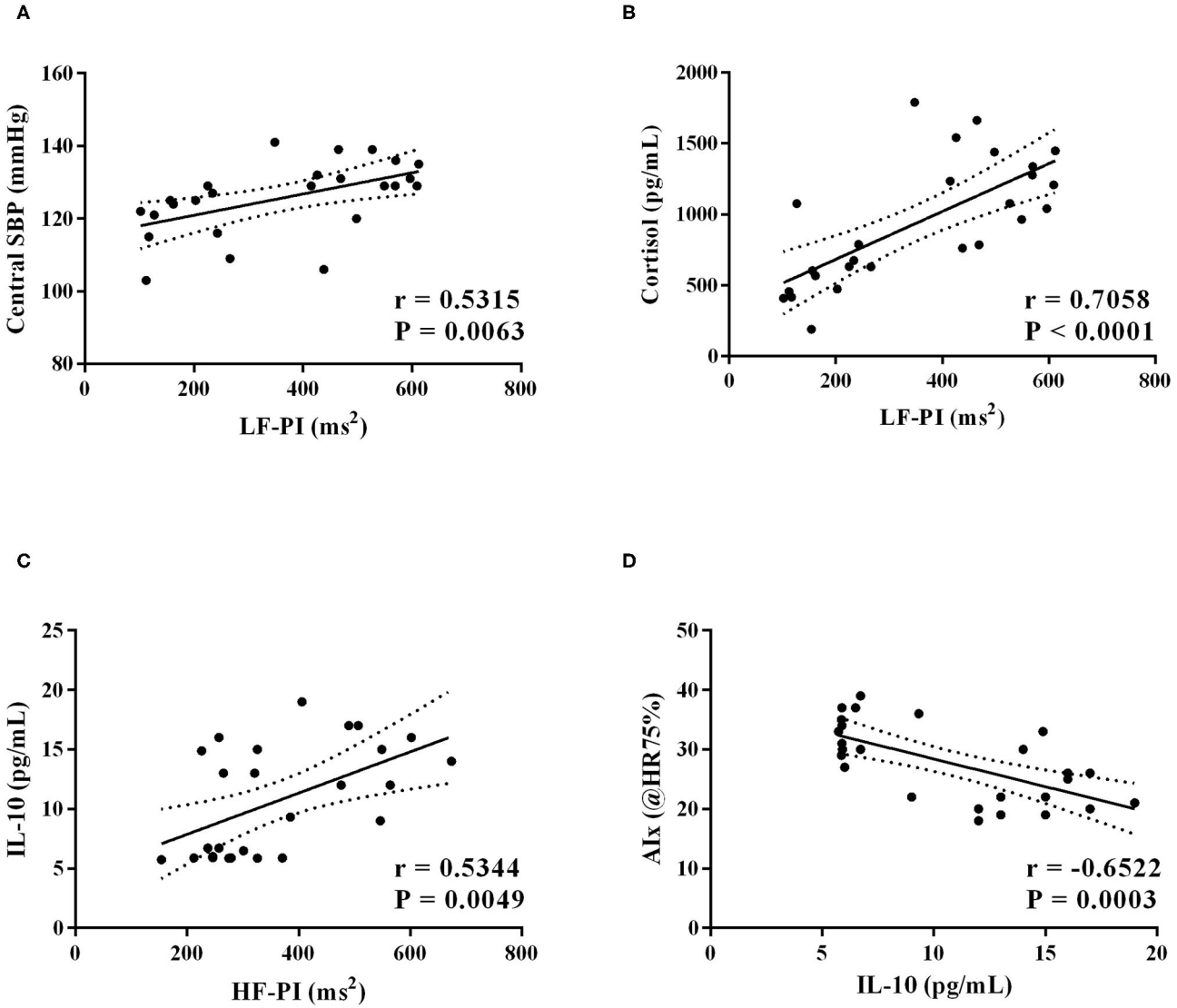

FIGURE 5 | Short-term intervention (10 sessions): Linear regression analysis was carried out and, if the slope of the regression line is significantly larger than 0 with $P < 0.05$, the linear regression (solid line) and its 95% confidence interval (dotted lines) are plotted as well. **(A)** LF-PI and Central SBP [r = 0.5315; P =0.0063]; **(B)** LF-PI and Cortisol levels [r = 0.7058; $P < 0.0001$]; **(C)** HF-PI and IL-10 levels [r = 0.5344; $P = 0.0049$]; **(D)** IL-10 and AIx (@HR75%) [r = −0.6522; $P = 0.0003$].

0.0018], and LF-SBP [**Figure 3G**; $P = 0.0012$] vs. SHAM at the end of experiments.

Next, we focused on biochemical markers associated with blood pressure regulation, as well as inflammatory cytokines. tDCS condition reduced cortisol levels [vs. SHAM: $P = 0.0056$; vs. Baseline: P=0.0033] (**Figure 4A**); prevented an increase in noradrenaline [vs. SHAM: $P = 0.0004$], as observed in SHAM condition [vs. Baseline SHAM: $P = 0.0089$] (**Figure 4B**); and acetylcholinesterase measurement was reduced vs. SHAM at final moment [$P < 0.0001$] (**Figure 4C**). TNF-α values (**Figure 4D**) [$P = 0.5774$] were no changed by tDCS; however, IL-10 levels (**Figure 4E**) were increased when compared to SHAM [$P < 0.0001$] at the final, and as compared with baseline evaluation [$P = 0.0053$].

Additionally, we observed positive correlations between: i) LF-PI (ms^2) band and central SBP [r = 0.5315; $P = 0.0063$] (**Figure 5A**), ii) LF-PI (ms^2) band and cortisol levels [r = 0.7058; $P < 0.0001$] (**Figure 5B**), and iii) HF-PI (ms^2) band and IL-10 [r = 0.5344; $P = 0.0049$] (**Figure 5C**). Finally, we found a negative correlation between IL-10 levels and AIx (@HR75%, **Figure 5D**) [r = −0.6522; $P = 0.0003$].

DISCUSSION

In the past two decades, experimental and clinical studies of the physiological mechanisms accounting for blood pressure lowering with baroreflex activation (8) and renal denervation in RHT patients (9–11) have grown. We postulated that other forms

of non-pharmacologic autonomic modulation, such as tDCS, should be tested for RHT. Herein, we used acute (i.e., one session) and short-term (i.e., ten uninterrupted sessions) tDCS on the primary motor cortex region (M1) to demonstrate these effects since we previously demonstrated that an acute session of tDCS reduced blood pressure and improved cardiovascular autonomic balance in non-resistant hypertensive patients (14).

The present study provides evidence that brain stimulation using tDCS acutely (one session) reduced blood pressure, cardiac output, peripheral vascular resistance, and LF/HF ratio. In addition, short-term tDCS (10 sessions) was not able to reduce blood pressure values. Nevertheless, this short-term intervention reduces LF/HF ratio, central blood pressure, and arterial stiffness in patients with RHT. Another salient finding is that short-term tDCS reduced cortisol and noradrenaline (baseline vs. final) levels, and increases IL-10 plasma concentration. Lastly, we found significant associations between reducing the LF band of pulse interval and improving central systolic blood pressure and cortisol and between increased vagal modulation and higher IL-10 levels.

RHT is considered a disease of complex management, leading researchers to consider alternative treatment approaches (1, 5), and renal denervation has been extensively studied in rigorous design and follow-up (39–43). These studies included patients with early combined systolic/diastolic hypertension and a high probability of response, excluding volunteers with end-stage renal disease, severe hypertension, or isolated systolic hypertension. On the other hand, baroreceptor activation was only tested in experimental procedures or small clinical trials (8). In addition to these invasive interventions aimed at inhibiting the sympathetic activity and improving baroreflex control, our group previously demonstrated that one session of tDCS reduces 24-h ABPM and office BP in patients with controlled hypertension (14), possibly triggered by the reduction of sympathetic modulation. The precise mechanisms underlying the main findings of the present study are not fully understood, but some relevant points should be considered. The central circuitry associated with tDCS cardiovascular and autonomic effects might involve activating the insular cortex and its projections to autonomic brainstem nuclei (44). Notably, a few studies indicated that electrical stimulation applied over the insular cortex could affect autonomic cardiovascular control (45, 46). More specifically, Montenegro et al. (47) showed that tDCS at the left temporal lobe appears to target autonomic control areas, leading to improvements in heart rate variability indexes in healthy subjects. Although the underlying mechanisms are unclear, it is evident that the present results are of significant clinical importance.

In the present study, we demonstrated that tDCS intervention acutely reduces 24 h-ABPM and hemodynamic parameters in RHT. The improvement in cardiovascular autonomic balance triggered by tDCS may have reduced cardiac contractility, reducing stroke volume and cardiac output. However, studies investigating the effects of tDCS on cardiac function are needed.

Short-term (10 sessions) stimulation was not able to reduce blood pressure values in these patients. Several hypotheses can be speculated with regards to the lack of effect in blood pressure after 10 sessions of tDCS, including: tolerability (the development of adaptations at the molecular level similar to the use of drugs and other substances) (48); the sequence of tDCS sessions (there was no consensus about the quantity or interval time between sessions); as well as the use of certain substances such as caffeine, which could have affected the perpetuation of responses (49). On the other hand, central systolic blood pressure, pulse wave velocity, and augmentation index were reduced by short-term tDCS intervention. Increased large-artery stiffness is considered an independent predictor of cardiovascular events and mortality (50). The reduction of pulse wave velocity and improvement of the augmentation index observed in the present study may potentially reflect the prevention of cardiovascular events in RHT. Many studies support the idea that the sympathetic nervous system can modulate arterial stiffness in both healthy and hypertensive subjects, independent of prevailing hemodynamics and vasomotor tone (51, 52).

To further investigate whether tDCS reverses the autonomic imbalance in RHT patients, pulse interval variability and systolic blood pressure variability were assessed. In addition to being associated with vascular remodeling, sympathetic overdrive contributes to arterial hypertension and cardiovascular risk (50). We demonstrated that acute and ten sessions of tDCS increase vagal modulation (represented by RMSSD and HF band indexes) and reduced LF band of pulse interval and systolic blood pressure. These positive changes resulted in reduced autonomic balance (reducing LF/HF ratio) and systolic blood pressure variability. In addition, plasmatic noradrenaline levels were reduced at final evaluation (after ten sessions of tDCS) as compared with baseline. Added to the central circuitry possibly involved in the autonomic control of blood pressure, it is possible that the electrical stimulation in the M1 area directly reduced the release of noradrenaline by the adrenal medulla. This may be a plausible explanation, given that experiments with non-human primates, using trans-neuronal transport of rabies virus, showed that the control of the adrenal medulla is embedded in cortical areas involved in controlling movement (including M1 area), cognition, and affect. Thereby, corticospinal and corticobulbar-spinal pathways may mediate the influence of the motor network on the adrenal medulla (53, 54). On the other hand, SHAM patients displayed increased plasma levels of noradrenaline. We believe that tDCS prevented such an increase.

Studies have strengthened the hypothesis of a direct relationship between the autonomic nervous system and immune responses in recent years. Evidence indicates that cholinergic systems influence inflammatory responses, controlling the release of TNF-α, IL1β, IL-6, and IL-10. Thus, vagal activation appears to suppress inflammation by acetylcholine binding α7-nicotine receptor (26–28). In hypertensive individuals, the long-term elevation of inflammatory protein levels is associated with an accelerated increase of pulse wave velocity, and this accelerated increase is associated with accelerated longitudinal elevation of blood pressure (55). Here, we demonstrate that short-term tDCS intervention increases vagal modulation (HF band), which is associated with increased levels of IL-10. Altogether, we propose

that alterations in the autonomic nervous system by tDCS improve pulse wave behavior and contribute to the increase of the anti-inflammatory cytokine IL-10, which, in turn, reduces the production of pro-inflammatory factors, mitigating cardiac and vascular remodeling occurring during RHT. Finally, tDCS reduces cortisol levels in RHT patients. This finding is significant since glucocorticoids may increase the action of angiotensin II, leading to high sympathetic nerve activity, the release of vasopressin, and attenuating the baroreceptor reflex (56).

We recognize some limitations in this study. A small sample size (n = 13) was evaluated in the present study. Although we assessed pharmacological treatment during experiments via pill count, no toxicological evaluation of the adherence was performed. Regarding cardiovascular autonomic studies, the spectral analysis was performed through the pulse interval signals collected by photoplethysmography, being less accurate than the evaluation by the electrocardiogram. Additionally, microneurography's non-use as an additional tool to assess sympathetic nerve activity, and neurotransmitters evaluation involved in the regulation of vascular tone are significant limitations of our study, restricting the conclusions.

CONCLUSION

We conclude that acute tDCS can reduce blood pressure in RHT, possibly mediated by autonomic modulation positive changes. After short-term tDCS, resting blood pressure values were not affected. However, autonomic modulation was substantially improved by ten sessions of tDCS. Such changes may have contributed to beneficial alterations in pulse wave behavior and IL-10 concentration. As far as we searched, no previous investigations measured the effects of acute and short-term tDCS sessions on blood pressure and autonomic modulation in RHT subjects as the primary outcome. More extensive clinical trials, biotechnology advances, miniaturizing devices, software developments, and wireless systems may make the technique valuable and easy to use for cardiovascular disorders with autonomic unbalance such as RHT.

DATA AVAILABILITY STATEMENT

The raw data supporting the conclusions of this article will be made available by the authors, without undue reservation.

ETHICS STATEMENT

The studies involving human participants were reviewed and approved by Ethical in Research Committee of the School of Medical Sciences, University of Campinas (Campinas, Brazil). The patients/participants provided their written informed consent to participate in this study.

AUTHOR CONTRIBUTIONS

BR and HM-J contributed to the conception and design of the work. EM, CB, GM, SF-M, JC, CM, and WN contributed to the acquisition, analysis, and interpretation of data for the work. BR, HM-J, AC, and LV drafted the manuscript. LV and AC critically revised the manuscript. All authors gave final approval and agreed to be accountable for all aspects of work and ensuring integrity and accuracy.

FUNDING

This study was supported by São Paulo Research Foundation (FAPESP) [grant numbers #2017/21320/4, #2017/24726-1, and #2016/18104-5]. This study was financed in part by the Coordenação de Aperfeiçoamento de Pessoal de Nível Superior – Brasil (CAPES) – Finance Code 001 and National Council for Scientific and Technological Development (CNPq) [grant number #422979/2018-0]. BR and HM-J are fellowships from CNPq (BPQ) [CNPq, grant number #307646/2019-0].

ACKNOWLEDGMENTS

The authors thank Dr. Maria Teresa La Rovere for the extensive review of the manuscript.

REFERENCES

1. Calhoun DA, Jones D, Textor S, Goff DC, Murphy TP, Toto RD, et al. American Heart Association Professional Education Committee. Resistant hypertension: diagnosis, evaluation, and treatment: a scientific statement from the American Heart Association Professional Education Committee of the Council for High Blood Pressure Research. *Circulation.* (2008) 117:e510–26. doi: 10.1161/CIRCULATIONAHA.108.189141
2. Cardoso CRL, Salles GF. Associations Between Achieved Ambulatory Blood Pressures and Its Changes With Adverse Outcomes in Resistant Hypertension: Was There a J-Curve for Ambulatory Blood Pressures? *Hypertension.* (2021) 77:1895–905. doi: 10.1161/HYPERTENSIONAHA.121.17200
3. Casey DP, Curry TB, Joyner MJ, Charkoudian N, Hart EC. Relationship between muscle sympathetic nerve activity and aortic wave reflection characteristics in young men and women. *Hypertension.* (2011) 57:421–7. doi: 10.1161/HYPERTENSIONAHA.110.164517
4. Holwerda SW, Luehrs RE, DuBose L, Collins MT, Wooldridge NA, Stroud AK, et al. Elevated Muscle Sympathetic Nerve Activity Contributes to Central Artery Stiffness in Young and Middle-Age/Older Adults. *Hypertension.* (2019) 73:1025–35. doi: 10.1161/HYPERTENSIONAHA.118.12462
5. Carey RM, Calhoun DA, Bakris GL, Brook RD, Daugherty SL, Dennison-Himmelfarb CR, et al. American Heart Association Professional/Public Education and Publications Committee of the Council on Hypertension; Council on Cardiovascular and Stroke Nursing; Council on Clinical Cardiology; Council on Genomic and Precision Medicine; Council on Peripheral Vascular Disease; Council on Quality of Care and Outcomes Research; and Stroke Council. Resistant Hypertension: Detection, Evaluation, and Management: A Scientific Statement From the American Heart Association. *Hypertension.* (2018) 72:e53–90. doi: 10.1161/HYP.0000000000000084
6. Zubcevic J, Waki H, Raizada MK, Paton JF. Autonomic-immune-vascular interaction: an emerging concept for neurogenic hypertension. *Hypertension.* (2011) 57:1026–33. doi: 10.1161/HYPERTENSIONAHA.111.169748
7. Lohmeier TE, Hall JE. Device-Based Neuromodulation for Resistant Hypertension Therapy. *Circ Res.* (2019) 124:1071–93. doi: 10.1161/CIRCRESAHA.118.313221

8. Victor RG. Carotid baroreflex activation therapy for resistant hypertension. *Nat Rev Cardiol.* (2015) 12:451–63. doi: 10.1038/nrcardio.2015.96
9. Esler MD, Böhm M, Sievert H, Rump CL, Schmieder RE, Krum H, et al. Catheter-based renal denervation for treatment of patients with treatment-resistant hypertension: 36 month results from the SYMPLICITY HTN-2 randomized clinical trial. *Eur Heart J.* (2014) 35:1752–9. doi: 10.1093/eurheartj/ehu209
10. Mahfoud F, Azizi M, Ewen S, Pathak A, Ukena C, Blankestijn PJ, et al. Proceedings from the 3rd European Clinical Consensus Conference for clinical trials in device-based hypertension therapies. *Eur Heart J.* (2020) 41:1588–99. doi: 10.1093/eurheartj/ehaa121
11. Schlaich MP, Esler MD. Renal Denervation After the SPYRAL HTN-OFF MED Trial: Putting a Complex Study Into Context. *Hypertension.* (2017) 70:1076–9. doi: 10.1161/HYPERTENSIONAHA.117.10290
12. Fregni F, Freedman S, Pascual-Leone A. Recent advances in the treatment of chronic pain with noninvasive brain stimulation techniques. *Lancet Neurol.* (2007) 6:188–91. doi: 10.1016/S1474-4422(07)70032-7
13. Bikson M, Grossman P, Thomas C, Zannou AL, Jiang J, Adnan T, et al. Safety of Transcranial Direct Current Stimulation: Evidence Based Update 2016. *Brain Stimul.* (2016) 9:641–61. doi: 10.1016/j.brs.2016.06.004
14. Rodrigues B, Barboza CA, Moura EG, Ministro G, Ferreira-Melo SE, Castaño JB, et al. Transcranial direct current stimulation modulates autonomic nervous system and reduces ambulatory blood pressure in hypertensives. *Clin Exp Hypertens.* (2021) 43:320–7. doi: 10.1080/10641963.2021.1871916
15. Antal A, Alekseichuk I, Bikson M, Brockmöller J, Brunoni AR, Chen R, et al. Low intensity transcranial electric stimulation: Safety, ethical, legal regulatory and application guidelines. *Clin Neurophysiol.* (2017) 128:1774–809. doi: 10.1016/j.clinph.2017.06.001
16. Fertonani A, Ferrari C, Miniussi C. What do you feel if I apply transcranial electric stimulation? Safety, sensations and secondary induced effects. *Clin Neurophysiol.* (2015) 126:2181–8. doi: 10.1016/j.clinph.2015.03.015
17. Lauder L, Azizi M, Kirtane AJ, Böhm M, Mahfoud F. Device-based therapies for arterial hypertension. *Nat Rev Cardiol.* (2020) 17:614–28. doi: 10.1038/s41569-020-0364-1
18. Morya E, Monte-Silva K, Bikson M, Esmaeilpour Z, Biazoli CE Jr, Fonseca A, et al. Beyond the target area: an integrative view of tDCS-induced motor cortex modulation in patients and athletes. *J Neuroeng Rehabil.* (2019) 16:141. doi: 10.1186/s12984-019-0581-1
19. Piccirillo G, Ottaviani C, Fiorucci C, Petrocchi N, Moscucci F, Di Iorio C, et al. Transcranial direct current stimulation improves the QT variability index and autonomic cardiac control in healthy subjects older than 60 years. *Clin Interv Aging.* (2016) 11:1687–95. doi: 10.2147/CIA.S116194
20. Makovac E, Thayer JF, Ottaviani C. A meta-analysis of noninvasive brain stimulation and autonomic functioning: Implications for brain-heart pathways to cardiovascular disease. *Neurosci Biobehav Rev.* (2017) 74(Pt B):330–41. doi: 10.1016/j.neubiorev.2016.05.001
21. Keizer K, Kuypers HG. Distribution of corticospinal neurons with collaterals to the lower brain stem reticular formation in monkey (Macaca fascicularis). *Exp Brain Res.* (1989) 74:311–8. doi: 10.1007/BF00248864
22. Dum RP, Strick PL. The origin of corticospinal projections from the premotor areas in the frontal lobe. *J Neurosci.* (1991) 11:667–89. doi: 10.1523/JNEUROSCI.11-03-00667.1991
23. Dum RP, Strick PL. Frontal lobe inputs to the digit representations of the motor areas on the lateral surface of the hemisphere. *J Neurosci.* (2005) 25:1375–86. doi: 10.1523/JNEUROSCI.3902-04.2005
24. Wall PD, Pribram KH. Trigeminal neurotomy and blood pressure responses from stimulation of lateral cerebral cortex of Macaca mulatta. *J Neurophysiol.* (1950) 13:409–12. doi: 10.1152/jn.1950.13.6.409
25. Wall PD, Davis GD. Three cerebral cortical systems affecting autonomic function. *J Neurophysiol.* (1951) 14:507–17. doi: 10.1152/jn.1951.14.6.507
26. Tracey KJ. Reflex control of immunity. *Nat Rev Immunol.* (2009) 9:418–28. doi: 10.1038/nri2566
27. Huston JM, Tracey KJ. The pulse of inflammation: heart rate variability, the cholinergic anti-inflammatory pathway and implications for therapy. *J Intern Med.* (2011) 269:45–53. doi: 10.1111/j.1365-2796.2010.02321.x
28. Borovikova LV, Ivanova S, Zhang M, Yang H, Botchkina GI, Watkins LR, et al. Vagus nerve stimulation attenuates the systemic inflammatory response to endotoxin. *Nature.* (2000) 405:458–62. doi: 10.1038/35013070
29. Carrozzino D, Patierno C, Fava GA, Guidi J. The Hamilton Rating Scales for Depression: A Critical Review of Clinimetric Properties of Different Versions. *Psychother Psychosom.* (2020) 89:133–50. doi: 10.1159/000506879
30. Williams B, Mancia G, Spiering W, Agabiti Rosei E, Azizi M, Burnier M, et al.; List of authors/Task Force members. 2018 Practice Guidelines for the management of arterial hypertension of the European Society of Hypertension and the European Society of Cardiology: ESH/ESC Task Force for the Management of Arterial Hypertension. *J Hypertens.* (2018) 36:2284–309. doi: 10.1097/HJH.0000000000001961
31. Schäfer A, Vagedes J. How accurate is pulse rate variability as an estimate of heart rate variability? A review on studies comparing photoplethysmographic technology with an electrocardiogram. *Int J Cardiol.* (2013) 166:15–29. doi: 10.1016/j.ijcard.2012.03.119
32. Pernice R, Javorka M, Krohova J, Czippelova B, Turianikova Z, Busacca A, et al. Reliability of Short-Term Heart Rate Variability Indexes Assessed through Photoplethysmography. *Annu Int Conf IEEE Eng Med Biol Soc.* (2018) 2018:5610–5513. doi: 10.1109/EMBC.2018.8513634
33. Heart rate variability: standards of measurement, physiological interpretation and clinical use. Task Force of the European Society of Cardiology and the North American Society of Pacing and Electrophysiology. *Circulation.* (1996) 93:1043–65.
34. Stauss HM. Identification of blood pressure control mechanisms by power spectral analysis. *Clin Exp Pharmacol Physiol.* (2007) 34:362–8. doi: 10.1111/j.1440-1681.2007.04588.x
35. Parati G, Ochoa JE, Lombardi C, Bilo G. Assessment and management of blood-pressure variability. *Nat Rev Cardiol.* (2013) 10:143–55. doi: 10.1038/nrcardio.2013.1
36. Gedikli O, Ozturk S, Yilmaz H, Baykan M, Kiris A, Durmus I, et al. Relationship between arterial stiffness and myocardial damage in patients with newly diagnosed essential hypertension. *Am J Hypertens.* (2008) 21:989–93. doi: 10.1038/ajh.2008.235
37. de Andrade Barboza C, Moura EG, Ministro G, Castaño JB, Silva Santos GC, Dias Junior G, et al. Central blood pressure and aortic pulse wave reflection in water-exercised postmenopausal hypertensive women: a cross-sectional study. *Exp Gerontol.* (2021) 143:111146. doi: 10.1016/j.exger.2020.111146
38. Gandiga PC, Hummel FC, Cohen LG. Transcranial DC stimulation (tDCS): a tool for double-blind sham-controlled clinical studies in brain stimulation. *Clin Neurophysiol.* (2006) 117:845–50. doi: 10.1016/j.clinph.2005.12.003
39. Bhatt DL, Kandzari DE, O'Neill WW, D'Agostino R, Flack JM, Katzen BT, et al. SYMPLICITY HTN-3 Investigators. A controlled trial of renal denervation for resistant hypertension. *N Engl J Med.* (2014) 370:1393–401. doi: 10.1056/NEJMoa1402670
40. Persu A, Fadl Elmula FEM, Jin Y, Os I, Kjeldsen SE, Staessen JA. Renal Denervation After Symplicity HTN-3 - Back to Basics. Review of the Evidence. *Eur Cardiol.* (2014) 9:110–4. doi: 10.1007/s11906-014-0460-x
41. Townsend RR, Mahfoud F, Kandzari DE, Kario K, Pocock S, Weber MA, et al. SPYRAL HTN-OFF MED trial investigators*. Catheter-based renal denervation in patients with uncontrolled hypertension in the absence of antihypertensive medications (SPYRAL HTN-OFF MED): a randomised, sham-controlled, proof-of-concept trial. *Lancet.* (2017) 390:2160–70. doi: 10.1016/S0140-6736(17)32281-X
42. Kandzari DE, Böhm M, Mahfoud F, Townsend RR, Weber MA, Pocock S, et al. SPYRAL HTN-ON MED Trial Investigators. Effect of renal denervation on blood pressure in the presence of antihypertensive drugs: 6-month efficacy and safety results from the SPYRAL HTN-ON MED proof-of-concept randomized. *trial Lancet.* (2018) 391:2346–55. doi: 10.1016/S0140-6736(18)30951-6
43. Azizi M, Schmieder RE, Mahfoud F, Weber MA, Daemen J, Davies J, et al. RADIANCE-HTN Investigators. Endovascular ultrasound renal denervation to treat hypertension (RADIANCE-HTN SOLO): a multicentre, international, single-blind, randomised, sham-controlled trial. *Lancet.* (2018) 391:2335–45. doi: 10.1016/S0140-6736(18)31082-1
44. Kapp BS, Schwaber JS, Driscoll PA. The organization of insular cortex projections to the amygdaloid central nucleus and autonomic regulatory nuclei of the dorsal medulla. *Brain Res.* (1985) 360:355–60. doi: 10.1016/0006-8993(85)91254-5
45. Oppenheimer SM, Gelb A, Girvin JP, Hachinski VC. Cardiovascular effects of human insular cortex stimulation.

Neurology. (1992) 42:1727–32. doi: 10.1212/WNL.42.9.1727
46. Oppenheimer SM, Saleh T, Cechetto DF. Lateral hypothalamic area neurotransmission and neuromodulation of the specific cardiac effects of insular cortex stimulation. *Brain Res.* (1992) 581:133–42. doi: 10.1016/0006-8993(92)90352-A
47. Montenegro RA, Farinatti Pde T, Fontes EB, Soares PP, Cunha FA, Gurgel JL, et al. Transcranial direct current stimulation influences the cardiac autonomic nervous control. *Neurosci Lett.* (2011) 497:32–6. doi: 10.1016/j.neulet.2011.04.019
48. Ardolino G, Bossi B, Barbieri S, Priori A. Non-synaptic mechanisms underlie the after-effects of cathodal transcutaneous direct current stimulation of the human brain. *J Physiol*. (2005) 568(Pt 2):653–63. doi: 10.1113/jphysiol.2005.088310
49. McLaren ME, Nissim NR, Woods AJ. The effects of medication use in transcranial direct current stimulation: a brief review. *Brain Stimul*. (2018) 11:52–8. doi: 10.1016/j.brs.2017.10.006
50. Vlachopoulos C, Aznaouridis K, Stefanadis C. Prediction of cardiovascular events and all-cause mortality with arterial stiffness: a systematic review and meta-analysis. *J Am Coll Cardiol.* (2010) 55:1318–27. doi: 10.1016/j.jacc.2009.10.061
51. Nardone M, Floras JS, Millar PJ. Sympathetic neural modulation of arterial stiffness in humans. *Am J Physiol Heart Circ Physiol.* (2020) 319:H1338–46. doi: 10.1152/ajpheart.00734.2020
52. Prodel E, Barbosa TC, Mansur DE, Nóbrega AC, Vianna LC. Effects of face cooling on pulse waveform and sympathetic activity in hypertensive subjects. *Clin Auton Res.* (2017) 27:45–9. doi: 10.1007/s10286-016-0391-5
53. Dum RP, Levinthal DJ, Strick PL. Motor, cognitive, and affective areas of the cerebral cortex influence the adrenal medulla. *Proc Natl Acad Sci U S A.* (2016) 113:9922–7. doi: 10.1073/pnas.1605044113
54. Dum RP, Levinthal DJ, Strick PL. The mind-body problem: Circuits that link the cerebral cortex to the adrenal medulla. *Proc Natl Acad Sci U S A.* (2019) 116:26321–8. doi: 10.1073/pnas.1902297116
55. Tomiyama H, Shiina K, Matsumoto-Nakano C, Ninomiya T, Komatsu S, Kimura K, et al. The Contribution of Inflammation to the Development of Hypertension Mediated by Increased Arterial Stiffness. *J Am Heart Assoc.* (2017) 6:e005729. doi: 10.1161/JAHA.117.005729
56. Goodwin JE, Geller DS. Glucocorticoid-induced hypertension. *Pediatr Nephrol.* (2012) 27:1059–66. doi: 10.1007/s00467-011-1928-4

Conflict of Interest: The authors declare that the research was conducted in the absence of any commercial or financial relationships that could be construed as a potential conflict of interest.

Publisher's Note: All claims expressed in this article are solely those of the authors and do not necessarily represent those of their affiliated organizations, or those of the publisher, the editors and the reviewers. Any product that may be evaluated in this article, or claim that may be made by its manufacturer, is not guaranteed or endorsed by the publisher.

frontiers in Cardiovascular Medicine

ORIGINAL RESEARCH
published: 14 March 2022
doi: 10.3389/fcvm.2022.854361

Sustained Downregulation of Vascular Smooth Muscle Acta2 After Transient Angiotensin II Infusion: A New Model of "Vascular Memory"

*Lucie Pothen[1], Roxane Verdoy[1], Delphine De Mulder[1], Hrag Esfahani[1], Charlotte Farah[1], Lauriane Y. M. Michel[1], Flavia Dei Zotti[1], Bertrand Bearzatto[2], Jerome Ambroise[2], Caroline Bouzin[3], Chantal Dessy[1] and Jean-Luc Balligand[1]**

[1] Institute of Experimental and Clinical Research (IREC), Pole of Pharmacology and Therapeutics (FATH), Cliniques Universitaires St-Luc and Université Catholique de Louvain (UCLouvain), Brussels, Belgium, [2] Institute of Experimental and Clinical Research (IREC), Centre des Technologies Moléculaires Appliquées (CTMA), Cliniques Universitaires St-Luc and Université Catholique de Louvain (UCLouvain), Brussels, Belgium, [3] Institute of Experimental and Clinical Research (IREC), Imaging Platform (2IP), Cliniques Universitaires St-Luc and Université Catholique de Louvain (UCLouvain), Brussels, Belgium

OPEN ACCESS

Edited by:
Marco Mongillo,
University of Padua, Italy

Reviewed by:
Michele Ciccarelli,
University of Salerno, Italy
Tlili Barhoumi,
King Abdullah International Medical Research Center (KAIMRC), Saudi Arabia

***Correspondence:**
Jean-Luc Balligand
jean-luc.balligand@uclouvain.be

Specialty section:
This article was submitted to Hypertension, a section of the journal Frontiers in Cardiovascular Medicine

Received: 13 January 2022
Accepted: 14 February 2022
Published: 14 March 2022

Citation:
Pothen L, Verdoy R, De Mulder D, Esfahani H, Farah C, Michel LYM, Dei Zotti F, Bearzatto B, Ambroise J, Bouzin C, Dessy C and Balligand J-L (2022) Sustained Downregulation of Vascular Smooth Muscle Acta2 After Transient Angiotensin II Infusion: A New Model of "Vascular Memory". Front. Cardiovasc. Med. 9:854361. doi: 10.3389/fcvm.2022.854361

Background: Activation of the renin-angiotensin-aldosterone system (RAAS) plays a critical role in the development of hypertension. Published evidence on a putative "memory effect" of AngII on the vascular components is however scarce.

Aim: To evaluate the long-term effects of transient exposure to AngII on the mouse heart and the arterial tissue.

Methods: Blood pressure, cardiovascular tissue damage and remodeling, and systemic oxidative stress were evaluated in C57/B6/J mice at the end of a 2-week AngII infusion (*AngII*); 2 and 3 weeks after the interruption of a 2-week AngII treatment (*AngII+2W* and *AngII +3W*; so-called "memory" conditions) and control littermate (*CTRL*). RNAseq profiling of aortic tissues was used to identify potential key regulated genes accounting for legacy effects on the vascular phenotype. RNAseq results were validated by RT-qPCR and immunohistochemistry in a reproduction cohort of mice. Key findings were reproduced in a homotypic cell culture model.

Results: The 2 weeks AngII infusion induced cardiac hypertrophy and aortic damage that persisted beyond AngII interruption and despite blood pressure normalization, with a sustained vascular expression of ICAM1, infiltration by CD45+ cells, and cell proliferation associated with systemic oxidative stress. RNAseq profiling in aortic tissue identified robust *Acta2* downregulation at transcript and protein levels (α-smooth muscle actin) that was maintained beyond interruption of AngII treatment. Among regulators of *Acta2* expression, the transcription factor Myocardin (*Myocd*), exhibited a similar expression pattern. The sustained downregulation of *Acta2* and *Myocd* was associated with an increase in H3K27me3 in nuclei of aortic sections from mice in the "memory" conditions. A sustained downregulation of *ACTA2* and *MYOCD* was reproduced in the cultured human aortic vascular smooth muscle cells upon transient exposure to Ang II.

Conclusion: A transient exposure to Ang II produces prolonged vascular remodeling with robust *ACTA2* downregulation, associated with epigenetic imprinting supporting a "memory" effect despite stimulus withdrawal.

Keywords: angiotensin II, aortic tissue, VSMC, memory, ACTA2, smooth muscle actin (SMA)

INTRODUCTION

Hypertension is a well recognized cardiovascular risk factor, causing up to 7.6 million deaths per year worldwide (13.5% of total deaths) (1). Usually, it develops as a slow and gradual increase in blood pressure, with occasional acute hypertensive peaks. This silent disease can remain unrecognized until potentially fatal complications occur, such as hypertrophic cardiomyopathy, strokes, or ischemic heart disease.

Hypertension is conventionally associated with a neurohormonal activation from the sympathetic nervous and the renin-angiotensin-aldosterone systems (RAAS) (2, 3). The RAAS is involved in numerous physiological functions, including vasoconstriction, fluid volume regulation, cardiac remodeling, cell growth, and vascular wall integrity. Angiotensin II (AngII), as the main product and effector of the RAAS, is a potent regulator of blood pressure (4, 5). As such, it is also a key player in hypertension development, mainly through activation of the type 1 AngII receptors (AT_1R), that triggers structural remodeling and inflammation in the heart and vascular tissue (6). In particular, cellular processes underlying vascular injury include, among others, impaired endothelial function and a phenotypic switch of vascular smooth muscle cells (VSMCs), characterized by a reduced expression of myofibrillar proteins and contractility, evolving toward a more proliferative and synthetic state, with increased production, e.g., of proteoglycans (7–9).

Usually, activation of the RAAS accompanies the development of other cardiovascular risk factors than hypertension, such as diabetes or metabolic syndrome, including hypercholesterolemia. The resulting cardiovascular pathologies evolve with sustained deleterious effects despite the removal of the pathogenic stimulus (e.g., hyperglycemia), a phenomenon that has been coined "metabolic memory" (10). In the previous models of diabetes, temporary exposure to hyperglycemia leads to an epigenetic imprinting in endothelial cells, with sustained mitochondrial oxidative stress despite glycemic normalization (11, 12). Similar epigenetic mechanisms might explain the enduring increase in cardiovascular risk, despite glycemic control in the clinical studies, named as legacy effect (13, 14). The specific participation of the RAAS, particularly of AngII, in these enduring effects is less clear. Intriguingly, other clinical trials suggest that treatement with a RAAS inhibitor, e.g., sartans that inhibit AngII binding to the AT_1R, could prevent organ damage and reduce cardiovascular events through protective effects beyond blood pressure lowering in hypertensive patients (15). Published evidence on a putative "memory effect" of AngII is scarce. One previous study observed a sustained vascular injury with persistent activation of multiple signaling pathways (JNK1/2, STAT3, and NF-κB) and increase in the reactive oxygen species (ROS) production up to 1 week after withdrawal of an initial AngII infusion in mice; the data suggested a link with persistent NADPH oxidase activation. However, the upstream mechanism for this sustained oxidative stress was not established (16, 17).

Surprisingly, while transcriptomic profiles of AngII-treated organs/tissues are available in the kidneys (18), heart (19), or abdominal aortic aneurysm in ApoE-/- mice (20), the AngII treatment protocol varies widely between studies, and transcriptomic data on the arterial tissue of WT mice were rarely reported (21–23), with no attempt to analyze any legacy effect.

In this study, we developed an AngII "memory" model in which we examined long-term effects of temporary exposure to AngII on heart and arterial tissue, including cardiovascular remodeling and VSMC phenotypic switch. Longitudinal transcriptomic profiling of aortic tissues after AngII withdrawal identified uniquely regulated genes potentially involved in legacy effects on the vascular phenotype.

MATERIALS AND METHODS

Animal Experimental Protocol

11-week male C57B6/J mice were implanted with osmotic minipumps delivering of 2.8 mg/kg/d of AngII (Sigma, A9525) for 2 weeks. To confirm the effect of the pharmacological treatment, blood pressure signals from aortic arch before (*CTRL*); under AngII up to 2 weeks (*AngII*); and 2 and 3 weeks after the interruption of AngII (*AngII+2W*; *AngII+3w*, respectively) were recorded in selected, conscious, and unrestrained animals, with surgically implanted miniaturized telemetry devices (DSI, USA) as described previously (24). Mice were sacrificed after anesthesia at the same time points and age-matched littermate served as control (**Figure 1A**). All the investigations conformed to the Guide for the Care and Use of Laboratory Animals (NIH Publications no. 8023, revised 2011) and were approved by the Institutional Animal Care and Research Advisory Committee of the Université Catholique de Louvain.

Histomorphometric Analysis of Hearts

Morphometric and histologic measurements were obtained from hearts arrested in diastole in KCl solution, washed, subsequently fixed with 4% formaldehyde and paraffin embedded. To assess cardiac myocyte transverse area, tissue was costained with wheat germ agglutinin (WGA; for plasma membrane staining, rhodamine-conjugated) and isolectin B4 (GS-IB4; for endothelial staining, biotin-conjugated and revealed with fluorescein-conjugated streptavidin). Cell area from 150 to 200 cells per slide was determined using AxioVision software 4.8.2.0.

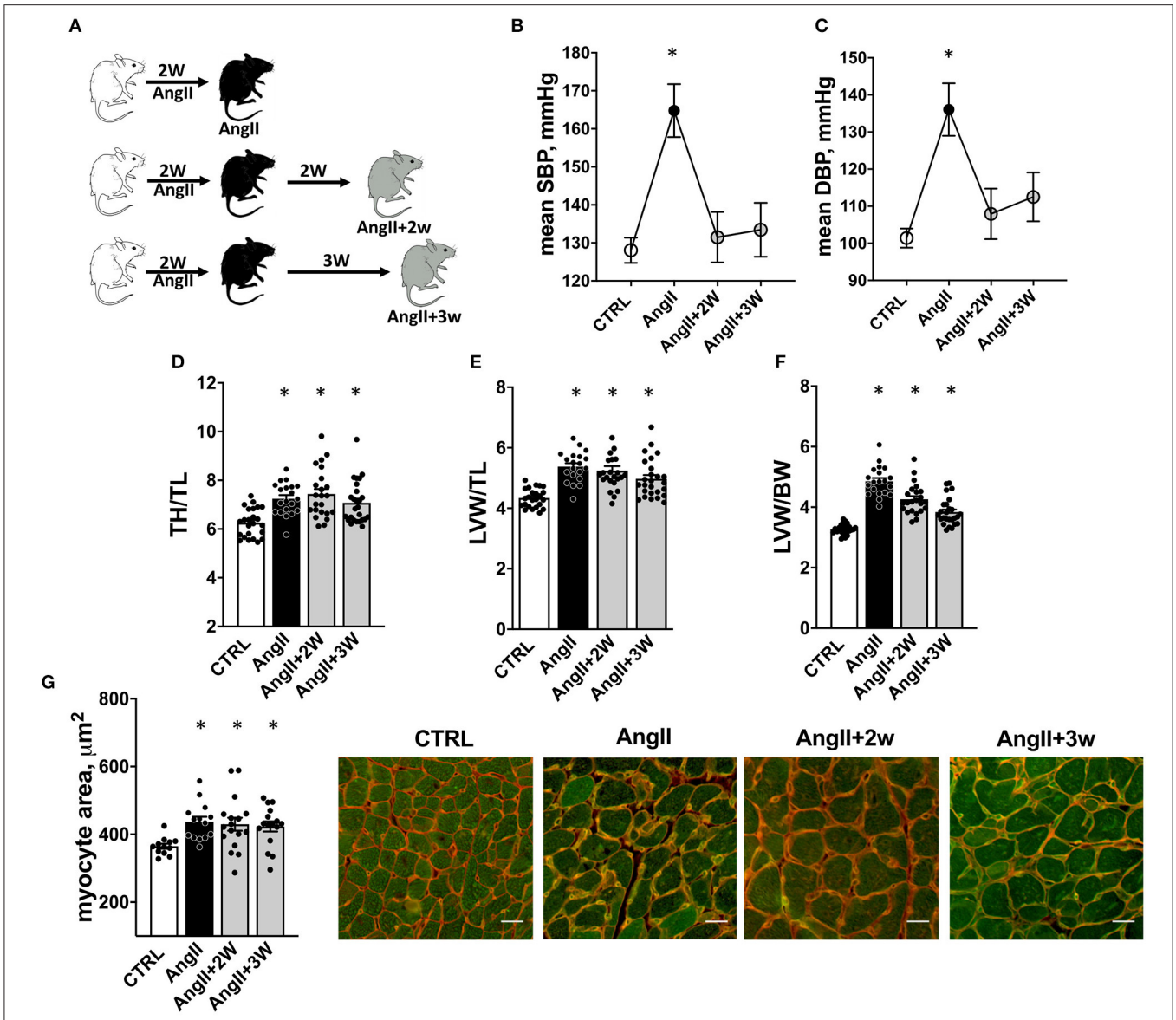

FIGURE 1 | Experimental procedure and cardiac hypertrophy. Experimental procedure: **(A)** C57Bl6 mice were implanted with osmotic minipump delivering 2.8mg/kg/d of AngII during 2 weeks. One group was sacrificed at the end of the treatment (*AngII*), 2 others were sacrificed, respectively, 2 weeks (*AngII+2W*) and 3 weeks (*AngII+3W*) after the end of the minipump, and were considered as "memory groups". Control mice (*CTRL*) were littermate age-matched mice sacrificed at each time point (2 weeks of AngII, 2 weeks of AngII + 2 weeks, 2 weeks of AngII +3 weeks). **(B)** Systolic and **(C)** Diastolic blood pressure measured with implanted telemetry devices. $n = 19$; $^*p < 0.05$, one-way ANOVA for repeated measures, mixed-effect analysis followed by Tukey's multiple comparison test. **(D–G)** Cardiac Hypertrophy: **(D)** Total heart/tibial length ratio (TH/TL); **(E)** Left ventricular weight/tibial length ratio (LVW/TL); and **(F)** Left ventricular weight/body weight ratio (LVW/BW). $n = 93$ (initial + replication cohorts); $^*p < 0.05$, one-way ANOVA followed by Holm-Sidak's multiple comparisons test. **(G)** Quantification of myocyte size area by isolectin/WGA staining and representative pictures (white bar scale = 20 μm). $n = 59$; $^*p < 0.05$, one-way ANOVA followed by Dunett's multiple comparisons test.

Immunostaining on Carotid Arteries and Aortas

Vessels (carotid arteries and aortas in totality) were carefully dissected, washed in cold PBS, and divided in several pieces for further experiments. One piece was subsequently fixed with 4% formaldehyde and paraffin embedded. To assess endothelial activation, carotid sections were stained with ICAM-1 primary antibody (R&D #AF796, 1/1000). On the aortic tissue, to evaluate inflammatory cells infiltration and proliferation, sections were stained with anti-CD45 primary antibody (BD Biosciences #55053P, 1/50) or rabbit anti-Ki67 primary antibody (CST #12202, 1/200), respectively. Smooth muscle actin and H3K27me3 stainings were performed using anti-αSMA primary antibody (CST #19245, 1/400) and anti-tri-methyl-histone H3 antibody (CST #9733, 1/200). Primary antibodies were revealed with EnVision-HRP systems (Agilent) and DAB (Agilent).

Finally, nuclei were counterstained with H&E (Agilent). Slides were digitized with a slide scanner (SCN400 Leica) and blindly analyzed with QuPath software (University of Edinburgh) (25).

RNA-seq on Aortic Tissue

One-third of aorta was immediately frozen in liquid nitrogen in dry Eppendorf. Because of low yield of RNA extracted in preliminary experiments, and to ensure sufficient amount and quality of RNA for sequencing, tissues from two animals were pooled in 1 ml of tri-reagent (TR118, MRC) for subsequent homogenization with the use of a Precellys Evolution homogenizer (Bertin Instrument, France). Total RNA was extracted with the PureLink™ RNA Micro Scale Kit (Invitrogen) according to the manufacturer's instructions, including a DNase step. In total, RNA from 8 samples, corresponding to 16 mice, were quantified by Qubit RNA BR assay kit (Thermo Fisher Scientific, Q10211) on a Qubit 4 Fluorometer (Thermo Fisher Scientific). RNA integrity was evaluated on the Agilent 2100 Bioanalyzer using the RNA 6000 nanokit (Agilent, 5067-1511). All the samples had RNA integrity number values between 6.8 and 7.7.

Libraries were prepared starting from 150 ng of total RNA using the KAPA RNA HyperPrep Kit with RiboErase (HMR) (KAPA Biosystems, KK8560) following the manufacturer's recommendations (KR1351—version 1.16). Libraries were equimolarly pooled and sequenced on a single lane on an Illumina NovaSeq 6000 platform. All the libraries were paired end (2 × 100 bp reads) sequenced and a minimum of 35 million paired end reads were generated per sample.

All the sequencing data were analyzed using the Automated Reproducible MOdular workflow for preprocessing and differential analysis of RNA-seq data (ARMOR) pipeline v.1.2.0 (26). In this pipeline, reads underwent a quality check using FastQC v0.11.7 (27). Quantification and quality control results were summarized in a MultiQC report (28) before being mapped using Salmon (29) to the transcriptome index which was built using all Ensembl cDNA sequences obtained in the Mus_musculus.GRCm38.cdna.all.fa (release 101) file (30). Then, the estimated transcript abundances from Salmon were imported into R using the tximeta (1.7.14) package (31, 32) and analyzed for differential gene expression with edgeR (3.31.4) package, in which *p*-value was adjusted using Benjamini-Hochberg method (33). Accordingly, each experimental group (*AngII, AngII+2W,* and *AngII+3W*) was compared against the control group (*CTRL*), thereby producing 3 lists of differentially expressed genes. Differential gene expression results from edgeR were used to conduct Over-Representation Analysis (ORA) and Gene Set Enrichment Analysis (GSEA) with the WebGestaltR (v.0.4.3) package (34). These analyses were conducted on the Kyoto Encyclopedia of Genes and Genomes (KEGG) and Reactome database. RNA-seq full data are available in the NCBI Gene Expression Omnibus (GEO) database under the study accession code GSE175588.

RT-qPCR on Aortas in a Replication Cohort

Total RNA was extracted from one-third of the total aorta in a replication cohort of mice, with the same protocol and extraction procedure, i.e., freeze drying, further homogenization in Trizol with Precellys Evolution homogenizer, and extraction with PureLink™ RNA Micro Scale Kit. Extracted RNA was reverse-transcribed and analyzed by quantitative polymerase chain reaction (qPCR) with *GAPDH* as housekeeping gene. The primer sequences used for qPCR are presented in **Table I** in **Supplemental Material**.

Human Aortic Vascular Smooth Muscle Cells (HVSMCs) Culture and *in-vitro* AngII Memory Model

Human aortic vascular smooth muscle cells (HAVSMC) were purchased at ScienCell Research Laboratories. Cells were grown in full Smooth Muscle Cell medium (ScienCell #1101), in T75 flask coated with polylysine (2 $\mu g/cm^2$); medium was renewed every 24 h as cells reached 80% confluence. After serum starvation (0.1% FBS for 18 h) cells were treated with AngII 1μM for 72 h (*AngII*), or 48 h and then 24 h in control, serum-deprived medium (*MemAngII*); and compared with the cells maintained 72 h in control, serum-deprived medium (*CTRL*). Cells between passages 4 and 8 were used for experiments. Total RNA was extracted with Maxwell Kit (Promega, #AS1340). Extracted RNA was reverse-transcribed and analyzed by quantitative polymerase chain reaction (qPCR) with *GAPDH* as housekeeping gene. The primer sequences used for qPCR are presented in **Table I** in **Supplemental Material**. For protein extraction, cells were scrapped in RIPA buffer containing proteinases and phosphates inhibitors. Denatured proteins (in Laemmli buffer) were separated by SDS-PAGE and transferred on PVDF membrane. Membranes were then blocked 1 h in 5% non-fat dry milk in TBS-Tween and incubated overnight at 4°C in 1% milk Tween-TBS with primary antibodies. Antibodies were αSMA (CST #19245, 1/10000) and HSP90 (BD Biosciences #610419, 1/2500). Membranes were visualized by enhanced chemiluminescence on CL-Xposure film (Thermo Fisher Scientific).

Statistics

Statistical tests were performed using GraphPadPrism (GraphPad Software Incorporation, San Diego, California, USA). Results are reported as mean and standard error of the mean. Statistical analysis was performed using parametric or non-parametric tests where appropriate after verifying normality of values distribution. $P < 0.05$ is considered as significant with * meaning $P < 0.05$.

RESULTS

The experimental design is illustrated in **Figure 1A**. Blood pressure was recorded longitudinally in each mouse by telemetry at four time points: at baseline (*CTRL*); at the end of the 2-week treatment with Ang II (*AngII*); and 2 and 3 weeks after the end of the Ang II infusion (*AngII+2W* and *AngII+3W*, respectively); the last two composing the "memory" groups. As expected, we observed an increase in systolic and diastolic blood pressure during AngII infusion (**Figures 1B,C**). Importantly,

blood pressure values reverted to normal levels after the end of the 2-week treatment, confirming treatment interruption and transient exposure to Ang II, as planned. We next evaluated specific parameters of cardiovascular remodeling classically affected by AngII and their eventual persistence at longer time points.

Cardiac Hypertrophy

As expected (4, 35), we observed a significant increase in total heart/tibial length (TH/TL), left ventricular weight/tibial length (LVW/TL), and left ventricular weight/body weight (LVW/BW) ratios in the *AngII* group (**Figures 1D–F**). This hypertrophic phenotype was sustained in time with ratios

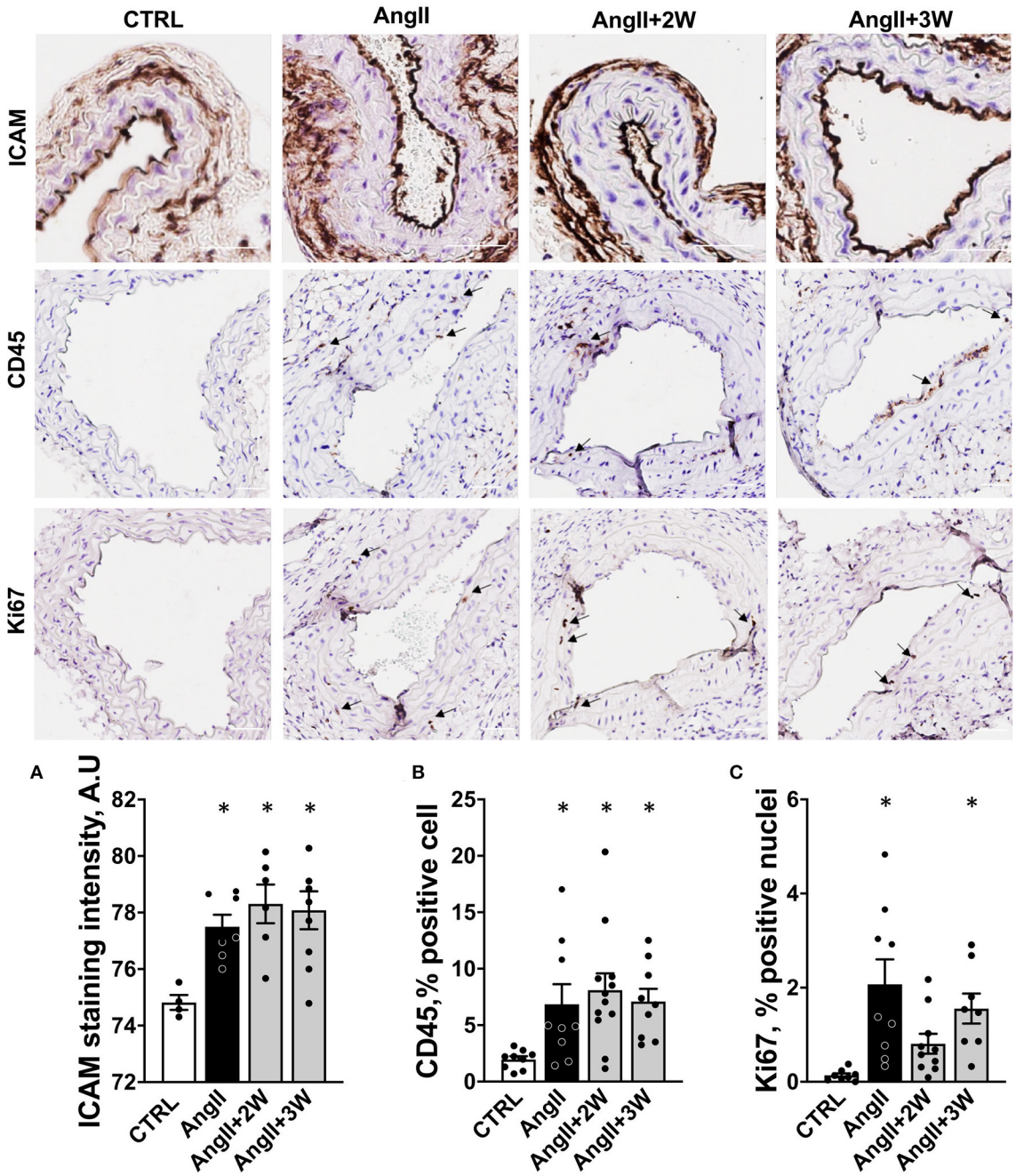

FIGURE 2 | Memory effect on vascular endothelial activation, cell proliferation, and inflammation. **(A)** Quantification of endothelial staining for ICAM-1 in paraffin embedded sections of carotid arteries, expressed in arbitrary units of staining intensity, $n = 26$. **(B)** Quantification of staining for CD45 in paraffin embedded sections of aortas, expressed as % of stained cell. **(C)** Quantification of staining for Ki67 in paraffin-embedded sections of aortas, expressed as % of stained cells. $^*p < 0.05$; $n = 39$ **(B,C)**; One-way ANOVA followed by Dunett's multiple comparisons test. Arrows indicate specific staining for CD45 and Ki67, scale bar = 100 μm.

significantly increased in the *AngII+2W* and *AngII+3W* groups (**Figures 1D–F**). This was reflected by concordant increases in cardiac myocyte transverse area in the *AngII* group (**Figure 1G**), which remained significantly elevated in the *AngII+2W* and *AngII+3W* groups.

Vascular Remodeling

Similar analyses were performed on the vascular phenotype. Histological analysis of carotid sections in the *AngII* group revealed an increased endothelial expression of ICAM-1, reflective of endothelial activation. ICAM-1 expression remained elevated in the *AngII+2W* and *AngII+3W* group (**Figure 2A**). Consistently, CD45 labeling was increased in the aortic tissue of the *AngII* group, reflective of inflammation that was also sustained in time in the *AngII+2W* and *AngII+3W* groups (**Figure 2B**). In line with the known proliferative effect of AngII in vascular tissue (36, 37), Ki67 labeling of aortic tissue was increased in the *AngII* group and, again, maintained in the *AngII+3W* group (**Figure 2C**).

Oxidative Stress

AngII stimulates tissue nicotinamide adenine dinucleotide phosphate (NADPH) oxidases in cardiac and vascular cells to produce superoxide anions and, upon dismutation with extracellular SOD, the secondary oxidizing product H_2O_2 (38). Accordingly, plasma hydroperoxides were elevated in the *AngII* group, and also in the *AngII+2W* group (**Supplementary Figure 1**), reflecting persistent systemic oxidant stress at least up to 2 weeks after Ang II removal in our model.

Comparative Transcriptomic Profiling of AngII vs. AngII "Memory" Conditions

To gain further mechanistic insight into the sustained effect of AngII on this vascular phenotype, we used an unbiased approach through whole aortic tissue RNA-sequencing. We first assessed the differential expression of genes and underlying signaling pathways in the *AngII* group compared with control, untreated mice. Next, we performed a similar comparison between the

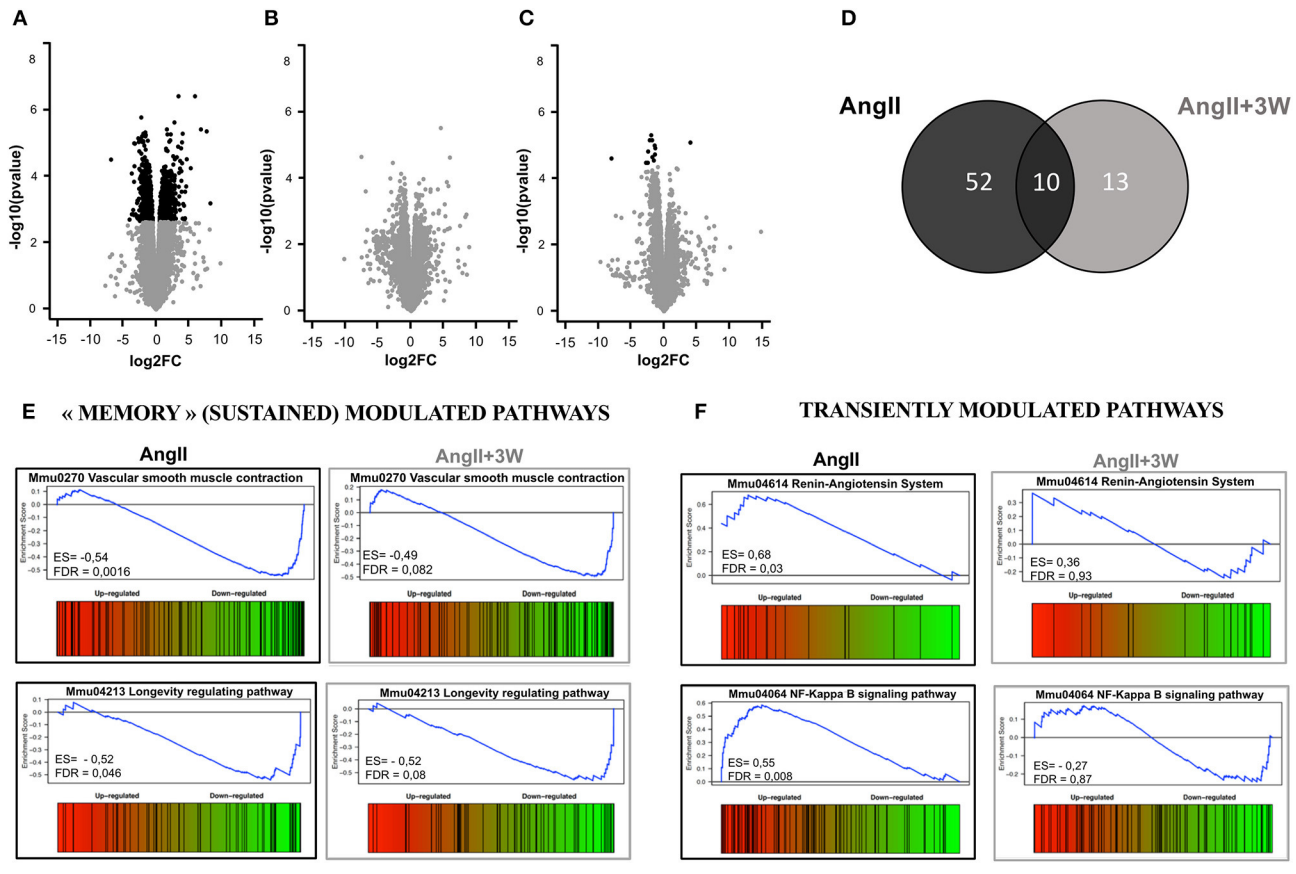

FIGURE 3 | Transcriptomic profiling of aortic tissue from AngII memory model. Volcano plot representing the analysis of differential expression of genes in **(A)** *AngII* vs. *CTRL*; **(B)** *AngII+2W* vs. *CTRL* and **(C)** *AngII+3W* vs. *CTRL* data sets. Black points mark the genes with significantly (FDR < 0.05) increased or decreased expression compared to CTRL. The x-axis shows $\log_2$fold-changes in expression and the y-axis the $-\log_{10}$(*p*-value). **(D)** Gene set enrichment analysis (GSEA) from compiled KEGG pathways. Venn diagram showing the number of gene sets differentially modulated in each condition, and the overlap for 10 of them (FDR value < 0.1) **(E)** Enrichment score diagram illustrating the expression pattern of 2 of the 10 commonly regulated pathways (e.g., present in *AngII* and in *AngII+3w*, and modulated in the same direction) "vascular smooth muscle contraction" and "longevity regulating pathway". **(F)** Enrichment score diagram illustrating the expression pattern of 2 transiently modulated pathways by Angiotensin II infusion: "Renin angiotensin System" and "NF KappaB signaling pathway".

AngII+2W and *AngII+3W* groups (i.e., "memory" conditions) vs. control, untreated mice. We also compared the resulting list of genes and pathways to identify transcripts similarly modulated in *AngII* and "memory" groups, assuming that these sustained up and/or downregulated transcripts may be related to the observed "memory" phenotype.

Volcano plots in **Figures 3A–C** represent differential expression of gene data sets comparing each condition to *CTRL*, considering FDR < 0.05 as a cutoff. As shown in **Figures 3A,C**, we found 808 genes significantly differentially expressed in *AngII* and 13 genes in *AngII+3W* memory condition. Unlike the *AngII* condition (**Figure 3A**) in which 55% of genes were upregulated, we found a vast majority of significantly underexpressed genes in *AngII+3W* memory condition (**Figure 3C**). As no significant differentially expressed gene was found with this FDR cutoff in the *AngII+2W* group (**Figure 3B**), we focused on the *AngII+3W* memory group compared with *AngII* for further analysis.

Gene set enrichment analysis of the 2 data sets is summarized in **Figures 3D–F**. A total of 62 KEGG pathways were significantly differentially modulated in *AngII* group, and 23 in *AngII+3W* group, using FDR < 0.1 as a cut-off. The Venn diagram in **Figure 3D** shows that 10 of them were commonly modulated pathways between the 2 groups. Among these 10 pathways, we next searched for those modulated in the same direction, e.g., up- or downregulated. Four of the 10 commonly modulated pathways were similarly downregulated, and identified as "dilated cardiomyopathy" (mmu05414); "hypertrophic cardiomyopathy" (mmu05410); "longevity regulating pathway" (mmu04213) and, notably, "vascular smooth muscle contraction" (mmu04270) (**Figure 3E**; **Supplementary Figure 2**). Conversely, other pathways known to be regulated by AngII, such as, "Renin angiotensin system" (mmu044614), "NF-KappaB signaling" (mmmu04064) and "cGMP signaling" (mmu04022) were, as expected, up (for the first two) or downregulated (for the latter) in the *AngII* group, but returned to normal level of enrichment in the *AngII+3W* "memory" group (**Figure 3F**; **Supplementary Figure 2**).

We next compared the gene lists to identify transcripts commonly regulated in both *AngII* and *AngII+3W* conditions. A total of 13 genes were commonly differentially expressed in both conditions, i.e., 13 genes similarly and significantly modulated both in the "memory" group vs. control, untreated mice and in the AngII group vs. control, untreated mice. **Figure 4A** represents a heat map with these 13 common transcripts, illustrating changes in the expression level in each condition (*AngII* and *AngII+3W*) compared with control, untreated condition (see also **Supplementary Figure 3**).

Among these, our attention was drawn to *Acta2*. *Acta2* is a gene coding for alpha-smooth muscle actin (αSMA), a protein of the cytoskeleton mainly expressed in smooth muscle cells that is involved in vascular contractility and blood pressure homeostasis. Mutations in this gene cause a variety of vascular diseases, such as thoracic dilated aortic disease, coronary artery disease, stroke, and Moyamoya disease (39), and also multisytemic smooth muscle dysfunction syndrome (40). Downregulation of αSMA expression induced by AngII has also been described in vascular SMC *in vitro* (41, 42).

To better delineate the putative role of *Acta2* in the context of our pathway enrichment analysis, we drew a virtual protein–protein interaction network using the Cytoscape software (fed from the String database). We only included the list of genes that were differentially expressed in *AngII+3W* memory condition (compared with *CTRL*), with enlarged FDR cut-off of < 0.1 for a more comprehensive picture (**Figure 4C**). Note that this interactome did not consider the direction of modulation (e.g., if a transcript was either up or downregulated, to the extent that protein abundance is modulated similarly). Interestingly, we observed that *Acta2* was located at a central hub of this protein–protein interaction network.

Based on the earlier observations, we focused on *Acta2* as a potential driver of our phenotype.

Sustained Downregulation of Acta2 in a Replication Cohort: Putative Role of Myocardin and Histone Methylation

We confirmed our RNAseq data in a replication cohort of identically treated mice, in which we found a downregulation of *Acta2* mRNA expression by RT-qPCR in *AngII*, and both *AngII+ 2W* and *AngII+3W* groups, compared with *CTRL* (**Figure 4B**); among the 13 genes identified in the RNAseq data, downregulation of *Myl9*, *Kcnc4*, and *Lancl3* mRNA expression were also confirmed (**Figure 4B**). αSMA protein levels were also evaluated through quantitative immunostaining on aortic tissue. We confirmed a significant decrease in αSMA protein expression in the *AngII* group, which was significantly maintained in both "memory" conditions, *AngII+2W* and *AngII+3W* group (**Figure 5A**). Remarkably, the cytoskeleton in smooth muscle cells of the arterial media in these two groups was profoundly altered, with important structural defects and disorganization (see representative pictures in **Figure 5**).

Among factors controling αSMA expression are transcription factors Myocardin (*Myocd*) and Serum Response Factor (*SRF*). Altogether they form a complex which binds CArG ($CCA/T_{(rich)}GG$) sequence motif upstream *Acta2* (and other contractile genes), *SRF* serving as doking platform for *Myocd* activity, leading to active contractile transcription machinery. In our RNAseq data, we observed that *Myocd* and *SRF* transcripts were significantly downregulated under AngII (−2,07 $\log_2$FC, FDR = 0,02), with the same trend in the memory condition for *Myocd* (−1,42 $\log_2$FC, FDR= 0,13). We decided to evaluate *Myocd* expression by RT qPCR in our replication group of mice. We observed that this transcription factor was robustly repressed under AngII infusion and that this repression was sustained in time despite the end of the pharmacological stimulation (**Figure 5B**).

To gain further understanding of the sustained downregulation of *Acta2* and *Myocd*, we examined putative epigenetic regulatory mechanisms. Indeed, our pathway analysis using ORA or GSEA, identified significant enrichement of several epigenetic pathways under AngII such as "HDAC's deacetylase histone" (R-MMU-3214815), "HATs acetylate histone" (R-MMU-3214847), and also "PRC2 methylates histone and DNA"(R-MMU-21230) (see **Table I** in **Supplemental Material**,

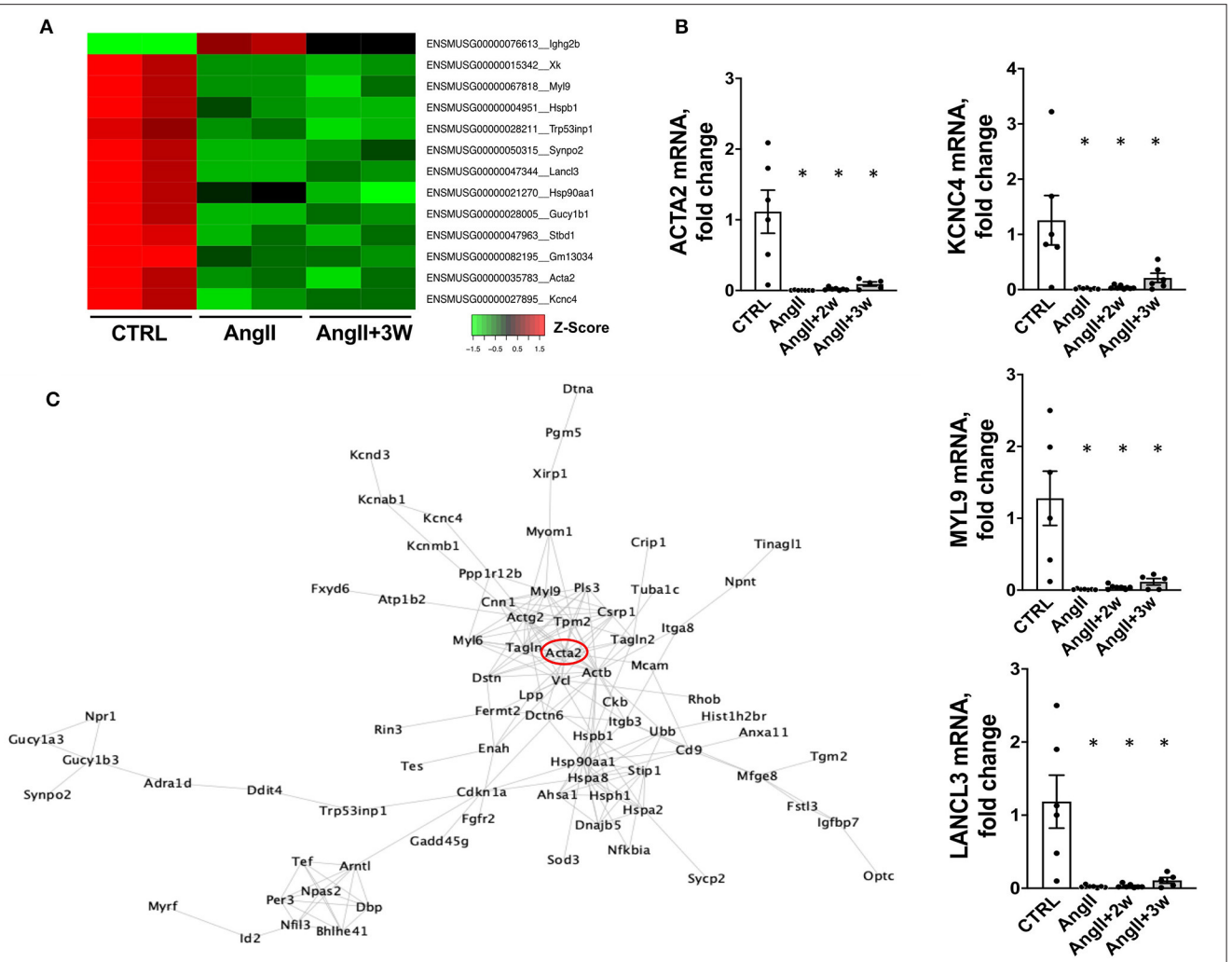

FIGURE 4 | Common downregulation of specific genes in aortic tissue from AngII and "memory model" and corresponding interactome mapping. **(A)** HeatMap representing expression level (Z-score) of the 13 identified commonly modulated transcripts in AngII+3W and AngII vs. CTRL conditions. **(B)** RT qPCR on a replication group of mice confirming RNA seq expression data on selected genes: *Lancl3*, *Kcnc4*, *Myl9*, and *Acta2*, $n = 25$; $^*p < 0{,}05$, one way ANOVA followed by Holm's-Sidak comparison test. **(C)** Protein–protein interaction network corresponding to differentially expressed genes in aorta in the "memory" condition (*AngII+3w*) vs. *CTRL*. To build a comprehensive picture, genes with FDR up to < 0,1 were included. Based on Cytoscape String Network database.

Reactome T1 ORA, Reactome T1 GSEA). Interstingly, PRC2 is a protein complex that keeps transcriptionally silent genes in a repressed state by trimethylating histone H3 on lysine 27. We then evaluated the status of this epigenetic mark in our model, using immunostaining on aortic sections. Notably, this revealed a significant increase in H3K27me3, only in the 2 memory conditions, *AngII+2W* and AngII+3W (**Figure 5C**).

In vitro AngII Memory Model in Human Aortic Vascular Smooth Muscle Cells

To verify these observations in a homotypic cell system of human origin, we developed an *in vitro* model of AngII memory on cultured human aortic VSMCs. Cells were exposed to continuous AngII at 1μM for 72 h (*AngII*); or to the same serum-deprived control medium for 72 h (*CTRL*), or 48 h of AngII, followed by 24 h of control medium (*MemAngII*). First, we observed the same downregulation of *ACTA2* under AngII stimulation, as depicted by mRNA expression and protein levels (**Figures 6A,C**). Notably, this downregulation was also maintained in the "memory" condition. This was paralleled with a downregulation of mRNA expression of the transcription factor *MYOCD*, upon continuous AngII, as well as in the "memory" condition (**Figure 6B**).

DISCUSSION

The main findings of this study can be summarized as follows: (i) an initial 2-week exposure to AngII induces profound changes in cardiac and vascular remodeling, including endothelial activation, vascular inflammation and oxidant stress, all of which are maintained up to 3 weeks after AngII withdrawal;

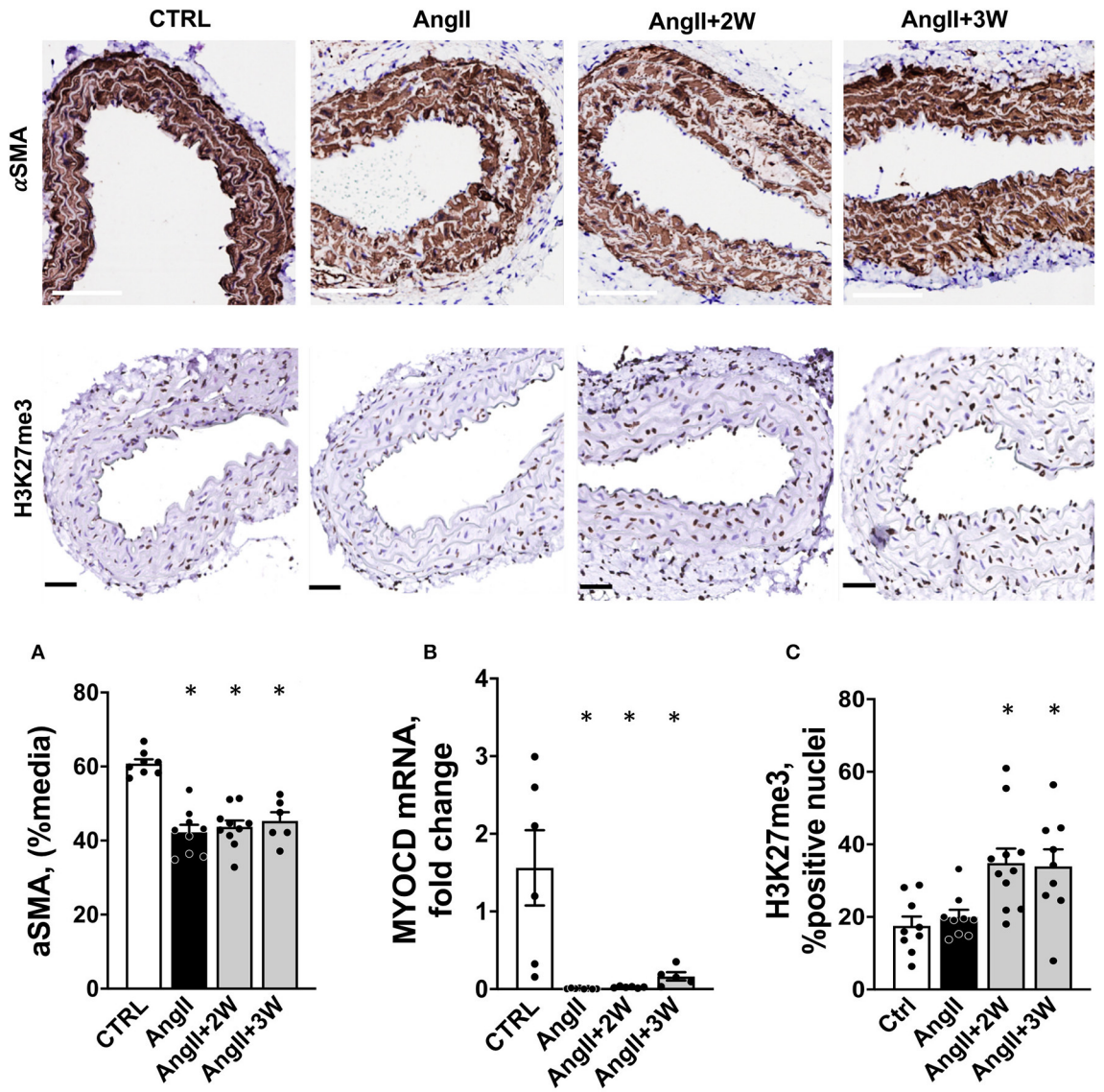

FIGURE 5 | Coordinated regulation of Alpha-Smooth Muscle Actin, its transcription factor *Myocd* and histone trimethylation in aortic tissue from the Ang II "memory" model. **(A)** Sustained down regulation of αSMA protein in aortic tissue from a replication cohort by immunostaining (white bar = 100 μm). $n = 33$; * = $p < 0.05$, one way ANOVA followed by Dunett's multiple comparison test. **(B)** *Myocd* mRNA expression by RTqPCR in mouse aortas from a replication cohort, $n = 26$; *$p < 0.05$, one way ANOVA followed by Holm's-Sidak comparison test. **(C)** H3K27me3 staining and quantification in paraffin-embedded sections of aortas, expressed as % of positive nuclei (black bar = 50 μm), $n = 39$; *$p < 0.05$, one way ANOVA followed by Dunett's multiple comparison test.

notably, this phenotype is sustained despite early normalization of blood pressure after AngII withdrawal, a proxy to a "legacy" or "memory" effect in this mouse model; (ii) comparison of the transcriptomic profiles at the end of the 2-week Ang II treatment (*AngII* group) or 3 weeks after Ang II withdrawal (*AngII+3 weeks* group) identified 13 commonly regulated transcripts (1 up and 12 down), and a set of 4 commonly modulated pathways by GSEA, some of which point to altered structural or contractile properties of the arterial wall. Conversely, many other transcripts classically associated with AngII effects and (mostly) upregulated in the *AngII* group, are not persistently regulated in the *AngII+3 weeks* group; this highlights the above 13 genes, corresponding to the sustained downregulated transcripts, as potential targets for a "memory" effect; (iii) among these, *Acta2* is a likely candidate, as first confirmed in a replication cohort, including at the protein level, but also from our observation of striking downregulation of Myocardin (*Myocd*), its transcriptional coregulator and from changes in histone methylation, as corresponding epigenetic repressive marks, in aortas of both the memory groups, *AngII+2W* and *AngII+3W* groups.

Ours is one of the few studies examining the effect of AngII on the full transcriptomic profile of mouse aortic or arterial tissues in "wild-type" (C57Bl6/J) mice. In a microarray study

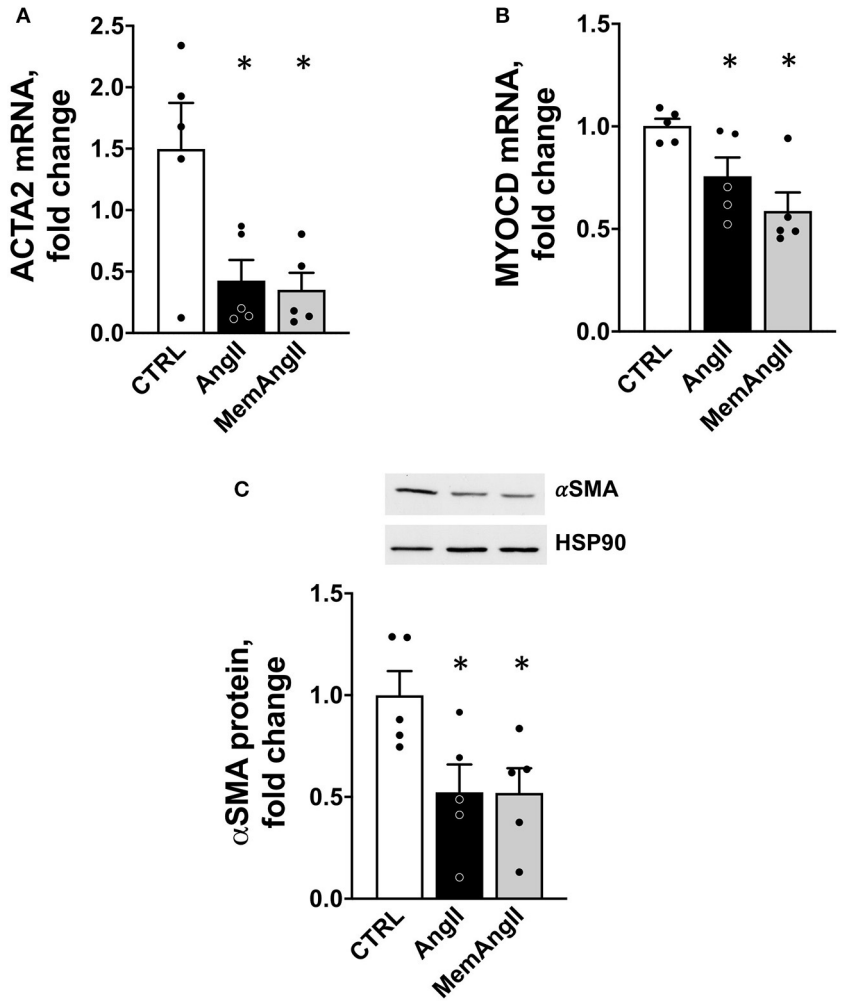

FIGURE 6 | Downregulation of *ACTA2* and *MYOCD* in a homotypic cell culture model of human vascular smooth muscle cells reproducing the AngII "memory" effect *in vitro*. **(A)** *ACTA2* mRNA expression (by RT qPCR) in HAVSMC exposed continuously (*AngII*) or transiently (*MemAngII*) to AngII compared with the control cells maintained in serum-deprived control media. **(B)** *MYOCD* mRNA expression in the same *in vitro* model **(C)** aSMA protein level in the same model, $N = 5$ independent experiments, $^*p < 0.05$ one way ANOVA followed by Sidak's multiple comparisons test.

on ApoE-/- mice-treated with AngII, Rush et al. identified genes overexpressed in mice that did not develop aneurysms under pharmacological Ang II stimulation, i.e., protective against abdominal aortic aneurysms (20). Consistent with their results, a majority of those transcripts were significantly downregulated in our *AngII* group of mice, such as *Sost*, *Dstn*, or *Hspaa1a* (see **Supplementary Data**). Our profiles are also in line with results by Spin et al. identifying genes decreased in prematurely ruptured anevrysm in AngII-treated ApoE-/- mice (e.g., *Bmp6*, *Ltbp1*, *Rock1*) (43). Another transcriptomic analysis of 3 differential arterial beds of C57Bl6 mice treated with AngII identified *Sphk1* as commonly modulated transcript in the 3 types of tissue. This transcript is also upregulated under AngII in our RNAseq data, albeit not significant with an FDR cutoff of 0.05. Other transcripts such as *Thy1* or *Htatip2,* described to be overexpressed in thoracic aorta, are similarly regulated in our *AngII* group. Notably, as we did, the same study identified a downregulation of *Gucy1b3* transcripts (corresponding to the beta subunit of soluble guanylyl cyclase) in thoracic and abdominal aortic tissue, expected to be associated with a reduced vascular relaxation (21). Finally, in a recent study in C57Bl6 mice treated for a longer time with lower dose of AngII, Lv et al. identified 773 genes differentially expressed in aortas of hypertensive mice (22). As in this study, under AngII, mostly were upregulated genes (22). Among identified transcripts, we confirmed the overexpression of IGF1 in our RNAseq data in AngII-infused mice.

Even fewer studies have attempted to develop an AngII "memory" model (16, 17, 44) and in none of them was a transcriptomic profiling performed. In concordance with the only 2 studies in mice found in the literature, we observed sustained macroscopic and microscopic cardiac hypertrophy

(16); ICAM-1 endothelial expression, inflammation in the vascular wall (e.g., CD45-positive cell infiltration), and oxidative stress (17) that persisted after AngII withdrawal. A major difference in the aforementionned study compared with ours is that blood pressure remained elevated 1 week after the end of AngII infusion, the only "remote" time-point examined (17). This could simply be explained by the different AngII dosage and timing for the "memory" condition (1 week vs. 2 weeks after the end of AngII infusion). Although the distinction between differential delays for phenotype reversal (e.g., slower for tissue remodeling, more rapid for blood pressure) vs. "memory" effect could be argued, the present model shows the persistence of remote effects (up to 3 weeks) despite clear evidence of termination of the initial stimulus (normalization of blood pressure). At the very least, and contrary to the previous study, it excludes that the long-lasting effects on remodeling result from sustained high blood pressure.

Another strengh of this study is the use of an unbiased approach to understand our phenotype through transcriptomic profiling. While differential transcript regulation did not reach the more stringent significance level in the *AngII+2W* group probably because of insufficient statistical power, the genes differentially expressed in the *AngII+3W* group at FDR < 0.05 were similary regulated in *AngII+2W* (**Supplementary Data**), suggesting a continuum in their regulation.

AngII, among other factors, promotes a switch in vascular smooth muscle cells from a contractile to "secretrory" phenotype (45). Through AT_1R, AngII stimulation produces changes in the contractile machinery, constisting in decreased expression of contractiles markers such as αSMA (*ACTA2*), SM22a (*TAGLN*), and SMMHC (*MYH11*) (9, 46). As others (41, 47), in parallel with vascular remodeling, we observed significant changes in contractile markers expression in aortas under AngII infusion, with downregulation of "vascular smooth muscle contraction" pathway, and *ACTA2* expression, but also *TAGLN* and *MYH11* (see raw data). In addition, this phenotypic switch was maintained in time despite the end of AngII stimulation, for the "vascular smooth muscle contraction pathway", and also for αSMA expression, both at mRNA and protein levels (**Figures 4B**, **5A**). Among factors controling VSMC phenotypic plasticity are transcription factors Myocardin (*Myocd*) and Serum Response Factor (*SRF*). Altogether they form a complex which binds CArG ($CCA/T_{(rich)}GG$) sequence motif upstream contractile genes, with SRF serving as doking platform for *Myocd* activity, leading to active contractile transcription machinery. Conversely, Krupple-like Factor 4 (*KLF4*) and ETS domain containign protein-1 (*ELK1*) binding to G/C repressor element, inhibit *Myocd/SRF* complex, leading to decressed expression of SMC differentiation markers (46). In our RNAseq data, we observed that *Myocd* and *SRF* transcripts were significantly downregulated under AngII (- 2,07 $\log_2$FC, FDR = 0,02), with the same trend in the *AngII+3W* memory condition for (-1,42 $\log_2$FC, FDR = 0,13). This was not the case for KLF4 and ELK1 (see raw data). We confirmed this downregulation of *Myocd* transcripts by RT-qPCR, including in the 2 memory conditions (*AngII+2W* and *AngII+3W* group) (**Figure 5B**). Interestingly, we could reproduce same results in HAVSMC in culture, in which we observed a sustained down expression of *ACTA2* and protein αSMA induced by AngII, associated with reduced expression of transcription factor *Myocd*; and despite removal of the pharmacologic stimulus. This makes *MYOCD* a likely candidate for upstream, sustained downregulation of *ACTA2* expression in AngII "memory" context.

Epigenetic regulation may also account for the sustained alteration of the vascular phenotype in the "memory" groups *in vivo*. Indeed, Histones H3 and H4 associated with CArG-containing regulatory elements of SM-MHCs (*MYH11*), SM22a (*TAGLN*), and αSMA (*ACTA2*) have been shown to be acetylated (a characteristic of chromatin accessibility) in contractile SMCs, facilitating SRF binding to the CArG box (48). Increased histone acetyltransferase (HAT) activity stimulates SM22a expression whereas increased histone deacetylases (HDACs) prevent SM22a expression (49). Consistently, our pathway analysis using ORA or GSEA, identified significant enrichement of several epigenetic pathways under AngII (such as "HDACs deacetylase histone" (R-MMU-3214815), "HATs acetylate histone" (R-MMU-3214847).

Other modalities of epigenetic regulation may also be at play. H3 histone dimethylation in lysine 4 (H3K4me2) is a marker of differentiated SMCs and is maintained even if SMCs undergo phenotypic modulation (50). DNA demethylation by TET2 increases DNA accessibility to transcription factors resulting in increased SMC differentiation marker expression (51). Of interest, the *ACTA2* promoter was shown to be hypermethylated (a usual mark of repressed expression) in genome-wide methylation studies in human atherosclerotic aortas (52, 53). As we observed sustained downregulation of *Acta2* transcripts in our "memory" condition, an AngII-induced methylation leading to repressive imprinting and phenotypic switch might well be involved. Again, our RNAseq pathway analysis suggests the involvement of epigenetic regulators involved in methylation, such as "PRC2 methylates histone and DNA"(R-MMU-21230) (see **Supplementary Data**, Reactome T1 ORA, Reactome T1 GSEA). In particular, PCR2 complex catalyzes trimethylation of histone H3 on lysine 27 (H3K27me3), a histone mark necessary for maintaining transcriptional repression during multicellular development. Cell type-specific patterns of H3K27me3 are crucial for preserving cell identity (54). Consistent with this analysis, we observed a significant increase in H3K27me3 epigenetic mark in the aortic tissue and, intriguingly, only in both memory conditions (**Figure 5C**). However, the signaling elements involved in this response to AngII remain to be studied in more details.

CONCLUSION

Altogether, our observations support a "memory" effect sustained beyond AngII-induced hypertension and leading to downregulation of specific gene expression, such as *Acta2*, and vascular injury. Future characterization of the underlying AngII-dependent signaling might unveil new targets for its therapeutic modulation and reversal of this adverse legacy effect.

DATA AVAILABILITY STATEMENT

The datasets presented in this study can be found in online repositories. The names of the repository/repositories and accession number(s) can be found below: https://www.ncbi.nlm.nih.gov/geo/query/acc.cgi?acc=GSE175588.

ETHICS STATEMENT

The animal study was reviewed and approved by Institutional Animal Care and Research Advisory Committee of the Université Catholique de Louvain.

AUTHOR CONTRIBUTIONS

LP, CD, and J-LB designed project and experiments. LP wrote manuscript and designed figures under J-LB supervision. J-LB reviewed and corrected, and other authors reviewed and commented. CB performed immunohistochemistry experiments and analysis. LP, BB, and JA performed RNAseq anaylsis (LP: RNA extraction and interactome, BB: pre-analytic and libraries, JA: bioinformatic analysis). LP, RV, DD, HE, CF, and LM performed in *in vivo* and *in vitro* experiments. HE especially for telemetries. All authors contributed to the article and approved the submitted version.

FUNDING

This study was funded by Belgian Fond National de la Recherche Scientifique (FNRS, CDR J.309.21) and Fondation Saint Luc (Grant Pierre de Merre).

ACKNOWLEDGMENTS

We thank M De Beukelaer for its precious assistance throughout immunohistochemistry experiments.

SUPPLEMENTARY MATERIAL

The Supplementary Material for this article can be found online at: https://www.frontiersin.org/articles/10.3389/fcvm.2022.854361/full#supplementary-material

REFERENCES

1. Lawes CM, Vander Hoorn S, Rodgers A. International society of, global burden of blood-pressure-related disease, 2001. *Lancet.* (2008) 371:1513–8. doi: 10.1016/S0140-6736(08)60655-8
2. Guyenet PG. The sympathetic control of blood pressure. *Nat Rev Neurosci.* (2006) 7:335–46. doi: 10.1038/nrn1902
3. Takimoto-Ohnishi E, Murakami K. Renin-angiotensin system research: from molecules to the whole body. *J Physiol Sci.* (2019) 69:581–7. doi: 10.1007/s12576-019-00679-4
4. Forrester SJ, Booz GW, Sigmund CD, Coffman TM, Kawai T, Rizzo V, et al. Angiotensin II signal transduction: an update on mechanisms of physiology and pathophysiology. *Physiol Rev.* (2018) 98:1627–738. doi: 10.1152/physrev.00038.2017
5. Karnik SS, Unal H, Kemp JR, Tirupula KC, Eguchi S, Vanderheyden PM, et al. International union of basic and clinical pharmacology. XCIX. angiotensin receptors: interpreters of pathophysiological angiotensinergic stimuli [corrected]. *Pharmacol Rev.* (2015) 67:754–819. doi: 10.1124/pr.114.010454
6. Carey RM, Siragy HM. Newly recognized components of the renin-angiotensin system: potential roles in cardiovascular and renal regulation. *Endocr Rev.* (2003) 24:261–71. doi: 10.1210/er.2003-0001
7. Owens GK, Kumar MS, Wamhoff BR. Molecular regulation of vascular smooth muscle cell differentiation in development and disease. *Physiol Rev.* (2004) 84:767–801. doi: 10.1152/physrev.00041.2003
8. Mulvihill ER, Jaeger J, Sengupta R, Ruzzo WL, Reimer C, Lukito S, et al. Atherosclerotic plaque smooth muscle cells have a distinct phenotype. *Arterioscler Thromb Vasc Biol.* (2004) 24:1283–9. doi: 10.1161/01.ATV.0000132401.12275.0c
9. Montezano AC, A. Nguyen Dinh Cat, Rios FJ, Touyz RM. Angiotensin II and vascular injury. *Curr Hypertens Rep.* (2014) 16:431. doi: 10.1007/s11906-014-0431-2
10. Ihnat MA, Thorpe JE, Ceriello A. Hypothesis: the 'metabolic memory', the new challenge of diabetes. *Diabet Med.* (2007) 24:582–6. doi: 10.1111/j.1464-5491.2007.02138.x
11. Paneni F, Volpe M, Luscher TF, Cosentino F. SIRT1, p66(Shc), and Set7/9 in vascular hyperglycemic memory: bringing all the strands together. *Diabetes.* (2013) 62:1800–7. doi: 10.2337/db12-1648
12. Villeneuve LM, Reddy MA, Natarajan R. Epigenetics: deciphering its role in diabetes and its chronic complications. *Clin Exp Pharmacol Physiol.* (2011) 38:451–9. doi: 10.1111/j.1440-1681.2011.05497.x
13. Holman RR, Paul SK, Bethel MA, Matthews DR, Neil HA. 10-year follow-up of intensive glucose control in type 2 diabetes. N Engl J Med (2008) 359:1577-89. doi: 10.1056/NEJMoa0806470
14. Diabetes C, I. Complications trial /epidemiology of diabetes, and G. complications study research, intensive diabetes treatment and cardiovascular outcomes in type 1 diabetes: the dcct/edic study 30-year follow-up. *Diabetes Care.* (2016) 39:686–93. doi: 10.2337/dc15-1990
15. Dahlof B, Devereux RB, Kjeldsen SE, Julius S, Beevers G, de Faire U, et al. Cardiovascular morbidity and mortality in the Losartan Intervention For Endpoint reduction in hypertension study (LIFE): a randomised trial against atenolol. *Lancet.* (2002) 359:995–1003. doi: 10.1016/S0140-6736(02)08089-3
16. Wang HX, Yang H, Han QY, Li N, Jiang X, Tian C, et al. NADPH oxidases mediate a cellular "memory" of angiotensin II stress in hypertensive cardiac hypertrophy. *Free Radic Biol Med.* (2013) 65:897–907. doi: 10.1016/j.freeradbiomed.2013.08.179
17. Li WJ, Liu Y, Wang JJ, Zhang YL, Lai S, Xia YL, et al. "Angiotensin II memory" contributes to the development of hypertension and vascular injury via activation of NADPH oxidase. *Life Sci.* (2016) 149:18–24. doi: 10.1016/j.lfs.2016.02.037
18. Makhanova NA, Crowley SD, Griffiths RC, Coffman TM. Gene expression profiles linked to AT1 angiotensin receptors in the kidney. *Physiol Genomics 42A.* (2010) 211-8. doi: 10.1152/physiolgenomics.00063.2010
19. Tsushima K, Osawa T, Yanai H, Nakajima A, Takaoka A, Manabe I, et al. IRF3 regulates cardiac fibrosis but not hypertrophy in mice during angiotensin II-induced hypertension. *FASEB J.* (2011) 25:1531–43. doi: 10.1096/fj.10-174615
20. Rush C, Nyara M, Moxon JV, Trollope A, Cullen B, Golledge J. Whole genome expression analysis within the angiotensin II-apolipoprotein E deficient mouse model of abdominal aortic aneurysm. *BMC Genomics.* (2009) 10:298. doi: 10.1186/1471-2164-10-298
21. Siedlinski M, Nosalski R, Szczepaniak P, Ludwig-Galezowska AH, Mikolajczyk T, Filip M, et al. Vascular transcriptome profiling identifies Sphingosine kinase 1 as a modulator of angiotensin II-induced vascular dysfunction. *Sci Rep.* (2017) 7:44131. doi: 10.1038/srep44131
22. Lv SJ, Ding YN, Pei XY, Zhao X, Hao L, Zhang ZQ, et al. Vascular transcriptome profiling reveals aging-related genes in angiotensin -induced hypertensive mouse aortas. *Chin Med Sci J.* (2020) 35:43–53.

23. Tan N, Zhang Y, Zhang Y, Li L, Zong Y, Han W, et al. Berberine ameliorates vascular dysfunction by a global modulation of lncRNA and mRNA expression profiles in hypertensive mouse aortae. *PLoS ONE.* (2021) 16:e0247621. doi: 10.1371/journal.pone.0247621
24. Desjardins F, Lobysheva I, Pelat M, Gallez B, Feron O, Dessy C, et al. Control of blood pressure variability in caveolin-1-deficient mice: role of nitric oxide identified in vivo through spectral analysis. *Cardiovasc Res.* (2008) 79:527–36. doi: 10.1093/cvr/cvn080
25. Bankhead P, Loughrey MB, Fernandez JA, Dombrowski Y, McArt DG, Dunne PD, et al. QuPath: Open source software for digital pathology image analysis. *Sci Rep.* (2017) 7:16878. doi: 10.1038/s41598-017-17204-5
26. Orjuela S, Huang R, Hembach KM, Robinson MD, Soneson C. ARMOR: An automated reproducible modular workflow for preprocessing and differential analysis of RNA-seq Data. *G3 (Bethesda).* (2019) 9:2089–2096. doi: 10.1534/g3.119.400185
27. S., FastQC: a quality control tool for high throughput sequence data. (2010).
28. Ewels P, Magnusson M, Lundin S, Kaller M. MultiQC: summarize analysis results for multiple tools and samples in a single report. *Bioinformatics.* (2016) 32:3047–8. doi: 10.1093/bioinformatics/btw354
29. Patro R, Duggal G, Love MI, Irizarry RA, Kingsford C. Salmon provides fast and bias-aware quantification of transcript expression. *Nat Methods.* (2017) 14:417–19. doi: 10.1038/nmeth.4197
30. Cunningham F, Achuthan P, Akanni W, Allen J, Amode MR, Armean IM, et al. Ensembl 2019. *Nucleic Acids Res.* (2019) 47:D745–51. doi: 10.1093/nar/gky1113
31. Soneson C, Love MI, Robinson MD. Differential analyses for RNA-seq: transcript-level estimates improve gene-level inferences. *F1000Res.* (2015) 4:1521. doi: 10.12688/f1000research.7563.1
32. Love M, Patro R, Hickey P, Soneson C. TranscriptQuantification import with automatic metadata. R package version1.1.16. *tximeta.* (2019) doi: 10.1371/journal.pcbi.1007664
33. Robinson MD, McCarthy DJ, Smyth GK. edgeR: a Bioconductor package for differential expression analysis of digital gene expression data. *Bioinformatics.* (2010) 26:139–40. doi: 10.1093/bioinformatics/btp616
34. Liao Y, Wang J, Jaehnig EJ, Shi Z, Zhang B. WebGestalt 2019: gene set analysis toolkit with revamped UIs and APIs. *Nucleic Acids Res.* (2019) 47:W199–W205. doi: 10.1093/nar/gkz401
35. Ferrario CM, Cardiac remodelling and RAS inhibition. Ther Adv Cardiovasc Dis (2016) 10:162-71. doi: 10.1177/1753944716642677
36. Ozasa Y, Akazawa H, Qin Y, Tateno K, Ito K, Kudo-Sakamoto Y, et al. Notch activation mediates angiotensin II-induced vascular remodeling by promoting the proliferation and migration of vascular smooth muscle cells. *Hypertens Res.* (2013) 36:859–65. doi: 10.1038/hr.2013.52
37. Moraes JA, Frony AC, Dias AM, Renovato-Martins M, Rodrigues G, Marcinkiewicz C, et al. Alpha1beta1 and integrin-linked kinase interact and modulate angiotensin II effects in vascular smooth muscle cells. *Atherosclerosis.* (2015) 243:477–85. doi: 10.1016/j.atherosclerosis.2015.09.026
38. Mehta PK, Griendling KK. Angiotensin II cell signaling: physiological and pathological effects in the cardiovascular system. *Am J Physiol Cell Physiol.* (2007) 292:C82–97. doi: 10.1152/ajpcell.00287.2006
39. Guo DC, Papke CL, Tran-Fadulu V, Regalado ES, Avidan N, Johnson RJ, et al. Mutations in smooth muscle alpha-actin (ACTA2) cause coronary artery disease, stroke, Moyamoya disease. along with thoracic aortic disease. *Am J Hum Genet.* (2009) 84:617–27. doi: 10.1016/j.ajhg.2009.04.007
40. Milewicz DM, Ostergaard JR, Ala-Kokko LM, Khan N, Grange DK, Mendoza-Londono R, et al. De novo ACTA2 mutation causes a novel syndrome of multisystemic smooth muscle dysfunction. *Am J Med Genet A.* (2010) 152:2437-43. doi: 10.1002/ajmg.a.33657
41. Chen S, Chen H, Zhong Y, Ge Y, Li C, Qiao Z, et al. Insulin-like growth factor-binding protein 3 inhibits angiotensin II-induced aortic smooth muscle cell phenotypic switch and matrix metalloproteinase expression. *Exp Physiol.* (2020) doi: 10.1113/EP088927
42. He X, Deng J, Yu XJ, Yang S, Yang Y, Zang WJ. Activation of m3achr (type 3 muscarinic acetylcholine receptor) and nrf2 (nuclear factor erythroid 2-related factor 2) signaling by choline alleviates vascular smooth muscle cell phenotypic switching and vascular remodeling. *Arterioscler Thromb Vasc Biol.* (2020) 40:2649–64. doi: 10.1161/ATVBAHA.120.315146
43. Spin JM, Hsu M, Azuma J, Tedesco MM, Deng A, Dyer JS, et al. Transcriptional profiling and network analysis of the murine angiotensin II-induced abdominal aortic aneurysm. *Physiol Genomics.* (2011) 43:993–1003. doi: 10.1152/physiolgenomics.00044.2011
44. Togashi N, Maeda T, Yoshida H, Koyama M, Tanaka M, Furuhashi M, et al. Angiotensin II receptor activation in youth triggers persistent insulin resistance and hypertension–a legacy effect? *Hypertens Res.* (2012) 35:334–40. doi: 10.1038/hr.2011.206
45. Liu M, Gomez D. Smooth Muscle Cell Phenotypic Diversity. *Arterioscler Thromb Vasc Biol.* (2019) 39:1715–23. doi: 10.1161/ATVBAHA.119.312131
46. Allahverdian S, Chaabane C, Boukais K, Francis GA, Bochaton-Piallat ML. Smooth muscle cell fate and plasticity in atherosclerosis. *Cardiovasc Res.* (2018) 114:540–50. doi: 10.1093/cvr/cvy022
47. Lu W, Zhou Y, Zeng S, Zhong L, Zhou S, Song H, et al. Loss of FoxO3a prevents aortic aneurysm formation through maintenance of VSMC homeostasis. *Cell Death Dis.* (2021) 12:378. doi: 10.1038/s41419-021-03659-y
48. McDonald OG, Wamhoff BR, Hoofnagle MH, Owens GK. Control of SRF binding to CArG box chromatin regulates smooth muscle gene expression in vivo. *J Clin Invest.* (2006) 116:36–48. doi: 10.1172/JCI26505
49. Gomez D, Swiatlowska P, Owens GK. Epigenetic control of smooth muscle cell identity and lineage memory. *Arterioscler Thromb Vasc Biol.* (2015) 35:2508–16. doi: 10.1161/ATVBAHA.115.305044
50. Alexander MR, Owens GK. Epigenetic control of smooth muscle cell differentiation and phenotypic switching in vascular development and disease. *Annu Rev Physiol.* (2012) 74:13–40. doi: 10.1146/annurev-physiol-012110-142315
51. Liu R, Jin Y, Tang WH, Qin L, Zhang X, Tellides G, et al. Ten-eleven translocation-2 (TET2) is a master regulator of smooth muscle cell plasticity. *Circulation.* (2013) 128:2047–57. doi: 10.1161/CIRCULATIONAHA.113.002887
52. Lacey M, Baribault C, Ehrlich KC, Ehrlich M. Atherosclerosis-associated differentially methylated regions can reflect the disease phenotype and are often at enhancers. *Atherosclerosis.* (2019) 280:183–91. doi: 10.1016/j.atherosclerosis.2018.11.031
53. Lacey M, Baribault C, Ehrlich KC, Ehrlich M. Data showing atherosclerosis-associated differentially methylated regions are often at enhancers. *Data Brief.* (2019) 23:103812. doi: 10.1016/j.dib.2019.103812
54. Holoch D, Margueron R. Mechanisms regulating prc2 recruitment and enzymatic activity. *Trends Biochem Sci.* (2017) 42:531–42. doi: 10.1016/j.tibs.2017.04.003

Conflict of Interest: The authors declare that the research was conducted in the absence of any commercial or financial relationships that could be construed as a potential conflict of interest.

Publisher's Note: All claims expressed in this article are solely those of the authors and do not necessarily represent those of their affiliated organizations, or those of the publisher, the editors and the reviewers. Any product that may be evaluated in this article, or claim that may be made by its manufacturer, is not guaranteed or endorsed by the publisher.

frontiers | Frontiers in Cardiovascular Medicine

REVIEW
published: 07 April 2022
doi: 10.3389/fcvm.2022.866957

Closed-Loop Vagus Nerve Stimulation for the Treatment of Cardiovascular Diseases: State of the Art and Future Directions

*Matteo Maria Ottaviani[1,2], Fabio Vallone[2], Silvestro Micera[2,3] and Fabio A. Recchia[1,4,5]**

[1] Institute of Life Sciences, Scuola Superiore Sant'Anna, Pisa, Italy, [2] Department of Excellence in Robotics and Artificial Intelligence, The BioRobotics Institute, Scuola Superiore Sant'Anna, Pisa, Italy, [3] Bertarelli Foundation Chair in Translational Neural Engineering, Center for Neuroprosthetics, Institute of Bioengineering, Ecole Polytechnique Federale de Lausanne, Lausanne, Switzerland, [4] Fondazione Toscana Gabriele Monasterio, Pisa, Italy, [5] Department of Physiology, Cardiovascular Research Center, Lewis Katz School of Medicine at Temple University, Philadelphia, PA, United States

The autonomic nervous system exerts a fine beat-to-beat regulation of cardiovascular functions and is consequently involved in the onset and progression of many cardiovascular diseases (CVDs). Selective neuromodulation of the brain-heart axis with advanced neurotechnologies is an emerging approach to corroborate CVDs treatment when classical pharmacological agents show limited effectiveness. The vagus nerve is a major component of the cardiac neuroaxis, and vagus nerve stimulation (VNS) is a promising application to restore autonomic function under various pathological conditions. VNS has led to encouraging results in animal models of CVDs, but its translation to clinical practice has not been equally successful, calling for more investigation to optimize this technique. Herein we reviewed the state of the art of VNS for CVDs and discuss avenues for therapeutic optimization. Firstly, we provided a succinct description of cardiac vagal innervation anatomy and physiology and principles of VNS. Then, we examined the main clinical applications of VNS in CVDs and the related open challenges. Finally, we presented preclinical studies that aim at overcoming VNS limitations through optimization of anatomical targets, development of novel neural interface technologies, and design of efficient VNS closed-loop protocols.

Keywords: autonomic nervous system, vagus nerve stimulation, cardiovascular diseases, neural decoding, closed-loop

OPEN ACCESS

Edited by:
Deborah Hunt,
Mercy College, United States

Reviewed by:
Ankit Gilani,
Cornell University, United States
Charles C. Horn,
University of Pittsburgh, United States

***Correspondence:**
Fabio A. Recchia
fabio.recchia@santannapisa.it

Specialty section:
This article was submitted to Hypertension, a section of the journal Frontiers in Cardiovascular Medicine

Received: *31 January 2022*
Accepted: *14 March 2022*
Published: *07 April 2022*

Citation:
Ottaviani MM, Vallone F, Micera S and Recchia FA (2022) Closed-Loop Vagus Nerve Stimulation for the Treatment of Cardiovascular Diseases: State of the Art and Future Directions. Front. Cardiovasc. Med. 9:866957. doi: 10.3389/fcvm.2022.866957

INTRODUCTION

Cardiovascular diseases (CVDs) still represent a major disease burden worldwide, despite advances in pharmacological treatments (1). Therefore, new therapeutical strategies are currently being investigated as an alternative to classical schemes. Among those, the solutions offered by Bioelectronic Medicine (BM) (2–5)—a new, highly interdisciplinary field incorporating neuroscience, engineering, and molecular medicine (4, 6)—are emerging as appealing candidates. The development of BM was inspired by the growing comprehension of the autonomic nervous system (ANS), which plays a key role in the control of whole-body homeostasis. Dysfunctions

of the ANS are consequently implicated in the development and progression of many diseases, including those affecting the cardiovascular system (4, 7–13). BM utilizes this body of knowledge as a reference for the design of implantable devices (5) that modulate signals of the peripheral nervous system to visceral organs for therapeutic purposes (14–16).

The neural control of cardiovascular functions involves multiple interactions among central and peripheral components of the so-called "cardiac neuraxis" (17), which comprises the intrinsic cardiac nervous system, vagus nerves (VNs), intrathoracic sympathetic ganglia, spinal cord, brain stem, and multiple central regions up to the insular cortex. Acting together, these hierarchically organized functional units coordinate and regulate cardiac activity to preserve an adequate match between cardiac output and blood flow demand (18). Autonomic dysregulation at various levels of the cardiac neuroaxis, from central nuclei to peripheral effectors, is now recognized as a fundamental contributor to the progression of CVDs (1, 19). For instance, altered neural signals, such as the pathological activation of cardiac afferent neurons by acute myocardial ischemia and reperfusion, induce maladaptive responses such as sympathetic overdrive and parasympathetic withdrawal (autonomic imbalance) that in turn contribute to the development of systemic cardiovascular alterations (1, 19, 20). Therefore, the selective modulation of the cardiac neuraxis to achieve targeted control of cardiovascular functions has been proposed as a potentially impactful application of BM (21, 22). Peripheral nerves and ganglia of the ANS are attractive targets for BM for their favorable location for surgical interventions compared with deep and anatomically less characterized ANS centers of the CNS like the periaqueductal gray matter of the midbrain or hypothalamic nuclei (11, 23). In this perspective, the most widely studied intervention is represented by the electrical stimulation of the VN (VNS) (24, 25).

The VN (or X cranial nerve) is a paired asymmetric and the most extensively distributed nerve in the body, as well as a major component of the cardiac neuraxis (26). Sensory signaling through the VN plays a critical role in maintaining homeostasis of feeding, digestion, respiration, and cardiovascular functions (27). For this reason, VN neuromodulation is being tested as a potential therapeutical strategy for many pathological conditions, including CVDs (28). However, despite promising results achieved in preclinical studies (29), VNS is accompanied by side effects and still needs to be optimized for better exploitation of its full potential in the clinical setting. Herein we will review the state of the art of VNS for CVDs and discuss the current perspectives of VNS optimization. First, we will summarize the anatomy and physiology of the cardiac vagal system; then, we will describe the principles of VNS for CVDs and its main clinical applications, with related open challenges. Finally, we will review preclinical studies aimed at overcoming VNS limitations through optimization of anatomical targets, development of novel neural interface technologies, and design of efficient VNS closed-loop protocols. In the latter case, we will particularly focus on neural decoding strategies that aim at the identification of timely- and spatially selective feedback signals to drive VNS for CVDs properly (8, 30–32).

ANATOMY AND PHYSIOLOGY OF VAGUS NERVE IN THE CARDIOVASCULAR SYSTEM

Gross Anatomy

The VN originates bilaterally in the medulla as multiple filaments that extend toward the jugular foramen and then converge to form a single trunk. Within or just caudal to the jugular foramen are located the superior (jugular) and inferior (nodose) ganglia of the VN (**Figure 1A**) (26). At its emergence from the nodose ganglion, the VN can be anatomically divided into three segments along the rostro-caudal direction: cervical, thoracic and abdominal (26). The cervical VN generates multiple branches, including the superior cardiac and aortic branches (**Figure 1A**) (26, 33–36). Leaving the carotid sheath at the neck base, the VN enters the thorax, and it is referred to as the thoracic VN. Vagal cardiac branches include the superior and inferior cervical cardiac branches and the inferior or thoracic cardiac branch that originates from the thoracic VN (**Figures 1A,B**) (26, 37). The aortic branch or depressor nerve from the left VN contains afferent fibers innervating the aortic arch, while the one from the right VN innervates the bifurcation of the right brachio-cephalic trunk (35, 38). Within the mediastinum, the thoracic VN provides thoracic cardiac branches that are mainly observed between the aortic arch and the pulmonary arterial trunk and innervate the heart along the coronary arteries (37). Together with cardiac nerves from the sympathetic trunk, they contribute to form the cardiac plexus, which is usually divided into a superficial and a deep portion (**Figure 1B**). From a functional perspective, the right-sided nerves innervate mostly the sinoatrial node, while the left-sided nerves innervate mostly the atrioventricular node (36).

Microscopic Anatomy

Similar to other peripheral nerves, vagal fibers are grouped into a variable number of fascicles (39) with high variability among different species and even within the same species (40, 41). Several studies in human cadavers found the mean fascicles number of the cervical VN to oscillate between 5 and 10 (33, 40, 42, 43). The cervical VN in mice, rats, canines and non-human primates displays a less complex fascicular organization than in humans, typically consisting of 1–2 fascicles (43, 44). The porcine VN displays more fascicles than the human, containing 46 ± 10 and 43 ± 8 bundles at cervical and abdominal level, respectively (43, 44). In the somatic nervous system, all fascicles seem to conform a somatotopic organization (45, 46) and whether this occurs also in the ANS needs still to be assessed even if it is highly possible in complex nerves such as the VN (47). In fact, Settell et al. described a distinct bimodal organization of fascicles in the pig cervical VN. Specifically, they observed pseudounipolar cells aggregated in a large "fascicle" in nodose ganglion cross-sections and found a distinct group of fascicles arising from that large "fascicle" in caudal cross-sections of the cervical VN (**Figure 2**). This distinct organization of fascicles disappeared beyond the recurrent laryngeal nerve branching point; thus, they were identified as fascicles pertaining to the recurrent laryngeal

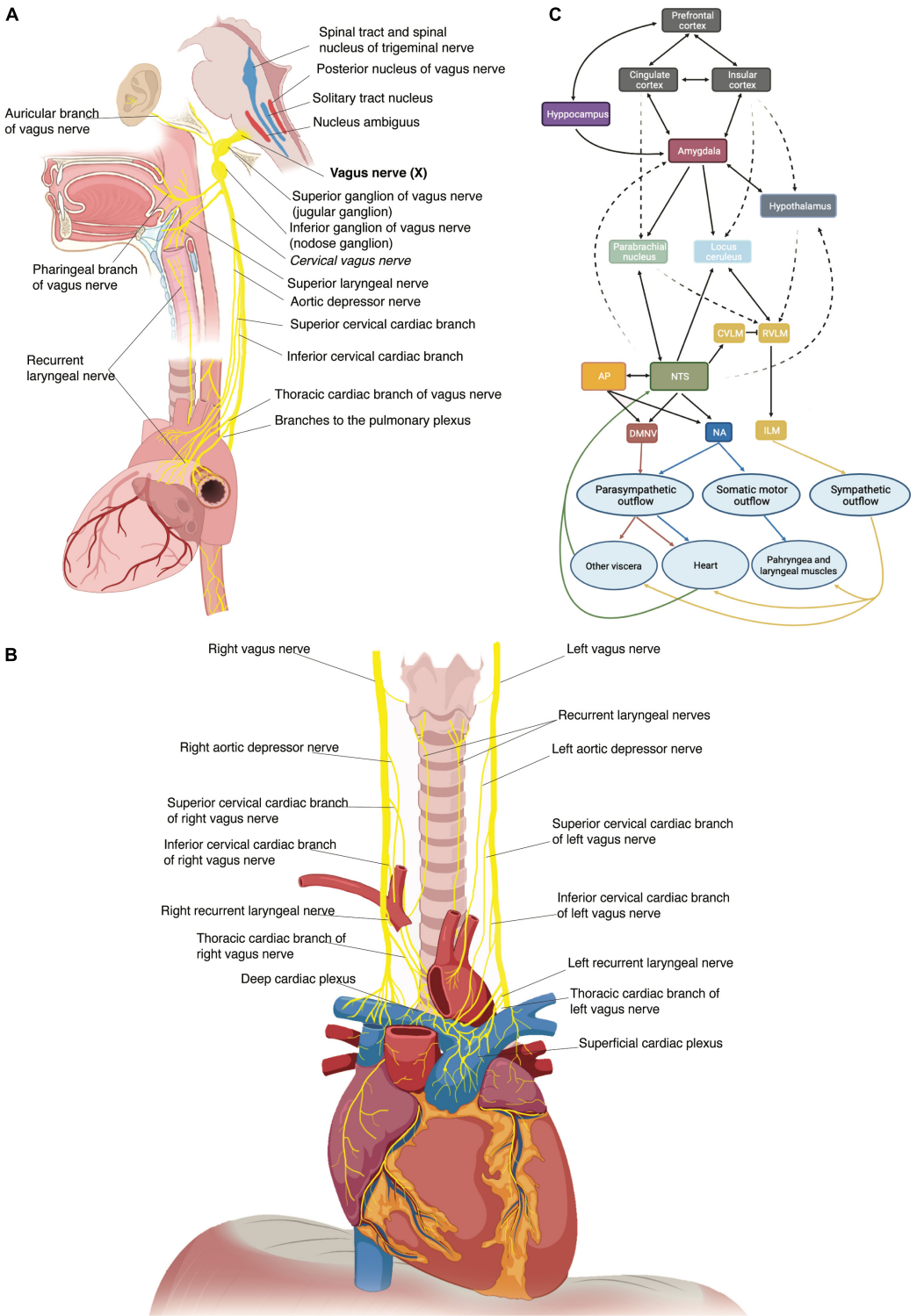

FIGURE 1 | (A) Schematic representation of the origin of the vagus nerve from the medulla, its ganglia and its major branches at the cervical and thoracic levels. **(B)** Thoracic vagus nerves with cervical and thoracic cardiac branches to the deep and superficial cardiac plexi and recurrent laryngeal nerves. **(C)** Schematic representation of the central autonomic network with internuclei connections. An autonomic vagovagal loop comprises visceral inputs to the nucleus tractus solitarii (NTS) which then sends outputs to the dorsal motor nucleus (DMNV), rostral ventrolateral medullary (RVLM), and intermediate lateral medulla (ILM) to adapt autonomic balance to physiological demands. The cross-talk between the NTS and brain regions (hypothalamus, amygdala, cingulate cortex, insula, prefrontal cortex) engaged in neuroendocrine, affective, and cognitive regulation of behavior modulates this autonomic forebrain loop. AP, area postrema; NA, nucleus accumbens.

nerve, separately from those coming from other visceral organs (**Figure 2**) (44). The precise distribution of fibers from the other visceral organs, especially fibers from peripheral cardiovascular targets, remains a matter of study, along with the definition of VN anatomical-functional models to guide the design of future VNS devices and protocols (48).

The VN is a mixed nerve with fibers carrying sensory, motor, and visceral information. It entails mostly afferent nerve fibers (80–90%) with fewer efferent fibers (10–20%) in the majority of mammalian species (26, 49). VN fibers are classified as "A-fibers," "B-fibers" and "C-fibers" in accordance with the classical Erlanger/Gasser classification (50). Among the afferents, C-fibers are thin unmyelinated, Aδ-fibers are thin myelinated and Aβ-fibers are thicker myelinated. Among the efferents, Aα-fibers are the thickest myelinated axons of α-motoneurons that innervate pharyngeal and laryngeal muscles, while B-fibers are tiny, myelinated and carry parasympathetic inputs to visceral organs (51, 52). The diameters of the unmyelinated and myelinated fibers of the VN are in the range of 0.25–1.0 μm and 1–4 μm, respectively, in most animal species (53). Nearly all the large (above 10 μm) and 40–50% of the small (below 4μm) myelinated fibers are efferent (49).

Preganglionic parasympathetic fibers originate from the dorsal motor nucleus of the vagus in the brain stem, branch out of the VN main trunk to join several autonomic plexuses and synapse at cell bodies of postganglionic neurons, generally located in the wall of the target organ. Afferent fibers consist of the T-shaped axons of pseudounipolar sensory neurons, with their neuronal soma residing in the nodose and jugular ganglia (52–54). In the brainstem, central processes of jugular ganglion neurons project to the trigeminal nucleus through the spinal trigeminal tract (26), while the primary relay of vagal visceral inputs from nodose ganglion neurons is the nucleus tractus solitarii in the medulla (55, 56). The nucleus tractus solitarii has direct and indirect connections with a wide range of neural structures, thus endowing the VN with the control of a broad array of processes (**Figure 1C**) (55, 57, 58). An autonomic vagovagal loop encompasses visceral inputs to secondary neurons in the nucleus tractus solitarii, which then contact efferent neurons of the dorsal motor nucleus and sympathetic neurons of the

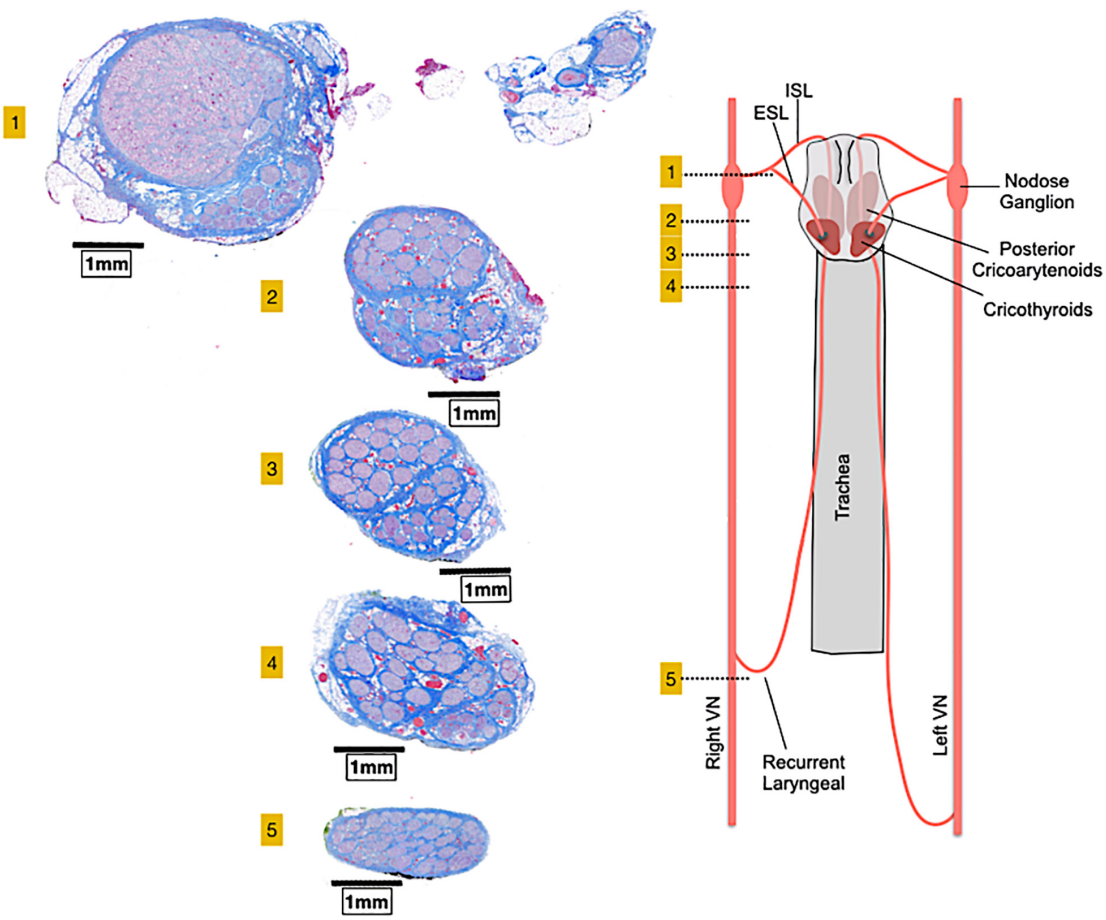

FIGURE 2 | A bimodal arrangement, or vagotopy, can be observed in histological sections collected at various levels along the pig vagus nerve. Section 1 comprises the nodose ganglion and the superior laryngeal branch and show pseudo-unipolar cells grouped in a huge "fascicle" from which arises a smaller group of fascicles in sections 2, 3, and 4. Caudally to the recurrent laryngeal nerve (section 5), the bimodal architecture is no longer visible. ESL, external superior laryngeal nerve; ISL, internal superior laryngeal nerve, VN, vagus nerve. Adapted from Settell et al. (44).

rostral ventrolateral medulla to adapt the autonomic balance to physiological demands (**Figure 1C**) (3).

Vagal Baroreceptors and Chemoreceptors

Vagal sensory neurons densely innervate great thoracic vessels and they include Piezo2 + /TTN3 + mechanosensory fibers, functioning as baroreceptors, and chemosensory fibers that detect arterial blood gas changes in the aortic bodies (**Figure 3**) (59). Afferent fibers from the left nodose ganglion innervate the apex of the aortic arch, while afferents from the right nodose ganglion innervate the right subclavian artery, near its branching from the innominate artery. These fibers run within the aortic depressor nerves forming fascicles that include both high-threshold mechanosensory and chemosensory afferents (59). The majority of vagal baroreceptors are myelinated fibers that convey information on stretch magnitude, pulse frequency and mean arterial pressure (59, 60) and, together with the carotid sinus innervated by the glossopharyngeal nerve, they represent the afferent arm of the arterial baroreflex (61–63).

Vagal Cardiac Receptors

The VN provides both sensory and parasympathetic innervation to the heart *via* cardiac branches. Nodose neurons terminate with chemoreceptors and/or low-threshold mechanoreceptors in cardiac atria, ventricles, and major veins (**Figure 3**). Under normal circumstances, cardiac receptors are necessary for fine-tuning of the cardiovascular system. In CVDs like heart failure (HF), sensory endings undergo pathological activation that causes autonomic imbalance, with sympathetic excitation prevailing over vagal excitation (21, 22, 64).

There are at least two different types of atrial receptors belonging to the VN system of several mammalian species: type B receptors, that fire in response to increased volume (stretch receptors), and type A, that respond to atrial contraction. Both receptor endings correspond to slightly myelinated/unmyelinated fibers located mainly in the endocardium at the pulmonary veins-atrium and caval-atrium junctions and, to a lesser extent, in the free wall and appendage of both atria (65). They function as slowly adapting stretch receptors with low-frequency firing (66). Other vagal afferent fibers from the atria are unmyelinated C-fibers with a diffuse distribution and activity patterns similar to those described for type A or type B receptors (64).

Two types of sensory vagal endings have been described in both cardiac ventricles: myocardial and epicardial receptors (**Figure 3**). Myelinated myocardial receptors are mechanosensitive fibers working as tension/pressure-sensitive receptors and fire at the onset of left ventricular contraction (59, 64). On the other hand, unmyelinated myocardial receptors include 5-HT3R + C-fibers, predominantly functioning as mechanoreceptors (**Figure 3**) (64, 67), and C-fibers predominantly functioning as chemoreceptors which transduce the pain sensation that characterizes angina pectoris (21). Finally, vagal afferent fibers innervating the parietal pericardium are finely myelinated and sensitive to pericardium distension (64).

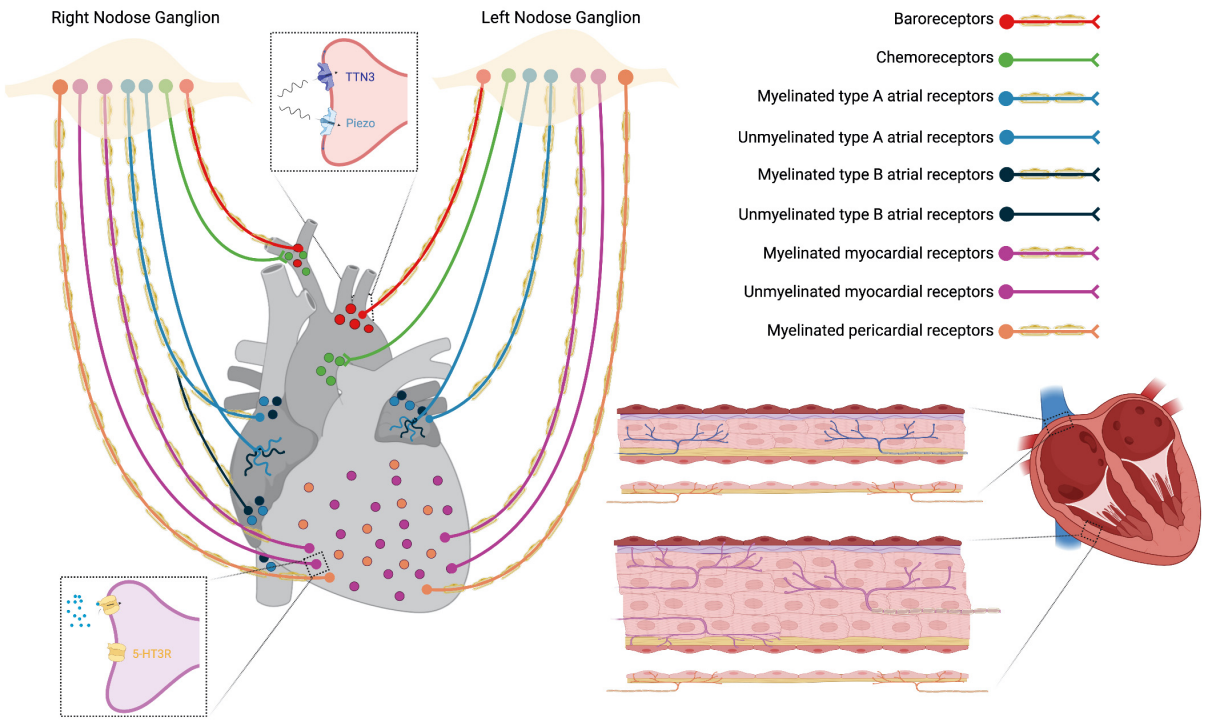

FIGURE 3 | Schematic representation of thoracic cardiovascular afferent fibers running in the vagus nerve. Insets: top, baroreceptors Piezo2 + and TTN3 + terminals; down, unmyelinated 5-HT3R + myocardial receptors.

Vagal Cardiac Efferent Fibers

The VN provides parasympathetic innervation to the heart *via* preganglionic cardioinhibitory neurons mainly located in the nucleus accumbens and to a lesser extent in the caudal dorsal motor nucleus of the vagus (21). Neurons of the nucleus accumbens possess thin myelinated axons with a diameter comprised in the B-fibers range (conduction velocity range 3–15 m/s) (68, 69) and exert strong respiratory- and cardio-modulatory and chronotropic effects. Efferent fibers from the nucleus accumbens of the right VN synapse with postganglionic cholinergic neurons that innervate the sino-atrial node, while fibers of the left VN project to postganglionic cholinergic neurons that innervate the atrioventricular node (21, 63). In contrast, neurons of the dorsal motor nucleus have unmyelinated axons, show little or no respiratory and cardiac modulation, exert smaller effects on HR and possibly stronger dromotropic and inotropic effects, as they project to postganglionic neurons innervating the left ventricle (70, 71). Cardiac neural control is realized *via* tonic interaction between sympathetic and parasympathetic limbs of the ANS, particularly in the mammalian heart, where many terminal fibers lie close to each other and exert reciprocal inhibitory effects at the synaptic level (21, 22, 72).

VAGUS NERVE STIMULATION FOR CARDIOVASCULAR DISEASES

Vagus nerve stimulation was first developed for the treatment of drug-resistant epilepsy and depression, obtaining FDA approval in 1994 (73–77) and 2005 (24, 78–81), respectively. Based on prior animal experiments, the first clinical studies defined the therapeutic range of VNS, the algorithm for stimulation titration up to the threshold of patient tolerance, and the safety and tolerability profile (73, 82). With the discovery of the inflammatory reflex in the early 2000s (83) and the evidence that VNS could attenuate inflammation normalizing the expression of proinflammatory cytokines (such as TNF-α and IL-6), VNS studies increased exponentially (28). At present, research labs worldwide are studying the effects of VNS in a multitude of conditions, spanning from neurological to inflammatory disorders, both in animal models and in patients (84).

The VN can be stimulated in different ways and at different levels. The classical VNS consists in an invasive procedure that is performed as a day case procedure under general anesthesia. The FDA-approved VNS device comprises a spiral anchor and two bipolar helical electrodes with a platinum ribbon functioning as an anode and a cathode. They wrap approximately 270° around the left cervical VN, below the origin of the superior and inferior cervical cardiac branches, and are connected *via* a cable tunneled subcutaneously to a pulse generator that is most commonly positioned in a infra-clavicular pocket (24, 85–90). Despite the fact that VNS is a minimally invasive treatment, surgery remains inherently risky and comes with a number of possible side effects (91, 92). Therefore, alternative non-surgical methods have been developed, such as cervical non-invasive or transcutaneous VNS directed to the auricular branch of the VN (**Figure 4**) (91, 93–95). In the current standard practice, VNS parameters are set individually and tuned periodically for each patient. An "adequate" stimulation is generally set between a minimum level of perception by the patient to a maximum level

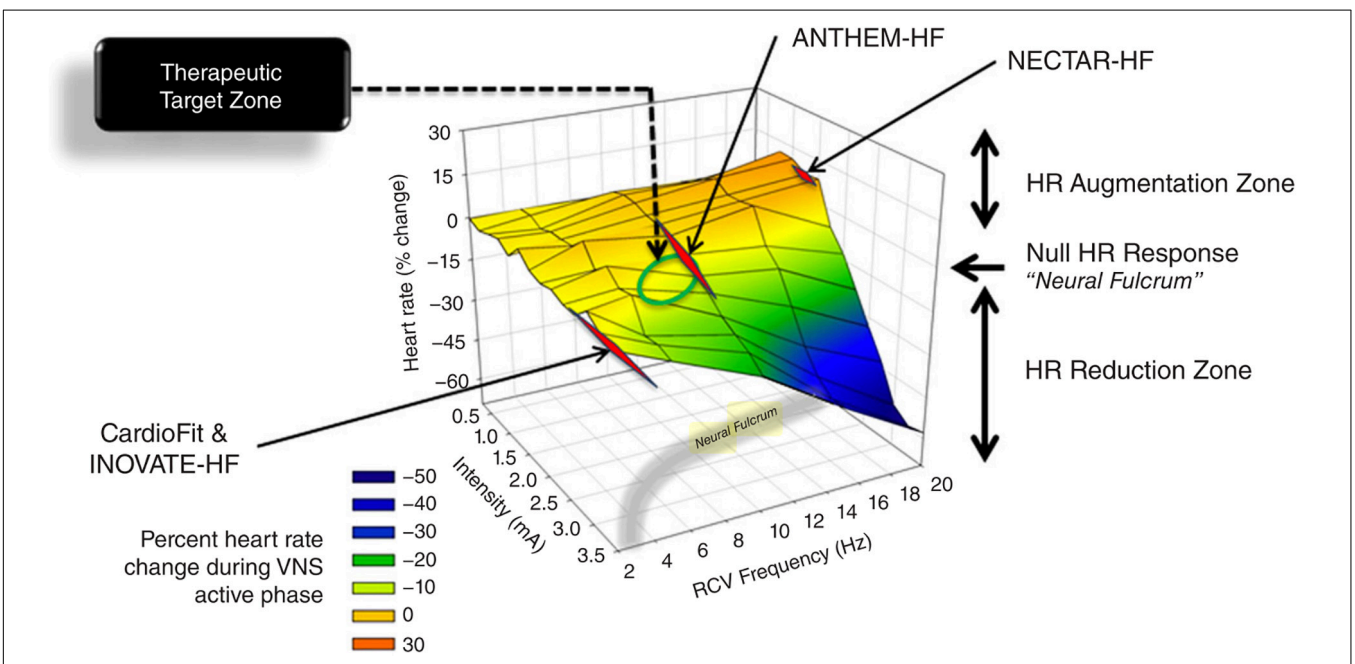

FIGURE 4 | 3D plot of percent change in heart rate against right VNS intensity and frequency, with representation of the neural fulcrum in the yellow-shaded region. Operational points used in the NECTAR-HF, INOVATE-HF, and the ANTHEM-HF studies. Adapted from Ardell et al. (17).

of intolerability due to side effects, both of which are subjective and variable (96).

Vagus Nerve Stimulation Mechanisms on the Cardiovascular System and Cardiovascular Diseases

Vagus nerve stimulation impacts cardiovascular control at multiple levels (97) *via* activation of afferent and efferent pathways and, depending on the frequency, pulse-width, and current intensity, of diverse fibers populations (43, 98).

In general, VNS of efferent cardiac fibers causes a reduction in heart rate (negative chronotropic effect on the sinoatrial node), in atrioventricular conduction (negative dromotropic effect on the atrioventricular node), and in ventricular contractility (negative inotropic effect on ventricular myocardium) (28, 99), with right VNS having mostly chronotropic effects while left VNS mostly dromotropic effects (100). VNS modulates left ventricular function increasing both action potential duration and the effective refractory period, either of which decreases intracellular calcium and ventricular contractility and wall motion (28, 89, 101). Activation of descending efferent projections can also mitigate sympathoexcitation *via* neural interactions within the intrinsic cardiac nervous system, modulate cardio-cardiac reflexes, and impart cardioprotection *via* direct effects on cardiomyocytes (1).

Vagus nerve stimulation of afferent fibers can impact central reflexes, including those that involve sympathetic and parasympathetic efferent outflows to the heart (1). For instance, VNS of vagal baroreceptors reflexively activates vagal cardioinhibitory efferent fibers to reduce heart rate and concurrently inhibits sympathetic efferent activity and down-regulates the renin-angiotensin-aldosterone system (28, 102).

Vagus nerve stimulation effects demonstrated beneficial effects in different animal models of CVDs. First of all, VNS has shown antiarrhythmic effects in several conditions, probably *via* multifactorial mechanisms that include a decrease in heart rate, the release of nitric oxide, anti-inflammatory effects, and antagonism of the sympathetic nervous system (28, 103). It was shown that VNS increases the threshold for ventricular arrhythmias *via* reduction in ventricular excitability and repolarization heterogeneity (effect on ventricular conduction system) (28, 99). In animal models of atrial fibrillation, VNS exhibited antifibrillatory effects by shortening atrial fibrillation duration and prolonging the atrial fibrillation cycle length (19, 28). Moreover, a VNS delivered below the threshold of bradycardia induction can effectively suppress atrial fibrillation in anesthetized dogs (89). VNS effects on the sympathetic nervous system contribute to the prevention of arrhythmias also during cardiopulmonary resuscitation (28). VNS-induced decrease in cardiac motion reduces cardiac metabolic demands during the vulnerable period of ventricular fibrillation, making VNS a potential intervention to improve the efficacy of defibrillation (101).

Vagus nerve stimulation was also shown to decrease infarct size and to halt post-myocardial infarction phenomena such as the remodeling of both the myocytes and the intrinsic cardiac neuronal system. These cardioprotective mechanisms include anti-inflammatory effects, prevention of Connexin 40 and Connexin 43 loss, antioxidative effects, and antiapoptotic effects such as decrease in cytochrome *c* release and in the proapoptotic Bcl-2-associated X protein levels (28, 89, 103–106). When applied during myocardial reperfusion, VNS was shown to improve ventricular function and reduce arrhythmic episodes *via* antagonization of the cardiac sympathetic outflow, reduction of reactive oxygen species and of ventricular excitability (28, 103–106). VNS improves left ventricular ejection fraction post-myocardial infarction restoring subcellular levels of calcium-binding proteins (such as SERCA2a, NCX1, and PLB) and can reestablish baroreceptor reflex to the pre-infarction baseline (28).

Vagus nerve stimulation can slow the progression of myocardial remodeling and atrial and ventricular dysfunction in animal models of chronic HF with reduced ejection fraction (28). VNS beneficial effects in HF can be attributed to improvements in left ventricular mechanics, attenuation of the sympathetic drive, down-regulation of the renin-angiotensin-aldosterone system, reduction of proinflammatory cytokines, normalization of the nitric oxide pathway, increase in myocardial expression of gap junction proteins and capillary density and tempering of myocardial interstitial fibrosis (1, 28, 104, 106–113). Optogenetic stimulation of cardioinhibitory neurons in the dorsal motor nucleus of the vagus can reduce myocardial expression of G-protein-coupled receptor kinase 2 (GRK2) and b-arrestin 2, which both contribute to the progressive decline of myocardial contractile function in HF (104).

Vagus nerve stimulation can ameliorate poststroke recovery *via* enhancement of motor cortex plasticity during rehabilitation, likely favoring the release of acetylcholine, norepinephrine, GABA, and brain-derived neurotrophic factor (28). VNS can also attenuate cerebral edema after brain injury by reducing cerebral blood flow, glutamate excitotoxicity, and inflammation (28).

Finally, VNS in hypertensive rats showed a significant blood pressure reduction, with static stimulation clinically more effective than pulsatile stimulation (28).

Vagus Nerve Stimulation in the Clinical Scenario

To date, despite the vast assortment of CVDs investigated in the pre-clinical scenario, VNS clinical applications in the cardiovascular field have been mostly focused on HF. This syndrome provides a strong rationale for ANS modulation, as its genesis and progression are heavily influenced by autonomic imbalance (21, 22, 114, 115). Preclinical studies have shown that VNS can exert very positive effects on the progression of HF, but clinical trials failed to achieve the same results. Complete clinical trials of VNS for HF with reduced ejection fraction include two randomized controlled trials, i.e., the INOVATE-HF (116) and the NECTAR-HF (117), and two open-label studies, i.e., the ANTHEM-HF (118) and the study by De Ferrari et al. (119). In the study by De Ferrari et al. (119) and in the INOVATE-HF, VNS was delivered using the CardioFit system that senses heart rate (*via* an intracardiac electrode) and delivers asymmetric stimulation at a variable delay (70–325 ms) from the R-wave

(85, 87, 119, 120). The stimulation lead is an asymmetric bipolar multi-contact cuff electrode specifically designed for cathodic induction of action potentials while simultaneously applying asymmetrical anodal blocks, thereby reducing the activation of A-fibers while preferentially activating efferent B-fibers (85, 87, 105). In the NECTAR-HF (117) and the ANTHEM-HF (118) trials the investigators utilized the Boston Scientific VNS device that activates VN fibers bidirectionally with no synchronization with the cardiac cycle (118). All trials recruited similar NYHA class II-III patients with reduced left ventricular ejection fraction and receiving optimal medical therapy (121). These trials did not raise safety issues but showed variable efficacy (116, 118, 121, 122). As highlighted by a recent meta-analysis, these trials showed significant improvement in the functional NYHA class, quality of life, 6-min walking test, and NT-proBNP levels, but VNS did not have any impact on mortality (123). The subjective measures that improved in all trials should be cautiously taken as subjects were not totally blind to the therapeutic procedures, notwithstanding the sham-controlled design (116, 118, 124). Only the two uncontrolled studies (ANTHEM-HF and the study by De Ferrari et al.) showed a positive effect of VNS on cardiac remodeling (118, 119), despite the success of preclinical experiments (118, 120). These trials employed diverse stimulation parameters, and subsequent analyses showed that the ANTHEM-HF study was the only one to achieve the therapeutic stimulation corresponding to the "neural fulcrum" (17). The neural fulcrum is defined as the combination of VNS parameters such as frequency–amplitude–pulse width that results in no heart rate response (**Figure 4**), and it corresponds to a dynamic equilibrium where VNS activates cardiac neural circuits while keeping reflex control of cardiovascular functions. In fact, VNS normally modifies cardiac neural circuits pushing them in one direction that tends to be physiologically counterbalanced by cardiovascular reflexes (17). For instance, low intensity/high frequency (20 Hz or more) stimulation preferentially activates afferent fibers causing tachycardia that leads to secondary activation of both central pathways and vagovagal, vagosympathetic, or vagoadrenal reflexes. On the other hand, higher intensity/lower frequency (10–15 Hz) stimulation activates parasympathetic neurons resulting in bradycardia and mitigation of sympatho-excitation *via* neural interactions within the intrinsic cardiac nervous system (1). Finally, low intensity/very low frequencies (1–2 Hz) stimulation determines little to no cardiomotor effects, as the afferent-driven decreases in central parasympathetic outflow are equivalently counteracted by direct activation of cardiac parasympathetic neurons (125).

ANTHEM-HF utilized the principle of neural fulcrum by determining the autonomic engagement *via* an automatic beat-to-beat pattern analysis throughout the initial phase of VNS titration (122). In the NECTAR-HF trial, the high frequency stimulation provoked patients intolerance and impeded titration to a therapeutic dose; in the INOVATE-HF study, not all patients received adequate stimulation levels (116, 121, 122, 126–128). On the basis of the results of ANTHEM-HF, a large, randomized, controlled trial of right VNS with the use of the same system is now underway (ANTHEM-HFrEF PIVOTAL trial, NCT03425422) (18), along with a novel study in patients suffering from HF with preserved and mid-range ejection fraction (127).

Unresolved Issues in Clinical Vagus Nerve Stimulation for Cardiovascular Diseases

The exploitation of VNS full potential and its transformation into a simple and cost-effective therapy for a wide range of conditions requires the completion of some major steps. A general problem is the still limited knowledge of VN function, with an ensuing lack of understanding of the mechanisms responsible for already established VNS treatments of diseases such as drug-resistant epilepsy (121, 126, 129). Consequently, optimum stimulation parameters tailored for patient-specific clinical characteristics and precise timing remain a matter of debate (74, 75, 79, 128, 129). VNS is normally up-titrated through a series of follow-up visits until a therapeutic dosage is attained without adverse effects and up to the tolerance threshold of the patients (73, 94). Given subjectivity of patients' tolerance and the uniqueness of the electrode-nerve interface, no standard therapeutic dose exist, the effectiveness of parameters adjustment during titration remains dubious, and the response prediction uncertain (92, 121, 122, 129, 130).

Another related problem is the definition of the target population using adequate "predictors" to discriminate between responders and non-responders. These predictors could be markers of autonomic imbalance represented by physiological parameters such as heart rate variability or innovative markers such as those derived from neural decoding of specific ANS circuits (78, 118, 129, 131).

While technology advances at a quick pace, neuromodulation's ultimate potential can be realized when the relationship between nerve activity and physiological function is thoroughly known (4, 6), thus allowing translation of biological information into appropriate engineering specifications (16, 132). The knowledge gap of vagal physiology, functional anatomy and neuromodulation mechanisms inevitably also affects the selectivity of neural interfaces and of neuromodulation protocols (133). First of all, most VNS systems lack functional selectivity, that is stimulation of distinct functional classes of fibers, and are far from mimicking patterns of action potential occurring in healthy nerve fibers (32, 133). Secondly, most VNS systems lack spatial selectivity, that is selective modulation of fibers in the specific anatomical territory innervated by a given fascicle (32). Electrodes commonly used for VNS are not selective enough to achieve targeted neuromodulation in a complex fasciculate nerve like the VN (133). The direct consequences are the failure to achieve therapeutical effects and the onset of side effects that include hoarseness, throat pain, voice alteration, difficulty swallowing, coughing, abdominal and chest pain, nausea, dyspnea, and bradycardia (36, 85–88, 90). The inadvertent stimulation of somatic nerve branches such as the superior and recurrent laryngeal nerve has been addressed as one of the main causes of VNS side effects (36). Selective stimulation of vagal cardiac B and C fibers can be challenging given that their thresholds are 2–100 times greater than A fibers,

as those branching to the laryngeal nerves (89). To achieve such selectiveness, several authors tried the combination of different stimulation parameters or to modify the pulse shape using different techniques such as the anodal block, slowly rising pulses or depolarizing pre-pulses (89). Other strategies are the modification of electrode design to allow preferential activation of efferent fibers (such as in the case of the CardioFit system) or the development of multicontact electrodes that exploit the topographical architecture of human nerves to target organ-specific fascicles (36, 88–90). This last approach would provide better spatial resolution and consequently improve the selectivity both for recordings and stimulation (36, 89). Therefore, new neural interfaces with higher electrode counts and spatial selectivity should be implemented (8, 30), along with advanced signal processing techniques and the use of hybrid models (134, 135) with extensive validation in experimental animals (136). With such technologies, the development of closed-loop VNS based on the combination of selective nerve stimulation and biosensing technologies could be one of the best solutions to overcome the aforementioned limitations emerged during VNS clinical trials (7, 133).

Closed-Loop Strategies for Vagus Nerve Stimulation

The current VNS systems provide stimulation in an open-loop fashion, meaning that parameters are pre-set and are not automatically adjusted according to the patient's clinical characteristics (137). Closed-loop stimulation strategies offer the advantage of providing treatment only in response to detection of altered biomarkers of disease, thus tuning the stimulation according to the patient's condition (138, 139). This approach potentially improves the efficacy of open-loop interventions and decreases the associated side effects (140). Closed-loop devices should continuously monitor internal biological variables to adjust therapy to individual conditions (7), thus allowing not only automatic but also adaptive neurostimulation that could maintain its efficacy over time and overcome the intrinsic plasticity of biological systems (8, 11, 141). In fact, plasticity and memory are crucial characteristics of the cardiac neuraxis, which undergoes profound alterations in chronic CVDs, causing the disruption of homeostatic cardiovascular functional responses (19).

Closed-loop VNS relies heavily on the precise selection and processing of physiological inputs (32, 142). To date, in the clinical scenario, only macro-biosignals like heart rate have been employed as input data for control loops. This concept is well illustrated in the work by Tosato et al. who achieved heart rate regulation with a closed-loop control system that continuously measured the RR interval, recalculated the difference between the measured and the target value and fed it back to the stimulator accordingly (100). Multiple other indirect and non-invasive measures can be used as indexes of cardiac VN activity (115), for instance heart rate variability, baroreflex sensitivity or respiratory sinus arrhythmia (21, 115). However, such clinical vagal indexes should be used with caution as they represent gross markers of the final net effect of parasympathetic and sympathetic action on the heart (72). On the other hand, local control loops can be obtained by recording feedback bio-signals from the same spot where the stimulus is delivered (142). This approach optimizes the spatial and temporal distribution of the local stimuli (142) but requires high-fidelity feedback signals that are not clinically obtainable due to current technological limitations (142, 143). A good example is represented by the lack of instruments to properly follow and locally evaluate in real-time the myriad of metabolic signals or the fluctuating levels of inflammatory stimuli. Nevertheless, all this information is collected by the peripheral sensors of the ANS and converted into electrical signals (neural encoding), a sort of "neural footprints" of physiological processes that can be recorded and decoded (**Figure 5**) (8, 30). Deciphering the neural language through decoding techniques would be essential to understand the underlying mechanisms of many diseases and to develop new methods and technologies that better engage with neural circuities (141). In the case of VNS, the copresence of afferent and efferent fibers in the VN offers the opportunity to build a feedback loop on the same anatomical site, that is to record from and then to stimulate the VN (**Figure 5**) (144, 145). Vagal sensory neurons are equipped with a vast arsenal of receptors to sense and respond to a huge variety of stimuli (27). Consequently, neural signals traveling through the VN represent a peerless source of information, and this helps the implementation of neural decoding strategies that usually benefit from an adequate number of signals (30, 32). Moreover, vagal neural signals offer the advantage of high temporal and spatial resolution (146), helping in the identification and classification of patterns difficult to see using other biosignals (8, 30) and potentially allowing devices to diagnose various conditions before symptoms presentation (32). New neural interfaces with higher electrode densities and spatial selectivity, such as intraneural electrodes, (147) and advanced signal processing techniques (8) will be necessary to take full advantage of the information traveling along with the VN. In the next section, we present the main preclinical studies that aim at the development of VNS closed-loop approaches based on different neural recording and decoding strategies for CVDs.

Decoding Techniques for Physiological Fiber Firing

Neural interfaces used for stimulation can also be used to record neural signals and monitor ANS activity in real-time (13). While innovative neural interfaces with multiple contacts are designed to improve the quality and information content of neural recordings (148–151), comparable efforts are being made to develop advanced signal processing and data analysis methods (152, 153). Several studies recently focused on the extrapolation of neural markers from spontaneous or physiologically enhanced VN activity, employing various decoding techniques. One technique is the coherent electroneurogram averaging that aims at the isolation of the neural activity of interest from the random noise by taking the average of N snippets from a recorded signal in correspondence to an external or an internal trigger, for instance a biological change (154). Using multicontact cuff electrodes, Plachta et al. employed the ECG rising edge as a trigger to remove stochastic noise, isolate baroreceptors activity from VN recordings and perform selective VNS reducing blood

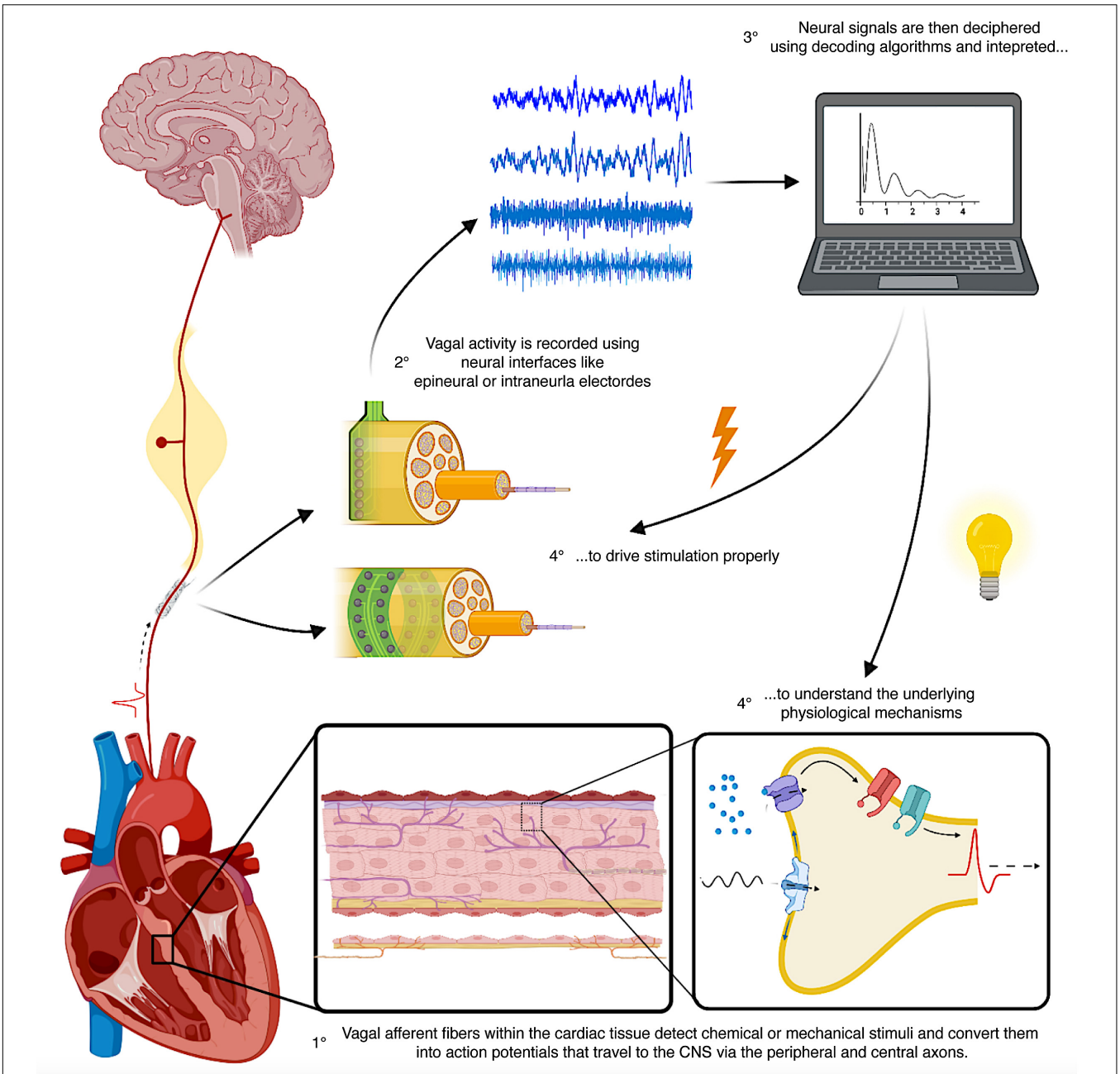

FIGURE 5 | Schematic representation of the principles of closed-loop neuromodulation using neural recordings and decoding strategies. The heart is densely innervated by vagal afferent fibers, which detect chemical and mechanical stimuli, convert them into electrical signals (action potential) and send them to the CNS *via* their peripheral and central axons. Using neural interfaces placed on the vagus nerve, it is possible to record and decode these electrical signals and identify the underlying physiological processes and set the spatiotemporal characteristics of stimulation. CNS, central nervous system.

pressure without producing side effects in rats (145). Sevcencu et al. recorded signals from the porcine left VN to extract intraneural and extraneural profiles resembling the temporal evolution of blood pressure during baseline activity. In particular, systolic peaks and dicrotic waves characterizing blood pressure were reflected by the neural counterpart (144, 155). Rozman and Ribarič employed 33-electrode spiral cuff to record from the left VN of a dog during stimulation of cardiovascular or respiratory stimulations and identified the channel that was best correlated with heart activity using the spectrum estimation technique (156).

Another common approach to extract physiological information from VN electrical activity consists of decoding fiber spike patterns using spikes sorting techniques (157–162). Typically, raw neural signals are band-passed from 200 Hz to a maximum of 10 kHz, robustly denoised, spikes are then

detected using thresholding methods and clustered using feature waveforms (46, 163). In general, there is not a universally adopted low-frequency cutoff as it usually depends on the quality and the nature of the signals. For instance, 200 Hz low-frequency cutoff was used in the context of intrafascicular sciatic nerve recordings (164), 1 kHz for intraneural recordings from the pig VN (136), 700 Hz (165) and 300 Hz (166) in the case of microneurographic recordings from the peroneal nerve and from the human VN, respectively. In the murine VN, spike sorting techniques within decoding frameworks have been employed to decode the activity of different fiber types enhanced by inflammatory stimuli such as particular cytokines (153) or metabolic ones like hypoglycemia/hyperglycemia (167). Spike sorting techniques are potentially usable in human patients as we recently obtained single-fiber recordings from the human cervical VN identifying tonically active neurons that discharged synchronously with the respiratory and cardiac cycles (166). Spike-like signals, as they reflect the activity of individual fibers, are preferable to cumulative signals to obtain maximal functional selectivity (162). Real-time implementations of complex spike sorting algorithms onto low-power off-the-shelf digital signal processors are currently available, as in the case of neuroprosthetic applications where the power consumption enabled more than 24 h processing at the maximum load (162). In the case of closed-loop VNS protocols, this would allow longer operational time scales, such as Holter-like monitoring at a neural level, i.e., a "Neural Holter" with biomarkers extracted directly from neural activity. As pointed out in Raspopovic et al. (136), signals recorded with intraneural electrodes can be classified as a hybrid category between cumulative and single-unit signals. This characteristic allows the development of more robust recording schemes and processing algorithms *via* a combination of decoding strategies developed on both cumulative and single-unit signals (136).

The identification of neural signals elicited by specific physiological stimuli could be extremely useful to distinguish among VN fibers coming from different cardiovascular sites and carrying information on multiple functional parameters that can vary over short time windows, such as cardiac output and blood pressure. Such distinction could be further appreciated using neural multielectrode devices with high spatial selectivity to better interface the potential topographical architecture of the VN (44, 46). However, cuff electrodes can only sense compound nerve action potentials and multi-unit activity and they do not allow access to single-fiber action potentials contrary to intraneural electrodes (89, 168). Intraneural electrodes offer the advantage of higher signal-to-noise ratio and higher spatial specificity compared to epineural electrodes and could allow more effective closed-loop decoding methods to be used (8, 139, 169). Intraneural electrodes such as the Longitudinal Intra-Fascicular Electrode (LIFE) or the Transversal Intra-Fascicular Multi-channel Electrodes (TIME) have provided rich and valuable sensory feedback in human amputees and detailed information from decoding hand movements in somatic nerves (139, 157, 159, 170). The LIFE is a flexible electrode consisting of 25–50 μm diameter Pt or Pt-Ir wires insulated with Teflon or metalized Kevlar fibers insulated with medical-grade silicone. The wire is surgically inserted into the nerve along the fascicle and then pinched out of the nerve again. The recording sites are areas of 0.5–1.5 mm long which are left uninsulated (149). A more recent version of LIFEs is the thin-filmLIFEs (tfLIFE), based on a thin highly flexible micropatterned polyimide substrate filament that can host eight contact sites (46, 149). The TIME consists of a thin, strip-like polyimide substrate with platinum electrode sites. The substrate is folded to align several electrodes and the folded substrate is threaded transversely through the nerve between the fascicles (149). The original design contained 10 sites with interelectrode spacing of 230 μm (148). The TIME was developed to achieve good contact with nerve fibers, selectively addresses several fascicles in a nerve with a single implant, and minimizes the mechanical mismatch between the implanted material and nerve tissue (168). The TIME has shown higher selectivity at low stimulation intensities than the single LIFE and multipolar cuffs (46, 148, 149). Our group combined the use of multichannel intrafascicular electrodes, machine learning principles and hybrid models (136) to study high frequency (>1,500 Hz) VN activity of anesthetized pigs during artificially produced alterations of physiological parameters, simulating increases in respiratory rate, tidal volume and arterial blood pressure (**Figure 6A**) (152). Using a new decoding algorithm that combines wavelet decomposition, dimensionality reduction, and ensemble learning classifiers, we could associate VN signals to specific functional changes (**Figure 6B**). Our approach was a machine learning-driven approach to find informative feature vectors for reliable decoding of cardio-respiratory alterations regardless of their precise nature, and future analysis will serve to get more interpretable features related to units and aggregate activities. Different from epineural electrodes that can only provide a global picture of neural signal trafficking (147, 171), we employed intraneural electrodes to enhance selectivity (147, 169) and to map a possible spatial functional organization of VN fascicles. Thus, we employed a hybrid modeling framework based on histological analysis combined with electrode discrimination ability properties measured *via* a novel quantitative measure called Discriminative Field Potential (DFP) and we obtained distinct spatial configurations of discriminative patterns generated by fascicles during the various functional challenges (**Figure 6C**) (152). This is extremely important for the development not only of timely, but also spatially selective stimulation protocols in a complex nerve with multiple fascicles like the human or porcine VN (152). In this perspective, the precise knowledge of cardiovascular fibers arrangement within the cervical vagal trunk would be crucial to establish effective VNS protocols for the treatment of CVDs. Anatomical models and non-invasive tests should be developed and used to better anticipate which site for neuromodulation would give the best outcomes and to overcome the anatomical variability that limits clinical VNS applications (116, 120, 129).

The biocompatibility and longevity of intraneural electrodes was demonstrated in animal models and preliminarily confirmed in human experiments with long-term stimulation for sensory feedback and chronic neural recordings (139, 172). However, the

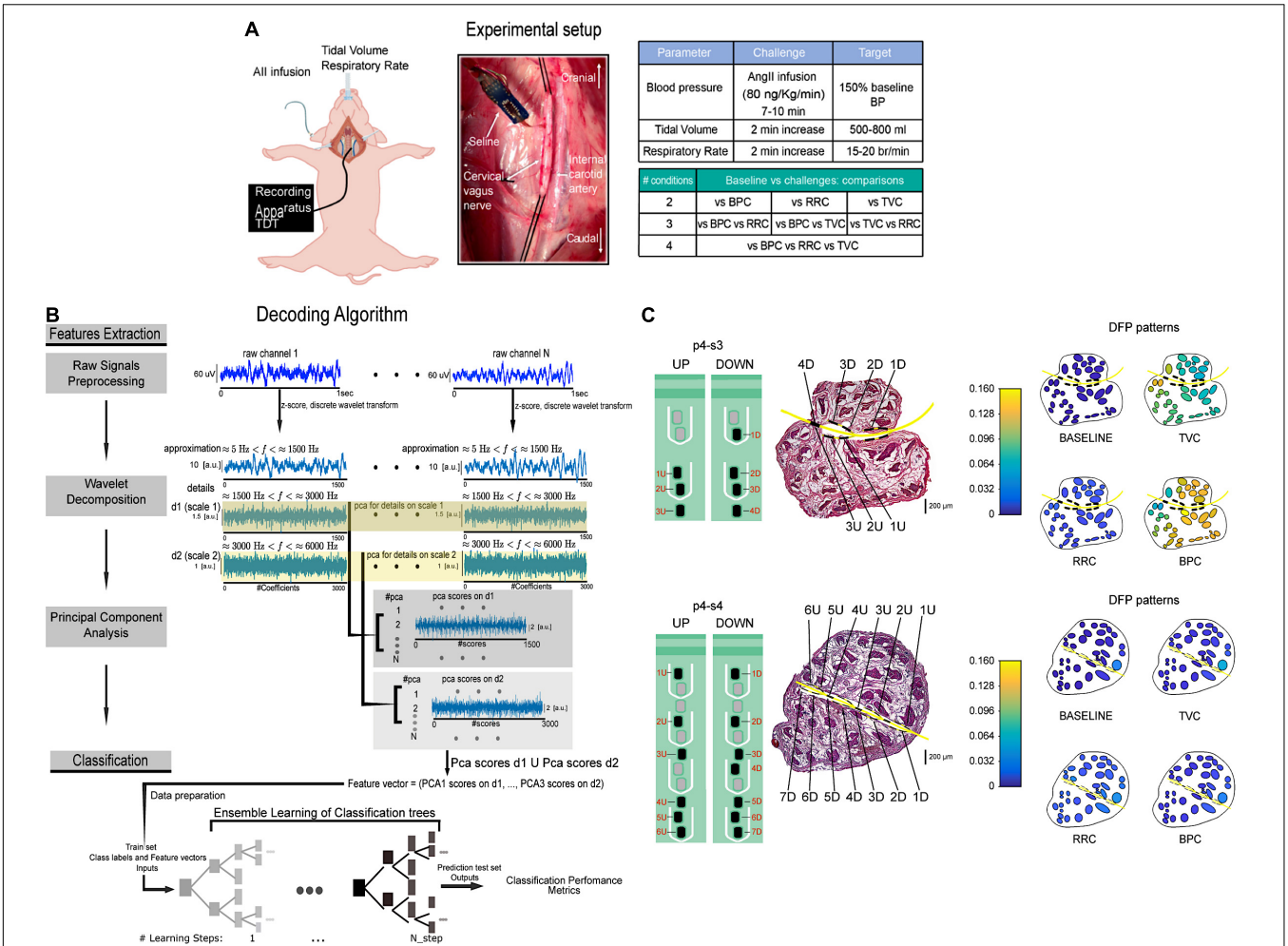

FIGURE 6 | Schematic representation of the experimental setup and decoding algorithm from Vallone et al. (152). **(A)** Recording apparatus, electrode implantation and summary of the *in vivo* protocol and functional challenges comparisons. **(B)** Decoding algorithm. Feature extraction was performed on 1 s portions of raw intraneural signals (dark blue traces) by applying principal component analysis on wavelet details relative to two different scales (1,500 Hz $< f <$ 3,000 Hz and 3,000 Hz $< f <$ 6,000 Hz). Neural signals recorded with intraneural electrodes were a combination of single-unit and compound action potentials. Decoding performed with ensemble learning based on classification trees combined with random undersampling and boosting procedure was applied on feature vectors. Decoding performance was assessed by means of confusion matrices and accuracy level. **(C)** Schematic description of two intraneural electrodes implantation in the VN of one pig and hybrid model simulations of fascicles activation at baseline and in response to functional challenges. The two intraneural electrodes are represented on a VN histological section (central panels). DFP patterns of activity during baseline and each functional challenge (left panels). DFP, discriminative field potentials. Adapted from Vallone et al. (152) with permission.

experience in chronic implantations in humans indicates that there is frequently a reduction in the number of functioning electrode active sites, an in- crease in the stimulation threshold, and a decrease of the signal-to-noise ratio along time. To further improve the usability of the neural electrodes, considerable efforts are being devoted in the engineering field for increasing robustness and flexibility at the same time of miniaturizing the electrodes and in the biological field to increase biocompatibility of the substrates and to modulate the foreign body reaction (46). On the computational side, since the drift in the amplitudes of signals and changes in the signal-to-noise ratio greatly hampers chronic neural recordings and decoding, new algorithms for drift compensation have been developed (173). In the case of the VN, carbon nanotube yarn electrodes have been used to make the first direct chronic measurements of vagal tone in freely moving rats (174). Thanks to their small size, high flexibility, and low impedance, carbon nanotube yarn electrodes have provided stable, high-signal-to-noise chronic recordings in rats VN with high-quality signals continuing up to 4 months after implantation (174).

Decoding Fiber Activity in Electrically Stimulated Nerves

Recording and decoding the spontaneous activity of vagal fibers would be useful to determine the precise timing for VNS delivery, but may prove limited for the definition of precise dosing (133). In this regard, recording and decoding fiber activity during VNS

may represent a complementary method to better define the relationship between stimulation and physiological effects.

The standard VNS dosing method does not rely on any measurement of fiber activation, since the commercial implants lack the capability to record from nerves during stimulation. Consequently, factors like electrode interface and nerve sensitivity are not controlled and VNS effects in a patient are neither uniquely determined over time nor comparable with

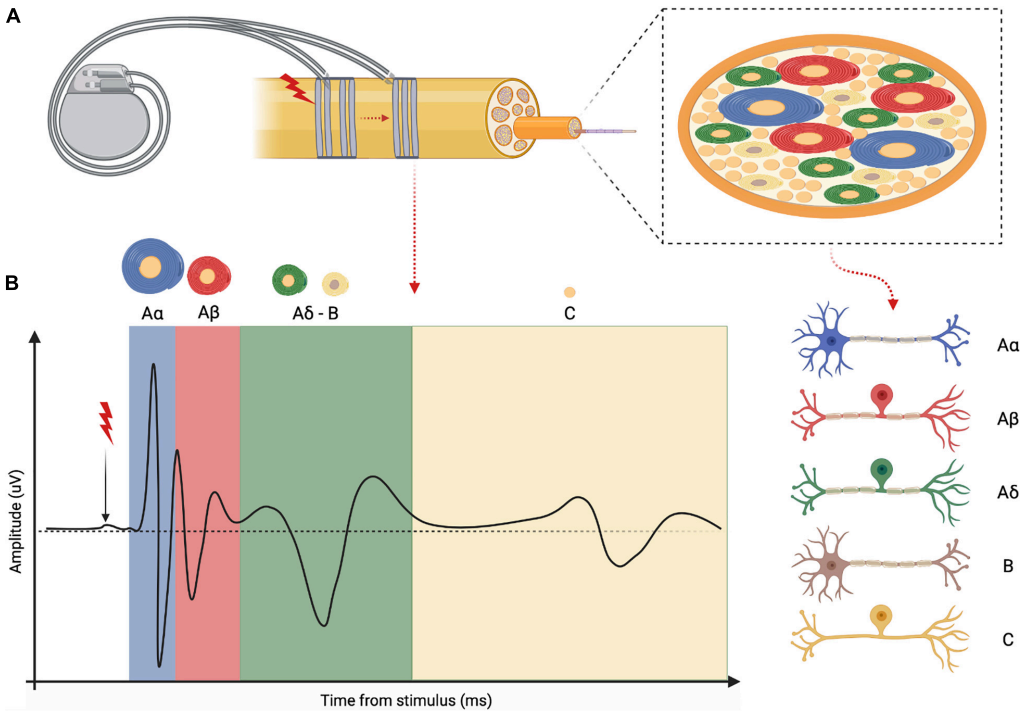

FIGURE 7 | Schematic representation and explanation of the electrically evoked compound action potential (eCAP). **(A)** Example of a VNS device that electrically stimulate the vagus nerve at one site while recording evoked activity at another site. Inset: vagal fascicle containing different fiber types distinguished by myelination degree and fiber caliber. **(B)** Example of a complete vagus nerve eCAP obtained with supra-threshold stimulation of all vagal fibers subtypes. Each peak of the eCAP corresponds to different fiber subtypes as indicated by the different color codes.

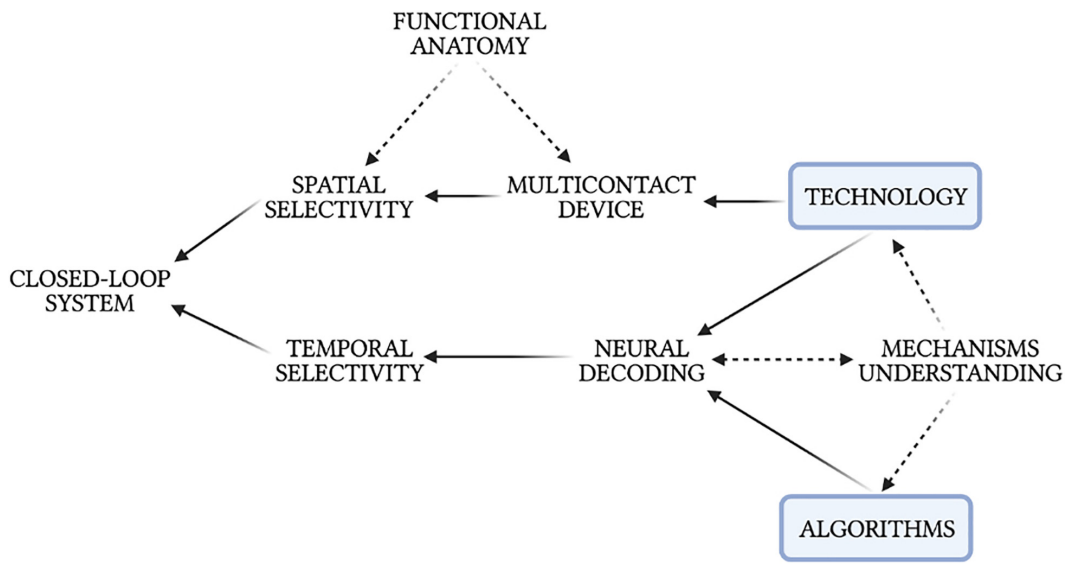

FIGURE 8 | Intercorrelations between neural decoding, technology, algorithms, physiological mechanisms, and the development of a closed-loop neuromodulation system.

other patients (133). The ability to distinguish between stimulated fibers could aid in correlating neural activity to external variables, thus increasing the ability to achieve targeted stimulation (175), with decreased variability in therapeutic responses and increased response rate (96).

In studies that employ extraneural interfaces, nerve activity is frequently analyzed in terms of evoked compound activity by electrical stimulation (eCAP) (176). The diverse conduction velocities of various fiber types, which ultimately depends on fiber caliber and degree of myelination, determine typical patterns and shapes with distinctive latencies and peaks in the eCAP (177), as shown in **Figure 7**. A sophisticated analysis of VN eCAPs would help in the assessment of the relationship between stimulus dose, neural recruitment and physiological effects (178).

Tahry et al. obtained, for the first time, VN eCAPs recordings after implanting the Advanced Nerve Stimulator version 300 (ADNS-300, Neurotech SA, Louvain-La-Neuve, Belgium) in the human VN (179). In preclinical studies, VNS-eCAP were used to optimize stimulation parameters and electrode design during VNS in dogs (176), pigs (180), and rodents (96), showing a strong correlation with the physiological effects of stimulation. For instance, vagal B-type fiber eCAP amplitude was correlated with changes in heart activity (176), indicating that parasympathetic B-fibers are the best predictors of cardiac activity during VNS (96, 177). Ordelman et al. found an indirect component in pig vagal eCAPs during VNS protocols, and they showed that it correlated with the state of the cardiovascular system (181).

CONCLUSION

In conclusion, the VN represents a key component of the cardiac neuraxis and VNS has shown a great potential for the treatment of a wide range of CVDs in the preclinical setting. Results in experimental animals may not be immediately translated into clinical applications, yet they are paving the way for fine-tuning and customized VNS applications. VNS represents a cheaper alternative/complementary solution to pharmacological remedies that lack of efficacy and present significant side effects and astronomical costs (4, 7, 182, 183). Closed-loop VNS would guide earlier, more accurate diagnosis and enable more effective, less costly prevention and intervention compared to pharmacological treatments (183). Moreover, access to personalized bioelectronic data would facilitate greater patient understanding of their conditions and greater engagement with their treatments, higher levels of health literacy, and greater communication and trust between patients and physicians (183). A plethora of promising research is advancing to overcome VNS limitations and develop closed-loop modalities. Advanced neural decoding strategies represent a major candidate. However, automatic closed-loop modalities will require not only advancements in biotechnologies but also improvements in the basic understanding of fundamental biological mechanisms (16). Progress in neural interface technology, big-data analysis methods, and signal processing techniques will accelerate biological breakthroughs that, in turn, will inform additional advancements in technology and methodology, creating a synergistic loop that ensues cross-disciplinary collaboration (**Figure 8**) (8).

AUTHOR CONTRIBUTIONS

MMO conceptualized, wrote the manuscript, and prepared the figures. FV wrote and revised the manuscript. SM and FR conceptualized and revised the manuscript. All authors authorized the submission of the manuscript.

FUNDING

This work was supported in part by the European Commission H2020-FETPROACT-2018-01 NeuHeart Project (#824071) (SM) and European Union's Horizon 2020 Research and Innovation Program under grant agreement number 874764 (FR).

REFERENCES

1. Buckley U, Shivkumar K, Ardell JL. Autonomic regulation therapy in heart failure. *Curr Heart Fail Rep.* (2015) 12:284–93. doi: 10.1007/s11897-015-0263-7
2. Wilks SJ, Hara SA, Ross EK, Nicolai EN, Pignato PA, Cates AW, et al. Non-clinical and pre-clinical testing to demonstrate safety of the barostim neo electrode for activation of carotid baroreceptors in chronic human implants. *Front Neurosci.* (2017) 11:438. doi: 10.3389/fnins.2017.00438
3. Bonaz B, Sinniger V, Pellissier S. Anti-inflammatory properties of the vagus nerve: potential therapeutic implications of vagus nerve stimulation. *J Physiol.* (2016) 594:5781–90. doi: 10.1113/JP271539
4. Pavlov VA, Tracey KJ. Neural circuitry and immunity. *Immunol Res.* (2015) 63:38–57. doi: 10.1007/s12026-015-8718-1
5. Waltz E. A spark at the periphery. *Nat Biotechnol.* (2016) 34:904–8. doi: 10.1038/nbt.3667
6. Chang EH. Changing the tune using bioelectronics. *Bioelectron Med.* (2021) 7:2. doi: 10.1186/s42234-021-00063-x
7. Olofsson PS, Tracey KJ. Bioelectronic medicine: technology targeting molecular mechanisms for therapy. *J Intern Med.* (2017) 282:3–4. doi: 10.1111/joim.12624
8. Bouton C. Cracking the neural code, treating paralysis and the future of bioelectronic medicine. *J Intern Med.* (2017) 282:37–45. doi: 10.1111/joim.12610
9. Karemaker JM. An introduction into autonomic nervous function. *Physiol Meas.* (2017) 38:R89–118. doi: 10.1088/1361-6579/aa6782
10. Cheng ZJ, Wang R, Chen QH. Autonomic regulation of the cardiovascular system: diseases, treatments, and novel approaches. *Neurosci Bull.* (2019) 35:1–3. doi: 10.1007/s12264-019-00337-0
11. Horn CC, Ardell JL, Fisher LE. Electroceutical targeting of the autonomic nervous system. *Physiology.* (2019) 34:150–62. doi: 10.1152/physiol.00030.2018
12. Guarino D, Nannipieri M, Iervasi G, Taddei S, Bruno RM. The role of the autonomic nervous system in the pathophysiology of obesity. *Front Physiol.* (2017) 8:665. doi: 10.3389/fphys.2017.00665
13. Debnath S, Levy TJ, Bellehsen M, Schwartz RM, Barnaby DP, Zanos S, et al. A method to quantify autonomic nervous system function in healthy, able-bodied individuals. *Bioelectron Med.* (2021) 7:1–38. doi: 10.1186/s42234-021-00075-7
14. Pavlov VA. Cholinergic modulation of inflammation. *Int J Clin Exp Med.* (2008) 1:203–12.

15. Tracey KJ. Physiology and immunology of the cholinergic antiinflammatory pathway. *J Clin Invest.* (2007) 117:289–96. doi: 10.1172/JCI30555
16. Won SM, Song E, Reeder JT, Rogers JA. Emerging modalities and implantable technologies for neuromodulation. *Cell.* (2020) 181:115–35. doi: 10.1016/j.cell.2020.02.054
17. Ardell JL, Nier H, Hammer M, Southerland EM, Ardell CL, Beaumont E, et al. Defining the neural fulcrum for chronic vagus nerve stimulation: implications for integrated cardiac control. *J Physiol.* (2017) 595:6887–903. doi: 10.1113/JP274678
18. Herring N, Kalla M, Paterson DJ. The autonomic nervous system and cardiac arrhythmias: current concepts and emerging therapies. *Nat Rev Cardiol.* (2019) 16:707–26. doi: 10.1038/s41569-019-0221-2
19. Dusi V, Ardell JL. Brain-heart afferent-efferent traffic. In: Govoni S, Politi P, Vanoli E editors. *Brain and Heart Dynamics*. Cham: Springer International Publishing (2020). p. 3–24. doi: 10.1007/978-3-030-28008-6_2
20. Amiya E, Watanabe M, Komuro I. The relationship between vascular function and the autonomic nervous system. *Ann Vasc Dis.* (2014) 7:109–19. doi: 10.3400/avd.ra.14-00048
21. Olshansky B, Sabbah HN, Hauptman PJ, Colucci WS. Parasympathetic nervous system and heart failure pathophysiology and potential implications for therapy. *Circulation.* (2008) 118:863–71. doi: 10.1161/CIRCULATIONAHA.107.760405
22. Schwartz PJ, De Ferrari GM. Sympathetic-parasympathetic interaction in health and disease: abnormalities and relevance in heart failure. *Heart Fail Rev.* (2011) 16:101–7. doi: 10.1007/s10741-010-9179-1
23. Basiago A, Binder DK. Effects of deep brain stimulation on autonomic function. *Brain Sci.* (2016) 6:33. doi: 10.3390/brainsci6030033
24. Bonaz B, Sinniger V, Pellissier S. The vagus nerve in the neuro-immune axis: implications in the pathology of the gastrointestinal tract. *Front Immunol.* (2017) 8:1452. doi: 10.3389/fimmu.2017.01452
25. Pavlov VA, Tracey KJ. Bioelectronic medicine: updates, challenges and paths forward. *Bioelectron Med.* (2019) 5:1. doi: 10.1186/s42234-019-0018-y
26. Câmara R, Griessenauer CJ. Anatomy of the vagus nerve. *Nerve Nerve Inj.* (2015) 1:385–97. doi: 10.1016/B978-0-12-410390-0.00028-7
27. Kupari J, Häring M, Agirre E, Castelo-Branco G, Ernfors P. An atlas of vagal sensory neurons and their molecular specialization. *Cell Rep.* (2019) 27:2508–23.e4. doi: 10.1016/j.celrep.2019.04.096
28. Capilupi MJ, Kerath SM, Becker LB. Vagus nerve stimulation and the cardiovascular system. *Cold Spring Harb Perspect Med.* (2020) 10:a034173. doi: 10.1101/cshperspect.a034173
29. Marmerstein JT, McCallum GA, Durand DM. Direct measurement of vagal tone in rats does not show correlation to HRV. *Sci Rep*. (2021) 11:1–12. doi: 10.1038/s41598-020-79808-8
30. Bouton C. Neural decoding and applications in bioelectronics medicine. *Bioelectron Med.* (2015) 2:20–4. doi: 10.15424/bioelectronmed.2014.00012
31. Ganzer PD, Sharma G. Opportunities and challenges for developing closed-loop bioelectronic medicines. *Neural Regen Res.* (2019) 14:46–50. doi: 10.4103/1673-5374.243697
32. Zanos TP. Recording and decoding of vagal neural signals related to changes in physiological parameters and biomarkers of disease. *Cold Spring Harb Perspect Med.* (2019) 9:a034157. doi: 10.1101/cshperspect.a034157
33. Hammer N, Löffler S, Cakmak YO, Ondruschka B, Planitzer U, Schultz M, et al. Cervical vagus nerve morphometry and vascularity in the context of nerve stimulation - a cadaveric study. *Sci Rep.* (2018) 8:1–9. doi: 10.1038/s41598-018-26135-8
34. Hammer N, Glätzner J, Feja C, Kühne C, Meixensberger J, Planitzer U, et al. Human vagus nerve branching in the cervical region. *PLoS One.* (2015) 10:e0118006. doi: 10.1371/journal.pone.0118006
35. Berthoud HR, Neuhuber WL. Functional and chemical anatomy of the afferent vagal system. *Auton Neurosci Basic Clin.* (2000) 85:1–17. doi: 10.1016/S1566-0702(00)00215-0
36. Thompson N, Mastitskaya S, Holder D. Avoiding off-target effects in electrical stimulation of the cervical vagus nerve: neuroanatomical tracing techniques to study fascicular anatomy of the vagus nerve. *J Neurosci Methods.* (2019) 325:108325. doi: 10.1016/j.jneumeth.2019.108325
37. Kawashima T. The autonomic nervous system of the human heart with special reference to its origin, course, and peripheral distribution. *Anat Embryol (Berl).* (2005) 209:425–38. doi: 10.1007/s00429-005-0462-1
38. Green JH, Heffron PF. The origin of the right aortic nerve in the rabbit. *Quart J Exper Physiol.* (1966) 51:276–83. doi: 10.1113/expphysiol.1966.sp001863
39. Cohen ML, Georgievskaya Z. Histopathology of the stimulated vagus nerve: primum non nocere. *Heart Fail Rev.* (2011) 16:163–9. doi: 10.1007/s10741-010-9182-6
40. Seki A, Green HR, Lee TD, Hong L, Tan J, Vinters HV, et al. Sympathetic nerve fibers in human cervical and thoracic vagus nerves. *Heart Rhythm.* (2010) 14:384–99.
41. Bassi GS, Kanashiro A, Coimbra NC, Terrando N, Maixner W, Ulloa L. Anatomical and clinical implications of vagal modulation of the spleen. *Neurosci Biobehav Rev.* (2020) 112:363–73. doi: 10.1016/j.neubiorev.2020.02.011
42. Verlinden TJM, Rijkers K, Hoogland G, Herrler A. Morphology of the human cervical vagus nerve: implications for vagus nerve stimulation treatment. *Acta Neurol Scand.* (2016) 133:173–82. doi: 10.1111/ane.12462
43. Stakenborg N, Gomez-Pinilla PJ, Verlinden TJM, Wolthuis AM, D'Hoore A, Farré R, et al. Comparison between the cervical and abdominal vagus nerves in mice, pigs, and humans. *Neurogastroenterol Motil.* (2020) 32:e13889. doi: 10.1111/nmo.13889
44. Settell ML, Knudsen BE, Dingle AM, Mcconico AL, Nicolai EN, Trevathan JK, et al. Functional vagotopy in the cervical vagus nerve of the domestic pig : implications for vagus nerve stimulation. *J Neural Eng.* (2020) 17:026022. doi: 10.1088/1741-2552/ab7ad4
45. Micera S, Navarro X, Carpaneto J, Citi L, Tonet O, Rossini PM, et al. On the use of longitudinal intrafascicular peripheral interfaces for the control of cybernetic hand prostheses in amputees. *IEEE Trans Neural Syst Rehabil Eng.* (2008) 16:453–72. doi: 10.1109/TNSRE.2008.2006207
46. Raspopovic S, Cimolato A, Panarese A, Vallone F, del Valle J, Micera S, et al. Neural signal recording and processing in somatic neuroprosthetic applications: a review. *J Neurosci Methods.* (2020) 337:108653. doi: 10.1016/j.jneumeth.2020.108653
47. Thompson N, Ravagli E, Mastitskaya S, Iacoviello F, Aristovich K, Perkins J, et al. MicroCT optimisation for imaging fascicular anatomy in peripheral nerves. *J Neurosci Methods.* (2020) 338:108652. doi: 10.1101/818237
48. Ravagli E, Mastitskaya S, Thompson N, Welle EJ, Chestek CA, Aristovich K, et al. Fascicle localisation within peripheral nerves through evoked activity recordings: a comparison between electrical impedance tomography and multi-electrode arrays. *J Neurosci Methods.* (2021) 358:109140. doi: 10.1016/j.jneumeth.2021.109140
49. Evans DHL, Murray JG. Histological and functional studies on the fibre composition of the vagus nerve of the rabbit. *J Anat.* (1954) 88:320–37.
50. Agostoni E, Chinnock JE, De Daly MB, Murray JG. Functional and histological studies of the vagus nerve and its branches to the heart, lungs and abdominal viscera in the cat. *J Physiol.* (1957) 135:182–205. doi: 10.1113/jphysiol.1957.sp005703
51. Ruffoli R, Giorgi FS, Pizzanelli C, Murri L, Paparelli A, Fornai F. The chemical neuroanatomy of vagus nerve stimulation. *J Chem Neuroanat.* (2011) 42:288–96. doi: 10.1016/j.jchemneu.2010.12.002
52. Carr MJ, Undem BJ. Bronchopulmonary afferent nerves. *Respirology.* (2003) 8:291–301. doi: 10.1046/j.1440-1843.2003.00473.x
53. Zhuo H, Ichikawa H, Helke CJ. Neurochemistry of the nodose ganglion. *Prog Neurobiol.* (1997) 52:79–107. doi: 10.1016/S0301-0082(97)00003-8
54. Mazzone SB, Undem BJ. Vagal afferent innervation of the airways in health and disease. *Physiol Rev.* (2016) 96:975–1024. doi: 10.1152/physrev.00039.2015
55. Thayer JF, Loerbroks A, Sternberg EM. Inflammation and cardiorespiratory control: the role of the vagus nerve. *Respir Physiol Neurobiol.* (2011) 178:387–94. doi: 10.1016/j.resp.2011.05.016
56. Travagli RA, Anselmi L. Vagal neurocircuitry and its influence on gastric motility. *Nat Rev Gastroenterol Hepatol.* (2016) 13:87–92. doi: 10.1016/j.coviro.2015.09.001.Human
57. Chang EH, Chavan SS, Pavlov VA. Cholinergic control of inflammation, metabolic dysfunction, and cognitive impairment in obesity-associated disorders: mechanisms and novel therapeutic opportunities. *Front Neurosci.* (2019) 13:263. doi: 10.3389/fnins.2019.00263
58. Rajendran PS, Challis RC, Fowlkes CC, Hanna P, Tompkins JD, Jordan MC, et al. Identification of peripheral neural circuits that regulate heart rate using

optogenetic and viral vector strategies. *Nat Commun.* (2019) 10:1–13. doi: 10.1038/s41467-019-09770-1
59. Min S, Chang RB, Prescott SL, Beeler B, Joshi NR, Strochlic DE, et al. Arterial baroreceptors sense blood pressure through decorated aortic claws. *Cell Rep.* (2019) 29:2192–201.e3. doi: 10.1016/j.celrep.2019.10.040
60. Paintal AS. The conduction velocities of respiratory and cardiovascular afferent fibres in the vagus nerve. *J Physiol.* (1953) 121:341–59. doi: 10.1113/jphysiol.1953.sp004950
61. Allen AM, Lewis SJ, Verberne AJM, Mendelsohn FAO. Angiotensin receptors and the vagal system. *Clin Exp Hypertens Part A Theory Pract.* (1988) 10:1239–49. doi: 10.1080/07300077.1988.11878914
62. Zeng WZ, Marshall KL, Min S, Daou I, Chapleau MW, Abboud FM, et al. PIEZOs mediate neuronal sensing of blood pressure and the baroreceptor reflex. *Science.* (2018) 362:464–7. doi: 10.1126/science.aau6324
63. Lumbers BYER, Mccloskey DI, Potter EK. Inhibition by angiotensin II of baroreceptor-evoked activity in cardiac vagal efferent nerves in the dog. *J Physiol.* (1979) 294:69–80. doi: 10.1113/jphysiol.1979.sp012915
64. Longhurst JC. Cardiac receptors: their function in health and disease. *Prog Cardiovasc Dis.* (1984) 27:201–22. doi: 10.1016/0033-0620(84)90005-7
65. Paintal AS. A study of right and left atrial receptors. *J Physiol.* (1953) 120:596–610. doi: 10.1113/jphysiol.1953.sp004920
66. Campbell T, Shenton F, Lucking E, Pyner S, Jones J. Electrophysiological characterisation of atrial volume receptors using ex−vivo models of isolated rat cardiac atria. *Exp Physiol.* (2020) 105:2190–206. doi: 10.1113/ep088972
67. Kashihara K, Kawada T, Yanagiya Y, Uemura K, Inagaki M, Takaki H, et al. Bezold-Jarisch reflex attenuates dynamic gain of baroreflex neural arc. *Am J Physiol Heart Circ Physiol.* (2003) 285:5–7. doi: 10.1152/ajpheart.01082.2002
68. McAllen RM, Spyer KM. Two types of vagal preganglionic motoneurones projecting to the heart and lungs. *J Physiol.* (1978) 282:353–64. doi: 10.1113/jphysiol.1978.sp012468
69. Jordan D, Khalid MEM, Schneiderman N, Spyer KM. The location and properties of preganglionic vagal cardiomotor neurones in the rabbit. *Pflügers Arch Eur J Physiol.* (1982) 395:244–50. doi: 10.1007/BF00584817
70. Machhada A, Marina N, Korsak A, Stuckey DJ, Lythgoe MF, Gourine AV. Origins of the vagal drive controlling left ventricular contractility. *J Physiol.* (2016) 594:4017–30. doi: 10.1113/JP270984
71. Chapleau MW, Sabharwal R. Methods of assessing vagus nerve activity and reflexes. *Heart Fail Rev.* (2010) 14:384–99.
72. Grossman P, Taylor EW. Toward understanding respiratory sinus arrhythmia: relations to cardiac vagal tone, evolution and biobehavioral functions. *Biol Psychol.* (2007) 74:263–85. doi: 10.1016/j.biopsycho.2005.11.014
73. Penry JK, Dean JC. Prevention of intractable partial seizures by intermittent vagal stimulation in humans: preliminary results. *Epilepsia.* (1990) 31:S40–3. doi: 10.1111/j.1528-1157.1990.tb05848.x
74. George R, Sonnen A, Upton A, Salinsky M, Ristanovic R, Bergen D, et al. A randomized controlled trial of chronic vagus nerve stimulation for treatment of medically intractable seizures. *Neurology.* (1995) 45:224–30. doi: 10.1212/WNL.45.2.224
75. DeGiorgio C, Heck C, Bunch S, Britton J, Green P, Lancman M, et al. Vagus nerve stimulation for epilepsy: randomized comparison of three stimulation paradigms. *Neurology.* (2005) 65:317–9. doi: 10.1212/01.wnl.0000168899.11598.00
76. Klinkenberg S, Aalbers MW, Vles JSH, Cornips EMJ, Rijkers K, Leenen L, et al. Vagus nerve stimulation in children with intractable epilepsy: a randomized controlled trial. *Dev Med Child Neurol.* (2012) 54:855–61. doi: 10.1111/j.1469-8749.2012.04305.x
77. Salinsky MC, Uthman BM, Ristanovic RK, Wernicke JF, Tarver WB. Vagus nerve stimulation for the treatment of medically intractable seizures. *Arch Neurol.* (1996) 53:1176–80. doi: 10.1001/archneur.1996.00550110128021
78. Rush AJ, George MS, Sackeim HA, Marangell LB, Husain MM, Giller C, et al. Vagus nerve stimulation (VNS) for treatment-resistant depressions: a multicenter study. *Biol Psychiatry.* (2000) 47:276–86. doi: 10.1016/S0006-3223(99)00304-2
79. Rush AJ, Marangell LB, Sackeim HA, George MS, Brannan SK, Davis SM, et al. Vagus nerve stimulation for treatment-resistant depression: a randomized, controlled acute phase trial. *Biol Psychiatry.* (2005) 58:347–54. doi: 10.1016/j.biopsych.2005.05.025
80. Ryvlin P, Gilliam FG, Nguyen DK, Colicchio G, Iudice A, Tinuper P, et al. The long-term effect of vagus nerve stimulation on quality of life in patients with pharmacoresistant focal epilepsy: the PuLsE (open prospective randomized long-term effectiveness) trial. *Epilepsia.* (2014) 55:893–900. doi: 10.1111/epi.12611
81. George MS, Rush AJ, Marangell LB, Sackeim HA, Brannan SK, Davis SM, et al. A one-year comparison of vagus nerve stimulation with treatment as usual for treatment-resistant depression. *Biol Psychiatry.* (2005) 58:364–73. doi: 10.1016/j.biopsych.2005.07.028
82. Tyler R, Cacace A, Stocking C, Tarver B, Engineer N, Martin J, et al. Vagus nerve stimulation paired with tones for the treatment of tinnitus: a prospective randomized double-blind controlled pilot study in humans. *Sci Rep.* (2017) 7:1–11. doi: 10.1038/s41598-017-12178-w
83. Tracey Kevin J. The inflammatory reflex. *Nature.* (2005) 257:122–5. doi: 10.1111/j.1365-2796.2004.01440.x
84. Fitchett A, Mastitskaya S, Aristovich K. Selective neuromodulation of the vagus nerve. *Front Neurosci.* (2021) 15:685872. doi: 10.3389/fnins.2021.685872
85. Farmer AD, Albu-Soda A, Aziz Q. Vagus nerve stimulation in clinical practice. *Br J Hosp Med.* (2016) 77:645–51. doi: 10.12968/hmed.2016.77.11.645
86. Beekwilder JP, Beems T. Overview of the clinical applications of vagus nerve stimulation. *J Clin Neurophysiol.* (2010) 27:130–8. doi: 10.1097/WNP.0b013e3181d64d8a
87. Yuan H, Silberstein SD. Vagus nerve and vagus nerve stimulation, a comprehensive review: part II. *Headache.* (2016) 56:259–66. doi: 10.1111/head.12650
88. Nicolai EN, Settell ML, Knudsen BE, McConico AL, Gosink BA, Trevathan JK, et al. Sources of off-target effects of vagus nerve stimulation using the helical clinical lead in domestic pigs. *J Neural Eng.* (2020) 17:046017. doi: 10.1088/1741-2552/ab9db8
89. Guiraud D, Andreu D, Bonnet S, Carrault G, Couderc P, Hagège A, et al. Vagus nerve stimulation: state of the art of stimulation and recording strategies to address autonomic function neuromodulation. *J Neural Eng.* (2016) 13:041002. doi: 10.1088/1741-2560/13/4/041002
90. Settell ML, Skubal AC, Chen RCH, Kasole M, Knudsen BE, Nicolai EN, et al. In vivo visualization of pig vagus nerve "vagotopy" using ultrasound. *Front Neurosci.* (2021) 15:676680. doi: 10.3389/fnins.2021.676680
91. Aihua L, Lu S, Liping L, Xiuru W, Hua L, Yuping W. A controlled trial of transcutaneous vagus nerve stimulation for the treatment of pharmacoresistant epilepsy. *Epilepsy Behav.* (2014) 39:105–10. doi: 10.1016/j.yebeh.2014.08.005
92. Yap JYY, Keatch C, Lambert E, Woods W, Stoddart PR, Kameneva T. Critical review of transcutaneous vagus nerve stimulation : challenges for translation to clinical practice. *Front Neurosci.* (2020) 14:284. doi: 10.3389/fnins.2020.00284
93. Silberstein SD, Mechtler LL, Kudrow DB, Calhoun AH, McClure C, Saper JR, et al. Non–invasive vagus nerve stimulation for the ACute treatment of cluster headache: findings from the randomized, double-blind, sham-controlled ACT1 study. *Headache.* (2016) 56:1317–32. doi: 10.1111/head.12896
94. Stefan H, Kreiselmeyer G, Kerling F, Kurzbuch K, Rauch C, Heers M, et al. Transcutaneous vagus nerve stimulation (t-VNS) in pharmacoresistant epilepsies: a proof of concept trial. *Epilepsia.* (2012) 53:115–8. doi: 10.1111/j.1528-1167.2012.03492.x
95. Henssen DJHA, Derks B, van Doorn M, Verhoogt NC, Staats P, Vissers K, et al. Visualizing the trigeminovagal complex in the human medulla by combining ex-vivo ultra-high resolution structural MRI and polarized light imaging microscopy. *Sci Rep.* (2019) 9:1–11. doi: 10.1038/s41598-019-47855-5
96. Qing KY, Wasilczuk KM, Ward MP, Phillips EH, Vlachos PP, Goergen CJ, et al. B fibers are the best predictors of cardiac activity during vagus nerve stimulation. *Bioelectron Med.* (2018) 4:5. doi: 10.1186/s42234-018-0005-8
97. Kaniusas E, Kampusch S, Tittgemeyer M, Panetsos F, Gines RF, Papa M, et al. Current directions in the auricular vagus nerve stimulation I - a physiological perspective. *Front Neurosci.* (2019) 13:854. doi: 10.3389/fnins.2019.00854

98. de Lartigue G. Role of the vagus nerve in the development and treatment of diet-induced obesity. *J Physiol.* (2016) 594:5791–815. doi: 10.1113/JP271538
99. Shen MJ. The cardiac autonomic nervous system: an introduction. *Herzschrittmachertherapie Elektrophysiologie.* (2021) 32:295–301. doi: 10.1007/s00399-021-00776-1
100. Tosato M, Yoshida K, Toft E, Nekrasas V, Struijk JJ. Closed-loop control of the heart rate by electrical stimulation of the vagus nerve. *Med Biol Eng Comput.* (2006) 44:161–9. doi: 10.1007/s11517-006-0037-1
101. Naggar I, Nakase K, Lazar J, Salciccioli L, Selesnick I, Stewart M. Vagal control of cardiac electrical activity and wall motion during ventricular fibrillation in large animals. *Auton Neurosci Basic Clin.* (2014) 183:12–22. doi: 10.1016/j.autneu.2014.01.009
102. Komisaruk BR, Frangos E. Vagus nerve afferent stimulation: projection into the brain, reflexive physiological, perceptual, and behavioral responses, and clinical relevance. *Auton Neurosci Basic Clin.* (2022) 237:102908. doi: 10.1016/j.autneu.2021.102908
103. Yamakawa K, So EL, Rajendran PS, Hoang JD, Makkar N, Mahajan A, et al. Electrophysiological effects of right and left vagal nerve stimulation on the ventricular myocardium. *AJP Heart Circ Physiol.* (2014) 307:H722–31. doi: 10.1152/ajpheart.00279.2014
104. Machhada A, Hosford PS, Dyson A, Ackland GL, Mastitskaya S, Gourine AV. Optogenetic stimulation of vagal efferent activity preserves left ventricular function in experimental heart failure. *JACC Basic to Transl Sci.* (2020) 5:799–810. doi: 10.1016/j.jacbts.2020.06.002
105. De Ferrari GM, Schwartz PJ. Vagus nerve stimulation: from pre-clinical to clinical application: challenges and future directions. *Heart Fail Rev.* (2011) 16:195–203. doi: 10.1007/s10741-010-9216-0
106. Zhao S, Dai Y, Ning X, Tang M, Zhao Y, Li Z, et al. Vagus nerve stimulation in early stage of acute myocardial infarction prevent ventricular arrhythmias and cardiac remodeling. *Front Cardiovasc Med.* (2021) 8:648910. doi: 10.3389/fcvm.2021.648910
107. Beaumont E, Southerland EM, Hardwick JC, Wright GL, Ryan S, Li Y, et al. Vagus nerve stimulation mitigates intrinsic cardiac neuronal and adverse myocyte remodeling postmyocardial infarction. *Am J Physiol Heart Circ Physiol.* (2015) 309:H1198–206. doi: 10.1152/ajpheart.00393.2015
108. Li M, Zheng C, Sato T, Kawada T, Sugimachi M, Sunagawa K. Vagal nerve stimulation markedly improves long-term survival after chronic heart failure in rats. *Circulation.* (2004) 109:120–4. doi: 10.1161/01.CIR.0000105721.71640.DA
109. Zhang Y, Popović ZB, Bibevski S, Fakhry I, Sica DA, Van Wagoner DR, et al. Chronic vagus nerve stimulation improves autonomic control and attenuates systemic inflammation and heart failure progression in a canine high-rate pacing model. *Circ Heart Fail.* (2009) 2:692–9. doi: 10.1161/CIRCHEARTFAILURE.109.873968
110. Uitterdijk A, Yetgin T, te Lintel Hekkert M, Sneep S, Krabbendam-Peters I, van Beusekom HMM, et al. Vagal nerve stimulation started just prior to reperfusion limits infarct size and no-reflow. *Basic Res Cardiol.* (2015) 110:508. doi: 10.1007/s00395-015-0508-3
111. Shinlapawittayatorn K, Chinda K, Palee S, Surinkaew S, Kumfu S, Kumphune S, et al. Vagus nerve stimulation initiated late during ischemia, but not reperfusion, exerts cardioprotection via amelioration of cardiac mitochondrial dysfunction. *Heart Rhythm.* (2014) 11:2278–86. doi: 10.1016/j.hrthm.2014.08.001
112. Nuntaphum W, Pongkan W, Wongjaikam S, Thummasorn S, Tanajak P, Khamseekaew J, et al. Vagus nerve stimulation exerts cardioprotection against myocardial ischemia/reperfusion injury predominantly through its efferent vagal fibers. *Basic Res Cardiol.* (2018) 113:1–20. doi: 10.1007/s00395-018-0683-0
113. Shinlapawittayatorn K, Chinda K, Palee S, Surinkaew S, Thunsiri K, Weerateerangkul P, et al. Low-amplitude, left vagus nerve stimulation significantly attenuates ventricular dysfunction and infarct size through prevention of mitochondrial dysfunction during acute ischemia-reperfusion injury. *Heart Rhythm.* (2013) 10:1700–7. doi: 10.1016/j.hrthm.2013.08.009
114. Menuet C, Connelly AA, Bassi JK, Melo MR, Le S, Kamar J, et al. Prebötzinger complex neurons drive respiratory modulation of blood pressure and heart rate. *Elife.* (2020) 9:1–30. doi: 10.7554/eLife.57288
115. Thayer JF, Lane RD. The role of vagal function in the risk for cardiovascular disease and mortality. *Biol Psychol.* (2007) 74:224–42. doi: 10.1016/j.biopsycho.2005.11.013
116. Gold MR, Veldhuisen DJ, Hauptman PJ, Borggrefe M, Kubo SH, Lieberman RA, et al. Vagus nerve stimulation for the treatment of heart failure: the INOVATE-HF trial. *J Am Coll Cardiol.* (2016) 68:149–58. doi: 10.1016/j.jacc.2016.03.525
117. De Ferrari GM, Tuinenburg AE, Ruble S, Brugada J, Klein H, Butter C, et al. Rationale and study design of the neurocardiac therapy for heart failure study: NECTAR-HF. *Eur J Heart Fail.* (2014) 16:692–9. doi: 10.1002/ejhf.80
118. Zannad F, De Ferrari GM, Tuinenburg AE, Wright D, Brugada J, Butter C, et al. Chronic vagal stimulation for the treatment of low ejection fraction heart failure: results of the neural cardiac therapy for heart failure (NECTAR-HF) randomized controlled trial. *Eur Heart J.* (2015) 36:425–33. doi: 10.1093/eurheartj/ehu345
119. De Ferrari GM, Crijns HJGM, Borggrefe M, Milasinovic G, Smid J, Zabel M, et al. Chronic vagus nerve stimulation: a new and promising therapeutic approach for chronic heart failure. *Eur Heart J.* (2011) 32:847–55. doi: 10.1093/eurheartj/ehq391
120. Schwartz PJ, De Ferrari GM, Sanzo A, Landolina M, Rordorf R, Raineri C, et al. long term vagal stimulation in patients with advanced heart failure first experience in man. *Eur J Heart Fail.* (2008) 10:884–91. doi: 10.1016/j.ejheart.2008.07.016
121. De Ferrari GM, Stolen C, Tuinenburg AE, Wright DJ, Brugada J, Butter C, et al. Long-term vagal stimulation for heart failure: eighteen month results from the neural cardiac therapy for heart failure (NECTAR-HF) trial. *Int J Cardiol.* (2017) 244:229–34. doi: 10.1016/j.ijcard.2017.06.036
122. Nearing BD, Libbus I, Amurthur B, Kenknight BH, Verrier RL. Acute autonomic engagement assessed by heart rate dynamics during vagus nerve stimulation in patients with heart failure in the ANTHEM-HF trial. *J Cardiovasc Electrophysiol.* (2016) 27:1072–7. doi: 10.1111/jce.13017
123. Sant'Anna LB, Couceiro SLM, Ferreira EA, Sant'Anna MB, Cardoso PR, Mesquita ET, et al. Vagal neuromodulation in chronic heart failure with reduced ejection fraction: a systematic review and meta-analysis. *Front Cardiovasc Med.* (2021) 8:766676. doi: 10.3389/fcvm.2021.766676
124. Hauptman PJ, Schwartz PJ, Gold MR, Borggrefe M, Van Veldhuisen DJ, Starling RC, et al. Rationale and study design of the increase of vagal tone in heart failure study: INOVATE-HF. *Am Heart J.* (2012) 163:954–62.e1. doi: 10.1016/j.ahj.2012.03.021
125. Yamaguchi N, Yamakawa K, Rajendran PS, Takamiya T, Vaseghi M. Antiarrhythmic effects of vagal nerve stimulation after cardiac sympathetic denervation in the setting of chronic myocardial infarction. *Heart Rhythm.* (2018) 15:1214–22. doi: 10.1016/j.hrthm.2018.03.012
126. Tran N, Asad Z, Elkholey K, Scherlag BJ, Po SS, Stavrakis S. Autonomic neuromodulation acutely ameliorates left ventricular strain in humans. *J Cardiovasc Transl Res.* (2019) 12:221–30. doi: 10.1007/s12265-018-9853-6
127. DiCarlo LA, Libbus I, Kumar HU, Mittal S, Premchand RK, Amurthur B, et al. Autonomic regulation therapy to enhance myocardial function in heart failure patients: the ANTHEM-HFpEF study. *ESC Heart Fail.* (2018) 5:95–100. doi: 10.1002/ehf2.12241
128. Libbus I, Nearing BD, Amurthur B, KenKnight BH, Verrier RL. Autonomic regulation therapy suppresses quantitative T-wave alternans and improves baroreflex sensitivity in patients with heart failure enrolled in the ANTHEM-HF study. *Heart Rhythm.* (2016) 13:721–8. doi: 10.1016/j.hrthm.2015.11.030
129. Klein HU, De Ferrari GM. Vagus nerve stimulation: a new approach to reduce heart failure. *Cardiol J.* (2010) 17:638–43.
130. Murray K, Reardon C. The cholinergic anti-inflammatory pathway revisited. *Neurogastroenterol Motil.* (2018) 30:1–6. doi: 10.1111/nmo.13288
131. Aaronson ST, Carpenter LL, Conway CR, Reimherr FW, Lisanby SH, Schwartz TL, et al. Vagus nerve stimulation therapy randomized to different amounts of electrical charge for treatment-resistant depression: acute and chronic effects. *Brain Stimul.* (2013) 6:631–40. doi: 10.1016/j.brs.2012.09.013
132. Famm K, Litt B, Tracey KJ, Boyden ES, Slaoui M. A jump-start for electroceuticals. *Nature.* (2013) 496:159–61. doi: 10.1038/496159a
133. Cracchiolo M, Ottaviani MM, Panarese A, Strauss I, Vallone F, Mazzoni A, et al. Bioelectronic medicine for the autonomic nervous system: clinical

applications and perspectives. *J Neural Eng.* (2021) 18. doi: 10.1088/1741-2552/abe6b9
134. Raspopovic S, Capogrosso M, Micera S. A computational model for the stimulation of rat sciatic nerve using a transverse intrafascicular multichannel electrode. *IEEE Trans Neural Syst Rehabil Eng.* (2011) 19:333–44. doi: 10.1109/TNSRE.2011.2151878
135. Romeni S, Valle G, Mazzoni A, Micera S. Tutorial: a computational framework for the design and optimization of peripheral neural interfaces. *Nat Protoc.* (2020) 15:3129–53. doi: 10.1038/s41596-020-0377-6
136. Raspopovic S, Capogrosso M, Badia J, Navarro X, Micera S. Experimental validation of a hybrid computational model for selective stimulation using transverse intrafascicular multichannel electrodes. *IEEE Trans Neural Syst Rehabil Eng.* (2012) 20:395–404. doi: 10.1109/TNSRE.2012.2189021
137. Sun FT, Morrell MJ. Closed-loop Neurostimulation: the clinical experience. *Neurotherapeutics.* (2014) 11:553–63. doi: 10.1007/s13311-014-0280-3
138. Romero-Ugalde HM, Le Rolle V, Bonnet J-L, Henry C, Mabo P, Carrault G, et al. Closed-loop vagus nerve stimulation based on state transition models. *IEEE Trans Biomed Eng.* (2018) 65:1630–8. doi: 10.1109/TBME.2017.2759667
139. Cracchiolo M, Valle G, Petrini F, Strauss I, Granata G, Stieglitz T, et al. Decoding of grasping tasks from intraneural recordings in trans-radial amputee. *J Neural Eng.* (2020) 17:026034. doi: 10.1088/1741-2552/ab8277
140. Jastrzebska-Perfect P, Chowdhury S, Spyropoulos GD, Zhao Z, Cea C, Gelinas JN, et al. Translational neuroelectronics. *Adv Funct Mater.* (2020) 1909165:1–31. doi: 10.1002/adfm.201909165
141. Ereifej ES, Shell CE, Schofield JS, Charkhkar H, Cuberovic I, Dorval AD, et al. Neural engineering: the process, applications, and its role in the future of medicine. *J Neural Eng.* (2019) 16:063002. doi: 10.1088/1741-2552/ab4869
142. Kaniusas E, Kampusch S, Tittgemeyer M, Panetsos F, Gines RF, Papa M, et al. Current directions in the auricular vagus nerve stimulation II - an engineering perspective. *Front Neurosci.* (2019) 13:772. doi: 10.3389/fnins.2019.00772
143. Dirr EW, Urdaneta ME, Patel Y, Johnson RD, Campbell-Thompson M, Otto KJ. Designing a bioelectronic treatment for type 1 diabetes: targeted parasympathetic modulation of insulin secretion. *Bioelectron Med.* (2020) 3:17–31. doi: 10.2217/bem-2020-0006
144. Sevcencu C, Nielsen TN, Struijk JJ. An intraneural electrode for bioelectronic medicines for treatment of hypertension. *Neuromodulation.* (2018) 21:777–86. doi: 10.1111/ner.12758
145. Plachta DTT, Gierthmuehlen M, Cota O, Espinosa N, Boeser F, Herrera TC, et al. Blood pressure control with selective vagal nerve stimulation and minimal side effects. *J Neural Eng.* (2014) 11:036011. doi: 10.1088/1741-2560/11/3/036011
146. Gonzalez AG, Etienne-cummings R, Georgiou P. Closed-loop bioelectronic medicine for diabetes management. *Bioelectron Med.* (2020) 6:4. doi: 10.1186/s42234-020-00046-4
147. Navarro X, Krueger TB, Lago N, Micera S, Stieglitz T, Dario P. A critical review of interfaces with the peripheral nervous system for the control of neuroprotheses and hybrid bionic systems. *J Peripher Nerv Syst.* (2005) 10:229–58. doi: 10.1111/j.1085-9489.2005.10303.x
148. Boretius T, Badia J, Pascual-Font A, Schuettler M, Navarro X, Yoshida K, et al. A transverse intrafascicular multichannel electrode (TIME) to interface with the peripheral nerve. *Biosens Bioelectron.* (2010) 26:62–9. doi: 10.1016/j.bios.2010.05.010
149. Rijnbeek EH, Eleveld N, Olthuis W. Update on peripheral nerve electrodes for closed-loop neuroprosthetics. *Front Neurosci.* (2018) 12:350. doi: 10.3389/fnins.2018.00350
150. Cutrone A, Valle J, Del, Santos D, Badia J, Filippeschi C, Micera S, et al. A three-dimensional self-opening intraneural peripheral interface ({SELINE}). *J Neural Eng.* (2015) 12:16016. doi: 10.1088/1741-2560/12/1/016016
151. Strauss I, Niederhoffer T, Giannotti A, Panarese AM, Bernini F, Gabisonia K, et al. The Q-PINE: a quick-to-implant peripheral intraneural electrode. *J Neural Eng.* (2020) 17. doi: 10.1088/1741-2552/abc52a
152. Vallone F, Ottaviani MM, Dedola F, Cutrone A, Romeni S, Macrì Panarese A, et al. Simultaneous decoding of cardiovascular and respiratory functional changes from pig intraneural vagus nerve signals. *J Neural Eng.* (2021) 18. doi: 10.1088/1741-2552/ac0d42
153. Zanos TP, Silverman HA, Levy T, Tsaava T, Battinelli E, Lorraine PW, et al. Identification of cytokine-specific sensory neural signals by decoding murine vagus nerve activity. *Proc Natl Acad Sci USA.* (2018) 115:E4843–52. doi: 10.1073/pnas.1719083115
154. Plachta DTT, Espinosa N, Gierthmuehlen M, Cota O, Herrera TC, Stieglitz T. Detection of baroreceptor activity in rat vagal nerve recording using a multi-channel cuff-electrode and real-time coherent averaging. *Proc Annu Int Conf IEEE Eng Med Biol Soc EMBS.* (2012) 2012:3416–9. doi: 10.1109/EMBC.2012.6346699
155. Sevcencu C, Nielsen TN, Struijk JJ. A neural blood pressure marker for bioelectronic medicines for treatment of hypertension. *Biosens Bioelectron.* (2017) 98:1–6. doi: 10.1016/j.bios.2017.06.031
156. Rozman J, Ribarič S. Selective recording of electroneurograms from the left vagus nerve of a dog during stimulation of cardiovascular or respiratory systems. *Chin J Physiol.* (2007) 50:240–50.
157. Citi L, Carpaneto J, Yoshida K, Hoffmann KP, Koch KP, Dario P, et al. On the use of wavelet denoising and spike sorting techniques to process electroneurographic signals recorded using intraneural electrodes. *J Neurosci Methods.* (2008) 172:294–302. doi: 10.1016/j.jneumeth.2008.04.025
158. Rossini PM, Micera S, Benvenuto A, Carpaneto J, Cavallo G, Citi L, et al. Double nerve intraneural interface implant on a human amputee for robotic hand control. *Clin Neurophysiol.* (2010) 121:777–83. doi: 10.1016/j.clinph.2010.01.001
159. Micera S, Citi L, Rigosa J, Carpaneto J, Raspopovic S, Di Pino G, et al. Decoding information from neural signals recorded using intraneural electrodes: toward the development of a neurocontrolled hand prosthesis. *Proc IEEE.* (2010) 98:407–17. doi: 10.1109/JPROC.2009.2038726
160. Musick KM, Rigosa J, Narasimhan S, Wurth S, Capogrosso M, Chew DJ, et al. Chronic multichannel neural recordings from soft regenerative microchannel electrodes during gait. *Sci Rep.* (2015) 5:1–9. doi: 10.1038/srep14363
161. Tombini M, Rigosa J, Zappasodi F, Porcaro C, Citi L, Carpaneto J, et al. Combined analysis of cortical (EEG) and nerve stump signals improves robotic hand control. *Neurorehabil Neural Repair.* (2012) 26:275–81. doi: 10.1177/1545968311408919
162. Pani D, Barabino G, Citi L, Meloni P, Raspopovic S, Micera S, et al. Real-time neural signals decoding onto off-the-shelf DSP processors for neuroprosthetic applications. *IEEE Trans Neural Syst Rehabil Eng.* (2016) 24:993–1002. doi: 10.1109/TNSRE.2016.2527696
163. Rey HG, Pedreira C, Quian Quiroga R. Past, present and future of spike sorting techniques. *Brain Res Bull.* (2015) 119:106–17. doi: 10.1016/j.brainresbull.2015.04.007
164. Kamavuako EN, Jensen W, Yoshida K, Kurstjens M, Farina D. A criterion for signal-based selection of wavelets for denoising intrafascicular nerve recordings. *J Neurosci Methods.* (2010) 186:274–80. doi: 10.1016/j.jneumeth.2009.11.022
165. Diedrich A, Charoensuk W, Brychta RJ, Ertl AC, Shiavi R. Analysis of raw microneurographic recordings based on wavelet de-noising technique and classification algorithm: wavelet analysis in microneurography. *EEE Trans Biomed Eng.* (2003) 50:41–50. doi: 10.1109/TBME.2002.807323.Analysis
166. Ottaviani MM, Wright L, Dawood T, Macefield VG. In vivo recordings from the human vagus nerve using ultrasound—guided microneurography. *J Physiol.* (2020) 598:3569–76. doi: 10.1113/JP280077
167. Battinelli E, Levy T, Tsaava T, Bouton CE, Tracey KJ, Chavan SS, et al. Identification of hypoglycemia-specific neural signals by decoding murine vagus nerve. *Bioelectron Med.* (2018) 115:E4843–52.
168. Spearman BS, Desai VH, Mobini S, McDermott MD, Graham JB, Otto KJ, et al. Tissue-engineered peripheral nerve interfaces. *Adv Funct Mater.* (2018) 28:1–18. doi: 10.1002/adfm.201701713
169. Micera S, Rossini PM, Rigosa J, Citi L, Carpaneto J, Raspopovic S, et al. Decoding of grasping information from neural signals recorded using peripheral intrafascicular interfaces. *J Neuroeng Rehabil.* (2011) 8:53. doi: 10.1186/1743-0003-8-53
170. Badia J, Raspopovic S, Carpaneto J, Micera S, Navarro X. Spatial and functional selectivity of peripheral nerve signal recording with the transversal intrafascicular multichannel electrode (TIME). *IEEE Trans Neural Syst Rehabil Eng.* (2016) 24:20–7. doi: 10.1109/TNSRE.2015.2440768

171. Raspopovic S, Carpaneto J, Udina E, Navarro X, Micera S. On the identification of sensory information from mixed nerves by using single-channel cuff electrodes. *J Neuroeng Rehabil.* (2010) 7:1–15. doi: 10.1186/1743-0003-7-17
172. Wurth S, Capogrosso M, Raspopovic S, Gandar J, Federici G, Kinany N, et al. Long-term usability and bio-integration of polyimide-based intra-neural stimulating electrodes. *Biomaterials.* (2017) 122:114–29. doi: 10.1016/j.biomaterials.2017.01.014
173. Davey CE, Soto-Breceda A, Shafton A, McAllen RM, Furness JB, Grayden DB, et al. A new algorithm for drift compensation in multi-unit recordings of action potentials in peripheral autonomic nerves over time. *J Neurosci Methods.* (2020) 338:108683. doi: 10.1016/j.jneumeth.2020.108683
174. Marmerstein JT, Mccallum GA, Durand DM. Decoding vagus-nerve activity with carbon nanotube sensors in freely moving rodents. *Biosensors.* (2022) 12:114. doi: 10.3390/bios12020114
175. Vespa S, Stumpp L, Bouckaert C, Delbeke J, Smets H, Cury J, et al. Vagus nerve stimulation-induced laryngeal motor evoked potentials: a possible biomarker of effective nerve activation. *Front Neurosci.* (2019) 13:880. doi: 10.3389/fnins.2019.00880
176. Yoo PB, Liu H, Hincapie JG, Ruble SB, Hamann JJ, Grill WM. Modulation of heart rate by temporally patterned vagus nerve stimulation in the anesthetized dog. *Physiol Rep.* (2016) 4:1–10. doi: 10.14814/phy2.12689
177. Chang YC, Cracchiolo M, Ahmed U, Mughrabi I, Gabalski A, Daytz A, et al. Quantitative estimation of nerve fiber engagement by vagus nerve stimulation using physiological markers. *Brain Stimul.* (2020) 13:1617–30. doi: 10.1016/j.brs.2020.09.002
178. Parker JL, Shariati NH, Karantonis DM. Electrically evoked compound action potential recording in peripheral nerves. *Bioelectron Med.* (2018) 1:71–83. doi: 10.2217/bem-2017-0005
179. El Tahry R, Raedt R, Mollet L, De Herdt V, Wyckuys T, Van Dycke A, et al. A novel implantable vagus nerve stimulation system (ADNS-300) for combined stimulation and recording of the vagus nerve: pilot trial at Ghent university hospital. *Epilepsy Res.* (2010) 92:231–9. doi: 10.1016/j.eplepsyres.2010.10.007
180. Rozman J, Pečlin P, Ribarič S, Godec M, Burja J. An improved method of crafting a multi-electrode spiral cuff for the selective stimulation of peripheral nerves. *Sci Rep.* (2018) 8:915. doi: 10.1038/s41598-018-19318-w
181. Ordelman SCMA, Kornet L, Cornelussen R, Buschman HPJ, Veltink PH. An indirect component in the evoked compound action potential of the vagal nerve. *J Neural Eng.* (2010) 7:066001. doi: 10.1088/1741-2560/7/6/066001
182. Stieglitz T. Of man and mice: translational research in neurotechnology. *Neuron.* (2020) 105:12–5. doi: 10.1016/j.neuron.2019.11.030
183. Asirvatham S, Londoner K, Aravamudan M, Deering T, Heidbuchel H, Kapa S, et al. Building a bioelectronic medicine movement 2019: insights from leaders in industry, academia, and research. *Bioelectron Med.* (2020) 6:1–11. doi: 10.1186/s42234-020-0037-8

Conflict of Interest: The authors declare that the research was conducted in the absence of any commercial or financial relationships that could be construed as a potential conflict of interest.

Publisher's Note: All claims expressed in this article are solely those of the authors and do not necessarily represent those of their affiliated organizations, or those of the publisher, the editors and the reviewers. Any product that may be evaluated in this article, or claim that may be made by its manufacturer, is not guaranteed or endorsed by the publisher.

frontiers | Frontiers in Cardiovascular Medicine

ORIGINAL RESEARCH
published: 02 May 2022
doi: 10.3389/fcvm.2022.843144

Heart Rate Variability Reveals Altered Autonomic Regulation in Response to Myocardial Infarction in Experimental Animals

*Emanuele Pizzo[1], Silvia Berrettoni[1], Ridhima Kaul[1], Daniel O. Cervantes[1], Valeria Di Stefano[1], Sudhir Jain[2], Jason T. Jacobson[1,3] and Marcello Rota[1]**

[1] Department of Physiology, New York Medical College, Valhalla, NY, United States, [2] Department of Pathology, Microbiology and Immunology, New York Medical College, Valhalla, NY, United States, [3] Department of Cardiology, Westchester Medical Center, Valhalla, NY, United States

The analysis of beating rate provides information on the modulatory action of the autonomic nervous system on the heart, which mediates adjustments of cardiac function to meet hemodynamic requirements. In patients with myocardial infarction, alterations of heart rate variability (HRV) have been correlated to the occurrence of arrhythmic events and all-cause mortality. In the current study, we tested whether experimental rodent models of myocardial infarction recapitulate dynamics of heart rate variability observed in humans, and constitute valid platforms for understanding mechanisms linking autonomic function to the development and manifestation of cardiovascular conditions. For this purpose, HRV was evaluated in two engineered mouse lines using electrocardiograms collected in the conscious, restrained state, using a tunnel device. Measurements were obtained in naïve mice and animals at 3–∼28 days following myocardial infarction, induced by permanent coronary artery ligation. Two mouse lines with inbred and hybrid genetic background and, respectively, homozygous (Homo) and heterozygous (Het) for the MerCreMer transgene, were employed. In the naïve state, Het female and male mice presented prolonged RR interval duration (∼9%) and a ∼4-fold increased short- and long-term RR interval variability, with respect to sex-matched Homo mice. These differences were abrogated by pharmacological interventions inhibiting the sympathetic and parasympathetic axes. At 3–∼14 days after myocardial infarction, RR interval duration increased in Homo mice, but was not affected in Het animals. In contrast, Homo mice had minor modifications in HRV parameters, whereas substantial (> 50%) reduction of short- and long-term RR interval variation occurred in Het mice. Interestingly, *ex vivo* studies in isolated organs documented that intrinsic RR interval duration increased in infarcted vs. non-infarcted Homo and Het hearts, whereas RR interval variation was not affected. In conclusion, our study documents that, as observed in humans, myocardial infarction in rodents is associated with alterations in heart rhythm dynamics consistent with sympathoexcitation and parasympathetic withdrawal. Moreover, we report that mouse strain is an important variable when evaluating autonomic function via the analysis of HRV.

Keywords: heart rate variability (HRV), myocardial infarction, autonomic regulation of heart, mouse, electrocardiogram

OPEN ACCESS

Edited by:
Marco Mongillo,
University of Padua, Italy

Reviewed by:
Tania Zaglia,
University of Padova, Italy
Baopeng Tang,
First Affiliated Hospital of Xinjiang Medical University, China

****Correspondence:***
Marcello Rota
marcello_rota@nymc.edu

Specialty section:
This article was submitted to Hypertension, a section of the journal Frontiers in Cardiovascular Medicine

Received: *24 December 2021*
Accepted: *04 April 2022*
Published: *02 May 2022*

Citation:
Pizzo E, Berrettoni S, Kaul R, Cervantes DO, Di Stefano V, Jain S, Jacobson JT and Rota M (2022) Heart Rate Variability Reveals Altered Autonomic Regulation in Response to Myocardial Infarction in Experimental Animals. Front. Cardiovasc. Med. 9:843144. doi: 10.3389/fcvm.2022.843144

INTRODUCTION

The autonomic nervous system modulates beating rate and modality of myocardial excitation, contraction, and relaxation allowing adjustments of cardiac performance to meet hemodynamic requirements under various conditions. Cardiac autonomic regulation occurs via feedback loop mechanisms involving, on the one hand, afferent sensory information transmitted from mechanoreceptors and chemoreceptors of heart and vasculature to intrathoracic ganglia and central nervous system. On the other hand, efferent cardiomotor neural impulses originating in the nervous system return to the heart via sympathetic and parasympathetic nerves, influencing heart rate, electrical conduction, and myocardial function (1, 2).

Sympathetic and parasympathetic stimulation, respectively, increases and decreases heart rate by modulating sinoatrial node discharge (3, 4). Norepinephrine, released by sympathetic nerves, binds β-adrenergic receptors activating adenylyl cyclase and cyclic AMP production, which induces faster diastolic depolarization and rapid firing rate. In contrast, acetylcholine, released by parasympathetic nerves, opens G-protein regulated K^+ channels and binds muscarinic receptors that inhibit adenylyl cyclase, with the overall effect of reducing firing rate of the sinoatrial node. Although β-adrenergic and muscarinic receptors share common downstream transduction molecules, the pattern of beating rate adjustment following stimulation of the two signaling axes occurs with different kinetics. Specifically, parasympathetic activation has instantaneous and brief consequences on heart rate, whereas sympathetic stimulation has longer latency effects (5–9). Thus, based on the modalities of action of the two branches of the autonomic system on sinoatrial node discharge, the analysis of heart rate dynamics provides information on the influence of sympathetic and parasympathetic tone on the heart (5, 6, 9, 10).

Myocardial infarction and other cardiac pathologies interfering with pump function largely affect autonomic regulation. Acutely, sympathoexcitation and parasympathetic tone withdrawal allow for the preservation of cardiac output, but this initial response is often associated with chronic changes in the autonomic nervous system, involving abnormal cardiac afferent activity, excessive neuronal interactive excitability, and altered neuronal hierarchy (1, 2). The ensuing autonomic dysfunction together with neurohumoral activation, secondary to circulatory changes (11), are important factors in the progression of the diseased condition and enhanced vulnerability of the heart to arrhythmias (1, 12).

Heart rate variability (HRV) has been studied in patients suffering from myocardial infarction and indices of heart rate dynamics have been correlated to recurrent coronary events, cardiac arrhythmias, sudden cardiac death, and all-cause mortality (13, 14). Clinical investigations not only have strengthened the prognostic value of specific parameters of heart rate variability for patients with ischemic damage or other cardiovascular complications, but have also substantiated the prominent role of cardiac autonomic regulation in the initiation and progression of pathological conditions (2).

In the current study, we have attempted to clarify whether experimental animal models of cardiac disease recapitulate features of heart rate dynamics observed in humans, constituting valid platforms for the understanding of mechanisms linking heart rate variability and the development and manifestation of diseased conditions. Specifically, we have evaluated the acute and long terms consequences of myocardial infarction on heart rate dynamics in two mouse lines, using electrocardiograms (ECGs) collected in the conscious, restrained state, using a tunnel device (Emka Technologies). This analysis has been complemented with *ex vivo* studies in isolated organs to assess intrinsic beating rate of normal and infarcted hearts. Importantly, this investigation was conducted in mouse lines typically employed as control animals for studies allowing for conditional and inducible gene manipulations in the heart, as done previously by our group (15). These refined genetically engineered models represent remarkable tools for the elucidation of signaling pathways that underlie normal and diseased states, and have gained widespread use and recognition (16, 17). Our findings indicate that myocardial infarction reduces long- and short-term heart rate variability, which is consistent with enhanced sympathetic and reduced parasympathetic tone. Moreover, we found that, experimentally, mouse strain is an important variable when assessing heart rate variability in normal and pathological status.

MATERIALS AND METHODS

All data, materials, and methods of this study are available from the corresponding author upon reasonable request.

Experimental Animals

Mice were maintained in accordance with the Guide for Care and Use of Laboratory Animals; animal experiments were approved by the local institutional animal care committees (IACUC) of New York Medical College. When needed, isoflurane (1–1.5%, inhalation) was employed as a methodology of anesthesia. Euthanasia was attained under anesthesia by bilateral thoracotomy and removal of the heart.

For this investigation, data collected from single transgenic mice homozygous or heterozygous for the alpha-MHC-MerCreMer (αMHC-MCM) transgene were used. In these animals, the mouse cardiac-specific alpha-myosin heavy chain promoter (αMHC) directs expression of a tamoxifen-inducible Cre recombinase (MerCreMer), allowing for the temporally regulated modulation of loxP-flanked targeted genes in cardiomyocytes of bi-transgenic mice (17). Mice homozygous or heterozygous for the αMHC-MCM transgene and presenting LoxP-flanked sequences have been widely employed for inducible and conditional gene targeting. Currently, according to the Web of Science database, there are >400 published research articles citing the original investigation reporting the development of the αMHC-MCM mouse line (17). Therefore, based on the relevance of this engineered mouse line, we employed homozygous and heterozygous αMHC-MCM animals, which are typically used as control mice in studies with conditional and temporal regulation of the expressions of genes of interest.

For this purpose, *B6.FVB (129)-A1cf*$^{Tg\ (Myh6-cre/Esr1*)1Jmk}$*/J* mice (αMHC-MCM, Jackson Labs, Stock No. 005657) (15, 17), backcrossed onto C57BL/6J inbred mice by the vendor to obtain a congenic strain, were utilized for breeding. Homozygous αMHC-MerCreMer mice (Homo) were obtained by inbreed crossing. In contrast, heterozygous αMHC-MerCreMer mice (Het) were generated by selecting the F1 hybrid progeny of mice originated from the crossing of αMHC-MCM homozygous animals with hemizygous ZEG-NICD mice (Jackson Labs, Stock No. 6850), originally derived on 129/Sv strain (15, 18). The F1 hybrid progeny consisted of single transgenic heterozygous αMHC-MCM mice and double transgenic heterozygous αMHC-MCM and ZEG-NICD mice born with normal Mendelian ratio of ∼1:1. From the progeny of the latter breeding scheme, only heterozygous αMHC-MCM mice and lacking ZEG-NICD transgene were used for this study. Therefore, no genes other than the αMHC-MCM were deleted or overexpressed in mice studied in this investigation. Moreover, C57Bl/6 mice and non-carrier mice used as control for the ZEG-NICD strain (wild-type) were introduced to provide information on the influence of genetic background on parameters studies in this investigation. C57Bl/6 mice were obtained from Charles River.

Cre recombinase expression in homozygous and heterozygous αMHC-MerCreMer mice was induced by administration of tamoxifen (Sigma-Aldrich) dissolved in 10% ethanol and 90% peanut oil (Sigma-Aldrich) for 4 days (30 mg/Kg of body weight/day, i.p.) over a period of 4–8 days (15, 19). The dose of tamoxifen was optimized to minimize off-target and confounding effects of drug administration and Cre recombinase expression in the heart, including the development of transient cardiomyopathy and DNA-damage response (19, 20). Mice were enrolled in the study at 3 or more weeks after induction of gene expression. Animals in the naïve state were studied before and after tamoxifen administration and Cre recombinase expression.

Unless otherwise specified, collected data were disaggregated by sex. Electrocardiographic analysis was performed in mice with age ranging from 2.4 to 6.6 months. For tests addressing the influence of the autonomic nervous system on heart rate dynamics of *ex vivo* perfused hearts, organs were obtained from homozygous αMHC-MerCreMer male and female mice at 4.3–8.5 months of age.

Myocardial Infarction

Myocardial infarction was performed under sterile conditions via thoracotomy and coronary artery ligation (21, 22). Under isoflurane anesthesia (∼1.5%), the animal was intubated and ventilated continuously during the surgical procedure. A local anesthetic (lidocaine, ∼4 mg/kg) was injected subcutaneously in the incision site before and after the surgical procedure. The thorax was opened via the third intercostal space, the atrial appendage elevated. The left coronary artery was located, and suture (6–0 Silk DR12 Black 18" Braid, Henry Schein) was inserted around the vessel near the origin and the artery occluded. The chest was closed with suture and pneumothorax reduced by negative pressure. Skin incision was closed using a 9 mm wound clip (Fine Science Tool). To reduce postoperative pain following the procedure, buprenorphine hydrochloride (Buprenex), 0.5–1 mg/kg body weight, was injected i.p. every 12 h for a period of 48 h after surgery.

Electrocardiographic Recording in the Conscious State

To record electrocardiograms (ECGs) in conscious animals an ECG-tunnel device (Emka Technologies) was employed (23–25). Animals were placed in a tunnel and ECGs recorded for a period of 10 min. Electrical signals were amplified with a 12 Lead ECG Amplifier (DSI, Ponemah), digitized using a 160 kHz A/D converter (DI-1120 HS, Dataq) and recorded with WinDaq software (Dataq). The bipolar lead I, II, and III and the unipolar lead aVL were collected. Electrical signals were evaluated offline with LabChart 8 for the analysis of heart rate variability and occurrence of rhythm disturbances (24).

In vivo Cardiac Function

Echocardiography was performed in conscious mice, with singlehanded manual restraint method, using an Acuson Sequoia c512 equipped with a 13 MHz (15L8) linear transducer (26–29). By this approach, m-mode images in the parasternal short axis view of the left ventricle (LV) were employed to evaluate chamber diameter and wall thickness in diastole and systole, for computation of LV volume, mass, and ejection fraction (EF) by the Teichholz formula (26–29).

Drugs

Effects of pharmacological compounds on heart rate and heart rate variability (HRV) were tested by comparing 10 min ECG recordings obtained before and after drug administration. In between acquisitions, mice were returned to their cages.

To interfere with autonomic nervous system, mice were administered with the combination of atropine (0.5 mg/kg body weight, i.p.) plus propranolol (1 mg/kg body weight, i.p.) for combined block of sympathetic and parasympathetic branches of the autonomic nervous system (combined autonomic block) (24, 28). Drugs were dissolved in USP saline solution. Effects of combined autonomic block were evaluated ∼10 min after drug(s) administration.

Ex vivo Properties of the Mouse Heart

With the animal under deep anesthesia (isoflurane) and following administration of heparin (∼200 unit, i.p.), bilateral thoracotomy was performed, the ascending aorta was cannulated with PE50 tubing connected to a 23G 3/4 needle, and the heart was excised. Subsequently, hearts were perfused in a Langendorff apparatus (Radnoti). Perfusion was accomplished at a constant pressure of ∼80 mmHg with pre-warmed Krebs–Henseleit buffer (KHB; Sigma-Aldrich) containing, in mmol/L: 118 NaCl, 4.7 KCl, 11 glucose, 1.2 $MgSO_4$, 1.2 KH_2PO_4, 1.8 $CaCl_2$, and 25 $NaHCO_3$, gassed with 95% O_2 and 5% CO_2 (pH 7.4) at 37°C (27–31). The temperature was maintained by immersing the heart in a water-heated glassware reservoir (Radnoti), containing preheated KHB.

To assess electrical activity of perfused hearts in sinus rhythm, two-lead mini ECG electrodes (Harvard Apparatus) were placed

on the right atrium and apex of the left ventricle, respectively, to obtain pseudo-ECG (28–30) for 5–10 min. Electrical signals were amplified (6,600 Amplifier, Gould Instruments), digitized using a 160 kHz A/D converter (DI-1120 HS, Dataq) and recorded with WinDaq software (Dataq). Approximately 5 continuous minutes of ECGs collected in sinus rhythm were employed to assess heart rate dynamics of perfused hearts. At the completion of the procedure, the four chambers of the heart were dissected. A transverse section of the left ventricle was fixed in neutral buffered, 10% formalin solution (Sigma-Aldrich) for histological analysis. Electrophysiological data were analyzed offline with LabChart 8 software.

To assess the influence of intrinsic cardiac ganglia and neural terminations on heart rate dynamics of the excised, isolated heart, ECGs were obtained from organs perfused in the Langendorff system with KHB alone or in combination with 100 nM atropine or 1 μM propranolol. Concentration of these compounds was based on previous studies utilizing isolated or innervated (32) Langendorff perfused rodent hearts (33, 34).

Settings for Data Analysis

Analysis of heart rate and heart rate variability (HRV) was conducted on electrocardiographic recordings using LabChart 8 (ADinstruments) and the HRV module, as reported previously (24). Lead I was used to obtain HRV parameters and other leads were employed as alternative source of analysis and/or for validation of obtained results. The entire 10 min of recording was analyzed. Company presets of LabChart HRV module for the mouse were adopted, with minor modifications of parameters for beat classification to include valid RR intervals detected by the QRS complex. Ectopic beats were excluded from the computation. A report, providing parameters of HRV, was generated by the software and values exported to Microsoft Excel for quantification.

Parameters Employed to Describe Heart Rate Dynamics

The RR interval duration was quantified by the average of RR intervals (average RR) obtained during the 10 min of acquisition. Heart rate variability (HRV) was quantified by using time-domain and frequency domain variables, together with non-linear parameters obtained from the Poincaré plots (5, 6, 24, 35, 36). Specifically, time-domain variables included standard deviation of RR intervals (SDRR), coefficient of variation of RR intervals (CVRR, obtained by dividing SDRR by the average RR interval), square root of the mean of the squared differences between adjacent RR intervals (RMSSD, an index of short-term variability). Frequency-domain variables included total power (ms^2), corresponding to energy in the entire power spectrum analyzed (0–5 Hz). The spectrum of oscillations of RR interval duration was separated in very low-frequency power (VLF, between 0 and 0.15 Hz), low-frequency power (LF, between 0.15 and 1.5 Hz), and high-frequency power (HF, between 1.5 and 5 Hz). Data for VLF, LF, and HF were computed as percentage of the total power (%). Moreover, low-frequency/high-frequency ratio (LF/HF, ms^2/ms^2) was computed. High-frequency components of RR interval variations are attributed to respiratory-mediated modulation of heart rate by the parasympathetic system, whereas low-frequency components are attributed to baroreflex-mediated modulation of heart rate (5, 24, 37). Very low-frequency components of RR interval variation are attributed to the modulatory action of the renin-angiotensin system, thermoregulation, and partly, parasympathetic activity (24, 37). It is generally accepted that low-frequency components are influenced by both the sympathetic and parasympathetic system (5) and LF/HF ratio is an index of sympathovagal balance, estimating the ratio of sympathetic to vagus nerve tone (5, 6). However, caution has to be exercised when considering LF/HF ratio as indicator of sympathovagal balance based on the fact that low-frequency components of RR interval variability are affected by sympathetic, parasympathetic, and other unidentified factors (10, 24). Non-linear parameters were obtained from the Poincaré plot, a graphical representation of RR interval (RR_n) plotted against the next one (RR_{n+1}) (38, 39). Standard deviation of instantaneous beat-to-beat interval variability (SD1) and standard deviation of continuous long-term RR interval variability (SD2) were obtained by an ellipse-fitting technique of plotted data. The SD1 index correlates with the short-term variability of RR interval variation and is mainly influenced by parasympathetic modulation whereas SD2 is a measure of long-term variability and reflects sympathetic activation (24, 39). The SD1/SD2 ratio is an index of autonomic balance and it inversely correlates with the LF/HF ratio (37).

Histological Analysis and Assessment of Myocardial Infarct Size

Macroscopic images of formalin-fixed transverse sections of the left ventricle (LV) at the mid-ventricular level were obtained with a stereo microscope (SW-3T13X, Amscope) equipped with a digital camera (MU1003, Amscope). Images were employed to evaluate infarct size using the midline length approach (40). Briefly, using ImageJ software and collected images, a line was manually drawn at the center of the surviving myocardium between the epicardial and endocardial surfaces and at the level of the thin transmural scar tissue. The two lines related to surviving myocardium and scar tissue formed a circumference. Infarct size expressed in percentage was derived by dividing the length of midline at the level of the scar tissue by the total length of the circumference, and multiplying by 100.

For a subgroup of hearts, transverse sections of the LV at the mid-ventricular level were embedded in paraffin and sliced to obtain thin sections (∼4 mm thickness) (21, 28). For detection of fibrotic tissue, slides were trichrome-stained (Masson's Trichrome Stain Kit, Mastertech, StatLab) following manufacturer's instruction (28, 41). Images were acquired using a stereo microscope (SW-3T13X, Amscope) equipped with a digital color camera (MU1003, Amscope). Images were employed to evaluate scar size using the area approach (40). Briefly, using collected images, areas of the fibrotic tissue and total area of LV section were traced manually using ImageJ software. Fibrotic

tissue size was expressed as percentage of the sum of fibrotic areas by the total LV area or the section.

Statistical Analysis

Data are presented in the text as fold- or percentage- change based on ratio of median values. Graphically, data are presented as scattered plots with indication of median and interquartile ranges, unless otherwise specified. Statistical analysis was performed using GraphPad Prism 9. Data were initially tested for normality (Shapiro-Wilk) and equal variance for assignment to parametric or non-parametric analysis. Parametric tests included Student's *t*-test or analysis of variance followed by Bonferroni test for non-paired comparison between two or among multiple groups, respectively. For paired statistical analysis, paired *t*-test was employed. When normality or equal variance were not met, analysis was performed using Mann–Whitney Rank sum test or Kruskal–Wallis one-way analysis of variance on ranks followed by Dunn's method, for non-paired comparison between two or among multiple groups, respectively. Wilcoxon signed rank test was employed for paired comparisons (15, 24, 27–29, 31, 41). Fisher's exact test and survival curve comparison with Gehan-Breslow-Wilcoxon and Log-rank (Mantel-Cox) tests were performed using GraphPad Prism software. $P < 0.05$ was considered significant. Graphs were prepared using GraphPad Prism.

RESULTS

Heart Rate Dynamics in Naïve Mice

Heart rate variability was evaluated in naïve mice obtained from a transgenic line routinely employed in studies for temporal regulation of the expression of genes of interest in the heart. Specifically, single transgenic mice homozygous or heterozygous for a genetic construct allowing for expression of a tamoxifen-inducible Cre recombinase (MerCreMer, MCM) under the alpha-myosin heavy chain promoter (αMHC) were employed (αMHC-MCM) (15, 17). Animals were single transgenic and negative for loxP-flanked sequences. Thus, no genes other than Cre recombinase had purposely altered expression.

Homozygous αMHC-MCM$^{+/+}$ mice (Homo) were derived by inbreed crossing of animals developed and maintained in a C57Bl/6 background. In contrast, heterozygous αMHC-MCM$^{\pm}$ mice (Het) were selected from the single transgenic F1 hybrid progeny of Homo mice crossed with hemizygous ZEG-NICD animals, derived on the 129/Sv strain (15, 18). Double heterozygous mice derived from the latter breeding scheme were not included in the study. Thus Homo and Het mice employed in this investigation differed for the number of MerCreMer alleles and for the hybrid genetic background introduced with the ZEG-NICD strain in Het hybrid mice.

Parameters of heart rate variability were obtained from electrocardiographic recordings in conscious, restrained Homo and Het mice maintained in a tunnel device over a period of 10 min (25). With respect to sex-matched Homo animals, female Het mice presented prolonged average RR interval duration (+7%) (**Figures 1A,B**) and enhanced RR interval variation, quantified by standard deviation of RR intervals (SDRR, 4.3-fold increase), the coefficient of variance of RR intervals (CVRR, 4-fold increase), and the square root of the mean of the squared differences between adjacent RR intervals (RMSSD, 2.6-fold increase), which reflects short-term variability (**Figure 1C**).

By frequency-domain analysis, total power and very low-, low-, and high-frequency components of RR interval variations were larger in Het female mice with respect to sex-matched Homo animals (**Figure 1D**). However, the relative distribution of the three frequency components and the LF/HF ratio, which is generally accepted as an index of sympathovagal balance (5, 6), were similar in the two groups of mice (**Figures 1E,F**).

By Poincaré plots and non-linear analysis, beat-to-beat (SD1) and long-term (SD2) RR interval variability were, respectively, 2.6- and 4.4-fold larger in Het female mice with respect to sex-matched Homo animals, whereas SD1/SD2 ratio, generally accepted an index of autonomic balance (37), was reduced (**Figures 1G,H**).

Differences in parameters of RR interval duration and heart rate variability observed between Homo and Het female mice were also detected in cohorts of male animals (**Supplementary Figure 1**).

Because Homo and Het animals had different genetic background, a group of C57Bl/6 mice and wild-type (non-carrier, WT) mice derived on the 129/Sv strain (18) were studied. With respect to C57Bl/6, female WT mice had prolonged RR interval duration and enhanced RR interval variation, as quantified by SDRR (7.2-fold increase), CVRR (5.3-fold increase), and RMSSD (13-fold increase) (**Supplementary Figures 2A,B**). Similarly, total power and very low-, low-, and high-frequency components of RR interval variations were larger in female WT mice, with respect to sex-matched C57Bl/6 animals (**Supplementary Figure 2C**). However, the relative distribution of the three frequency components and the LF/HF ratio, were comparable between the animals with different genetic background (**Supplementary Figures 2D,E**). By Poincaré plots and non-linear analysis, SD1 and SD2 were, respectively, 13- and 6.7-fold larger in female WT mice with respect to sex-matched C57Bl/6 animals (**Supplementary Figure 2F**). Similar results were obtained in male mice (**Supplementary Figure 3**).

Subsequently, to evaluate the influence of genetic background on heart rate dynamics of Homo and Het mice, parameters of heart rate variability for C57Bl/6, Homo (C57Bl/6 background), Het (hybrid C57Bl/6 and 129/Sv background) and WT (129/Sv background) mice were compared. For this analysis data for male and female animals were combined. Overall, for time-domain, frequency domain, and non-linear parameters, C57Bl/6 and Homo mice behaved similarly, but differed from Het and WT animals. In contrast, Het and WT animals had a comparable behavior in the settings of the multiple comparison test (**Supplementary Figure 4**). Similar results were obtained when data was disaggregated by sex (data not shown).

Therefore, inbred homozygous mice for the MerCreMer transgene present reduced RR interval duration and attenuated short- and long-term heart rate variability with respect to hybrid heterozygous animals. Similar trends were observed between C57Bl/6 and WT mice, suggesting that mouse

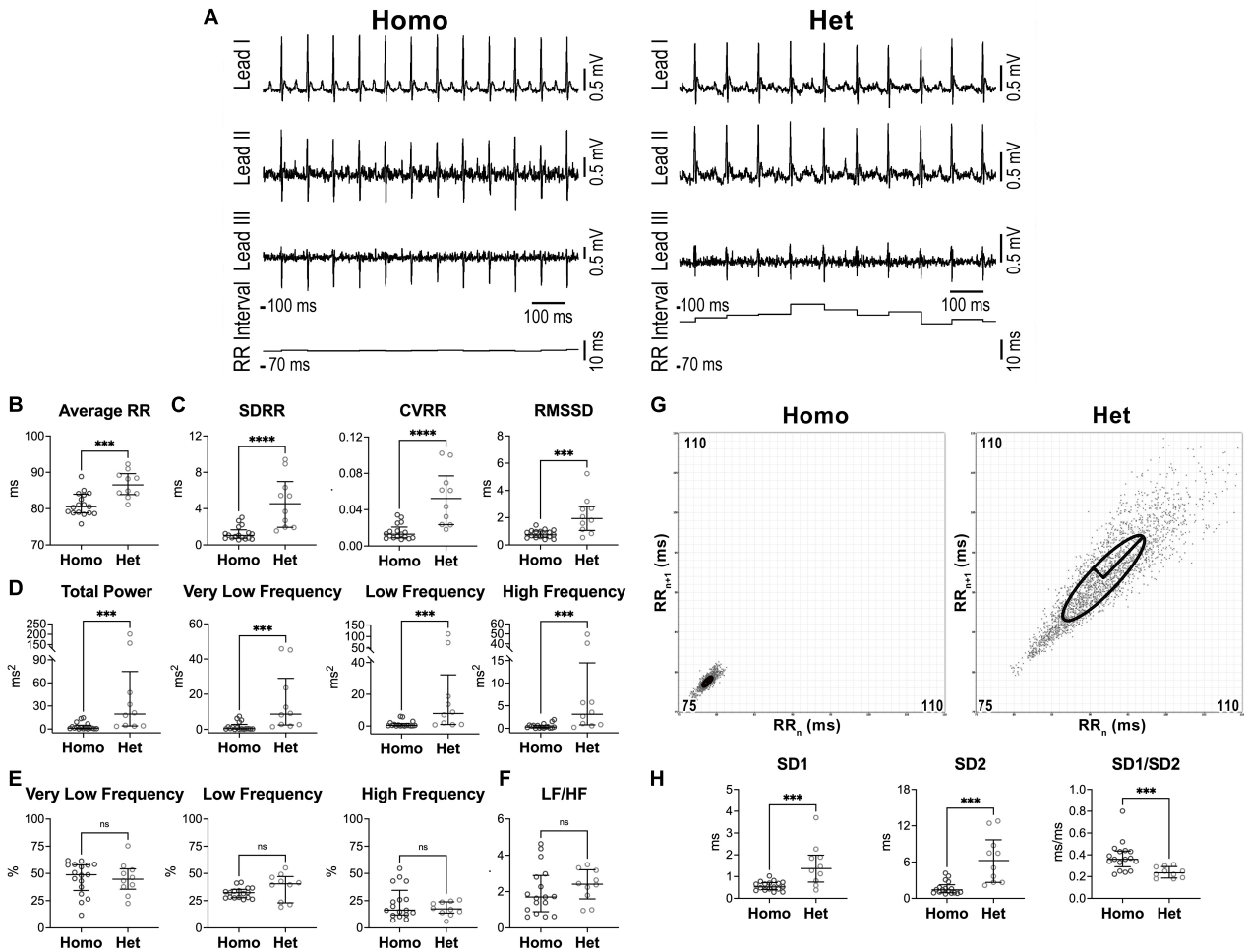

FIGURE 1 | Heart rate dynamics in naïve female Homo and Het mice. **(A)** ECGs recorded in Homo and Het female mice. Traces for the three leads and RR interval duration are reported. **(B)** Quantitative data for average RR interval duration. **(C)** Data for time-domain parameters of HRV. SDRR, standard deviation of RR intervals; CVRR, coefficient of variation of RR intervals; RMSSD, square root of the mean of the squared differences between adjacent RR. **(D)** Data for frequency-domain parameters of HRV. **(E)** Data for frequency bands normalized by total power. **(F)** Data for LF/HF ratio. **(G)** Poincaré plots obtained from ECGs recorded from female Homo and Het mice reported in A. RR$_n$ and RR$_{n+1}$ axes span from 75 to 110 ms. **(H)** Data for non-linear indices. Quantitative data were obtained from naïve Homo (n = 17) and Het (n = 10) female mice. Data are shown as scattered plots with median and interquartile ranges. ns, not significant, ***$P < 0.001$, ****$P < 0.0001$ using unpaired t-test or Mann-Whitney test.

genetic background represents a variable when considering heart rate dynamics.

Autonomic Regulation and Heart Rate Dynamics in Naïve Mice

To establish the contribution of autonomic nervous tone and circulating catecholamines to differences of heart rate dynamics in homozygous and heterozygous animals studied here, heart rate variability (HRV) was evaluated in the presence of blockers of muscarinic and beta-adrenergic receptors, to inhibit the effects of sympathetic/parasympathetic branches of the autonomic nervous system and circulating factors. Specifically, electrocardiographic recordings were obtained in naïve mice before (baseline, Base) and after combined autonomic block (CAB), which was achieved by administration of atropine, a muscarinic receptor antagonist, and propranolol, a beta-adrenergic receptor blocker (24, 28). CAB prolonged average RR interval duration (+10%, +12%) and reduced RMSSD (−43%, −51%) in both Homo and Het female mice, but attenuated SDRR only in Het mice (−36%) (**Figure 2A**). Additionally, in Het mice, CAB reduced low- (−92%) and high-frequency (−89%) oscillations of RR interval duration (**Figure 2B**), whereas only low-frequency components were reduced in Homo mice (−77%). For non-linear parameters, CAB affected SD1/SD2 ratio by reducing SD1 in both groups of mice, but SD2 only in Het mice (**Figure 2C**). Importantly, CAB abrogated differences of RR interval duration, time-domain parameters, and non-linear SD1 and SD2 observed between Homo and Het mice with intact autonomic nervous function. Moreover, CAB was equally effective in abrogating differences in heart

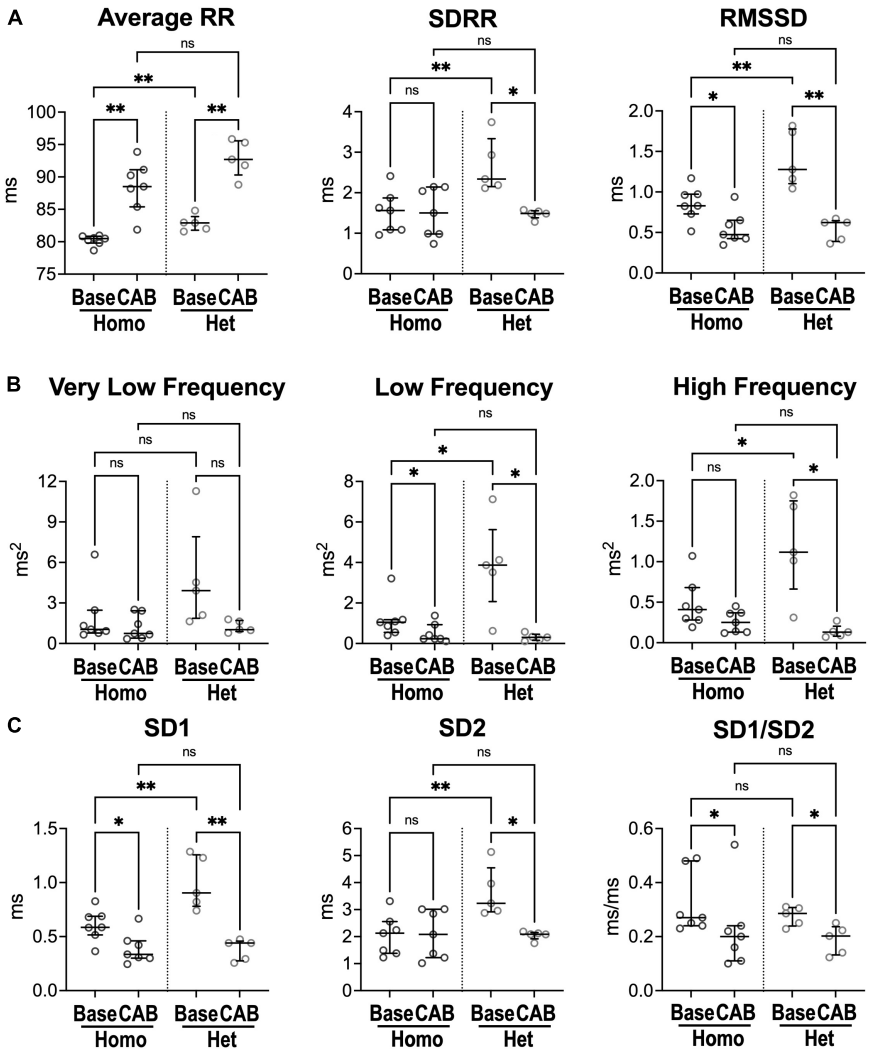

FIGURE 2 | Inhibition of the autonomic nervous system and heart rate dynamics in naïve Homo and Het mice. **(A)** Quantitative data for RR interval duration and time-domain parameters of HRV for Homo and Het mice before (baseline, Base) and after combined autonomic block with atropine and propranolol (CAB). **(B)** Data for frequency-domain parameters of HRV. **(C)** Data for non-linear indices. Quantitative data were obtained from naïve Homo (n = 7) and Het (n = 5) female mice. Data are shown as scattered plots with median and interquartile ranges. ns, not significant, $^{*}P < 0.05$, $^{**}P < 0.01$ using paired t-test or Wilcoxon signed rank test for comparisons within each genotype and unpaired t-test or Mann-Whitney test for comparisons across genotypes.

rate variability observed between C57Bl/6 and WT mice (**Supplementary Figure 5**).

Thus, inhibition of sympathovagal tone response renders HRV parameters comparable in homozygous and heterozygous mice, as well as in C57Bl/6 and WT animals, suggesting that differences in heart rate dynamics in mice with different genetic background are secondary, at least in part, to altered autonomic nervous inputs.

Sex and Cre Recombinase Expression and Heart Rate Dynamics in Naïve Mice

Studies in humans and experimental models have documented that sex is an important biological variable in the physiology of the heart, in normal and diseased conditions (42–45). Thus, to define whether sex affects heart rate dynamics in the cohort of Homo and Het mice, RR interval parameters obtained from male and female naïve animals were compared. No significant differences were observed between the two sexes for each genotype, with respect to RR interval duration, time- and frequency-domain parameters, and non-linear variables (**Supplementary Figures 6**, **7**).

Moreover, based on the genetic construct of the experimental model employed here, heart rate dynamics in Homo and Het mice was compared in cohorts of naïve mice non-treated or treated with tamoxifen, to induce Cre recombinase expression. When considering male and female animals together, differences observed between Homo and Het non-treated mice for RR interval duration and parameters of HRV were maintained following tamoxifen

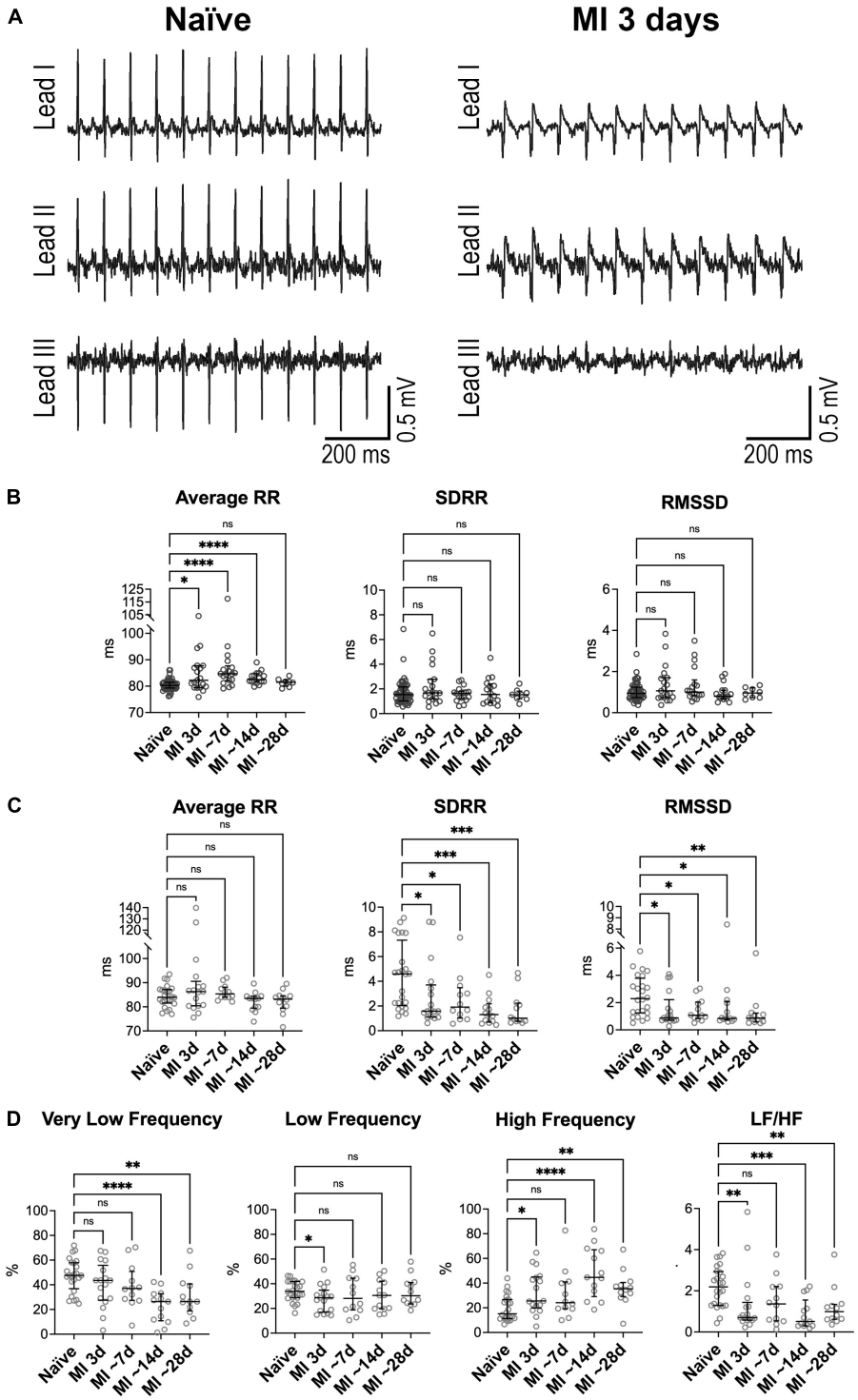

FIGURE 3 | Heart rate dynamics in mice following myocardial infarction in Homo and Het mice. **(A)** ECGs obtained from a Homo mouse before (Naïve) and at 3 days after myocardial infarction (MI). **(B)** Quantitative data for average RR interval duration and time-domain parameters of HRV in Homo naïve male and female mice (n = 53) and Homo male and female mice at 3 (n = 19), 7–9 (~7, n = 18), 13–15 (~14, n = 16), and 28 (~28, n = 8) days after MI. **(C,D)** Quantitative data for average RR interval duration, time-domain parameters **(C)** and frequency-domain indices **(D)** of HRV in Het naïve male and female mice (n = 24) and Het male and female mice at 3 (n = 17), 7–8 (~7, n = 12), 13–15 (~14, n = 13), and 29–33 (~28, n = 12) days after MI. Data are shown as scattered plots with median and interquartile ranges. ns, not significant, $^{*}P < 0.05$, $^{**}P < 0.01$, $^{***}P < 0.001$, $^{****}P < 0.0001$ using unpaired t-test or Mann-Whitney test.

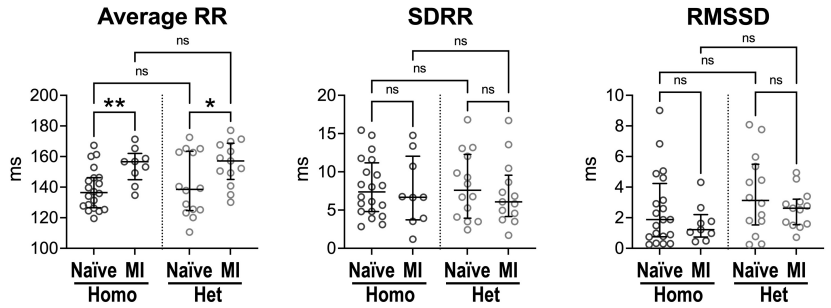

FIGURE 4 | Intrinsic beating rate dynamics in normal and infarcted Homo and Het hearts. Quantitative data for average RR interval duration and time-domain parameters of HRV in naïve and infarcted hearts from Homo (n = 20, n = 9) and Het (n = 14, n = 13) male and female mice. Data are shown as scattered plots with median and interquartile ranges. ns, not significant, $^{*}P < 0.05$, $^{**}P < 0.01$, using unpaired t-test or Mann-Whitney test.

(Tmxf) treatment (**Supplementary Figure 8**). Additionally, following tamoxifen administration, male and female mice for each genotype had comparable parameters of HRV (data not shown).

To establish whether differences in heart rate dynamics observed in Homo and Het mice were coupled with alterations of cardiac performance, echocardiography was conducted. Sex- and age-matched Homo and Het mice had comparable left ventricular (LV) end-diastolic volume, ejection fraction, and cardiac output (**Supplementary Figures 9A,B**). LV mass was larger in male Het mice with respect to their female counterparts and with respect to male Homo animals. However, normalization of LV mass by chamber volume or body weight abrogated these differences (**Supplementary Figure 9C**).

Therefore, for each genotype, heart rate dynamics are comparable between male and female mice. Moreover, Homo and Het mice maintain different behavior of HRV in the absence and presence of Cre recombinase expression.

Myocardial Infarction and Heart Rate Dynamics in Mice

To establish the consequences of myocardial infarction (MI) on heart rate and its variability, permanent coronary artery ligation (21) was performed in Homo and Het mice. Electrocardiograms were then collected at regular time intervals up to ∼1 month after induction of the ischemic insult. Male and female mice were used in combination.

With respect to the naïve state, ECG waveforms were substantially affected in mice following myocardial infarction (**Figure 3A**). Specifically, QRS complex, for the various collected leads, presented abnormal orientation in infarcted animals, a feature consistent with lack of electrical activation of the damaged myocardium. By echocardiography at 2 and 4 weeks after coronary artery ligation, all infarcted animals presented akinetic anterior LV free wall (**Supplementary Figure 10A**), low ejection fraction, and dilated LV chamber. Importantly, Homo and Het infarcted animals had comparable LV ejection fraction, cardiac output, and LV mass. However, with respect to Homo mice, LV end-diastolic volume was increased, and the posterior wall thickness-to-chamber radius ratio was reduced in Het mice (**Supplementary Figure 10B**). Infarct size, evaluated by measuring the fraction of the thin, scarred tissue with respect to the entire myocardial transverse sections of the LV at the mid-ventricular level, was ∼39% in Homo and ∼44% in Het mice (**Supplementary Figure 11A**). For a subgroup of animals, sections were processed histologically and trichrome-stained for the identification of fibrotic tissue (**Supplementary Figure 11B**). The fibrotic tissue constituted ∼33 and 28% of the total area of the LV section for Homo and Het hearts (**Supplementary Figure 11C**).

By electrocardiographic analysis, low heart rate was transiently observed at ∼24 h after the surgical procedure, when animals were under buprenorphine treatment. Specifically, at 1 day after MI, RR interval duration increased by 16% in Homo and 19% in Het mice, with respect to naïve animals of the same genotype. This behavior, which is consistent with the reported drop in heart rate secondary to buprenorphine treatment in mice at postoperative day 1 (46), precluded the consideration of this time point for evaluation of heart rate variability.

In Homo mice, with respect to naïve animals of the same genotype, RR interval duration was prolonged at 3 days (+2%), ∼7 days (+6%), and ∼14 days after MI (+3%). In contrast, long- and short-term RR interval variation, quantified by SDRR and RMSSD, respectively, were not affected at after MI (**Figure 3B**). The relative contribution of low-frequency components of RR interval variation was reduced at 3 days after MI, whereas at ∼7 days, contribution of very low-frequency was attenuated and high-frequency was increased (**Supplementary Figure 12**). No changes were observed for non-linear parameters. When data for Homo infarcted mice were disaggregated by sex, overall comparable results were seen (data not shown).

In Het mice, with respect to naïve animals of the same genotype, RR interval duration was not altered from 3 to ∼28 days after MI. In contrast, both SDRR and RMSSD were decreased with respect to naïve mice by ∼58–78% at time points comprised between 3 and ∼28 days after MI (**Figure 3C**). Additionally, the relative contribution of very low-frequency components of RR interval variation was reduced at ∼14 and ∼28 days after MI with respect to naïve animals, whereas high-frequency components were increased, with consequent attenuation of LF/HF ratio (**Figure 3D**). The non-linear

parameter SD1 and SD2 followed the pattern of reduction observed for time-domain indices (**Supplementary Figure 13**). When data for Het infarcted mice were disaggregated by sex, overall similar results were detected (data not shown).

Differences in RR interval duration, short- and long-term RR variability, and total power of RR interval variation between Homo and Het mice observed in the naïve state (see **Figure 1** and **Supplementary Figures 1**, **8**) were abrogated at 3–∼28 days after induction of MI. In contrast, the relative contribution of high-frequency band of RR interval variation and of LF/HF ratio, that were comparable between naïve Homo and naïve Het mice, became different for the two groups of mice at ∼14–28 days after MI (**Supplementary Figure 14**).

Therefore, myocardial infarction in Het, but not in Homo mice, attenuates long- and short-term RR interval variation, affects the relative contribution of very low- and high-frequency components of RR interval oscillations, and alters sympathovagal inputs in the settings of measurements in the conscious, restrained state.

Myocardial Infarction and Intrinsic Heart Rate Dynamics of the Mouse Heart

To better define putative mechanisms underlying differences of heart rate dynamics observed *in vivo* in Homo and Het mice in the naïve state and with chronic myocardial infarction, hearts obtained from naïve animals and animals at ∼1 month after MI were studied using a Langendorff system. Male and female mice were used in combination.

Ex vivo, isolated hearts from Homo and Het naïve animals had comparable intrinsic RR interval duration, SDRR and RMSSD (**Figure 4**). For both Homo and Het groups, intrinsic RR interval duration was increased in infarcted hearts (+15 and +13%, respectively) in comparison to corresponding non-infarcted organs. However, RR interval variation, assessed by SDRR and RMSSD, was not affected.

In the attempt to establish the contribution of intrinsic cardiac ganglia (33, 47) on RR interval properties of explanted, perfused hearts, organs were studied in the absence or presence of muscarinic or beta-adrenergic receptor inhibitors. Duration of RR interval, SDRR, and RMSSD were comparable for heart perfused without receptor blockers, with atropine, or with propranolol (**Supplementary Figure 15**). These results suggest that intrinsic cardiac ganglia have limited influence on the firing rate of the sinoatrial node, under experimental conditions employed here.

Therefore, in the absence of higher centers of autonomic nervous system modulation and extrinsic factors, intrinsic heart rate dynamics is comparable in Homo and Het intact organs. Chronic infarct increases RR interval duration in hearts from Homo and Het mice, suggesting that the diseased condition affects mechanisms of pacemaker discharge.

Myocardial Infarction and Occurrence of Adverse Events

To establish whether the peculiar behavior of heart rate dynamics in Homo and Het mice was associated with the propensity of animals to develop adverse events following MI, occurrence of premature ventricular complexes (PVCs) and ventricular tachycardia (VT) were evaluated from electrocardiographic recordings. Moreover, post-MI survival was computed for the two groups of animals. Male and female mice were used in combination.

Ventricular ectopic events were not detected in naïve mice (data not shown), but isolated or recurrent PVCs (>10 PVCs/10 min) together with VT were observed following myocardial infarction. Specifically, at 1 day after MI, recurrent PVCs were observed in 48% of Homo and 19% of Het mice, but occurrence of ectopic event progressively disappeared at later time points (**Figures 5A,B**). Also, VT was only detected at 1 day after MI in 17% of Homo and 11% of Het mice. For both Homo and Het mice at 1 day after MI, HRV parameters were overall comparable in mice without or with recurrent PVCs (**Supplementary Figure 16**).

Importantly, survival after MI was significantly reduced in Het mice with respect to Homo animals (**Figure 5C**). Parameter of HRV evaluated at 1 and 3 days after MI for each genotype did not discriminate between animals that survived or did not-survive (data not shown).

Thus, Homo and het mice have a different propensity to develop ectopic events and to survive in the early phase following myocardial infarction.

DISCUSSION

Results of the current study document that myocardial infarction in rodents affects heart rate dynamics and influences intrinsic sinoatrial node discharge. Interestingly, the use of two mouse lines has allowed us to identify, under our experimental conditions, strain-related differences of heart rate variability in the naïve state, which appear to be secondary, at least in part, to altered tone of sympathetic and parasympathetic inputs. These dissimilarities in autonomic function partly hinder the manifestation of autonomic imbalance induced by myocardial damage.

Studies conducted in male and female naive animals revealed that, for mouse lines studied here, sex has minor effects on heart rate dynamics, indicating that sympathovagal balance in male and female mice is comparable when evaluated in the conscious, restrained state, using the tunnel device. Moreover, RR interval duration and heart rate variability were comparable between mice homozygous for the αMHC-MerCreMer transgene (Homo) and syngeneic C57Bl/6 mice, suggesting that the transgene does not interfere with heart rate dynamics. Additionally, we found that mice with homozygous or heterozygous expression of Cre recombinase have heart rate variability comparable to animals of the same genotype before induction of gene expression. Overall, these findings suggest that the αMHC-MerCreMer transgene and Cre recombinase expression, in the homozygous and heterozygous state, do not affect heart rate dynamics.

Inbred Homo mice, used in this study, were developed and maintained in a C57Bl/6 background (15, 17), whereas Het hybrid mice were obtained by crossing Homo animals with mice

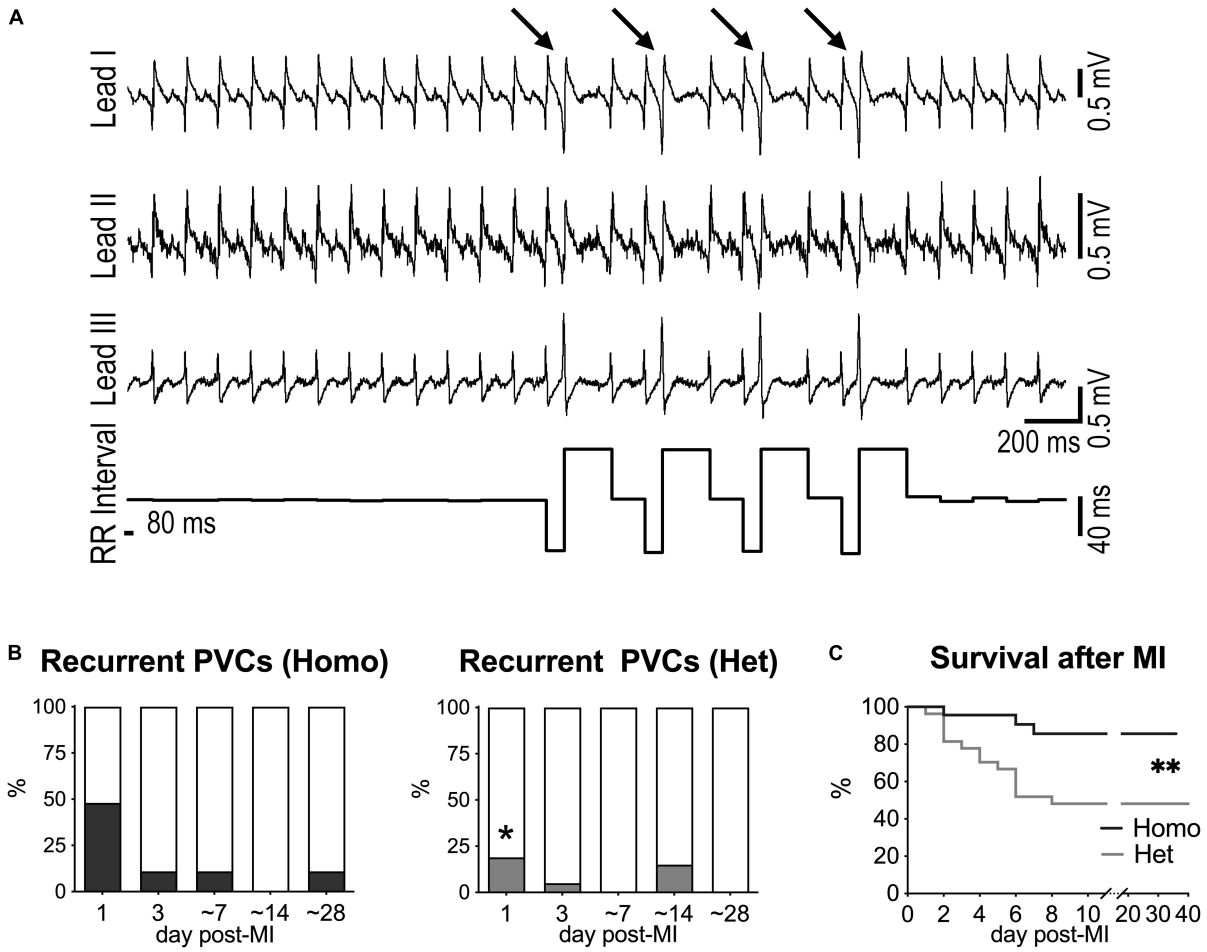

FIGURE 5 | Myocardial infarction and occurrence of ectopic events in Homo and Het mice. **(A)** ECGs recorded in a Homo female mouse at 1 day after MI. Traces for the three leads and RR interval duration are reported. Arrows indicate PVCs. **(B)** Quantitative data for occurrence of recurrent PVCs (> 10 PVCs/10 min) at 1, 3, ∼7, ∼14, and ∼28 days after MI in Homo (n = 23, 19, 18, 16, 9, respectively) and Het (n = 27, 20, 13, 13, 13, respectively) male and female mice. *$P < 0.05$ vs. Homo, using Fisher's exact test. **(C)** Survival curves for Homo (n = 23; 14 males, 9 females) and Het (n = 27; 10 males, 17 females) mice following MI. **$P < 0.01$, using Gehan–Breslow–Wilcoxon and log-rank (Mantel–Cox) tests. In the cohort of Het mice, survival for male and female animals following MI was 40 and 53%, respectively.

originally derived in the 129/Sv strain (18). We found that, with respect to Homo animals, both male and female Het naïve mice have increased RR interval duration and enhanced heart rate variability, as assessed by time-domain, frequency-domain, and non-linear parameter of RR interval variation. Importantly, these differences were abrogated following combined autonomic block, strengthening the role of sympathovagal inputs in modulating heart rate dynamics in mouse of the two lines. Moreover, *ex vivo* tests revealed that RR interval duration and time-domain parameters of variability are comparable in Homo and Het hearts deprived from the influence of higher centers of the autonomic nervous system. Thus, these findings suggest that the two groups of mice have different autonomic behavior under experimental conditions employed here. Specifically, Het mice, with respect to Homo, appear to have lower sympathetic and/or increased parasympathetic input. Importantly, differences for heart rate variability between C57Bl/6 mice and non-carrier, wild-type mice, derived on the 129/Sv strain, are consistent with alterations observed between Homo and Het mice. These results point to mouse strain as an important variable in modulating heart rate dynamics.

It is recognized that differences exist between C57Bl/6 and 129/Sv strains in relation to behavioral traits and autonomic response to stress and anxiety (48, 49). It has been reported that 129/Sv have attenuated increase in heart rate in response to a mild-intensity stressor, with respect to C57Bl/6 mice (49). These findings are consistent with observed differences in RR interval duration and RR interval variability between naïve C57Bl/6 and WT mice, as well as Homo and Het mice, under forced immobilization during ECG collection, a condition that induces physical and emotional stress (24, 50, 51). Thus, differences of HRV observed between Homo and Het mice appear to be secondary to autonomic modulation pertaining to the strain of these animals, a factor that may be relevant when assessing,

experimentally, sympathovagal tone in response to stressors or pathological conditions.

Clinical studies have documented that various cardiac pathologies, including myocardial infarction, are coupled with perturbations of autonomic regulation that manifest with reduced HRV (2, 13). It has been reported that, in patients with MI, reduced short-term heart rate variability and declined very low- and low-frequency spectral components of RR interval variation correlate with poor prognosis and increased risk of all-cause mortality (13, 52–54). Moreover, very low-frequency components are associated with fatal or near fatal arrhythmic events in individuals with MI and depressed left ventricular function (55). Interestingly, with respect to patients at 2 weeks after acute myocardial infarction, spectral components of HRV were found to be partly restored in individuals at 6 and 12 months after the acute event, suggesting a progressive recovery of vagal tone and a normalization of sympathovagal interaction (56). Thus, in patients with myocardial infarction, the analysis of heart rate dynamics predicts future outcomes and provides information on the level of progression/recovery from the diseased state.

Experiments performed here have allowed us to establish alterations of heart rhythm dynamics occurring in mice following myocardial infarction, and to evaluate the validity of this rodent model in recapitulating features of autonomic regulation in humans with ischemic disease. In Homo mice, characterized by high beating rate and low RR interval variability in the naïve state, which is consistent with high sympathetic input, no major changes in HRV parameters were induced after MI, except for the prolongation of RR interval duration observed at 3–∼14 days after coronary ligation. Prolonged RR intervals were also found in explanted infarcted hearts, with respect to non-infarcted organ. Together, these data suggest that the high level of sympathetic activation observed in homo naïve animals may have blunted sympathoexcitation secondary to the ischemic damage, preventing increases in heart rate and revealing the intrinsic prolongation of RR interval duration of the infarcted heart. In contrast, in Het mice, myocardial infarction was associated with reduced long and short-term RR interval variation, consistent with sympathoexcitation and parasympathetic tone withdrawal. The lack of changes in RR interval duration following MI in Het mice may have resulted from the combination of sympathetic activation and reduced parasympathetic input counteracting the prolongation of the intrinsic RR interval, which was observed in isolated infarcted organs. Importantly, Het mice following MI had reduced short-term RR variability and attenuation of very low-frequency and, in part, low-frequency oscillations, reiterating alterations observed in human with ischemic disease.

Interestingly, HRV parameters were comparable in Homo and Het mice following myocardial infarction, suggesting that common autonomic adaptations occurred in the two mouse lines in response to the ischemic damage. However, at ∼14 and ∼28 days after MI, Het mice had increased relative contribution of high-frequency components of RR interval variation and decreased LF/HF ratio, with respect to Homo infarcted animals. These differences may partly reflect adjustments of autonomic control in response to the evolution of the diseased condition for the two mouse lines. In this regard, although cardiac function was equally depressed in the two groups at 2 and 4 weeks after MI, Het mice had higher degree of LV dilation and reduced wall thickness/chamber radius ratio with respect to Homo animals, which are consistent with maladaptive remodeling.

Time-domain, frequency-domain, and non-linear analyses provide complementary and corroborating information on properties of heart rate and putative regulatory mechanisms active under various conditions. In Het mice, following myocardial infarction, both long- and short-term RR interval variation, quantified by SDRR and RMSSD, were reduced. Non-linear analysis led to similar findings, as indicated by the reduced SD1 and SD2. While both sympathetic and parasympathetic inputs affect long-term variability, short-term RR interval variation is mainly under vagal influence (37), suggesting that alterations of the two inputs of the autonomic nervous system occurred after MI. Frequency-domain analysis not only provided indication that heart rate properties were altered after infarction, but also revealed that the relative contribution of very low-frequency bands (RR interval variations occurring at frequencies <0.15 Hz) were reduced whereas contribution of high-frequency bands (RR interval variations occurring at frequencies 1.5–5 Hz) increased. As previously discussed (see "Materials and Methods" section), very low-frequency components of RR interval variation are attributed to the modulatory action of the renin-angiotensin system, thermoregulation, and, partly, parasympathetic activity, whereas high-frequency components of RR interval variations are attributed to respiratory-mediated modulation of heart rate by the parasympathetic system (5, 24, 37). Overall, the time course analysis of heart rate variability and combination of time- and frequency-domain parameters appear to reflect the complex adaptations associated with the acute and chronic phases of myocardial infarction (57).

Studies addressing the effects of myocardial infarction on HRV in rodents are limited. Previous investigations using FVB (36) and C57Bl/6 (58) mice suggested that autonomic nervous system function, measured by indices of HRV from ECGs recorded by telemetry, was not altered during ischemia or infarction. Interestingly, conscious heart rate is higher in FVB and C57Bl/6 mice with respect to 129/Sv animals (59), and this factor favors the possibility that enhanced sympathetic input in FVB and C57Bl/6 mice may have masked sympathoexcitation following the ischemic damage, as document for the Homo mouse line studied here. Similarly, no changes were detected in HRV parameters in Sprague-Dawley rats at 28 and 56 days after coronary artery ligation, with respect to non-infarcted animals (60). However, at 3 and 28 days after MI, baroreflex sensitivity was found to be transiently reduced, as determined by decreased reflex bradycardia (60). Moreover, in a separate study using Wistar rats, standard deviation of beat-to-beat interval duration, low-frequency components, and LF/HF ratio were found to be reduced at ∼3 months after MI (61). Thus, while clinical studies document an association between myocardial infarction and reduced HRV (2, 13), this relationship appears to be less apparent in small experimental animals. Our results tend to suggest that sympathetic predominance and low vagal tone in naïve

rodents may represent key factors hindering the manifestations of sympathoexcitation and sympathetic withdrawal on HRV, in the settings of MI.

Homo and Het infarcted mice used in our investigation presented different propensity to develop ectopic ventricular events, mainly detected at 1 day after the surgical procedure. This time point, however, coincided with the treatment of animals with analgesia, which exerts negative chronotropic effects on the heart (46) and imposes caution on data interpretation. Although animals with ectopic events tended to have longer RR interval duration with respect to mice without PVCs, no major differences were observed for parameters of HRV. Thus, as previously reported for rodent models of aging (24), for mice with myocardial ischemic damage there is no clear correlation between heart rate variability and occurrence of ectopic ventricular events.

Post-MI survival was found to be higher in Homo mice with respect to Het, a behavior that appears to be consistent with reported strain-related differences in ventricular rupture, which in mice occurs within the first week after myocardial infarction (45, 62). Specifically, previous studies documented that occurrence of myocardial laceration is higher in 129/Sv mice with respect to C57Bl/6 animals (45, 62). Although we have not evaluated whether acute heart failure or myocardial rupture affected survival of animals studied here, our findings align with the notion that our Het hybrid mice, derived from crossing 129/Sv background, are more vulnerable to myocardial laceration and subsequent death.

In the current investigation, we did not directly address factors possibly involved in the alterations of heart rate dynamics observed in mice following myocardial infarction. In this regard, remodeling of intrathoracic ganglia and/or intrinsic cardiac nervous system, including ganglia located in the right atrium (63–66), may have affected sympathetic and parasympathetic inputs at the level of the sinoatrial node of mice studied here. Moreover, in addition to variations of locally released neurotransmitters (67–69), circulating catecholamines, which are increased after myocardial infarction (70–72), may have contributed to the reduction of heart rate variability observed in Het mice following coronary artery ligation. Thus, the observed effects are likely multifactorial in origin.

CONCLUSION

In conclusion, our study document that myocardial infarction in rodents is associated with alterations in heart rhythm dynamics consistent with sympathoexcitation and parasympathetic withdrawal. Moreover, we found that mouse strain is an important variable when evaluating autonomic function via HRV, a factor that may interfere with the assessment of the consequence of cardiac pathologies on autonomic regulation.

DATA AVAILABILITY STATEMENT

The raw data supporting the conclusions of this article will be made available by the authors, without undue reservation.

ETHICS STATEMENT

The animal study was reviewed and approved by the New York Medical College IACUC.

AUTHOR CONTRIBUTIONS

MR conceived, designed the research, and drafted the manuscript. EP, SB, SJ, JJ, and MR designed and prepared the reagents. EP, SB, DC, VD, and MR performed the experiments and acquired the data. EP, SB, RK, DC, VD, and MR analyzed the data, performed statistical analysis, and interpreted results. SJ, JJ, and MR provided funding support and experimental resource. EP, SB, RK, DC, and MR edited and revised the manuscript. EP, SB, RK, DC, VD, SJ, JJ, and MR approved the manuscript. All authors contributed to the article and approved the submitted version.

FUNDING

This work was supported by the National Institutes of Health (R01AG055407), the American Heart Association (19TPA34850067), and the intramural resources at New York Medical College (NYMC), the including funds from the NYMC Translational Science Institute. SB was supported by the Overworld Scholarship of the University of Parma. RK was supported by the Medical Student Research Award by Weill-Cornell Medicine-Qatar.

SUPPLEMENTARY MATERIAL

The Supplementary Material for this article can be found online at: https://www.frontiersin.org/articles/10.3389/fcvm.2022.843144/full#supplementary-material

REFERENCES

1. Fukuda K, Kanazawa H, Aizawa Y, Ardell JL, Shivkumar K. Cardiac innervation and sudden cardiac death. *Circ Res.* (2015) 116: 2005–19.
2. Goldberger JJ, Arora R, Buckley U, Shivkumar K. Autonomic nervous system dysfunction: JACC focus seminar. *J Am Coll Cardiol.* (2019) 73:1189–206. doi: 10.1016/j.jacc.2018.12.064
3. Vassalle M, Catanzaro JN, Nett MP, Rota M. Essential role of diastolic oscillatory potentials in adrenergic control of guinea pig sino-atrial node discharge. *J Biomed Sci.* (2009) 16:101. doi: 10.1186/1423-0127-16-101
4. Vassalle M, Nett MP, Catanzaro JN, Rota M. Novel oscillatory mechanisms in the cholinergic control of Guinea pig sino-atrial node discharge. *J Cardiovasc Electrophysiol.* (2011) 22:71–80. doi: 10.1111/j.1540-8167.2010.01839.x
5. Nicolini P, Ciulla MM, De Asmundis C, Magrini F, Brugada P. The prognostic value of heart rate variability in the elderly, changing the perspective: from

sympathovagal balance to chaos theory. *Pacing Clin Electrophysiol.* (2012) 35:622–38. doi: 10.1111/j.1540-8159.2012.03335.x
6. Task Force of the European Society of Cardiology and the North American Society of Pacing and Electrophysiology. Heart rate variability: standards of measurement, physiological interpretation and clinical use. *Circulation.* (1996) 93:1043–65. doi: 10.1161/01.cir.93.5.1043
7. MacDonald EA, Rose RA, Quinn TA. Neurohumoral control of sinoatrial node activity and heart rate: insight from experimental models and findings from humans. *Front Physiol.* (2020) 11:170. doi: 10.3389/fphys.2020.00170
8. Lyashkov AE, Vinogradova TM, Zahanich I, Li Y, Younes A, Nuss HB, et al. Cholinergic receptor signaling modulates spontaneous firing of sinoatrial nodal cells via integrated effects on PKA-dependent Ca(2+) cycling and I(KACh). *Am J Physiol Heart Circ Physiol.* (2009) 297:H949–59. doi: 10.1152/ajpheart.01340.2008
9. Draghici AE, Taylor JA. The physiological basis and measurement of heart rate variability in humans. *J Physiol Anthropol.* (2016) 35:22. doi: 10.1186/s40101-016-0113-7
10. Billman GE. The LF/HF ratio does not accurately measure cardiac sympathovagal balance. *Front Physiol.* (2013) 4:26. doi: 10.3389/fphys.2013.00026
11. Hartupee J, Mann DL. Neurohormonal activation in heart failure with reduced ejection fraction. *Nat Rev Cardiol.* (2017) 14:30–8. doi: 10.1038/nrcardio.2016.163
12. Shen MJ, Zipes DP. Role of the autonomic nervous system in modulating cardiac arrhythmias. *Circ Res.* (2014) 114:1004–21. doi: 10.1161/CIRCRESAHA.113.302549
13. Huikuri HV, Stein PK. Clinical application of heart rate variability after acute myocardial infarction. *Front Physiol.* (2012) 3:41. doi: 10.3389/fphys.2012.00041
14. Perkiomaki JS. Heart rate variability and non-linear dynamics in risk stratification. *Front Physiol.* (2011) 2:81. doi: 10.3389/fphys.2011.00081
15. Borghetti G, Eisenberg CA, Signore S, Sorrentino A, Kaur K, Andrade-Vicenty A, et al. Notch signaling modulates the electrical behavior of cardiomyocytes. *Am J Physiol Heart Circ Physiol.* (2018) 314:H68–81. doi: 10.1152/ajpheart.00587.2016
16. Doetschman T, Azhar M. Cardiac-specific inducible and conditional gene targeting in mice. *Circ Res.* (2012) 110:1498–512. doi: 10.1161/CIRCRESAHA.112.265066
17. Sohal DS, Nghiem M, Crackower MA, Witt SA, Kimball TR, Tymitz KM, et al. Temporally regulated and tissue-specific gene manipulations in the adult and embryonic heart using a tamoxifen-inducible Cre protein. *Circ Res.* (2001) 89:20–5. doi: 10.1161/hh1301.092687
18. Liu J, Lobe CG. Cre-conditional expression of constitutively active Notch1 in transgenic mice. *Genesis.* (2007) 45:259–65. doi: 10.1002/dvg.20282
19. Bersell K, Choudhury S, Mollova M, Polizzotti BD, Ganapathy B, Walsh S, et al. Moderate and high amounts of tamoxifen in alphaMHC-MerCreMer mice induce a DNA damage response, leading to heart failure and death. *Dis Model Mech.* (2013) 6:1459–69. doi: 10.1242/dmm.010447
20. Koitabashi N, Bedja D, Zaiman AL, Pinto YM, Zhang M, Gabrielson KL, et al. Avoidance of transient cardiomyopathy in cardiomyocyte-targeted tamoxifen-induced MerCreMer gene deletion models. *Circ Res.* (2009) 105:12–5. doi: 10.1161/CIRCRESAHA.109.198416
21. Cimini M, Cannata A, Pasquinelli G, Rota M, Goichberg P. Phenotypically heterogeneous podoplanin-expressing cell populations are associated with the lymphatic vessel growth and fibrogenic responses in the acutely and chronically infarcted myocardium. *PLoS One.* (2017) 12:e0173927. doi: 10.1371/journal.pone.0173927
22. Ferreira-Martins J, Rondon-Clavo C, Tugal D, Korn JA, Rizzi R, Padin-Iruegas ME, et al. Spontaneous calcium oscillations regulate human cardiac progenitor cell growth. *Circ Res.* (2009) 105:764–74. doi: 10.1161/CIRCRESAHA.109.206698
23. Fenske S, Probstle R, Auer F, Hassan S, Marks V, Pauza DH, et al. Comprehensive multilevel in vivo and in vitro analysis of heart rate fluctuations in mice by ECG telemetry and electrophysiology. *Nat Protoc.* (2016) 11:61–86. doi: 10.1038/nprot.2015.139
24. Comelli M, Meo M, Cervantes DO, Pizzo E, Plosker A, Mohler PJ, et al. Rhythm dynamics of the aging heart: an experimental study using conscious, restrained mice. *Am J Physiol Heart Circ Physiol.* (2020) 319:H893–905. doi: 10.1152/ajpheart.00379.2020
25. Mongue-Din H, Salmon A, Fiszman MY, Fromes Y. Non-invasive restrained ECG recording in conscious small rodents: a new tool for cardiac electrical activity investigation. *Pflugers Arch.* (2007) 454:165–71. doi: 10.1007/s00424-006-0197-8
26. Rota M, Boni A, Urbanek K, Padin-Iruegas ME, Kajstura TJ, Fiore G, et al. Nuclear targeting of Akt enhances ventricular function and myocyte contractility. *Circ Res.* (2005) 97:1332–41. doi: 10.1161/01.RES.0000196568.11624.ae
27. Meo M, Meste O, Signore S, Sorrentino A, Cannata A, Zhou Y, et al. Reduction in Kv current enhances the temporal dispersion of the action potential in diabetic myocytes: insights from a novel repolarization algorithm. *J Am Heart Assoc.* (2016) 5:e003078. doi: 10.1161/JAHA.115.003078
28. Signore S, Sorrentino A, Borghetti G, Cannata A, Meo M, Zhou Y, et al. Late Na(+) current and protracted electrical recovery are critical determinants of the aging myopathy. *Nat Commun.* (2015) 6:8803. doi: 10.1038/ncomms9803
29. Sorrentino A, Borghetti G, Zhou Y, Cannata A, Meo M, Signore S, et al. Hyperglycemia induces defective Ca2+ homeostasis in cardiomyocytes. *Am J Physiol Heart Circ Physiol.* (2017) 312:H150–61. doi: 10.1152/ajpheart.00737.2016
30. Signore S, Sorrentino A, Ferreira-Martins J, Kannappan R, Shafaie M, Del Ben F, et al. Inositol 1, 4, 5-trisphosphate receptors and human left ventricular myocytes. *Circulation.* (2013) 128:1286–97.
31. Meo M, Meste O, Signore S, Rota M. Novel Methods for High-resolution Assessment of Cardiac Action Potential Repolarization. *Biomed Signal Process Control.* (2019) 51:30–41. doi: 10.1016/j.bspc.2019.02.003
32. Paton JF. A working heart-brainstem preparation of the mouse. *J Neurosci Methods.* (1996) 65:63–8. doi: 10.1016/0165-0270(95)00147-6
33. Pickard JMJ, Burke N, Davidson SM, Yellon DM. Intrinsic cardiac ganglia and acetylcholine are important in the mechanism of ischaemic preconditioning. *Basic Res Cardiol.* (2017) 112:11. doi: 10.1007/s00395-017-0601-x
34. Ross SA, Rorabaugh BR, Chalothorn D, Yun J, Gonzalez-Cabrera PJ, McCune DF, et al. The alpha(1B)-adrenergic receptor decreases the inotropic response in the mouse Langendorff heart model. *Cardiovasc Res.* (2003) 60:598–607. doi: 10.1016/j.cardiores.2003.09.020
35. Gehrmann J, Hammer PE, Maguire CT, Wakimoto H, Triedman JK, Berul CI. Phenotypic screening for heart rate variability in the mouse. *Am J Physiol Heart Circ Physiol.* (2000) 279:H733–40. doi: 10.1152/ajpheart.2000.279.2.H733
36. Gehrmann J, Frantz S, Maguire CT, Vargas M, Ducharme A, Wakimoto H, et al. Electrophysiological characterization of murine myocardial ischemia and infarction. *Basic Res Cardiol.* (2001) 96:237–50. doi: 10.1007/s003950170054
37. Shaffer F, Ginsberg JP. An overview of heart rate variability metrics and norms. *Front Public Health.* (2017) 5:258. doi: 10.3389/fpubh.2017.00258
38. Fishman M, Jacono FJ, Park S, Jamasebi R, Thungtong A, Loparo KA, et al. A method for analyzing temporal patterns of variability of a time series from Poincare plots. *J Appl Physiol (1985).* (2012) 113:297–306. doi: 10.1152/japplphysiol.01377.2010
39. Roy B, Ghatak S. Nonlinear methods to assess changes in heart rate variability in type 2 diabetic patients. *Arq Bras Cardiol.* (2013) 101:317–27. doi: 10.5935/abc.20130181
40. Takagawa J, Zhang Y, Wong ML, Sievers RE, Kapasi NK, Wang Y, et al. Myocardial infarct size measurement in the mouse chronic infarction model: comparison of area- and length-based approaches. *J Appl Physiol (1985).* (2007) 102:2104–11. doi: 10.1152/japplphysiol.00033.2007
41. Sorrentino A, Signore S, Qanud K, Borghetti G, Meo M, Cannata A, et al. Myocyte repolarization modulates myocardial function in aging dogs. *Am J Physiol Heart Circ Physiol.* (2016) 310:H873–90. doi: 10.1152/ajpheart.00682.2015
42. Cavasin MA, Tao Z, Menon S, Yang XP. Gender differences in cardiac function during early remodeling after acute myocardial infarction in mice. *Life Sci.* (2004) 75:2181–92. doi: 10.1016/j.lfs.2004.04.024
43. Ramaekers D, Ector H, Aubert AE, Rubens A, Van de Werf F. Heart rate variability and heart rate in healthy volunteers. Is the female autonomic nervous system cardioprotective? *Eur Heart J.* (1998) 19:1334–41. doi: 10.1053/euhj.1998.1084
44. Prabhavathi K, Selvi KT, Poornima KN, Sarvanan A. Role of biological sex in normal cardiac function and in its disease outcome - a review. *J Clin Diagn Res.* (2014) 8:BE01–4. doi: 10.7860/JCDR/2014/9635.4771

45. Gao XM, Xu Q, Kiriazis H, Dart AM, Du XJ. Mouse model of post-infarct ventricular rupture: time course, strain- and gender-dependency, tensile strength, and histopathology. *Cardiovasc Res.* (2005) 65:469–77. doi: 10.1016/j.cardiores.2004.10.014
46. Ratsep MT, Barrette VF, Winterborn A, Adams MA, Croy BA. Hemodynamic and behavioral differences after administration of meloxicam, buprenorphine, or tramadol as analgesics for telemeter implantation in mice. *J Am Assoc Lab Anim Sci.* (2013) 52:560–6.
47. Armour JA. Potential clinical relevance of the 'little brain' on the mammalian heart. *Exp Physiol.* (2008) 93:165–76. doi: 10.1113/expphysiol.2007.041178
48. Abramov U, Puussaar T, Raud S, Kurrikoff K, Vasar E. Behavioural differences between C57BL/6 and 129S6/SvEv strains are reinforced by environmental enrichment. *Neurosci Lett.* (2008) 443:223–7. doi: 10.1016/j.neulet.2008.07.075
49. van Bogaert MJ, Groenink L, Oosting RS, Westphal KG, van der Gugten J, Olivier B. Mouse strain differences in autonomic responses to stress. *Genes Brain Behav.* (2006) 5:139–49. doi: 10.1111/j.1601-183X.2005.00143.x
50. Liu J, Wei W, Kuang H, Zhao F, Tsien JZ. Changes in heart rate variability are associated with expression of short-term and long-term contextual and cued fear memories. *PLoS One.* (2013) 8:e63590. doi: 10.1371/journal.pone.0063590
51. Meijer MK, Spruijt BM, van Zutphen LF, Baumans V. Effect of restraint and injection methods on heart rate and body temperature in mice. *Lab Anim.* (2006) 40:382–91. doi: 10.1258/002367706778476370
52. Wolf MM, Varigos GA, Hunt D, Sloman JG. Sinus arrhythmia in acute myocardial infarction. *Med J Aust.* (1978) 2:52–3. doi: 10.5694/j.1326-5377.1978.tb131339.x
53. Bigger JT Jr., Fleiss JL, Rolnitzky LM, Steinman RC. Frequency domain measures of heart period variability to assess risk late after myocardial infarction. *J Am Coll Cardiol.* (1993) 21:729–36. doi: 10.1016/0735-1097(93)90106-b
54. Kleiger RE, Miller JP, Bigger JT Jr., Moss AJ. Decreased heart rate variability and its association with increased mortality after acute myocardial infarction. *Am J Cardiol.* (1987) 59:256–62. doi: 10.1016/0002-9149(87)90795-8
55. Huikuri HV, Raatikainen MJ, Moerch-Joergensen R, Hartikainen J, Virtanen V, Boland J, et al. Prediction of fatal or near-fatal cardiac arrhythmia events in patients with depressed left ventricular function after an acute myocardial infarction. *Eur Heart J.* (2009) 30:689–98. doi: 10.1093/eurheartj/ehn537
56. Lombardi F, Sandrone G, Pernpruner S, Sala R, Garimoldi M, Cerutti S, et al. Heart rate variability as an index of sympathovagal interaction after acute myocardial infarction. *Am J Cardiol.* (1987) 60:1239–45. doi: 10.1016/0002-9149(87)90601-1
57. Prabhu SD, Frangogiannis NG. The biological basis for cardiac repair after myocardial infarction: from inflammation to fibrosis. *Circ Res.* (2016) 119:91–112. doi: 10.1161/CIRCRESAHA.116.303577
58. Korte T, Fuchs M, Guener Z, Bonin J, de Sousa M, Niehaus M, et al. In-vivo electrophysiological study in mice with chronic anterior myocardial infarction. *J Interv Card Electrophysiol.* (2002) 6:121–32. doi: 10.1023/a:1015359332161
59. Ho D, Zhao X, Gao S, Hong C, Vatner DE, Vatner SF. Heart rate and electrocardiography monitoring in mice. *Curr Protoc Mouse Biol.* (2011) 1:123–39. doi: 10.1002/9780470942390.mo100159
60. Kruger C, Kalenka A, Haunstetter A, Schweizer M, Maier C, Ruhle U, et al. Baroreflex sensitivity and heart rate variability in conscious rats with myocardial infarction. *Am J Physiol.* (1997) 273:H2240–7. doi: 10.1152/ajpheart.1997.273.5.H2240
61. Rodrigues B, Mostarda CT, Jorge L, Barboza CA, Grans CF, De Angelis K, et al. Impact of myocardial infarction on cardiac autonomic function in diabetic rats. *J Diabetes Complications.* (2013) 27:16–22. doi: 10.1016/j.jdiacomp.2012.08.002
62. Gao XM, Ming Z, Su Y, Fang L, Kiriazis H, Xu Q, et al. Infarct size and post-infarct inflammation determine the risk of cardiac rupture in mice. *Int J Cardiol.* (2010) 143:20–8. doi: 10.1016/j.ijcard.2009.01.019
63. Dawson TA, Li D, Woodward T, Barber Z, Wang L, Paterson DJ. Cardiac cholinergic NO-cGMP signaling following acute myocardial infarction and nNOS gene transfer. *Am J Physiol Heart Circ Physiol.* (2008) 295:H990–8. doi: 10.1152/ajpheart.00492.2008
64. Hardwick JC, Ryan SE, Beaumont E, Ardell JL, Southerland EM. Dynamic remodeling of the guinea pig intrinsic cardiac plexus induced by chronic myocardial infarction. *Auton Neurosci.* (2014) 181:4–12. doi: 10.1016/j.autneu.2013.10.008
65. Hadaya J, Ardell JL. Autonomic modulation for cardiovascular disease. *Front Physiol.* (2020) 11:617459. doi: 10.3389/fphys.2020.617459
66. Ajijola OA, Yagishita D, Reddy NK, Yamakawa K, Vaseghi M, Downs AM, et al. Remodeling of stellate ganglion neurons after spatially targeted myocardial infarction: neuropeptide and morphologic changes. *Heart Rhythm.* (2015) 12:1027–35. doi: 10.1016/j.hrthm.2015.01.045
67. Dart AM, Schomig A, Dietz R, Mayer E, Kubler W. Release of endogenous catecholamines in the ischemic myocardium of the rat. Part B: effect of sympathetic nerve stimulation. *Circ Res.* (1984) 55:702–6. doi: 10.1161/01.res.55.5.702
68. Schomig A, Dart AM, Dietz R, Mayer E, Kubler W. Release of endogenous catecholamines in the ischemic myocardium of the rat. Part A: locally mediated release. *Circ Res.* (1984) 55:689–701. doi: 10.1161/01.res.55.5.689
69. Schomig A. Catecholamines in myocardial ischemia. Systemic and cardiac release. *Circulation.* (1990) 82(Suppl. 3):II13–22.
70. Karlsberg RP, Cryer PE, Roberts R. Serial plasma catecholamine response early in the course of clinical acute myocardial infarction: relationship to infarct extent and mortality. *Am Heart J.* (1981) 102:24–9. doi: 10.1016/0002-8703(81)90408-7
71. Lymperopoulos A, Rengo G, Gao E, Ebert SN, Dorn GW II, Koch WJ. Reduction of sympathetic activity via adrenal-targeted GRK2 gene deletion attenuates heart failure progression and improves cardiac function after myocardial infarction. *J Biol Chem.* (2010) 285:16378–86. doi: 10.1074/jbc.M109.077859
72. Rengo G, Lymperopoulos A, Zincarelli C, Femminella G, Liccardo D, Pagano G, et al. Blockade of beta-adrenoceptors restores the GRK2-mediated adrenal alpha(2) -adrenoceptor-catecholamine production axis in heart failure. *Br J Pharmacol.* (2012) 166:2430–40. doi: 10.1111/j.1476-5381.2012.01972.x

Conflict of Interest: The authors declare that the research was conducted in the absence of any commercial or financial relationships that could be construed as a potential conflict of interest.

frontiers | Frontiers in Cardiovascular Medicine

TYPE Original Research
PUBLISHED 26 July 2022
DOI 10.3389/fcvm.2022.869585

OPEN ACCESS

EDITED BY
Kiyotake Ishikawa,
Icahn School of Medicine at Mount Sinai, United States

REVIEWED BY
Ibrahim El-Battrawy,
Ruhr University Bochum, Germany
Marco Mongillo,
University of Padua, Italy

*CORRESPONDENCE
Matthew H. Tranter
matthew.tranter@oriel.ox.ac.uk

†These authors have contributed equally to this work and share first authorship
‡These authors have contributed equally to this work and share last authorship

SPECIALTY SECTION
This article was submitted to Heart Failure and Transplantation, a section of the journal Frontiers in Cardiovascular Medicine

RECEIVED 07 February 2022
ACCEPTED 04 July 2022
PUBLISHED 26 July 2022

CITATION
Tranter MH, Redfors B, Wright PT, Couch LS, Lyon AR, Omerovic E and Harding SE (2022) Hyperthermia as a trigger for Takotsubo syndrome in a rat model.
Front. Cardiovasc. Med. 9:869585.
doi: 10.3389/fcvm.2022.869585

Hyperthermia as a trigger for Takotsubo syndrome in a rat model

Matthew H. Tranter[1,2*†], Bjorn Redfors[3†], Peter T. Wright[1,4], Liam S. Couch[1], Alexander R. Lyon[1], Elmir Omerovic[3‡] and Sian E. Harding[1‡]

[1]Faculty of Medicine, Imperial College London, Hammersmith Campus, National Heart and Lung Institute (NHLI), London, United Kingdom, [2]Oriel College, University of Oxford, Oxford, United Kingdom, [3]Department of Molecular and Clinical Medicine/Cardiology, Sahlgrenska Academy, University of Gothenburg, Gothenburg, Sweden, [4]School of Life and Health Sciences, University of Roehampton, London, United Kingdom

Takotsubo syndrome is a well-characterized cause of acute yet reversible heart failure associated with periods of intense emotional stress, often mimicking on presentation an acute coronary syndrome. Animal models of Takotsubo syndrome have been developed, either through the application of a stressor, or administration of exogenous catecholamine. We found that in a model of isoproterenol-induced Takotsubo syndrome in anesthetized rats hyperthermia (40–41°C) would occur after the administration of isoproterenol. Maintenance of this hyperthermia would result in an apical hypocontractility typical of the syndrome, whereas prevention of hyperthermia with active cooling to maintain a euthermic core body temperature prevented (but did not subsequently reverse) apical hypocontractility. *In vitro* experimentation with isolated cardiomyocytes showed no effect of hyperthermia on either baseline contractility or contractility change after beta-adrenoceptor stimulation. We suggest that the rise in body temperature that is characteristic of catecholamine storm may be a component in the development of Takotsubo syndrome.

KEYWORDS

Takotsubo, stress, hyperthermia, catecholamine, isoprenaline

Introduction

Takotsubo syndrome (TTS), previously known as Takotsubo cardiomyopathy or stress cardiomyopathy, is an acute and reversible heart failure that typically occurs after a period of intense emotional or physical stress; symptoms include chest pain and dyspnea and, as a result, can mimic an acute coronary syndrome (1). However, no culprit macrovascular pathology can be found on coronary angiography and a diagnosis of TTS is made due to the observation of the characteristic hypocontractile apex coupled to a hypercontractile base, although variants on this pattern have been observed, e.g., midventricular or basal hypocontractility and also right ventricular involvement (2, 3).

A number of models have been developed to study TTS, including rat *in vivo* and cellular models (4–6), and human induced pluripotent stem cells from Takotsubo syndrome patients (7), as well as healthy controls (8). These have produced insights

on the various phases of Takotsubo syndrome, from the very acute response which includes adrenaline surge, lipotoxicity, nitric oxide generation [and a potential increase in nitrosative stress (9)] and endothelial damage, to the long-term effects through maintained inflammatory damage (10). Many models consist of the exogenous administration of catecholamines, such as the recently described induction of TTS-like contractile dysfunction using intraperitoneal (IP) 50 mg.kg^{-1} isoproterenol (5). We attempted to reproduce this model in our laboratory as the time course of dysfunction is similar to the human disease course, and with a prolonged period of apical hypokinesia there would be scope to test therapies during the establishment of TTS-like contractility rather than having to administer them before (4). However, the dysfunction observed in (5) could not be recreated in our laboratory.

It was noticed during initial experiments that body temperature tended to rise after isoprenaline administration. A rise in body temperature is known to be produced by high catecholamine levels (once known as "emotional fever") (11), as is a suite of immunoinflammatory changes (12). In our experiments, the rise in body temperature was controlled by adjusting the external heating support for the anesthetized animal, which remained euthermic throughout. After discussion with the Omerovic group at the University of Gothenberg (the authors of the original IP isoprenaline study) a study was carried out to determine whether allowing this temperature rise in a controlled manner would also allow the apical dysfunction characteristic of TTS to occur. We found that hyperthermia was an essential component in the induction of TTS in this rat model, yet the removal of the hyperthermia after the initial induction phase did not change outcome. This may have relevance to the circumstances leading to the clinical presentation of Takotusbo syndrome.

Methods

All studies complied with Animals (Scientific Procedures) Act (1986), European Directive 2010/63/EU and with the 8th edition of the *Guide for the Care and Use of Laboratory Animals* published by the US National Institutes of Health. Animals were housed in groups of four and experiences a 12 h light/dark cycle. All rats were male and of the Sprague Dawley strain and obtained from Charles River Laboratories (UK). All animals were killed at the end of the procedure by an approved Schedule 1 method.

Induction of experimental Takotsubo syndrome model

Rats were anesthetized using IP ketamine-midazolam (50 and 5 mg.kg^{-1}, respectively) with 25/2.5 mg.kg^{-1} administered PRN to maintain a sufficient plane of anesthesia for consistent echocardiographic measurement. 50 mg.kg^{-1} (-)-isoproterenol was administered IP and rats were monitored by two-dimensional parasternal long axis echocardiography (Visualsonics Vevo 770), with M-mode echocardiography used to assess regional cardiac function, compared to a baseline reading taken before catecholamine administration. A lead II ECG was taken using subdermal electrodes connected *via* a BioAmp to a PowerLab data acquisition system (AD Instruments).

Body temperature manipulation

Before catecholamine administration, body temperature was maintained between 37 and 38°C using a homeothermic temperature monitor, rectal temperature probe, and heating blanket (Harvard Apparatus). Heating was maintained at a similar level after the administration of isoprenaline, with a new set-point of 41°C used. Cooling, if required at either 60 or 90 min post-isoproterenol administration (Figure 1), was achieved through the removal of external heat sources and the application of ice packs to the abdomen until the rectal temperature was back in the euthermic zone, after which external heating was reapplied as required to maintain euthermia. For experiments shown in the Supplementary Figures, male rats were randomized to either of two groups and subsequently received 50 mg/kg isoprenaline intraperitoneally. Body temperature was maintained at 37.5 ± 0.5°C (normothermia) for the duration of the experiments in the first group whereas in the second group body temperature was first allowed to rise spontaneously and, starting at 15 min post isoprenaline, was maintained at 41 ± 0.5°C (hyperthermia) for the remainder of the experiment. Extent of akinesia was traced in the long axis and expressed as percentage of total LV endocardial length.

Rat cardiomyocyte isolation and *in vitro* contractility studies

Cardiomyocytes were isolated from adult male rats as previously described using a two-enzyme technique (13) and studied using a video edge detection and tracking system (IonOptix) as previously described (4). Cardiomyocytes were paced at 0.5 Hz throughout all studies and contraction was determined as shortening relative to the diastolic length. For studies assessing changes in baseline (i.e., without catecholamines present), cells were perfused with Krebs-Henseleit (KH) solution (1 mM Ca^{2+}) at 37°C for 10 min, after which the temperature either remained constant or was elevated to 41°C. Contractility was measured at 10 and 20 min post-temperature change and changes are expressed relative to contractility at the end of the 10 min baseline period. For

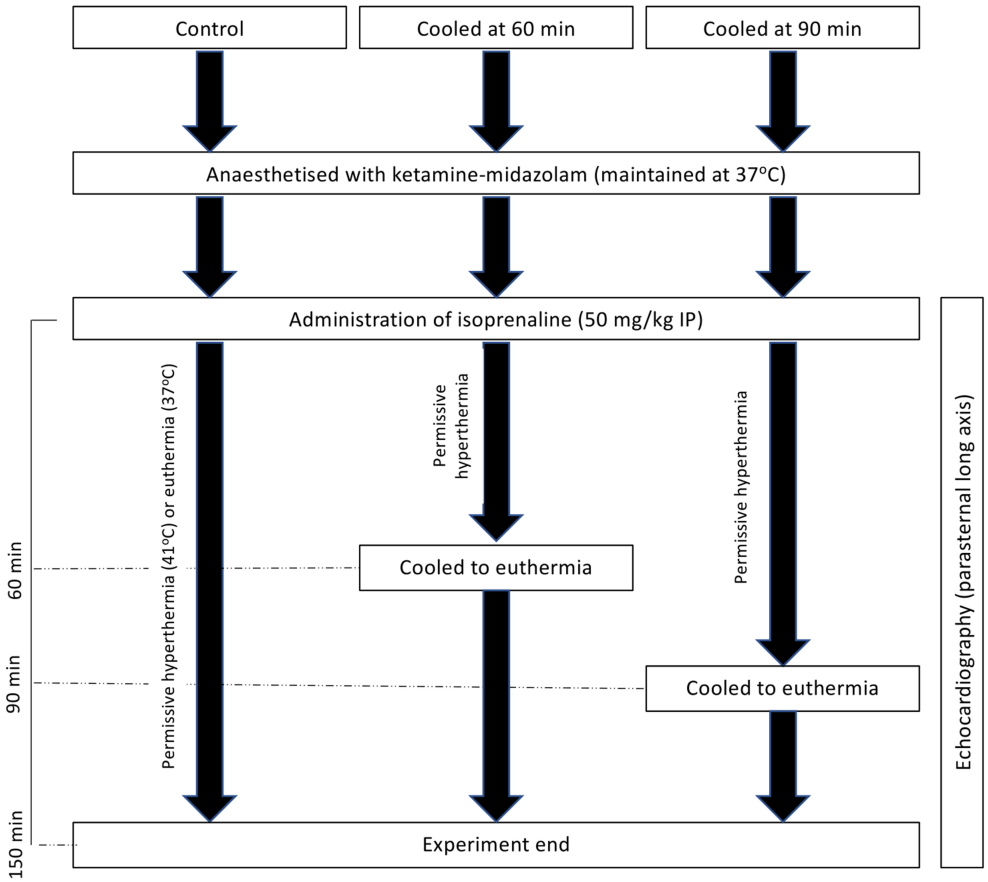

FIGURE 1
Experimental schematic of hyperthermic experiments with and without cooling to 150 min post-isoprenaline administration.

isoproterenol hyperthermia studies, cells were perfused with KH at either 37 or 41°C for 10 min, at the end of which a baseline recording was taken. 10^{-6} M isoproterenol was then perfused and contractility measurements taken at 10 and 20 min post-isoproterenol, and expressed as a relative change in contractility compared to the end of the 10 min baseline.

Statistical analysis

All *in vivo* contractility and temperature data was analyzed using two-way repeated measures ANOVA calculations with either Tukey's (for whole experiment analysis) or Dunnett's (individual time-point analysis) *post-hoc* tests for comparison to baseline or apex vs. base. One-way ANOVA with Sidak's *post-hoc* test was used to compare time-points with baseline for body temperature changes, and for cellular contractility studies. Statistical significance was defined as $P < 0.05$ and data was tested for normality using a Komogorov–Smirnov test. All statistical analyses were carried out using GraphPad Prism 6 and data is presented at Mean ± SEM unless otherwise stated. Intra-experimental mortality was not observed in any study and therefore not presented graphically.

Results

50 mg.kg^{-1} isoproterenol at euthermic temperatures does not cause a recapitulation of the Takotsubo-like contractility pattern

Rats were injected with 50 mg.kg^{-1} IP while under constant ketamine-midazolam anesthesia and serial M-mode measurements of apical and basal segment contractility were taken. Over the 100 min period following isoproterenol administration, no overall apical hypocontractility was seen, but rather a mild and sustained positive inotropy in both segments (Figure 2A). However, no information on right ventricular function was gathered. A mild yet significant increase in body

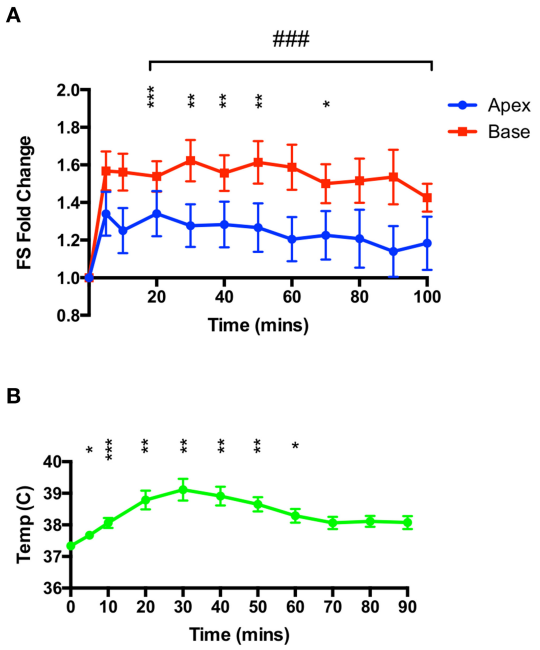

FIGURE 2
High-dose isoproterenol (50 mg.kg^{-1}) under euthermic conditions does not result in TTS-like contractility. **(A)** 50 mg.kg^{-1} isoprenaline under ketamine-midazolam anesthesia resulted in a significant positive inotropic response in both apical and basal myocardial segments, although not for all time-points in the apex. No significant difference was seen between apical and basal contractility ($n = 8$). $^{*}P < 0.05$, $^{**}P < 0.01$, $^{***}P < 0.001$ vs. baseline (apex); $^{\#\#\#}P < 0.001$ vs. baseline (base) two-way repeated measures ANOVA. **(B)** Rectal temperature increases after isoproterenol, although this is attenuated by removing heating from the animal. $^{*}P < 0.05$, $^{**}P < 0.01$, $^{***}P < 0.001$ relative to time 0, one-way ANOVA ($n = 8$ animals).

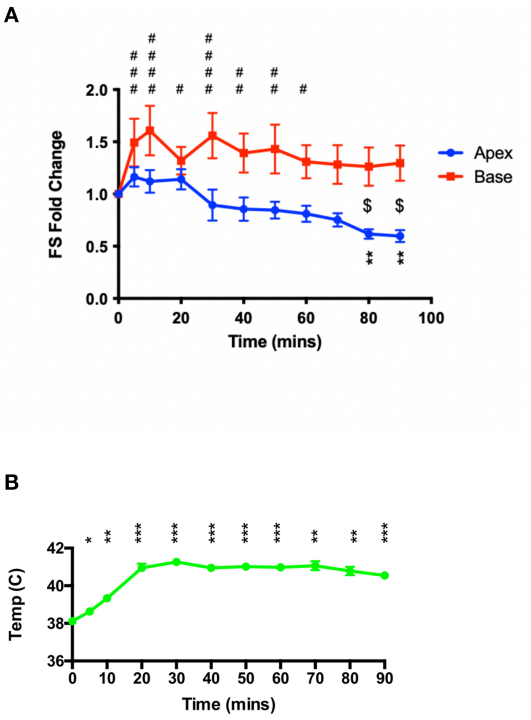

FIGURE 3
High-dose isoproterenol (50 mg.kg^{-1}) administration under hyperthermic conditions (~41°C) results in apical-hypocontractility. **(A)** 50 mg.kg^{-1} isoprenaline under ketamine-midazolam anesthesia resulted a significant positive inotropic response was seen in the basal myocardial segment for the first 60 min, whereas the apical myocardial segment showed a significant negative inotropic response at 80 and 90 min post-isoprenaline. $^{**}P < 0.01$ apex vs. baseline; $^{\$}P < 0.05$ apex vs. base; $^{\#}P < 0.05$, $^{\#\#}P < 0.01$, $^{\#\#\#}P < 0.001$, $^{\#\#\#\#}P < 0.0001$ base vs. baseline, two-way repeated measures ANOVA ($n = 6$). **(B)** Sustained heating of the animal maintains a significant elevated body temperature post-isoproterenol. $^{*}P < 0.05$, $^{**}P < 0.01$, $^{***}P < 0.001$ relative to baseline temperature, one-way ANOVA ($n = 6$ animals).

temperature was seen (Figure 2B), which was attenuated by removing all heating and applying cooling as needed.

TTS-like contractility can be recapitulated with a 50 mg.kg^{-1} isoproterenol dose when the hyperthermic response can manifest

As shown in Figure 2, 50 mg.kg^{-1} isoproterenol, when administered under ketamine-midazolam anesthesia, causes a hyperthermia response that was, in initial studies, attenuated to maintain a euthermic temperature. In a second set of studies, animals were allowed to reach 41°C and maintained at that temperature throughout the 90 min of serial echocardiographic recording post-isoproterenol. This resulted in a negative inotropy in the apex at the 80 and 90 min timepoints compared to baseline, and a significant difference in inotropic change between apex and base at the 80 and 90 min timepoints (Figure 3). Heart rates for these animals can be found in the Supplementary Data.

Cooling animals back to euthermia after the initial induction phase does not reverse or attenuate the apical dysfunction caused by high dose isoproterenol

As hyperthermia was essential to the induction of apical dysfunction, we hypothesized that restoration of a euthermic body temperature would either attenuate or reverse the dysfunction. In a separate set of studies shown in Figure 4, rats were randomized prior to study either to be cooled at 60

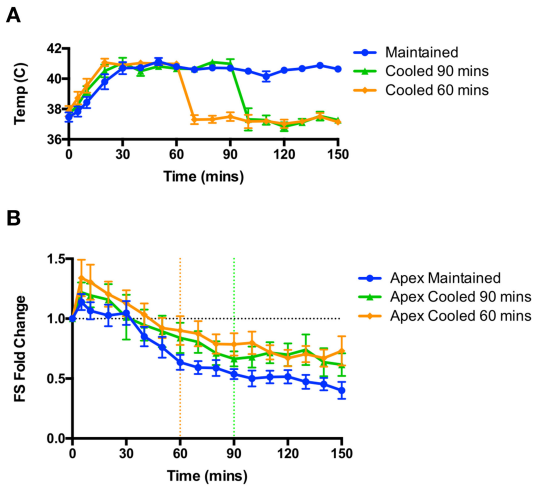

FIGURE 4
Rapid cooling of animals after the induction of apical dysfunction did not reverse or attenuate the hypocontractility. **(A)** Rapid changes in body temperature could be achieved through the application of cooling. **(B)** No effect of cooling was observed on apical dysfunction on rats cooled at 60 min (from orange dotted line) or 90 min (from green dotted line); $n = 6$ animals per group. Repeated measures ANOVA.

or 90 min post-isoproterenol, or be maintained at 41°C; all animals were studied to 150 min post-isoproterenol regardless of group. Through the application of cooling packs we were able to rapidly reduce the body temperature back into the euthermic range (Figure 4A). We found no significant change in apical hypocontractility in either cooled group compared to the maintained group; apical hypocontractility was sustained in all three groups (Figure 4B).

In vitro hyperthermia had no effect on baseline contractility or beta adrenoceptor responsiveness

Isolated rat left ventricular cardiomyocytes were perfused with Krebs-Henseleit (KH) solution at 37°C for 10 min, after which a measurement of cellular shortening was taken and perfusion temperature increased to either 41°C or maintained at 37°C (control). No significant changes in contractility were seen with this increase in temperature (Figure 5A). In a separate set of experiments, isolated cardiomyocytes were perfused with KH at either 37°C or 41°C, and after a 10 min stabilization period, a baseline measurement of cellular shortening was taken and isoproterenol (10^{-6} M) was added to the perfusate. Measurements were taken at 10 and 20 min post-isoproterenol addition, and no significant differences were seen between the two temperature groups at either time point (Figure 5B).

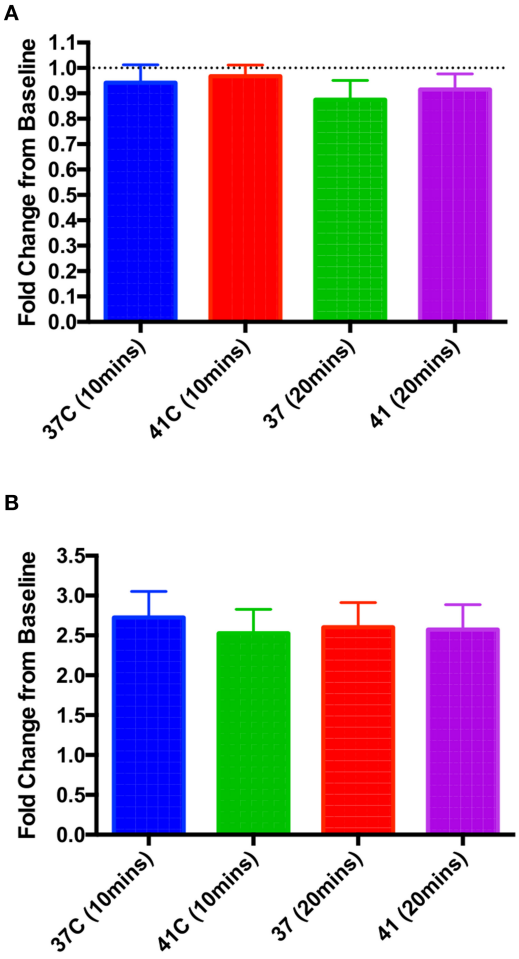

FIGURE 5
In vitro hyperthermia had no significant effect on either baseline contractility at 10 or 20 min post-temperature change **(A)** or the increase in contractility when 10^{-6} M isoproterenol was applied at either 10 or 20 min post-isoproterenol **(B)**. One-way ANOVA, $n = 9$ and 10 cells **(A)**, 8 and 7 **(B)**, 37 and 41°C, respectively.

Discussion

TTS is a syndrome well-associated with an excess of catecholamines (14), and therefore pre-clinical models using excess catecholamines are useful to delineate the steps the lead to the induction of TTS. In a previous model of TTS developed by the Imperial laboratory (4) a single IV dose to produce a high epinephrine level (approximately equivalent to an Epi-Pen in human) was sufficient to induce a transient apical dysfunction in male rats, where contractility was at a nadir at 20–25 min post-epinephrine and recovered at 60 min post-epinephrine. While this is important to study immediate effects of a catecholamine spike, there are longer-term changes triggered which may underlie a persistent cardiac damage.

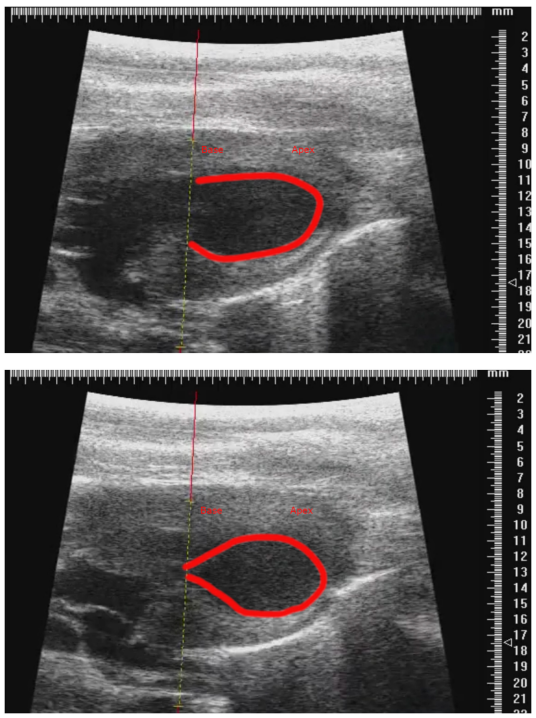

FIGURE 6
Representative parasternal long axis B-mode images of end-diastole **(top)** and end-systole **(bottom)** after induction of TTS-like contractility (base: left; apex: right), with trace (red line) drawn around endocardial border. Scale in mm.

Models using an intraperitoneal injection of isoproterenol, where animals are studied over hours to days/weeks, have shown an activation of immune responses (12) and an upregulation of pathways involved in inflammation (15). However, while attempting to reproduce the well-validated model of Shao et al. (5) we experienced difficulties, which we resolved in a collaborative effort with the Omerovic laboratory.

We noticed that after isoprenaline administration, animals tended to increase their body temperature, and after discussion between the two groups we determined that allowing the development of the natural transient isoproterenol-induced hyperthermia was essential for the consistent induction of TTS-like contractility in this animal model (Figure 6). Groups wishing to replicate this TTS model should pay close attention to body temperature and allow moderate hyperthermia to occur.

There has been an anecdotal or correlative association between increased body temperature and Takotsubo syndrome in a number of circumstances. Takotsubo syndrome is statistically more likely to occur in summer or early autumn (unlike the winter presentation preference for most cardiac diseases) and is separately associated with higher ambient temperatures (16, 17). There has also been an afternoon predominance for TTS presentation compared to night-time (18) Fever and particularly sepsis have strong associations with Takotsubo syndrome (19), and high temperature was a predictor of worse outcomes in a series of 421 admissions for the syndrome (20). Hyperthyroidism, which is associated with raised body temperature, has been observed in a proportion of patients with Takotsubo syndrome (21). It is tempting to speculate that the temperature dysregulation and hot flushes in post-menopausal women may be an additional trigger for the syndrome. Furthermore, there have been increasing reports of TTS associated with COVID (22), and an early review has suggested that the morbidity and mortality of TTS may be exacerbated when superimposed on the hyper-inflammatory COVID background (23).

As hyperthermia was essential for the induction of TTS-like contractility changes, we sought to determine its importance in the maintenance of this contractility pattern. We found that cooling the animals back to a physiological body temperature at either 60 or 90 min post-isoproterenol had no effect on apical dysfunction, and changes in contraction followed a similar trend to animals maintained at 41°C. However, we do not know the effect of this cooling on long-term prognosis. Cellular experiments showed that hyperthermia alone did not increase contractility of cardiomyocytes, nor increase beta-adrenoceptor responsiveness, and therefore hyperthermia is affecting either the heart on an organ level, or at an integrated body level. The role of circulating immune cells was evident in the study on immune activation by single dose isoproterenol, and adoptive transfer of splenocytes from the isoproterenol-treated mice induced left ventricular dilation and impaired cardiac function in healthy recipients (12).

Mechanism of hyperthermia in TTS induction

Hyperthermia causes a wide range of physiological responses at enzymatic, cellular, organ, and whole-body levels. Through both pre-clinical models and clinical evidence, a number of hypotheses for the pathophysiology of TTS have been proposed. These include microvascular dysfunction (24), lipotoxicity within cardiomyocytes (5), and beta-adrenoceptor stimulus trafficking at the level of the cardiomyocyte (4). It may be that hyperthermia is acting on these, or through other mechanisms to increase apical dysfunction: there are a number of candidate underlying pathways, and their actions may not be mutually exclusive.

Increases in body temperature from 38 to 41°C in rats have been shown to increase sympathetic nerve discharge rate (11, 25), and may be supporting the hyper-catecholaminergic state present in the rat when isoproterenol is administered, particularly given the half-life of isoprenaline is <5 minu and a single dose of isoprenaline has been shown to induce

persistent pathological cardiac changes (12). AMP-activated protein kinase (AMPK) is ubiquitously expressed throughout the body, and has been implicated in the pathophysiology of TTS as endomyocardial tissue biopsies taken during the acute TTS phase show increased PI3K/Akt pathway activity (26), which can be activated by AMPK (27). Hyperthermia has been shown to activate AMPK in cancer cells (28), and hypothermia shown to inhibit AMPK in the brain (29). If AMPK is activated by hyperthermia in the setting of TTS, this could be contributing to the protective mechanisms thought to be present in this disease as AMPK activation has been shown to reduce cardiomyocyte apoptosis (30, 31). Heat shock proteins are also likely to be activated by this thermal stress (32), and have been shown to reduce both isoproterenol-induced cardiac apoptosis (33) and remodeling (34). One study has demonstrated the inhibition of the late-sodium currents by hyperthermia in iPS-derived cardiomyocytes (35), which interestingly was also seen in an iPS-derived cardiomyocyte model of TTS (8). We know that nitrosative stress may play a role in TTS (36, 37), which has been shown to be induced by hyperthermia (38). It has also been shown that alpha-1 adrenoceptor signaling *via* reactive oxidative stress increases the arrhythmogenicity of the myocardium during high levels of catecholamines (39), although in our study isoproterenol was used, which does not act as an agonist on alpha-1 adrenoceptors. Given the increased incidence of a prolonged QT interval in TTS in both models and patient cohort analysis (8, 40), the role of hyperthermia on reactive oxygen species generation and its arrhythmogenicity in the setting of excess catecholamines should be further assessed.

The role of hyperthermia directly on beta-adrenoceptors at a molecular level is poorly understood: one conference abstract has demonstrated reduced beta-adrenoceptor responsiveness in bladder detrusor muscle between 37 and 42°C (41), whereas many studies have been carried out on beta-adrenoceptor responses at hypothermic temperatures. In isolated rat cardiomyocytes, decreases in temperature to 15°C showed an increase in beta-adrenoceptor affinity (using radioactive-labeled propranolol) compared to normothermia (37°C). Hypothermia also does not prevent a beta-adrenoceptor response, as shown in a porcine model of hypothermia, where 30 ng/kg/min infusion of epinephrine resulted in a positive inotropic response at 32°C (42). However, in another experiment at 25°C, isoprenaline resulted in no positive inotropic response (43). Therefore, there is conflicting evidence with regards to catecholamine stimulation with varying body temperature, and further work to elucidate the molecular changes in this model of hyperthermia-facilitated TTS is required.

In a recent computational model of TTS a failure of the Frank-Starling mechanism was shown to increase apical ballooning at end systole (44). In a study that assessed the effects of hyperthermia on the Frank-Starling mechanism in anesthetized dogs, it was shown that hyperthermia of a similar range to the animals presented in this paper (40–41°C) resulted in a significant decrease in the gradient of inotropy change with respect to preload, thereby showing a failure of the Frank-Starling mechanism (45). This could also partly explain the lack of effect seen in isolated cardiomyocytes as they are unloaded. Although a tempting proposition, and one which certainly fits with the aforementioned computational model of TTS (44), the necessary role of hyperthermia is likely multifactorial, particularly in the maintenance of a hypercateholaminergic state as would be present in human TTS precipitated by a stressful event.

Clinical perspective

We have shown that hyperthermia is essential for the induction of TTS in this isoproterenol-induced model, and therefore it may be prudent that patients at risk of TTS are monitored for pyrexia and anti-pyretics are prescribed with a lower threshold. Furthermore, early echocardiographic imaging in patients with severe hyperthermic states, such as malignant hyperthermia or ICU admissions for sepsis, could reveal cardiac dysfunction, and guide clinical care. Nevertheless, the role of hyperthermia in human TTS is currently unknown, and as we were able to remove the hyperthermic state within 60 min of the induction agent being given (equivalent to the emotional stressor in humans), we cannot conclude that a reduction in body temperature *per se* would be of use in the management of the acute syndrome.

Summary

In summary, we have shown that hyperthermia is essential in the induction of TTS in an isoproterenol-induced rat model, and the removal of hyperthermia around the time of the development of apical dysfunction does not attenuate or reverse it. Isolated cardiomyocyte studies showed that, at least in the unloaded state, baseline contractility, or isoproterenol-induced inotropic changes were not affected by hyperthermia. Further studies are needed to assess the role of hyperthermia in patients and, if so, whether this can be manipulated to improve patient outcome.

Data availability statement

The raw data supporting the conclusions of this article will be made available by the authors, without undue reservation.

Ethics statement

The animal study was reviewed and approved by Central Animal Welfare and Ethical Review Board, Imperial College London Animal Ethics Committee, Gothenburg University.

Author contributions

MT, BR, and PW performed the experiments and analysis of data in this manuscript. MT wrote the initial draft of the manuscript, with contributions from PW, SH, and EO for the final draft. AL, EO, and SH supervised the research and had overall responsibility for the project. All authors contributed to the design of the experiments and analysis and interpretation of data. All authors contributed to the article and approved the submitted version.

Funding

The study was financed by grants from the Swedish state under the agreement between the Swedish government and the county councils (the ALF-agreement), the Swedish Heart-Lung Foundation and the Swedish Scientific Council; by RG/17/13/33173, PG/17/3/32722; RG/17/6/32944; RG/12/18/30088; Medical Research Council UKMR/L006855/1; the National Heart and Lung Institute Foundation and British Heart Foundation BHF FS/16/52/32259.

Acknowledgments

The authors would like to thank Peter O'Gara for the expert isolation of cardiomyocytes used in the *in vitro* studies. MT would like to thank the National Heart and Lung Institute Foundation for the funding of his Ph.D.

Conflict of interest

The authors declare that the research was conducted in the absence of any commercial or financial relationships that could be construed as a potential conflict of interest.

Publisher's note

Supplementary material

The Supplementary Material for this article can be found online at: https://www.frontiersin.org/articles/10.3389/fcvm.2022.869585/full#supplementary-material

References

1. Tranter MH, Wright PT, Sikkel MB, Lyon AR. Takotsubo cardiomyopathy: the pathophysiology. *Heart Fail Clin*. (2013) 9:187–96. doi: 10.1016/j.hfc.2012.12.010

2. Lyon AR, Bossone E, Schneider B, Sechtem U, Citro R, Underwood SR, et al. Current state of knowledge on Takotsubo syndrome: a position statement from the taskforce on Takotsubo syndrome of the Heart Failure Association of the European Society of Cardiology. *Eur J Heart Fail*. (2016) 18:8–27. doi: 10.1002/ejhf.424

3. El-Battrawy I, Santoro F, Stiermaier T, Möller C, Guastafierro F, Novo G, et al. Incidence and clinical impact of right ventricular involvement (biventricular ballooning) in Takotsubo syndrome: results from the GEIST registry. *Chest*. (2021) 160:1433–41. doi: 10.1016/j.chest.2021.04.072

4. Paur H, Wright PT, Sikkel MB, Tranter MH, Mansfield C, O'Gara P, et al. High levels of circulating epinephrine trigger apical cardiodepression in a β2-adrenergic receptor/Gi-dependent manner: a new model of Takotsubo cardiomyopathy. *Circulation*. (2012) 126:697–706. doi: 10.1161/CIRCULATIONAHA.112.111591

5. Shao Y, Redfors B, Scharin Täng M, Möllmann H, Troidl C, Szardien S, et al. Novel rat model reveals important roles of β-adrenoreceptors in stress-induced cardiomyopathy. *Int J Cardiol*. (2013) 168:1943–50. doi: 10.1016/j.ijcard.2012.12.092

6. Ueyama T, Kasamatsu K, Hano T, Yamamoto K, Tsuruo Y, Nishio I. Emotional stress induces transient left ventricular hypocontraction in the rat *via* activation of cardiac adrenoceptors: a possible animal model of "Tako-Tsubo" cardiomyopathy. *Circ J Off J Jpn Circ Soc*. (2002) 66:712–3. doi: 10.1253/circj.66.712

7. Hübscher D, Rebs S, Maurer W, Ghadri JR, Dressel R, Templin C, et al. Generation of iPSC-lines from two independent Takotsubo syndrome patients with recurrent Takotsubo events. *Stem Cell Res*. (2020) 44:101746. doi: 10.1016/j.scr.2020.101746

8. El-Battrawy I, Zhao Z, Lan H, Schünemann JD, Sattler K, Buljubasic F, et al. Estradiol protection against toxic effects of catecholamine on electrical properties in human-induced pluripotent stem cell derived cardiomyocytes. *Int J Cardiol*. (2018) 254:195–202. doi: 10.1016/j.ijcard.2017.11.007

9. Ridnour LA, Thomas DD, Mancardi D, Espey MG, Miranda KM, Paolocci N, et al. The chemistry of nitrosative stress induced by nitric oxide and reactive nitrogen oxide species. Putting perspective on stressful biological situations. *Biol Chem*. (2004) 385:1–10. doi: 10.1515/BC.2004.001

10. Fan X, Yang G, Kowitz J, Akin I, Zhou X, El-Battrawy I. Takotsubo syndrome: translational implications and pathomechanisms. *Int J Mol Sci*. (2022) 23:1951. doi: 10.3390/ijms23041951

11. Nakamura K, Morrison SF. Central sympathetic network for thermoregulatory responses to psychological stress. *Auton Neurosci Basic Clin*. (2022) 237:102918. doi: 10.1016/j.autneu.2021.102918

12. Forte E, Panahi M, Baxan N, Ng FS, Boyle JJ, Branca J, et al. Type 2 MI induced by a single high dose of isoproterenol in C57BL/6J mice triggers a persistent adaptive immune response against the heart. *J Cell Mol Med*. (2021) 25:229–43. doi: 10.1111/jcmm.15937

13. Sato M, O'Gara P, Harding SE, Fuller SJ. Enhancement of adenoviral gene transfer to adult rat cardiomyocytes *in vivo* by immobilization and ultrasound treatment of the heart. *Gene Ther*. (2005) 12:936–41. doi: 10.1038/sj.gt.3302476

14. Wittstein IS, Thiemann DR, Lima JAC, Baughman KL, Schulman SP, Gerstenblith G, et al. Neurohumoral features of myocardial stunning due to sudden emotional stress. *N Engl J Med*. (2005) 352:539–48. doi: 10.1056/NEJMoa043046

15. Oras J, Redfors B, Ali A, Lundgren J, Sihlbom C, Thorsell A, et al. Anaesthetic-induced cardioprotection in an experimental model of the Takotsubo syndrome - isoflurane vs. propofol. *Acta Anaesthesiol Scand*. (2017) 61:309–21. doi: 10.1111/aas.12857

16. Looi JL, Lee M, Grey C, Webster M, To A, Kerr AJ. Seasonal variation in Takotsubo syndrome compared with myocardial infarction: ANZACS-QI 16. *N Z Med J*. (2018) 131:21–9.

17. Kanaoka K, Okayama S, Terasaki S, Nakano T, Ishii M, Nakai M, et al. Role of climatic factors in the incidence of Takotsubo syndrome: a nationwide study from 2012 to 2016. *ESC Heart Fail*. (2020) 7:2629–36. doi: 10.1002/ehf2.12843

18. El-Battrawy I, Aweimer A, Lang S, Ansari U, Gietzen T, Ullrich N, et al. Impact of chronobiological variation in Takotsubo syndrome: prognosis and outcome. *Front Cardiovasc Med*. (2021) 8:676950. doi: 10.3389/fcvm.2021.676950

19. Cappelletti S, Ciallella C, Aromatario M, Ashrafian H, Harding S, Athanasiou T. Takotsubo Cardiomyopathy and sepsis. *Angiology*. (2017) 68:288–303. doi: 10.1177/0003319716653886

20. Kimura A, Yoshikawa T, Isogai T, Tanaka H, Ueda T, Yamaguchi T, et al. Impact of body temperature at admission on hospital outcomes in patients with Takotsubo syndrome: insights from the Tokyo cardiovascular care unit network registry. *Eur Heart J Acute Cardiovasc Care*. (2020) 9:703–10. doi: 10.1177/2048872619886313

21. Aweimer A, El-Battrawy I, Akin I, Borggrefe M, Mügge A, Patsalis PC, et al. Abnormal thyroid function is common in Takotsubo syndrome and depends on two distinct mechanisms: results of a multicentre observational study. *J Intern Med*. (2021) 289:675–87. doi: 10.1111/joim.13189

22. Eftekharzadeh P, Patel A, Sokolova E, Rodas A, Ahmed S. Takotsubo cardiomyopathy: a COVID-19 complication. *Cureus*. (2022) 14:e22803. doi: 10.7759/cureus.22803

23. Techasatian W, Nishimura Y, Nagamine T, Ha G, Huang R, Shah P, et al. Characteristics of Takotsubo cardiomyopathy in patients with COVID-19: systematic scoping review. *Am Heart J Plus Cardiol Res Pract*. (2022) 13:100092. doi: 10.1016/j.ahjo.2022.100092

24. Galiuto L, De Caterina AR, Porfidia A, Paraggio L, Barchetta S, Locorotondo G, et al. Reversible coronary microvascular dysfunction: a common pathogenetic mechanism in apical ballooning or Tako-Tsubo syndrome. *Eur Heart J*. (2010) 31:1319–27. doi: 10.1093/eurheartj/ehq039

25. Kenney MJ, Barney CC, Hirai T, Gisolfi CV. Sympathetic nerve responses to hyperthermia in the anesthetized rat. *J Appl Physiol*. (1995) 78:881–9. doi: 10.1152/jappl.1995.78.3.881

26. Nef HM, Möllmann H, Hilpert P, Troidl C, Voss S, Rolf A, et al. Activated cell survival cascade protects cardiomyocytes from cell death in Tako-Tsubo cardiomyopathy. *Eur J Heart Fail*. (2009) 11:758–64. doi: 10.1093/eurjhf/hfp076

27. Tao R, Gong J, Luo X, Zang M, Guo W, Wen R, et al. AMPK exerts dual regulatory effects on the PI3K pathway. *J Mol Signal*. (2010) 5:1. doi: 10.1186/1750-2187-5-1

28. Lee H, Park HJ, Park CS, Oh ET, Choi BH, Williams B, et al. Response of breast cancer cells and cancer stem cells to metformin and hyperthermia alone or combined. *PLoS ONE*. (2014) 9:e87979. doi: 10.1371/journal.pone.0087979

29. Li J, Benashski S, McCullough LD. Post-stroke hypothermia provides neuroprotection through inhibition of AMP-activated protein kinase. *J Neurotrauma*. (2011) 28:1281–8. doi: 10.1089/neu.2011.1751

30. Dyck JRB, Lopaschuk GD. AMPK alterations in cardiac physiology and pathology: enemy or ally? *J Physiol*. (2006) 574(Pt 1):95–112. doi: 10.1113/jphysiol.2006.109389

31. Zou MH, Xie Z. Regulation of interplay between autophagy and apoptosis in the diabetic heart: new role of AMPK. *Autophagy*. (2013) 9:624–5. doi: 10.4161/auto.23577

32. O'Connor MJ, Rembold CM. Heat-induced force suppression and HSP20 phosphorylation in swine carotid media. *J Appl Physiol*. (2002) 93:484–8. doi: 10.1152/japplphysiol.00009.2002

33. Fan GC, Chu G, Mitton B, Song Q, Yuan Q, Kranias EG. Small heat-shock protein HSP20 phosphorylation inhibits β-agonist-induced cardiac apoptosis. *Circ Res*. (2004) 94:1474–82. doi: 10.1161/01.RES.0000129179.66631.00

34. Fan GC, Yuan Q, Song G, Wang Y, Chen G, Qian J, et al. Small heat-shock protein Hsp20 attenuates β-agonist-mediated cardiac remodeling through apoptosis signal-regulating kinase 1. *Circ Res*. (2006) 99:1233–42. doi: 10.1161/01.RES.0000251074.19348.af

35. El-Battrawy I, Lang S, Zhao Z, Akin I, Yücel G, Meister S, et al. Hyperthermia influences the effects of sodium channel blocking drugs in human-induced pluripotent stem cell-derived cardiomyocytes. *PLoS ONE*. (2016) 11:e0166143. doi: 10.1371/journal.pone.0166143

36. Surikow SY, Nguyen TH, Stafford I, Chapman M, Chacko S, Singh K, et al. Nitrosative stress as a modulator of inflammatory change in a model of Takotsubo syndrome. *JACC Basic Transl Sci*. (2018) 3:213–26. doi: 10.1016/j.jacbts.2017.10.002

37. Surikow SY, Raman B, Licari J, Singh K, Nguyen TH, Horowitz JD. Evidence of nitrosative stress within hearts of patients dying of Takotsubo cardiomyopathy. *Int J Cardiol*. (2015) 189:112–4. doi: 10.1016/j.ijcard.2015.03.416

38. Lambert GP, Gisolfi CV, Berg DJ, Moseley PL, Oberley LW, Kregel KC. Selected contribution: hyperthermia-induced intestinal permeability and the role of oxidative and nitrosative stress. *J Appl Physiol*. (2002) 92:1750–61; discussion: 1749. doi: 10.1152/japplphysiol.00787.2001

39. Huang M, Fan X, Yang Z, Cyganek L, Li X, Yuecel G, et al. Alpha 1-adrenoceptor signalling contributes to toxic effects of catecholamine on electrical properties in cardiomyocytes. *Europace*. (2021) 23:1137–48. doi: 10.1093/europace/euab008

40. Syed FF, Asirvatham SJ, Francis J. Arrhythmia occurrence with takotsubo cardiomyopathy: a literature review. *Europace*. (2011) 13:780–8. doi: 10.1093/europace/euq435

41. Farr S, Chess-Williams R, McDermott C. *Hyperthermia Therapy Causes Depessed Detrusor and Urothelial Responses With Muscarinic, Adrenergic and Neurogenic Stimulation*. Barcelona: International Continence Society (2013). Available online at: https://www.ics.org/Abstracts/Publish/180/000694.pdf

42. Dietrichs ES, Schanche T, Kondratiev T, Gaustad SE, Sager G, Tveita T. Negative inotropic effects of epinephrine in the presence of increased β-adrenoceptor sensitivity during hypothermia in a rat model. *Cryobiology*. (2015) 70:9–16. doi: 10.1016/j.cryobiol.2014.10.012

43. Lauri T. Cardiovascular responses to beta-stimulation with isoproterenol in deep hypothermia. *J Appl Physiol*. (1996) 81:573–7. doi: 10.1152/jappl.1996.81.2.573

44. Land S, Niederer SA, Louch WE, Røe ÅT, Aronsen JM, Stuckey DJ, et al. Computational modeling of Takotsubo cardiomyopathy: effect of spatially varying β-adrenergic stimulation in the rat left ventricle. *Am J Physiol*. (2014) 307:H1487–96. doi: 10.1152/ajpheart.00443.2014

45. Sagach VF, Shimanskaya TV. Cardiodynamics and pumping function of the heart under conditions of hyperthermia. *Bull Exp Biol Med*. (1993) 116:893–5. doi: 10.1007/BF00786048

frontiers | Frontiers in Cardiovascular Medicine

TYPE Original Research
PUBLISHED 06 October 2022
DOI 10.3389/fcvm.2022.909399

OPEN ACCESS

EDITED BY
Deborah Hunt,
Adelphi University, United States

REVIEWED BY
Olli-Pekka Smolander,
Tallinn University of Technology, Estonia
Mirolyuba Ilieva,
Aalborg University, Denmark

*CORRESPONDENCE
Yiming Zhong
yimingdoc@126.com
Genfa Xiao
iesvev1986@foxmail.com

SPECIALTY SECTION
This article was submitted to Hypertension, a section of the journal Frontiers in Cardiovascular Medicine

RECEIVED 31 March 2022
ACCEPTED 13 September 2022
PUBLISHED 06 October 2022

CITATION
Chen Y, Wu C, Wang X, Zhou X, Kang K, Cao Z, Yang Y, Zhong Y and Xiao G (2022) Weighted gene co-expression network analysis identifies dysregulated B-cell receptor signaling pathway and novel genes in pulmonary arterial hypertension. *Front. Cardiovasc. Med.* 9:909399. doi: 10.3389/fcvm.2022.909399

Weighted gene co-expression network analysis identifies dysregulated B-cell receptor signaling pathway and novel genes in pulmonary arterial hypertension

Yuanrong Chen[1], Chaoling Wu[1], Xiaoping Wang[2], Xufeng Zhou[2], Kunpeng Kang[2], Zuofeng Cao[2], Yihong Yang[2], Yiming Zhong[1,2,3]* and Genfa Xiao[1,2,3]*

[1]Key Laboratory of Prevention and Treatment of Cardiovascular and Cerebrovascular Diseases of Ministry of Education, Gannan Medical University, Ganzhou, China, [2]Department of Cardiology, The First Affiliated Hospital of Gannan Medical University, Ganzhou, China, [3]Gannan Branch Center of National Geriatric Disease Clinical Medical Research Center, Gannan Medical University, Ganzhou, China

Background: Pulmonary arterial hypertension (PAH) is a devastating cardio-pulmonary vascular disease in which chronic elevated pulmonary arterial pressure and pulmonary vascular remodeling lead to right ventricular failure and premature death. However, the exact molecular mechanism causing PAH remains unclear.

Methods: RNA sequencing was used to analyze the transcriptional profiling of controls and rats treated with monocrotaline (MCT) for 1, 2, 3, and 4 weeks. Weighted gene co-expression network analysis (WGCNA) was employed to identify the key modules associated with the severity of PAH. Gene Ontology (GO) and Kyoto Encyclopedia of Genes and Genomes (KEGG) enrichment analyses were performed to explore the potential biological processes and pathways of key modules. Real-time PCR and western blot analysis were used to validate the gene expression. The hub genes were validated by an independent dataset obtained from the Gene Expression Omnibus database.

Results: A total of 26 gene modules were identified by WGCNA. Of these modules, two modules showed the highest correlation with the severity of PAH and were recognized as the key modules. GO analysis of key modules showed the dysregulated inflammation and immunity, particularly B-cell-mediated humoral immunity in MCT-induced PAH. KEGG pathway analysis showed the significant enrichment of the B-cell receptor signaling pathway in the key modules. Pathview analysis revealed the dysregulation of the B-cell receptor signaling pathway in detail. Moreover, a series of humoral immune response-associated genes, such as BTK, BAFFR, and TNFSF4, were found to be differentially expressed in PAH. Additionally, five genes, including BANK1, FOXF1, TLE1, CLEC4A1, and CLEC4A3, were identified and validated as the hub genes.

Conclusion: This study identified the dysregulated B-cell receptor signaling pathway, as well as novel genes associated with humoral immune response in MCT-induced PAH, thereby providing a novel insight into the molecular mechanisms underlying inflammation and immunity and therapeutic targets for PAH.

KEYWORDS

pulmonary arterial hypertension, B-cell receptor signaling pathway, weighted gene co-expression network analysis, humoral immunity, hub genes

Introduction

Pulmonary arterial hypertension (PAH) is a devastating cardio-pulmonary vascular disease. Despite novel pharmacotherapy strategies improved symptoms and physical signs in patients with PAH, the prognosis remains poor (1). Occlusive and obliterative alterations in the small to medium pulmonary arteries are widely observed. Dysfunctional and altered structure in pulmonary vasculature leads to elevated mean pulmonary arterial pressure (mPAP), culminating in right ventricular failure and premature death (2). Dysregulated immunity and perivascular inflammation have attracted broad attention and have been inextricably associated with the development of PAH (2). Although there was accumulating research in PAH pathogenesis, with considerable progress in recent years, the exact molecular mechanism underlying inflammation and immunity in PAH remains unclear.

Monocrotaline (MCT), a plant-derived alkaloid, was extensively employed to induce PAH models for over 50 years (3). The development of MCT-induced PAH was closely associated with dysfunctional inflammatory and immune responses. In the MCT-induced PAH model, we found the thickened vascular wall, occlusive and/or obliterative vascular lumen, impaired endothelium, and perivasculitis in pulmonary arteries (4). Moreover, the parameters of pulmonary vascular remodeling, the percentage of total wall thickness to external diameters of pulmonary arterioles diameter (WT%), and the percentage of wall area to the total area of vessels (WA%) were gradually increased in the progression of MCT-induced PAH (4). In addition, we performed RNA sequencing (RNA-seq) analysis of MCT-induced PAH and found that inflammatory and immune responses occurred at the early stage of PAH and were involved in the initiation and progression of PAH (5).

The rapid development of systemic biology provides a powerful tool for exploring disease-associated genes (6). Weighted gene co-expression network analysis (WGCNA) is a novel systemic biology analysis approach (7) that divides the gene expression matrix into different gene modules and detects the relationship between gene modules and external phenotypical characteristics. WGCNA provides a system-level perspective into the genes and phenotypical traits and has been broadly used for probing the hub genes that drive key signaling pathways in diseases (8). For example, Hao et al. (9) identified specialized miRNA-mRNA regulatory networks composed of 6 miRNA and 12 mRNA in idiopathic pulmonary hypertension by using WGCNA. Zheng et al. (10) identified four key genes as potential therapeutic targets and early biomarkers in systemic sclerosis-related pulmonary hypertension by using WGCNA. In addition, Cai et al. (11) identified five immune cell-related marker genes by using WGCNA in pulmonary fibrosis-associated pulmonary hypertension, and these marker genes could divide these samples into various subgroups.

In this study, we constructed a gene co-expression network and identified the key modules related to the severity of PAH by performing WGCNA analysis, as well as characterized hub genes and signaling pathways, aiming to provide a deeper understanding of molecular mechanisms underlying inflammation and immunity in PAH.

Materials and methods

Data preparation

The detailed methods regarding animals and treatment, RNA extraction, cDNA library preparation, and RNA sequencing are described in our previous study (5, 12). Briefly, a total of 17 rats were used, in which 12 rats were randomly assigned to four MCT-treatment groups ($n = 3$, per group) and the remaining 5 rats served as a control group. The MCT-treated rats were sacrificed at the end of weeks 1, 2, 3, and 4. Five control rats were sacrificed at different time points, including week 0 (MCT was given) and each time when MCT-treated rats were sacrificed. Rat lungs were isolated for further RNA extraction, cDNA library preparation, and RNA-seq. The raw sequencing data have been deposited in Gene Expression Omnibus (GEO) with an accession number GSE149713. In addition, an independent dataset with an accession number GSE149899 was used to validate the hub genes. The raw read counts of the GSE149899 dataset were downloaded from GEO (https://www.ncbi.nlm.nih.gov/geo/query/acc.cgi?acc=

GSE149899). The GSE149899 dataset included RNA-seq data of lung tissues from six irreversible PAH (MCT-induced PAH cannot be reversed by hemodynamic unloading) rats, 12 reversible PAH (MCT-induced PAH can be reversed by hemodynamic unloading) rats, and five normal control rats. The values of FPKM (fragments per kilobase of transcript per million fragments mapped) were usually used to estimate the relative expression abundance of transcripts. In the present study, the GSE149899 dataset was processed by transferring the raw read count into FPKM value in R software, so the gene expression value could be estimated and compared. The processed data of the GSE149899 dataset is attached in Supplementary Table 1.

Construction of weighted gene co-expression network

In our previous study, a total of 23,200 transcripts were identified in MCT-induced PAH (5). To maintain data integrity, an expression matrix containing 17 samples and 23,200 transcripts was used to construct the co-expression network by using the "WGCNA" R package (7). First, the gene expression matrix was converted into the co-expression matrix by calculating the absolute value of each gene's correlation coefficient. Next, the co-expression matrix was transformed into the adjacency matrix by a thresholding procedure. Then, the "pickSoftThreshold" function of the "WGCNA" R package was used to perform an analysis of scale-free topology for soft-thresholding. Here, the soft-thresholding power $\beta = 4$ (scale-free $R^2 = 0.9$) was chosen to meet the scale-free network. After that, the adjacency matrix was transformed into the topological overlap matrix (TOM) and dissimilarity TOM. Lastly, hierarchical clustering and the dynamic tree cut method were used to divide modules. The minimal gene number in each gene module was set as 50, and similar modules were merged based on a height cutoff of 0.25.

Identification of key modules associated with PAH

Module eigengene (ME) is the first principal component of a given module and is considered a representative of the gene expression in the given module (7). ME was calculated for each module. The correlation between the MEs and the phenotypic traits was calculated by using the Pearson correlation coefficient to assess the relationship between each gene co-expression module and phenotypic trait. The phenotypic traits include WT%, WA%, mPAP, and right ventricular hypertrophy index (RVHI). These phenotypic traits were the parameters commonly used for assessing PAH severity (4). The modules showing the most highly positive or negative correlation with four phenotypic traits were selected as the key modules.

Enrichment analysis of the key modules

Gene Ontology (GO) and Kyoto Encyclopedia of Genes and Genomes (KEGG) enrichment analysis were performed by the "clusterProfiler" R package (13). P-value < 0.05 was viewed as significant enrichment.

Visualization of B-cell receptor signaling pathway

The genes annotated in the B-cell receptor (BCR) signaling pathway were extracted from KEGG PATHWAY DATABASE (https://www.genome.jp/kegg/pathway.html). The Pathview (https://pathview.uncc.edu/analysis) is a visual tool that maps, integrates, and renders a large variety of biological data onto molecular pathway graphs (14). The altered genes in the BCR signaling pathway were visualized by using a modified Pathview that showed P-value instead of expression value ratio change. The details of the statistical analysis are described in the figure legends.

Identification of the hub genes

The genes with high connectivity in the key modules were viewed as the hub genes (7), which were considered to play a more significant biological role in the gene regulatory network. Module membership (MM) was used to represent intramodular connectivity by correlating the gene expression profile with the ME of a given module (15). The closer the MM of a gene is to 1 or −1, the higher the connection to the given module (7). Similarly, gene significance (GS) was used to assess the correlation between the gene expression profile and the phenotypic trait. The closer the GS of the gene is to 1, the more highly it is associated with the given phenotypic trait. In this study, genes with $|GS|$ and $|MM| \geq 0.8$ were viewed as the candidate genes of the blue module, and genes with $|GS| \geq 0.5$ and $|MM| \geq 0.8$ were considered as the candidate genes of the dark red module. The differentially expressed genes (DEGs) in the candidate genes were defined as the hub genes in the present study. The hub genes were validated by GSE149899.

Real-time PCR analysis

Total RNA was extracted from the lung tissues of control and rats injected with MCT for 4 weeks (MCTW4), according to the manufacturer's instruction. First-strand cDNA

synthesis was performed by using the Transcriptor First Strand cDNA Synthesis Kit (Roche, Life Science, CH), according to the manufacturer's protocol. The quantification of mRNA expression was performed in a Step One Plus Real-time PCR System (Life Technologies™, Applied Biosystems, Gene Co., Ltd., Carlsbad, CA, USA). The rat origin primers used for real-time PCR analysis were listed as follows: forward-5′-ACA GCA ACA GGG TGG TGG AC-3′ and reverse-5′-TTT GAG GGT GCA GCG AAC TT-3′ for GAPDH; forward-5′-AGT CTG GTG GGC TGG AGG TGG-3′ and reverse-5′-GAA GGG TTT CCG AGG GGG GTA-3′ for BAFFR; forward-5′- ATG TGA GGG GGG AAG ACT A-3′ and reverse-5′- AGG TGG ATG AGA TAA AGC C-3′ for TNFSF4; forward-5′- CAA CAG CAG CAC CAA TCT CCA-3′ and reverse-5′-ATA CTC CTC GCC CTT TCG CAA-3′ for BTK; forward-5′-CTT GGG CAT TCT GTC GGT GAT-3′ and reverse-5′-GGA GGT GCT GGG AAG TTT ATT-3′ for CD20; and forward-5′-ATG GAC CAC CGC CTC TAC C-3′ and reverse-5′-TCC TCA GCC CCA CCA CAC A-3′ for IGHM. The relative quantification of the mRNA expression of genes was analyzed in accordance with the comparative $2^{-\Delta\Delta CT}$ method and expressed as fold changes.

Western blot analysis

Western blot analysis was performed as previously described (16). Lung tissues were isolated from the control group, and rats injected with MCT for 4 weeks. Then, the lung tissues were lysed with RIPA lysis buffer containing protease inhibitor cocktails (Meilunbio Biotech Co., Ltd, CHN). Tissue lysates were incubated on ice for 30 min and subsequently centrifuged at 12,000 rpm at 4°C for 5 min, and the supernatant was separated for further analysis. The protein concentration was measured by using the BCA kit (GBCBIO Biotech Co., Ltd, CHN). Equal amounts of total protein from different samples were separated by 12% SDS-PAGE and transferred into 0.45 μm PVDF membranes (IPVH00010, Merck Millipore, DEU). The PVDF membranes were blocked with 5% non-fat milk powder in TBST at room temperature for 2 h and incubated with primary antibodies overnight at 4°C. On the 2nd day, the membranes were washed three times with TBST and incubated with the appropriate horseradish peroxidase-conjugated secondary antibodies (Boster Biological Technology Co., Ltd, CHN, 1:10,000) for 2 h at room temperature. After being washed three times with TBST, the membranes were incubated with an ECL reagent (Affinity Biosciences, USA) for detecting the blots, and the blots were quantified by Image-Pro Plus software (version: 6.0). Primary antibodies, including mouse anti-BTK (1:1,000), rabbit anti-CD19 (1:1,000), rabbit anti-GAPDH (1:1,000), and rabbit anti-CD20 (1:2,000), were purchased from Jingjie PTM BioLab Co. Ltd, CHN.

Statistical analysis

All statistical analyses were performed using RStudio (version 2021.09.2) and R (version 4.1.2) software. Data were presented as mean ± SD (standard deviation). The "ggplot2 (version 3.3.6)," "pheatmap (version 1.0.12)", and "WGCNA (version 1.71)" R packages were used to draw graphics. The "DEseq2 (version 1.34.0)" R package was used to identify DEGs (a threshold of $|\log2 (\text{Fold Change})| \geq 1$ & $p \leq 0.05$). The difference between groups was compared by the two-tailed Student's *t*-test (normal distribution) or Wilcoxon signed-rank test (abnormal distribution). *P*-value < 0.05 was considered as statistical significance.

Results

Construction of the co-expression network and identification of the key modules

In this study, to ensure the integrity of transcriptional profiling, an expression matrix comprising 17 samples and 23,200 genes (Supplementary Table 2 and Figure 1A) was used to construct the co-expression network. Given the scale independence and mean connectivity, the power value $\beta = 4$ (scale-free $R^2 = 0.9$) was selected as the soft threshold for the present study (Figure 1B). In addition, based on the dynamic tree cut algorithm and merge cutoff of 0.25, a total of 26 gene co-expression modules were generated and were assigned with different colors for distinguishing each other (Figures 1C,D). It was shown that the turquoise module had the largest number of genes, whereas the saddle brown showed the lowest number of genes (Figure 2A). The heatmap plot of ME showed that all gene modules were independent of each other (Figure 2A). The severity of MCT-induced PAH was evaluated by the phenotypic traits, composed of mPAP, RVHI, WT%, and WA% in our previous study (4). Upon constructing the co-expression network, we assessed the relationship between the gene co-expression modules and phenotypic traits through Pearson correlation analysis. As shown in Figure 2B, the dark red module showed the most highly positive correlation with mPAP ($r = 0.66$, $P = 3.91e\text{-}03$), RVHI ($r = 0.65$, $P = 4.56e\text{-}01$), WT% ($r = 0.68$, $P = 2.58e\text{-}03$), and WA% ($r = 0.63$, $P = 6.62e\text{-}03$). In contrast, the blue module showed the most highly negative correlation with mPAP ($r = -0.77$, $P = 2.99e\text{-}04$), RVHI ($r = -0.77$, $P = 3.19e\text{-}04$), WT% ($r = -0.85$, $P = 1.35e\text{-}05$), and WA% ($r = -0.88$, $P = 3.20e\text{-}06$). As a result, two modules depicted with blue and dark red colors were the most relevant to the severity of PAH and were identified as the key modules for further analysis.

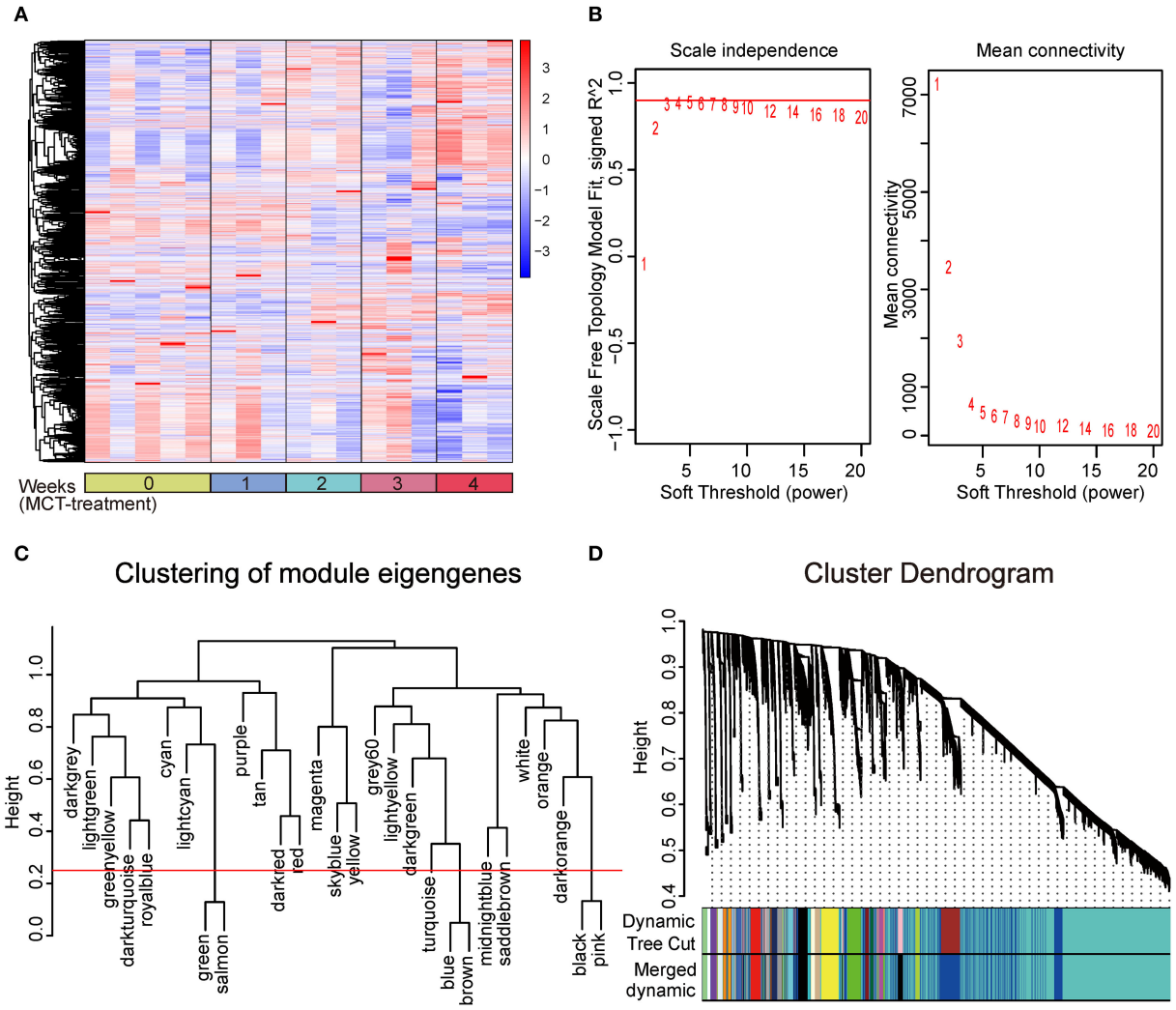

FIGURE 1
Construction of weighted gene co-expression network and division of gene co-expression module. **(A)** Clustering analysis heatmap plot of the expression matrix of 23,200 genes. The rows and columns represent gene expression levels and each sample, respectively. Red and blue represent the elevation and decrease of corresponding gene expression, respectively. **(B)** Analysis of the scale-free fit index (left) and the mean connectivity (right) for various soft-thresholding powers (β), among which four were chosen as the value to construct a scale-free network. **(C)** Clustering of module eigengenes. The cut height (red line) was 0.25. **(D)** Clustering dendrogram of all genes, with dissimilarity based on the topological overlap. Each color represents a gene co-expression module. Twenty-six gene co-expression modules were divided.

GO enrichment analysis of the key modules

To investigate potential biological processes of the dark red and blue module, GO enrichment analysis was performed. GO results of the dark red module showed that most of the biological processes were associated with humoral immune response, such as B-cell receptor signaling pathway, B-cell activation, B-cell proliferation, B-cell differentiation, antigen receptor-mediated signaling pathway, regulation of B-cell proliferation, and regulation of B-cell activation (Figure 3A). Similar to the dark red module, GO enrichment analysis of the blue module also showed a humoral immune response, such as antigen processing and presentation, B-cell-mediated immunity, and immunoglobulin-mediated immune response (Figure 3B). Taken together, these results suggested a role for B-cell-mediated humoral immune response in the development of MCT-induced PAH.

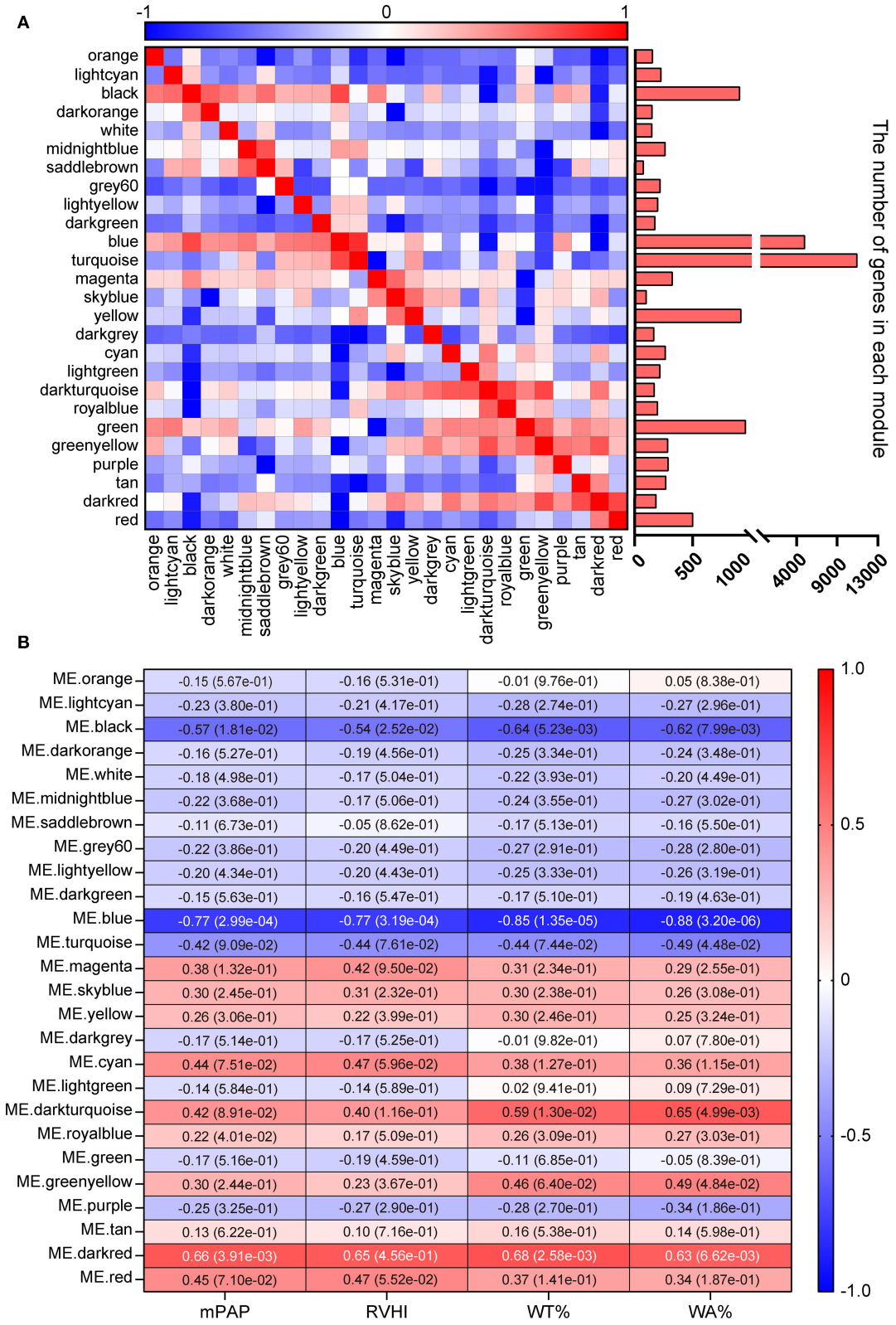

FIGURE 2
Identification of key modules. **(A)** Heatmap plot of module eigengene. Red and blue represent a positive and negative correlation, respectively. The bar chart represents the number of genes in each module. **(B)** Heatmap plot of module–trait relationship. Rows and columns represent different gene co-expression modules and phenotypic traits. The dark red and blue module showed the strongest correlation.

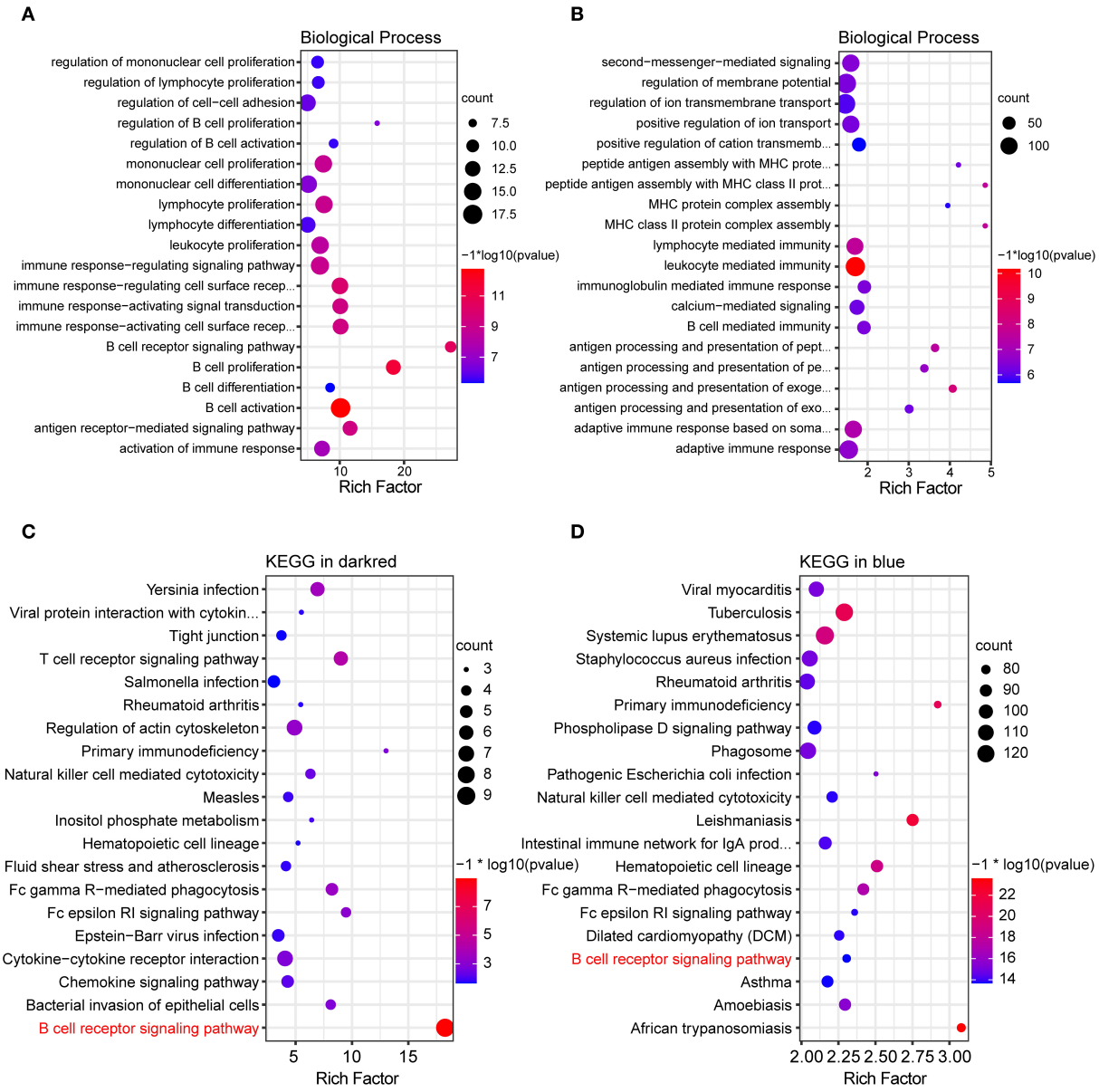

FIGURE 3
GO and KEGG functional enrichment analysis of key modules. **(A,B)** Bubble plot showing top 20 terms of biological process in the dark red and blue module, respectively. **(C,D)** Bubble plot showing top 20 pathways of KEGG functional enrichment analysis in the dark red and blue module, respectively.

KEGG enrichment analysis of the key modules

To further explore the inherent signaling pathways of the dark red and blue module, the KEGG enrichment analysis was performed. KEGG enrichment analysis of the dark red module revealed the inflammatory/immune-related pathways, including B-cell receptor (BCR) signaling pathway, T-cell receptor signaling pathway, primary immunodeficiency, chemokine pathway, natural killer cell-mediated cytotoxicity, and leukocyte trans-endothelial migration (Figure 3C). Consistently, the inflammatory/immune response-related pathways were also enriched in the blue module, owing to the enrichment of the BCR signaling pathway, primary immunodeficiency, and natural killer cell-mediated cytotoxicity (Figure 3D).

The change of BCR signaling pathway in MCT-induced PAH

It is worth noting that the BCR signaling pathway was the most significantly enriched pathway in the dark red module and was also significantly enriched in the blue module. Consequently, the BCR signaling pathway was chosen for further analysis. The BCR is an integral membrane complex composed of two immunoglobulin (Ig) heavy chains, two Ig light chains, and two heterodimers of Igα and Igβ (17). Ligation of the BCR with the specific antigen initiates highly sequential recruitment of critical intracellular mediators and adaptors, including LYN, SYK, BTK, BLNK, and VAV, and activates downstream pathways resulting in B-cell proliferation, differentiation, and secretion of various immunoglobulins and cytokines (18–20). Pathview and hierarchical clustering analysis showed the increased expression of BCR Igα (CD79A), Igβ (CD79B), LYN, BTK, SYK, BLNK, and CD19/21/81 in the BCR signaling pathway (Figures 4A,B). In addition, the altered expression of other genes was also shown, including upregulated genes FcgRIIB (FCGR2B), LEU13 (LFITM1), and PIR-B (LILRB3 and LILRB3A) and downregulated genes PLC-γ2 (PLCG2), PKCβ (PRKCB), SOS (SOS2), and IκBα (NFKBIA).

Identification and validation of humoral immune response-associated DEGs

Due to the enrichment of dysregulated BCR signaling pathway, we then analyzed the genes enriched in the humoral immune response by GO analysis. A total of 26 terms and 162 genes were associated with humoral immune response in the dark red and blue module (Supplementary Table 3). Differential expression analysis showed that 78 genes were differentially expressed, of which eight genes, including CD19, CD21, CD81, BTK, BLNK, CD79A, CD79B, and LILRB3A, were overlapped in the BCR signaling pathway (Figure 5A). To characterize these humoral immune response-associated DEGs, we applied a heatmap to exhibit them. The heatmap showed that the majority of genes were elevated in a time-dependent manner (Figures 5A–D). DEGs associated with cellular B-cell homeostasis (GO:0001782), activation (GO:0042113), and proliferation (GO:0042100) were upregulated in MCT-induced PAH, such as BAFFR, CD70, and CD20 (Figure 5B). In contrast, DEGs associated with immature B-cell differentiation (GO:0002327), immunoglobulin production, (GO:0002377), and humoral immune response (GO:0006959) showed dysregulated expression, due to the identification of both upregulated DEGs (IL-1β, IL-6, IGHM, JCHAIN, TNFSF4, TNFRSF4, and MZB1) and downregulated DEGs (IL-33, NOTCH1, CCR7, etc.) (Figure 5C). As shown in Figure 5D, the upregulation of DEGs associated with the regulation of B-cell activation (GO:0050864), proliferation (GO:0030888), differentiation (GO:0030183), humoral immune response (GO:0002920), and BCR signaling pathway (GO:0050855) was also identified, such as ACOD1 and FCRL5. Moreover, a set of DEGs was overlapped in various biological process terms. For instance, BTK was overlapped in B-cell-mediated immunity (GO:0019724), B-cell receptor signaling pathway (GO:0050853), and positive regulation of B-cell-mediated immunity (GO:0002714). BAFFR was overlapped in B-cell homeostasis (GO:0001782), activation (GO:0042113), proliferation (GO:0042100), and regulation of B-cell activation (GO:0050864) and proliferation (GO:0030888). TNFSF4 was overlapped in B-cell-mediated immunity (GO:0019724), immunoglobulin production (GO:0002377), and positive regulation of B-cell-mediated immunity (GO:0002714).

The DEGs overlapped in multiple GO terms may be more important and representative of humoral immunity. Therefore, we selected BAFFR, BTK, and TNFSF4 for further validation. Additionally, CD19, CD20, and IGHM were also selected, due to their essential roles in humoral immune response (21, 22). As shown in Figure 6A, the validation of the RNA-seq dataset by real-time PCR showed the upregulation of BAFFR, BTK, TNFSF4, CD20, and IGHM, thus confirming the upregulation of humoral immune response-associated genes in MCT-induced PAH. To further validate our RNA-seq dataset in protein levels, western blot analysis was performed to validate three critical humoral immune response-associated DEGs, including BTK, CD19, and CD20. Western blot analysis showed elevated protein levels of BTK, CD19, and CD20 (Figure 6B), further confirming the upregulation of humoral immune response-associated genes in MCT-induced PAH.

Identification and validation of the hub genes in key modules

According to the criteria mentioned in the methods, 38 and 52 candidate genes were identified in the dark red and blue module, respectively. Differential expression analysis showed that 7 of 38 candidate genes, including ACOD1, CLEC4A1, and CLEC4A3, were differentially expressed in the dark red module (Figure 7A and Supplementary Figure 1). Similarly, 37 of 52 candidate genes, including FOXF1, BANK1, and TLE1, were differentially expressed in the blue module (Figure 7B and Supplementary Figure 2). As shown in Figure 7C, the expression of the ACOD1, CLEC4A1, and CLEC4A3 was gradually increased in the dark red module. In contrast, the expression of the FOXF1, BANK1, and TLE1 was gradually reduced in the blue module (Figure 7D). We then confirmed the expression of these hub genes by

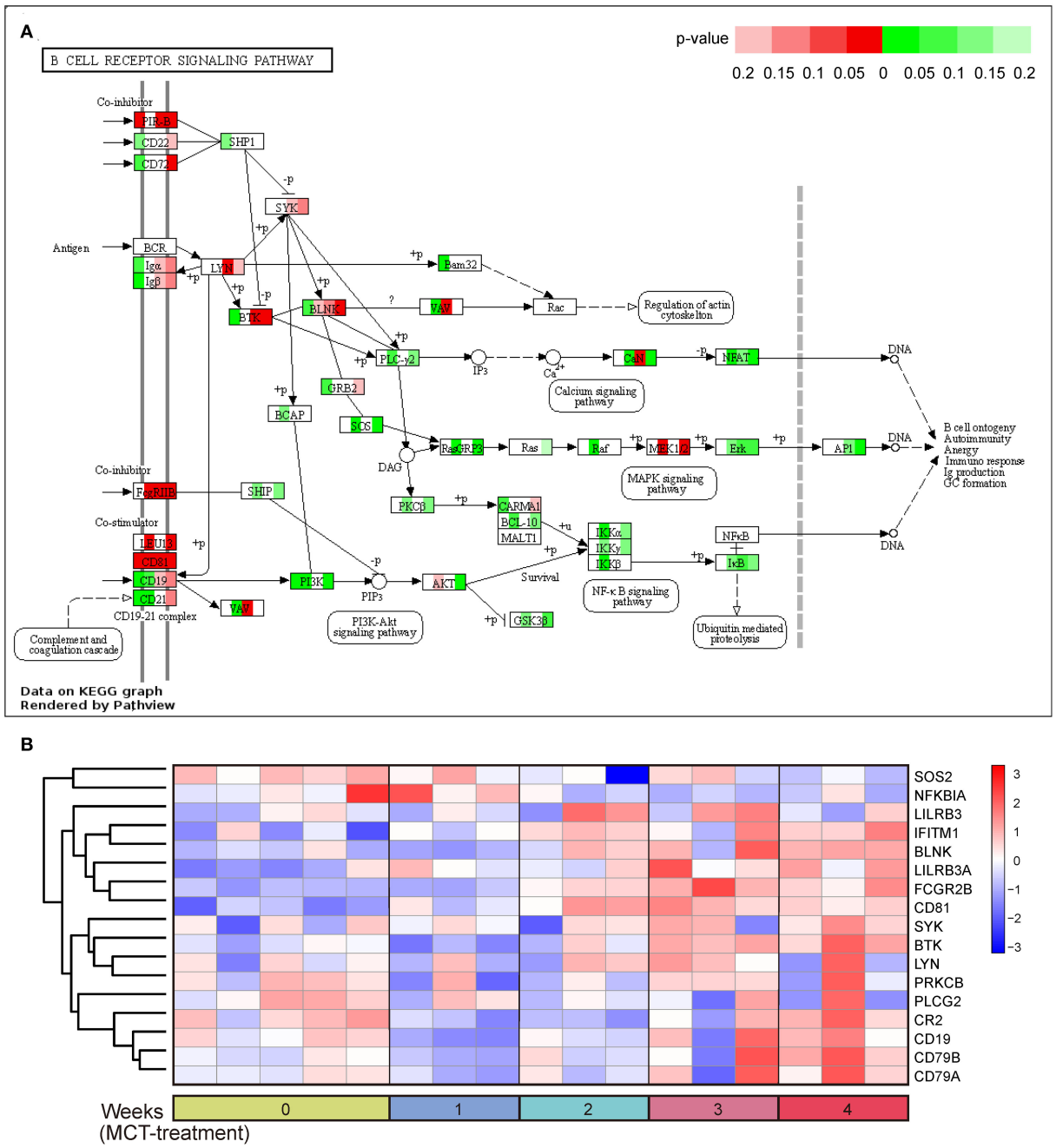

FIGURE 4
B-cell receptor signaling pathway in response to monocrotaline (MCT) treatment. **(A)** The integration and visualization of gene expression in B-cell receptor signaling pathway using modified Pathview. Each colored box represents the comparison of MCT treatment at week 1, 2, 3, and 4 with control, respectively. Color represents *P*-value for each comparison of MCT treatments with control (unpaired *t*-test), red and green represent the elevation and decrease of corresponding gene expression, respectively, while white represents $P \geq 0.2$ or not detected. **(B)** Heatmap plot of differentially expressed genes in B-cell receptor signaling pathway. Rows and columns represent gene expression levels and each sample, respectively. Red and blue represent the elevation and decrease of corresponding gene expression, respectively.

the GSE149899 dataset. As shown in Figure 8, in addition to ACOD1, the expression of CLEC4A1 and CLEC4A3 was increased, while that of FOXF1, BANK1, and TLE1 was reduced.

Discussion

In this study, WGCNA was used to identify pathways and hub genes related to the severity of PAH induced by MCT. We

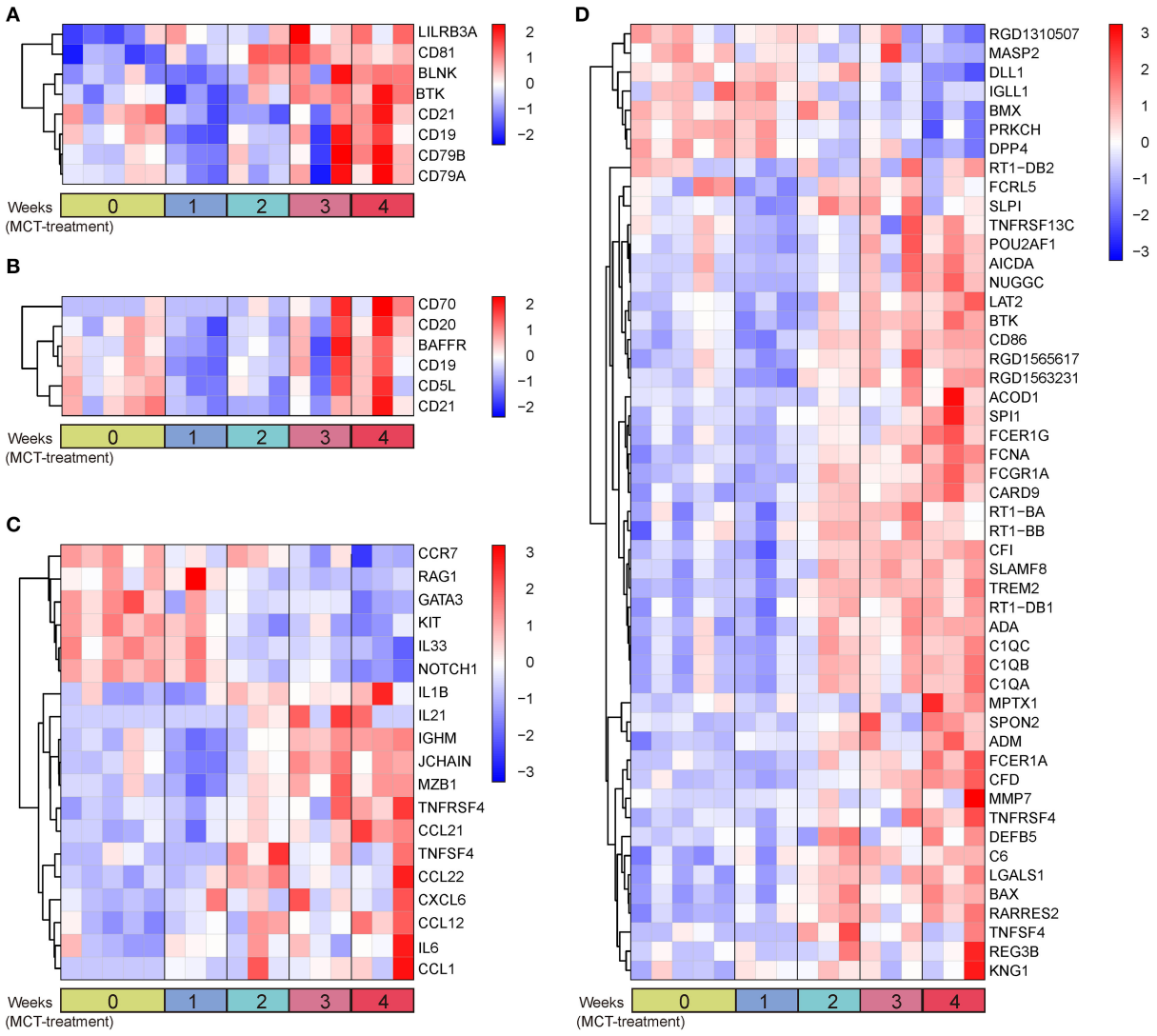

FIGURE 5
Heatmap plot of humoral immune response-associated DEGs. **(A)** Eight overlapped DEGs in GO terms and BCR signaling pathway. **(B)** DEGs in B-cell homeostasis (GO:0001782), activation (GO:0042113), and proliferation (GO:0042100). **(C)** DEGs in immature B-cell differentiation (GO:0002327), immunoglobulin production (GO:0002377), and humoral immune response (GO:0006959). **(D)** DEGs in remaining unassorted terms associated with humoral immune response. Rows and columns represent gene expression levels and each sample, respectively. Red and blue represent the elevation and decrease of corresponding gene expression, respectively.

found the dysregulated BCR signaling pathway and humoral immune response-associated genes in MCT-induced PAH.

We identified a total of 26 gene co-expression modules that were independent of each other. Further analysis was based on the module–trait relationships. Because the blue and dark red module showed the strongest correlation with the phenotypic traits that reflected the severity of PAH, we selected the dark red and blue module as the key modules, and further enrichment analysis was carried out. GO enrichment analysis showed that the genes in key modules were mainly associated with B-cell-mediated humoral response, including B-cell activation, regulation of B-cell activation, positive regulation of B-cell activation, and immunoglobulin production. Moreover, KEGG enrichment analysis showed that the BCR signaling pathway was enriched in both the dark red and blue module. Then, we used Pathview analysis to show the detailed changes in the BCR signaling pathway in MCT-induced PAH. As it was exhibited by Pathview, visualization of global pathway changes showed that the gene expression in the BCR signaling pathway was not synergistic. For instance, the decreased expression of PLC-γ2, PKCβ, and IκBα was identified in the BCR signaling pathway. The decreased levels of IκBα, an inhibitor of NF-κB, activates NF-κB signaling pathway, whereas the reduced levels of PLC-γ2 and PKCβ may limit the activation of the NF-κB signaling

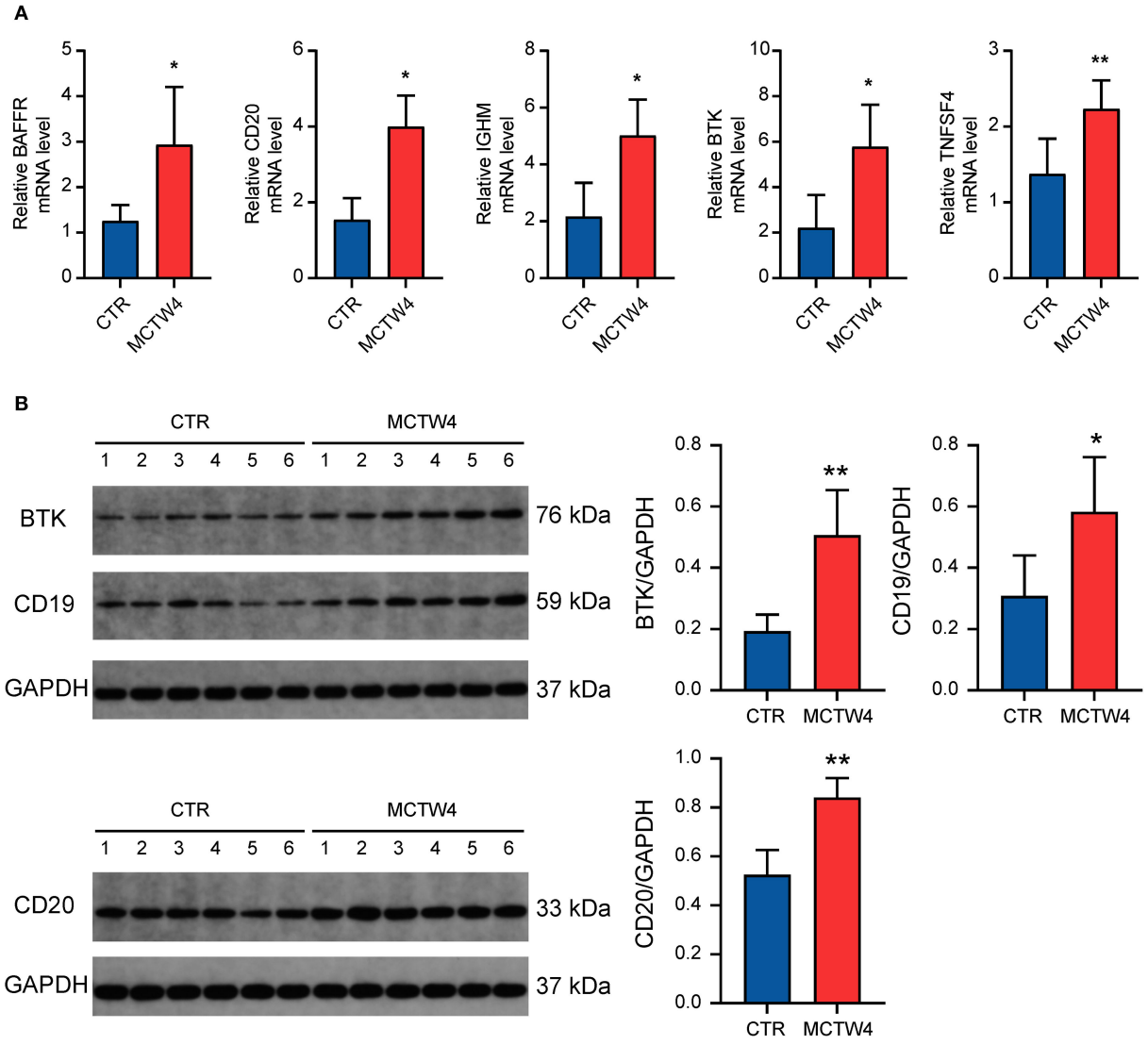

FIGURE 6
Validation of the expression of critical humoral immune response-associated genes. **(A)** Real-time PCR analysis. Data were shown as mean ± SD. $n = 3$ MCT-treated rats at 4 weeks, and $n = 5$ control. $^{*}P < 0.05$ vs control; $^{**}P < 0.01$ vs. control. **(B)** Western blot analysis. Data are shown as mean ± SD. $n = 6$ MCT-treated rats at week 4, and $n = 6$ control. $^{*}P < 0.05$ vs. control; $^{**}P < 0.01$ vs. control. CTR, control; MCTW4, MCT treatment for 4 weeks.

pathway. Therefore, it was possible that the presence of the negative feedback mechanisms restricted the over activated or prolonged BCR signaling pathway in the progression of PAH. The humoral immune response-associated GO terms and BCR signaling have already been enriched in our previous study (5, 12). As a result, the present study may extend and expand B-cell-mediated humoral immunity in the development of PAH.

It is well-established that B cells are essential to humoral immune response and are associated with autoimmune diseases (23). The B-cell-mediated humoral immune response involves a series of processes in which, upon recognition of the specific antigen, B cells are activated, and the activated B cells proliferate to form germinal centers and differentiate into plasma cells to produce antibodies (24). In the present study, a series of B-cell markers, including CD19, CD20, CD79A, and CD79B (25, 26), were elevated. The identification of increased B-cell markers indicated elevated B-cell infiltration in the lung tissues of MCT-induced PAH, which was consistent with current pathological findings (27, 28). Moreover, reduced CCR7 level was identified; of note, the lack of CCR7 resulted in the infiltration of perivascular lymphocytes, including B cells, in pulmonary hypertension (29). Furthermore, some of these B-cell markers were considered as potential targets of B-cell depletion therapy in PAH. For example, rituximab, an anti-CD20 B-cell

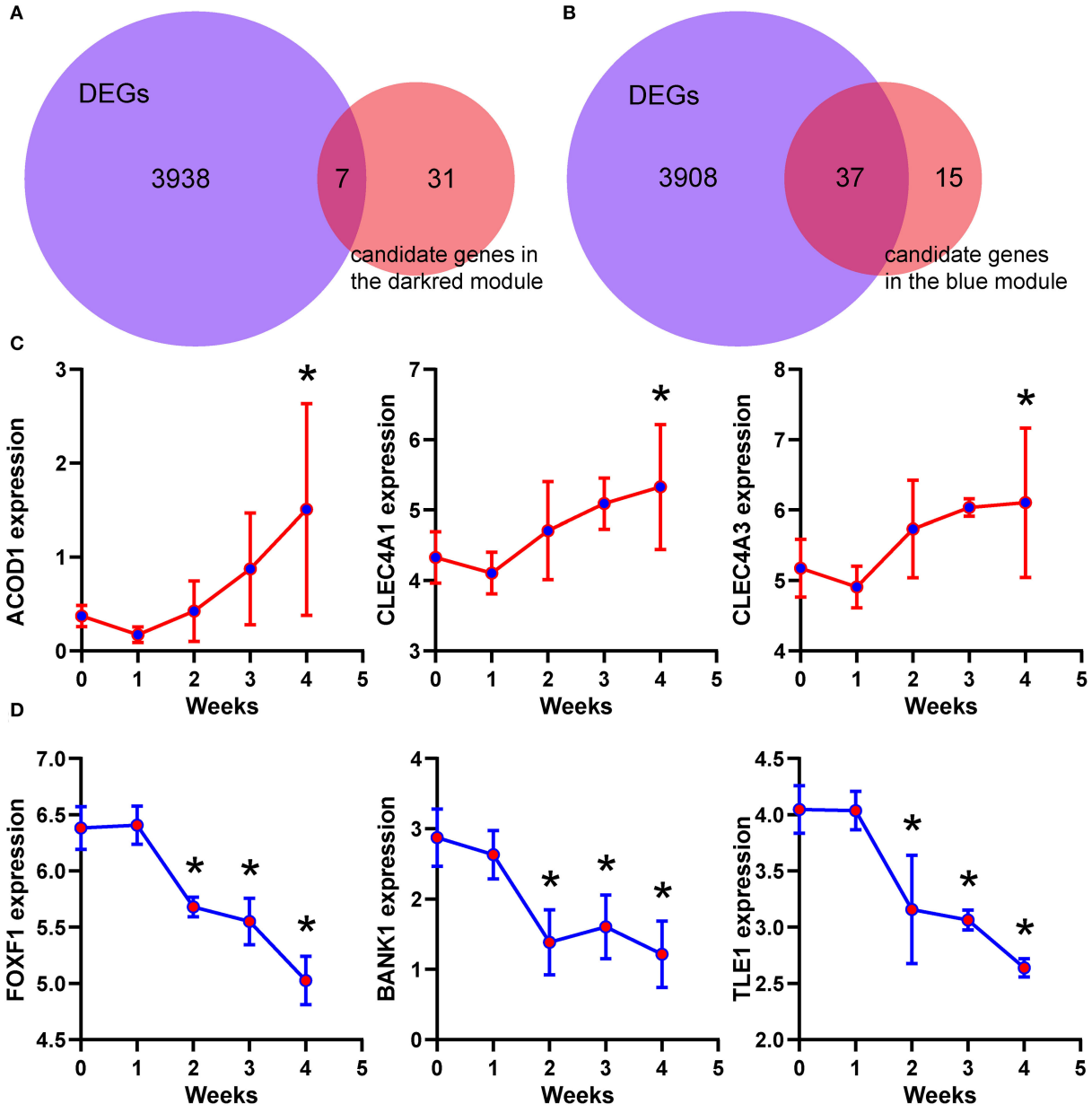

FIGURE 7
Identification of the hub genes. **(A,B)** Venn diagram showing the overlapped gene numbers between differentially expressed genes and candidate genes. **(C,D)** Temporal expression levels of six hub genes. Data are shown as mean ± S.E.M. $n = 3$ MCT-treated rats at each week, and $n = 5$ control. $^{*}P < 0.05$ vs. control.

antibody, had shown accepted safety and tolerability for the treatment of PAH with systemic sclerosis or systemic lupus erythematosus (30, 31).

A set of genes associated with humoral immune response were upregulated, including BAFFR, TNFSF4, TNFRSF4, MZB1, BTK, CD19, and immunoglobulin chain IGHM and JCHAIN. The BAFFR is indispensable for maintaining the development, maturation, and survival of B cells (32). Moreover, the deficiency of BAFFR in either mice or humans results in decreased titers of serum IgM (33, 34). The interaction between TNFSF4 and TNFRSF4 is necessary for differentiating activated B cells into plasma cells and producing antibodies (35). TNFSF4 promoted the affinity maturation of the secondary humoral immune response in B cells, and the knockout of TNFSF4 generated a reduced proportion of germinal center B cells and plasma cells (36). Moreover, a lack of TNFSF4 ameliorated the

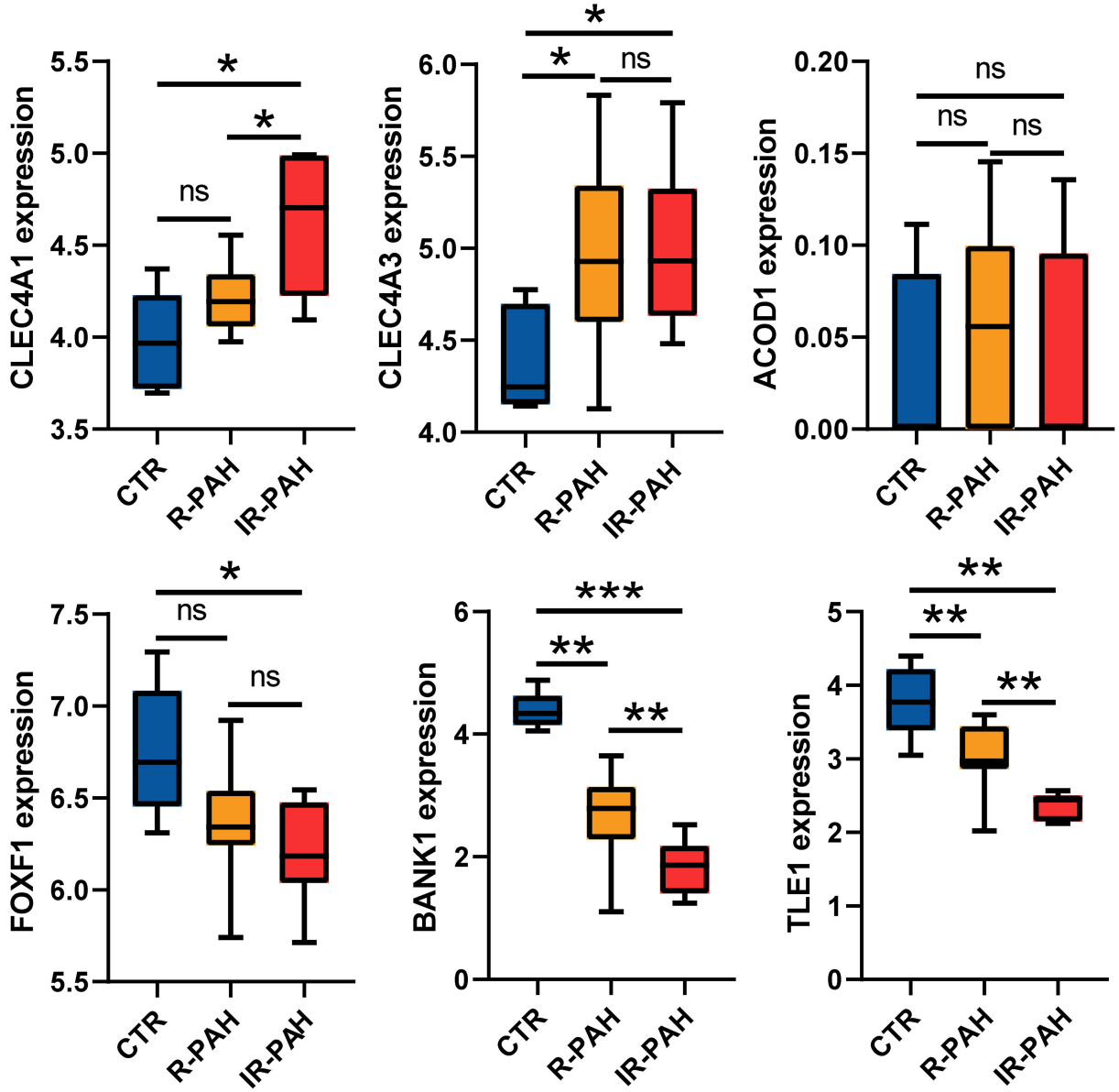

FIGURE 8
Validation of the hub genes. Boxplots showing the expression level of six real hub genes in dataset GSE149899. $^{*}P < 0.05$, $^{**}P < 0.01$, $^{***}P < 0.001$, ns, no significance. CTR, control; R-PAH, reversible pulmonary arterial hypertension; IR-PAH, irreversible pulmonary arterial hypertension.

autoimmune phenotype and reduced the total IgM (36). MZB1 regulates B cells to produce IgM antibodies, and downregulation or deficiency of MZB1 led to impaired IgM secretion (37). CD19 acts as the costimulatory molecule, and plays a crucial role in regulating B-cell-mediated humoral immune response. The deficiency of CD19 severely impaired B-cell maturation and germinal center formation, accompanied by a lack of B cells and IgM (21, 22). In contrast, hCD19 transgenic mice showed significantly spontaneous B-cell proliferation and an overall elevated level of immunoglobulins, including IgM (21). Interestingly, the expression of BAFFR, TNFSF4, TNFRSF4, MZB1, CD19, IGHM, and JCHAIN was elevated in the present study, indicating that B cells were activated to produce antibodies, thus in line with the evidence of local immunoglobulin production in PAH (38). It is noteworthy that activated B cells not only produce antibodies but also secrete a variety of cytokines involved in the immune response, such as IL-1β and IL-6 (20, 39). The identification of elevated cytokines IL-1β and IL-6 suggested enhanced B-cell-mediated antibody-independent functions. BTK is a crucial protein

in BCR signaling, and increased BTK levels are associated with autoimmune diseases (40). The overexpression of BTK-induced spontaneous germinal center formation and production of autoantibodies in CD19-hBTK transgenic mice (41), and moreover, induced pulmonary hypertension through activation of BCR signaling in pulmonary injury mice (42). The BTK expression was upregulated in the present study, further supporting the role of the dysregulated BCR signaling pathway in MCT-induced PAH.

BANK1 is a scaffold protein that is primarily expressed in B lineage cells (43). Functional variant and polymorphism of BANK1 are associated with susceptibility to autoimmune diseases, such as systemic lupus erythematosus (44), rheumatoid arthritis (45), diffuse cutaneous systemic sclerosis (46), and primary Sjogren's syndrome (47), suggesting an important role of BANK1 in autoimmune diseases. Upregulated BANK1 expression was mainly observed in immune tolerance patients (48). By contrast, decreased BANK1 expression was observed in activated B cells and plasma cells (48). It was reported that decreased BANK1 exacerbated B-cell response, resulting in the elevation of autoantibodies in collagen-induced arthritis mice (49) and also augmented germinal center formation and IgM production in BANK1-deficient mice (50). The reduced BANK1 was identified and validated in the present study. It was possible that the downregulation of BANK1 contributed to the loss of immune tolerance in patients and susceptibility to PAH.

FOXF1 is a transcription factor that plays an essential role in lung development (51). FOXF1 regulates pulmonary angiogenesis by regulating STAT3 (52) and VEGF (53, 54) signaling in endothelial cells. The deletion of heterozygous copy number variants and point mutations in FOXF1 is the primary cause of alveolar capillary dysplasia with misalignment of pulmonary veins (55, 56), which is a rare and fatal disease characterized by severe progressive hypoxia and pulmonary hypertension (57). The identification of reduced FOXF1 may partially explain angiogenesis deficiency in pulmonary hypertension.

TLE1 is a corepressor that regulates the transcription of downstream genes by interacting with transcription factors and other proteins (58). Overexpression of TLE1 causes a decrease in nuclear NF-κB translocation, and the deficiency of TLE1 enhanced inflammatory responses mediated by Toll-like receptors (59). Moreover, TLE1 regulates NOD2/NF-κB signaling to mediate inflammatory responses (60, 61). Interestingly, we have reported that dysregulated Toll-like receptor and Nod-like receptor pathways lead to inflammatory cell infiltration and pulmonary vascular remodeling in PAH (12). Thus, TLE1 may act as a negative regulator involved in Toll-like and Nod-like receptor pathways in PAH.

CLEC4A1 and CLEC4A3 are members of the transmembrane C-type lectin receptors (CLRs). CLRs are expressed in various cells, including dendritic cells, B cells, monocytes, and macrophages (62). Damage-associated molecular patterns (DAMPs) can initiate CLR-mediated inflammatory responses that have been linked to allergy (63). We have previously demonstrated that, in MCT-induced PAH, the RIPK3-mediated necroptosis released a series of DAMPs (12). It is likely that CLR-mediated inflammatory responses triggered by DAMPs also participated in the PAH pathogenesis.

Several limitations are present in this study. First, the biological replicates in each MCT treatment group may be limited. Second, the results in this study were based on transcriptomic data, and the protein levels remain unknown. Thus, further studies are needed to validate our results.

Conclusion

In this study, WGCNA was employed to analyze the transcriptome of MCT-induced PAH for the first time. We identify dysregulated BCR signaling pathways and novel genes related to humoral immune response. Thus, these results may provide a novel insight into the molecular mechanisms underlying inflammation and immunity and therapeutic targets for PAH.

Data availability statement

The datasets presented in this study can be found in online repositories. The names of the repository/repositories and accession number(s) can be found below: https://www.ncbi.nlm.nih.gov/geo/, GSE149713, GSE149899 public in 2020.

Author contributions

YC and GX conducted this study. YC wrote the first draft of the manuscript. GX conceptualized this study. GX and YZ revised this manuscript. CW, XW, XZ, ZC, YY, and YZ were responsible for the literature search and reviewed the manuscript. All authors contributed to the article and approved the final version.

Funding

This work was supported by the Open Project of Key Laboratory of Prevention and Treatment of Cardiovascular and Cerebrovascular Disease, Ministry of Education (Grant No. XN202010 to GX) and the Graduate Student Innovation Special Foundation of Jiangxi Province of China (Grant No. YC2021-S800 to YC).

Acknowledgments

We are grateful to Guangzhou Gene Denovo Biotechnology Co. Ltd. for assisting in bioinformatics analysis.

Conflict of interest

The authors declare that the research was conducted in the absence of any commercial or financial relationships that could be construed as a potential conflict of interest.

Publisher's note

Supplementary material

The Supplementary Material for this article can be found online at: https://www.frontiersin.org/articles/10.3389/fcvm.2022.909399/full#supplementary-material

SUPPLEMENTARY FIGURE 1
Heatmap of seven hub genes in the dark red module.

SUPPLEMENTARY FIGURE 2
Heatmap of 37 hub genes in the blue module.

SUPPLEMENTARY TABLE 1
A matrix of GSE149899 dataset.

SUPPLEMENTARY TABLE 2
A matrix of 23,200 transcripts.

SUPPLEMENTARY TABLE 3
Twenty-six biological processes related to humoral immune response.

References

1. Benza RL, Miller DP, Gomberg-Maitland M, Frantz RP, Foreman AJ, Coffey CS, et al. Predicting survival in pulmonary arterial hypertension: insights from the registry to evaluate early and long-term pulmonary arterial hypertension disease management (Reveal). *Circulation.* (2010) 122:164–72. doi: 10.1161/CIRCULATIONAHA.109.898122

2. Rabinovitch M, Guignabert C, Humbert M, Nicolls MR. Inflammation and immunity in the pathogenesis of pulmonary arterial hypertension. *Circ Res.* (2014) 115:165–75. doi: 10.1161/CIRCRESAHA.113.301141

3. Hill NS, Gillespie MN, McMurtry IF. 50 years of monocrotaline-induced pulmonary hypertension: what has it meant to the field? *Chest.* (2017) 152:1106–8. doi: 10.1016/j.chest.2017.10.007

4. Zhuang W, Lian G, Huang B, Du A, Xiao G, Gong J, et al. Pulmonary arterial hypertension induced by a novel method: twice-intraperitoneal injection of monocrotaline. *Exp Biol Med.* (2018) 243:995–1003. doi: 10.1177/1535370218794128

5. Xiao G, Wang T, Zhuang W, Ye C, Luo L, Wang H, et al. RNA sequencing analysis of monocrotaline-induced pah reveals dysregulated chemokine and neuroactive ligand receptor pathways. *Aging.* (2020) 12:4953–69. doi: 10.18632/aging.102922

6. Zupanic A, Bernstein HC, Heiland I. Systems biology: current status and challenges. *Cell Mol Life Sci.* (2020) 77:379–80. doi: 10.1007/s00018-019-03410-z

7. Langfelder P, Horvath S. Wgcna: an r package for weighted correlation network analysis. *BMC Bioinformatics.* (2008) 9:559. doi: 10.1186/1471-2105-9-559

8. Liu W, Li L, Ye H, Tu W. Weighted gene co-expression network analysis in biomedicine research. *Sheng Wu Gong Cheng Xue Bao.* (2017) 33:1791–801. doi: 10.13345/j.cjb.170006

9. Hao S, Jiang P, Xie L, Xiang G, Liu Z, Hu W, et al. Essential genes and mirna-mrna network contributing to the pathogenesis of idiopathic pulmonary arterial hypertension. *Front Cardiovasc Med.* (2021) 8:627873. doi: 10.3389/fcvm.2021.627873

10. Zheng JN Li Y, Yan YM, Shi H, Zou TT, Shao WQ, et al. Identification and validation of key genes associated with systemic sclerosis-related pulmonary hypertension. *Front Genet.* (2020) 11:816. doi: 10.3389/fgene.2020.00816

11. Cai H, Liu H. Immune infiltration landscape and immune-marker molecular typing of pulmonary fibrosis with pulmonary hypertension. *BMC Pulm Med.* (2021) 21:383. doi: 10.1186/s12890-021-01758-2

12. Xiao G, Zhuang W, Wang T, Lian G, Luo L, Ye C, et al. Transcriptomic analysis identifies toll-like and nod-like pathways and necroptosis in pulmonary arterial hypertension. *J Cell Mol Med.* (2020) 24:11409–21. doi: 10.1111/jcmm.15745

13. Yu G, Wang LG, Han Y, He QY. Clusterprofiler: an R package for comparing biological themes among gene clusters. *Omics.* (2012) 16:284–7. doi: 10.1089/omi.2011.0118

14. Luo W, Pant G, Bhavnasi YK, Blanchard SG Jr, Brouwer C. Pathview web: user friendly pathway visualization and data integration. *Nucleic Acids Res.* (2017) 45:W501–w8. doi: 10.1093/nar/gkx372

15. Bai Z, Xu L, Dai Y, Yuan Q, Zhou Z. Ecm2 and Glt8d2 in human pulmonary artery hypertension: fruits from weighted gene co-expression network analysis. *J Thorac Dis.* (2021) 13:2242–54. doi: 10.21037/jtd-20-3069

16. Xiao G, Lian G, Wang T, Chen W, Zhuang W, Luo L, et al. Zinc-mediated activation of creb pathway in proliferation of pulmonary artery smooth muscle cells in pulmonary hypertension. *Cell Commun Signal.* (2021) 19:103. doi: 10.1186/s12964-021-00779-y

17. Treanor B. B-cell receptor: from resting state to activate. *Immunology.* (2012) 136:21–7. doi: 10.1111/j.1365-2567.2012.03564.x

18. Harwood NE, Batista FD. Early events in B cell activation. *Annu Rev Immunol.* (2010) 28:185–210. doi: 10.1146/annurev-immunol-030409-101216

19. Siebenlist U, Brown K, Claudio E. Control of lymphocyte development by nuclear factor-Kappab. *Nat Rev Immunol.* (2005) 5:435–45. doi: 10.1038/nri1629

20. Shen P, Fillatreau S. Antibody-independent functions of B cells: a focus on cytokines. *Nat Rev Immunol.* (2015) 15:441–51. doi: 10.1038/nri3857

21. Engel P, Zhou LJ, Ord DC, Sato S, Koller B, Tedder TF. Abnormal B lymphocyte development, activation, and differentiation in mice that lack or overexpress the Cd19 signal transduction molecule. *Immunity.* (1995) 3:39–50. doi: 10.1016/1074-7613(95)90157-4

22. Rickert RC, Rajewsky K, Roes J. Impairment of T-cell-dependent B-cell responses and B-1 Cell Development in Cd19-Deficient Mice. *Nature.* (1995) 376:352–5. doi: 10.1038/376352a0

23. Khan WN, Wright JA, Kleiman E, Boucher JC, Castro I, Clark ES. B-lymphocyte tolerance and effector function in immunity and autoimmunity. *Immunol Res.* (2013) 57:335–53. doi: 10.1007/s12026-013-8466-z

24. Zhang Y, Garcia-Ibanez L, Toellner KM. Regulation of germinal center B-cell differentiation. *Immunol Rev.* (2016) 270:8–19. doi: 10.1111/imr.12396

25. Loken MR, Shah VO, Hollander Z, Civin CI. Flow cytometric analysis of normal B lymphoid development. *Pathol Immunopathol Res.* (1988) 7:357–70. doi: 10.1159/000157129

26. Wang M, Li Z, Peng Y, Fang J, Fang T, Wu J, et al. Identification of immune cells and mrna associated with prognosis of gastric cancer. *BMC Cancer.* (2020) 20:206. doi: 10.1186/s12885-020-6702-1

27. Colvin KL, Cripe PJ, Ivy DD, Stenmark KR, Yeager ME. Bronchus-associated lymphoid tissue in pulmonary hypertension produces pathologic autoantibodies. *Am J Respir Crit Care Med.* (2013) 188:1126–36. doi: 10.1164/rccm.201302-0403OC

28. Mansueto G, Di Napoli M, Campobasso CP, Slevin M. Pulmonary arterial hypertension (Pah) from autopsy study: T-Cells, B-cells and mastocytes detection

as morphological evidence of immunologically mediated pathogenesis. *Pathol Res Pract.* (2021) 225:153552. doi: 10.1016/j.prp.2021.153552

29. Larsen KO, Yndestad A, Sjaastad I, Loberg EM, Goverud IL, Halvorsen B, et al. Lack of Ccr7 induces pulmonary hypertension involving perivascular leukocyte infiltration and inflammation. *Am J Physiol Lung Cell Mol Physiol.* (2011) 301:L50–9. doi: 10.1152/ajplung.00048.2010

30. Zamanian RT, Badesch D, Chung L, Domsic RT, Medsger T, Pinckney A, et al. Safety and efficacy of B-cell depletion with rituximab for the treatment of systemic sclerosis-associated pulmonary arterial hypertension: a multicenter, double-blind, randomized, placebo-controlled trial. *Am J Respir Crit Care Med.* (2021) 204:209–21. doi: 10.1164/rccm.202009-3481OC

31. Hennigan S, Channick RN, Silverman GJ. Rituximab treatment of pulmonary arterial hypertension associated with systemic lupus erythematosus: a case report. *Lupus.* (2008) 17:754–6. doi: 10.1177/0961203307087610

32. Wang Y, Liu J, Burrows PD, Wang JY, B. Cell Development and maturation. *Adv Exp Med Biol.* (2020) 1254:1–22. doi: 10.1007/978-981-15-3532-1_1

33. Warnatz K, Salzer U, Rizzi M, Fischer B, Gutenberger S, Böhm J, et al. B-cell activating factor receptor deficiency is associated with an adult-onset antibody deficiency syndrome in humans. *Proc Natl Acad Sci U S A.* (2009) 106:13945–50. doi: 10.1073/pnas.0903543106

34. Sasaki Y, Casola S, Kutok JL, Rajewsky K, Schmidt-Supprian M. Tnf family member B cell-activating factor (Baff) receptor-dependent and -independent roles for baff in B cell physiology. *J Immunol.* (2004) 173:2245–52. doi: 10.4049/jimmunol.173.4.2245

35. Stuber E, Strober W. The T cell-B cell interaction Via Ox40-Ox40l is necessary for the t cell-dependent humoral immune response. *J Exp Med.* (1996) 183:979–89. doi: 10.1084/jem.183.3.979

36. Cortini A, Ellinghaus U, Malik TH, Cunninghame Graham DS, Botto M, Vyse TJ, et al. Cell Ox40l supports T follicular helper cell development and contributes to sle pathogenesis. *Ann Rheum Dis.* (2017) 76:2095–103. doi: 10.1136/annrheumdis-2017-211499

37. Wei H, Wang JY. Role of polymeric immunoglobulin receptor in Iga and Igm transcytosis. *Int J Mol Sci.* (2021) 22:2284. doi: 10.3390/ijms22052284

38. Shu T, Xing Y, Wang J. Autoimmunity in pulmonary arterial hypertension: evidence for local immunoglobulin production. *Front Cardiovasc Med.* (2021) 8:680109. doi: 10.3389/fcvm.2021.680109

39. Matsushita T. Regulatory and effector B cells: friends or foes? *J Dermatol Sci.* (2019) 93:2–7. doi: 10.1016/j.jdermsci.2018.11.008

40. Corneth OBJ, Klein Wolterink RGJ, Hendriks RW. Btk signaling in B cell differentiation and autoimmunity. *Curr Top Microbiol Immunol.* (2016) 393:67–105. doi: 10.1007/82_2015_478

41. Kil LP, de Bruijn MJ, van Nimwegen M, Corneth OB, van Hamburg JP, Dingjan GM, et al. Btk levels set the threshold for B-Cell activation and negative selection of autoreactive B cells in mice. *Blood.* (2012) 119:3744–56. doi: 10.1182/blood-2011-12-397919

42. Heukels P, Corneth OBJ, van Uden D, van Hulst JAC, van den Toorn LM, van den Bosch AE, et al. Loss of immune homeostasis in patients with idiopathic pulmonary arterial hypertension. *Thorax.* (2021). doi: 10.1136/thoraxjnl-2020-215460

43. Gómez Hernández G, Morell M, Alarcón-Riquelme ME. The role of Bank1 in B cell signaling and disease. *Cells.* (2021) 10:1184. doi: 10.3390/cells10051184

44. Ramírez-Bello J, Jiménez-Morales S, Montufar-Robles I, Fragoso JM, Barbosa-Cobos RE, Saavedra MA, et al. Blk and Bank1 polymorphisms and interactions are associated in mexican patients with systemic lupus erythematosus. *Inflamm Res.* (2019) 68:705–13. doi: 10.1007/s00011-019-01253-9

45. Ramírez-Bello J, Fragoso JM, Alemán-Ávila I, Jiménez-Morales S, Campos-Parra AD, Barbosa-Cobos RE, et al. Association of Blk and Bank1 polymorphisms and interactions with rheumatoid arthritis in a latin-american population. *Front Genet.* (2020) 11:58. doi: 10.3389/fgene.2020.00058

46. Rueda B, Gourh P, Broen J, Agarwal SK, Simeon C, Ortego-Centeno N, et al. Bank1 functional variants are associated with susceptibility to diffuse systemic sclerosis in caucasians. *Ann Rheum Dis.* (2010) 69:700–5. doi: 10.1136/ard.2009.118174

47. Montúfar-Robles I, Lara-García S, Barbosa-Cobos RE, Vargas-Alarcón G, Hernández-Molina G, Fragoso JM, et al. Blk and Bank1 variants and interactions are associated with susceptibility for primary sjögren's syndrome and with some clinical features. *Cell Immunol.* (2021) 363:104320. doi: 10.1016/j.cellimm.2021.104320

48. Le Berre L, Chesneau M, Danger R, Dubois F, Chaussabel D, Garand M, et al. Connection of Bank1, tolerance, regulatory B cells, and apoptosis: perspectives of a reductionist investigation. *Front Immunol.* (2021) 12:589786. doi: 10.3389/fimmu.2021.589786

49. Yang J, Ren J, Yang Y, Sun J, Zhou X, Zheng S, et al. Bank1 Alters B cell responses and influences the interactions between B cells and induced T regulatory cells in mice with collagen-induced arthritis. *Arthritis Res Ther.* (2018) 20:9. doi: 10.1186/s13075-017-1503-x

50. Aiba Y, Yamazaki T, Okada T, Gotoh K, Sanjo H, Ogata M, et al. Bank negatively regulates akt activation and subsequent B cell responses. *Immunity.* (2006) 24:259–68. doi: 10.1016/j.immuni.2006.01.002

51. Costa RH, Kalinichenko VV, Lim L. Transcription factors in mouse lung development and function. *Am J Physiol Lung Cell Mol Physiol.* (2001) 280:L823–38. doi: 10.1152/ajplung.2001.280.5.L823

52. Pradhan A, Dunn A, Ustiyan V, Bolte C, Wang G, Whitsett JA, et al. The S52f Foxf1 mutation inhibits Stat3 signaling and causes alveolar capillary dysplasia. *Am J Respir Crit Care Med.* (2019) 200:1045–56. doi: 10.1164/rccm.201810-1897OC

53. Karolak JA, Gambin T, Szafranski P, Maywald RL, Popek E, Heaney JD, et al. Perturbation of semaphorin and vegf signaling in acdmpv lungs due to Foxf1 deficiency. *Respir Res.* (2021) 22:212. doi: 10.1186/s12931-021-01797-7

54. Ren X, Ustiyan V, Pradhan A, Cai Y, Havrilak JA, Bolte CS, et al. Foxf1 transcription factor is required for formation of embryonic vasculature by regulating vegf signaling in endothelial cells. *Circ Res.* (2014) 115:709–20. doi: 10.1161/CIRCRESAHA.115.304382

55. Stankiewicz P, Sen P, Bhatt SS, Storer M, Xia Z, Bejjani BA, et al. Genomic and genic deletions of the fox gene cluster on 16q241 and inactivating mutations of Foxf1 cause alveolar capillary dysplasia and other malformations. *Am J Hum Genet.* (2009) 84:780–91. doi: 10.1016/j.ajhg.2009.05.005

56. Cai Y, Bolte C, Le T, Goda C, Xu Y, Kalin TV, et al. Foxf1 maintains endothelial barrier function and prevents edema after lung injury. *Sci Signal.* (2016) 9:ra40. doi: 10.1126/scisignal.aad1899

57. Slot E, Edel G, Cutz E, van Heijst A, Post M, Schnater M, et al. Alveolar capillary dysplasia with misalignment of the pulmonary veins: clinical, histological, and genetic aspects. *Pulm Circ.* (2018) 8:2045894018795143. doi: 10.1177/2045894018795143

58. Agarwal M, Kumar P, Mathew SJ. The Groucho/Transducin-like enhancer of split protein family in animal development. *IUBMB Life.* (2015) 67:472–81. doi: 10.1002/iub.1395

59. Ramasamy S, Saez B, Mukhopadhyay S, Ding D, Ahmed AM, Chen X, et al. Tle1 tumor suppressor negatively regulates inflammation in vivo and modulates Nf-?b inflammatory pathway. *Proc Natl Acad Sci USA.* (2016) 113:1871–6. doi: 10.1073/pnas.1511380113

60. Chen W, Zheng D, Mou T, Pu J, Dai J, Huang Z, et al. Tle1 attenuates hepatic ischemia/reperfusion injury by suppressing Nod2/Nf-Kb signaling. *Biosci Biotechnol Biochem.* (2020) 84:1176–82. doi: 10.1080/09168451.2020.1735928

61. Nimmo ER, Stevens C, Phillips AM, Smith A, Drummond HE, Noble CL, et al. Tle1 modifies the effects of Nod2 in the pathogenesis of Crohn's disease. *Gastroenterology.* (2011) 141:972-81. doi: 10.1053/j.gastro.2011.05.043

62. Eklow C, Makrygiannakis D, Backdahl L, Padyukov L, Ulfgren AK, Lorentzen JC, et al. Cellular distribution of the C-Type Ii lectin dendritic cell immunoreceptor (Dcir) and its expression in the rheumatic joint: identification of a subpopulation of Dcir+ T cells. *Ann Rheum Dis.* (2008) 67:1742–9. doi: 10.1136/ard.2007.076976

63. Kostarnoy AV, Gancheva PG, Lepenies B, Tukhvatulin AI, Dzharullaeva AS, Polyakov NB, et al. Receptor mincle promotes skin allergies and is capable of recognizing cholesterol sulfate. *Proc Natl Acad Sci USA.* (2017) 114:E2758–e65. doi: 10.1073/pnas.1611665114

Frontiers in
Cardiovascular Medicine

Innovations and improvements in cardiovascular treatment and practice

Focuses on research that challenges the status quo of cardiovascular care, or facilitates the translation of advances into new therapies and diagnostic tools.

Discover the latest Research Topics

See more →

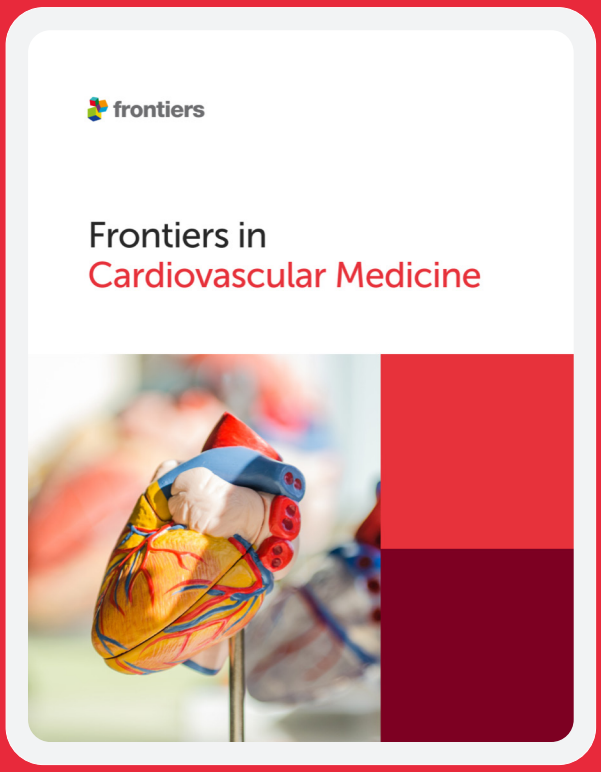

Frontiers

Avenue du Tribunal-Fédéral 34
1005 Lausanne, Switzerland
frontiersin.org

Contact us

+41 (0)21 510 17 00
frontiersin.org/about/contact